A Dissertation

Entitled

Creep, Fatigue, and Their Interaction at Elevated Temperatures in Thermoplastic Composites

by

Mohammadreza Eftekhari

Submitted to the Graduate Faculty as partial fulfillment of the
requirements for the Doctor of Philosophy Degree in Engineering

Dr. Ali Fatemi, Committee Chair

Dr. Mohamed Samir Hefzy, Committee Member

Dr. Saleh Jabarin, Committee Member

Dr. Joseph Lawrence, Committee Member

Dr. Efstratios Nikolaidis, Committee Member

Dr. Amanda Bryant-Friedrich, Dean
College of Graduate Studies

The University of Toledo

August 2016

An Abstract of

Creep, Fatigue, and Their Interaction at Elevated Temperatures in Thermoplastic Composites

by

Mohammadreza Eftekhari

Submitted to the Graduate Faculty as partial fulfillment of the
requirements for the Doctor of Philosophy Degree in Engineering

The University of Toledo
August 2016

Thermoplastic composites are suitable alternatives to metals in some load-bearing applications such as in the automotive industry due to a large number of advantages they present. These include light weight, ease of processing for complex geometries at high production rate, outstanding cost to performance ratio, ability to reprocess, and corrosion resistance. Addition of fillers such as talc or reinforcements such as short glass fibers can improve the mechanical performance of unreinforced thermoplastics to a high degree.

Components made of thermoplastic composites are typically subjected to complex loadings in applications including static, cyclic, thermal, and their combinations. These applications may also involve environmental conditions such as elevated temperature and moisture which can dramatically affect their mechanical properties.

This study investigated tensile, creep, fatigue, creep-fatigue interaction, and thermo-mechanical fatigue (TMF) behaviors of five thermoplastic composites including short glass fiber reinforced and talc-filled polypropylene, short glass fiber reinforced polyamide-6.6, and short glass fiber reinforced polyphenylene ether and polystyrene under a variety of conditions. The main objectives were to evaluate aforementioned mechanical behaviors of these materials at elevated temperatures and to develop predictive models to reduce their development cost and time.

Tensile behavior was investigated including effects of temperature, moisture, and hygrothermal aging. Kinetics of water absorption and desorption were investigated for polyamide-6.6 composite and Fickian behavior was observed. The reductions in tensile strength and elastic modulus due to water absorption were represented by mathematical relations as a function of moisture content. In addition to moisture content, aging time was also found to influence the tensile behavior. A parameter was introduced for correlations of normalized stiffness and strength with different aging times and temperatures. Higher strength and stiffness were obtained for re-dried specimens after aging which was explained by an increase in crystallinity. Mechanisms of failure were identified based on fracture surface microscopic analysis for different conditions.

Creep behavior was investigated and modeled at room and elevated temperatures. Creep strength decreased and both creep strain and creep rate increased with increasing temperature. The Larson-Miller parameter was able to correlate the creep rupture data of all materials. The Monkman-Grant relation and its modification were successfully used to correlate minimum creep rate, time to rupture, and strain at rupture data. The Findley power law and time-stress superposition principle (TSS) were used to represent non-linear viscoelastic creep curves. Long-term creep behavior was also satisfactory predicted based on short-term test data using the TSS principle.

Effect of cycling frequency on fatigue behavior was investigated by conducting load-controlled fatigue tests at several stress ratios and at several temperatures. A beneficial

or strengthening effect of increasing frequency was observed for some of the studied materials, before self-heating became dominant at higher frequencies. A reduction in loss tangent (viscoelastic damping factor), width of hysteresis loop, and displacement amplitude, measured in load-controlled fatigue tests, was observed by increasing frequency for frequency sensitive materials. Reduction in loss tangent was also observed for frequency sensitive materials in dynamic mechanical analysis tests. It was concluded that the fatigue behavior is also time-dependent for frequency sensitive materials. A Larson-Miller type parameter was used to correlate experimental fatigue data and relate stress amplitude, frequency, cycles to failure, and temperature together.

Effects of temperature and mean stress on fatigue behavior were also investigated by conducting load-controlled fatigue tests under positive stress ratios and at room and elevated temperatures. Larson-Miller parameter was used and a shift factor of Arrhenius type was developed to correlate fatigue data at various temperatures. Effect of mean stress on fatigue life was significant for some of the studied materials, however, for the polyphenylene ether and polystyrene blend no effect of mean stress was observed. Modified Goodman and Walker mean stress equations were evaluated for their ability to correlate mean stress data. A general fatigue life prediction model was also used to account for the effects of mean stress, temperature, anisotropy, and frequency.

Creep-fatigue tests were conducted using trapezoidal load signal with hold-time periods. Effects of temperature, frequency, load level, mean stress, and hold-stress position on creep-fatigue interaction behavior were studied. In-phase TMF tests were conducted on polyamide-based composite for the temperature variation between 85 to 120 °C. Significant non-linearity was observed for the interaction of creep and fatigue damage. The

applicability of Chaboche non-linear creep-fatigue interaction model to predict creep-fatigue and TMF lives for thermoplastic composites was investigated. A frequency term was added to the model to consider the beneficial effect of increased frequency observed for some the studied materials. The Chaboche model constants were obtained by using pure fatigue, pure creep, and one creep-fatigue interaction experimental data. More than 90% of life predictions by the Chaboche model were within a factor of 2 of the experimental life for both creep-fatigue and TMF test conditions.

This dissertation is dedicated to all my family.

Acknowledgments

I would like to thank continuous support of my dear adviser Prof. Ali Fatemi during the last four years. This work really would not be finished without his daily encouragement, patient and guidance. I also would like to acknowledge Dr. Mohammad Samir Hefzy, Dr. Saleh Jabarin, Dr. Joseph Lawrence and Dr. Efstratios Nikolaidis for serving as committee members.

General Motors provided the funding for this work and technical assistance of Dr. A.K. Khosrovaneh is very much appreciated. The assistance of Mr. John Jaegly at UT in helping troubleshooting of testing facilities and time and effort of Mr. Tim Grivanos in preparing test specimens are also appreciated. I am grateful to all my colleagues at the Fatigue and Fracture Research Laboratory for their support and fruitful relationships thorough my doctoral studies.

I would like to thank and dedicate all my success to my lovely wife, Farinaz for her continuous encouragement and support.

Last but not least, I would like to thank my parents for all their support throughout my education from elementary school to doctoral degree. Everyday support of my brother and sisters are also very much appreciated. Many thanks for my parents-in-law for their continuous encouragement.

Table of Contents

Abstract iii

Acknoledgments viii

Table of Contents ix

List of Figures xiii

List of Tables xxiv

List of Nomenclature xxvi

List of Abbreviations xxx

1. Introduction 1

1.1 Motivation for the Study and Objectives 1

1.2 Outline of Dissertation 4

2. Literature Review 8

2.1 Tensile Behavior 8

2.2 Effects of Thermal and Hygrothermal Agings on Tensile Behavior 15

2.3 Creep Behavior 23

2.4 Isothermal Fatigue Behavior 28

2.5 Thermo-Mechanical Fatigue and Creep-Fatigue Interaction 32

2.6 Summary 37

3. Experimental Program and Procedures 58

3.1 Material Fabrication and Descriptions 58

3.1.1 40 wt% talc-filled polypropylene (PP-T) and 30 wt% short glass fiber reinforced polypropylene (PP-G) 58

3.1.2 30 wt% short glass fiber reinforced polyamide-6.6 (PA66/B and PA66/D) 60

3.1.3 20 wt% short glass fiber reinforced polyphenylene ether and polystyrene (PPE/PS) 62

3.1.4 PP, PO, PA6, and PBT from previous works 63

3.2 Material Storage, Drying Conditions, Specimen Geometry and Preparation 63

3.3 Testing Equipment 64

3.4 Testing Procedures 66

4. Tension Test Results and Analysis 78

4.1 Introduction 78

4.2 Tensile Properties 81

4.3 Temperature Effect 82

4.4 Moisture and Hygrothermal Effects 85

4.5 Moisture Absorption of PA66/B 87

4.6 Effect of Water Absorption on Tensile Properties of PA66/B 90

5. Creep Test Results and Analysis 112

5.1 Introduction 112

5.2 Creep Properties 115

5.3 Creep Rupture Data and Modeling 115

5.4 Creep Strain-Time Behavior and Predictions 117

5.5 Minimum Creep Rate Data and Correlations 119

5.6 Long-Term Creep Tests and Predictions 122

  5.6.1 Time-stress superposition principle for long-term creep predictions 122

  5.6.2 Experimental results versus predictions 124

6. Viscoelastic Deformation and Frequency Effect on Fatigue Behavior 147

6.1 Introduction 147

6.2 Viscoelastic Behavior and Characterization 152

6.3 Frequency Effect 155

  6.3.1 Experimental results 155

  6.3.2 Discussion of results 158

6.4 Correlation of Fatigue Data with a Larson-Miller Type Model 161

7. Isothermal Fatigue Test Results and Analysis 177

7.1 Introduction 177

7.2 Temperature Effect 180

  7.2.1 Experimental results and failure mechanisms 180

  7.2.2 Modeling the temperature effect 181

7.3 The Effect of Talc and Short Glass Fiber Additions on Fatigue Behavior of Polypropylene 183

7.4 Mean Stress Effect and Modeling 184

7.5 Correlation of Fatigue Data with a General Model 188

8. Creep-Fatigue Interaction and Thermo-Mechanical Fatigue Test Results and Analysis 209

8.1 Introduction 210

8.2 Application of Chaboche Creep-Fatigue Interaction Model to the Studied Materials 213
8.2.1 Creep damage model 214
8.2.2 Fatigue damage model 215
8.2.3 Interaction effects of creep and fatigue damages 218
8.2.4 TMF modeling 219
8.3 Results of Experimental Work and Predictive Models 219
8.3.1 Creep and fatigue behaviors 219
8.3.2 Creep-fatigue interaction behavior 221
8.3.3 TMF behavior 223
8.4 Discussion of Results and Extension of the Chaboche Model for General Cases 224
9. Summary and Conclusions 239
9.1 Conclusions of Tensile Behavior Characterization 239
9.2 Conclusions of Creep Behavior Characterization 240
9.3 Conclusions of Isothermal Fatigue Behavior Characterization 241
9.4 Conclusions of Creep-Fatigue Interaction and TMF Behavior Characterizations 244
9.5 Possible Directions for Future Investigation 244
Refrences 246

List of Figures

Figure 1-1: Schematic load history, including fatigue, creep, and creep-fatigue loadings. 6

Figure 1-2: Overview of the study. 7

Figure 2-1: Failure behavior map for a short glass fiber reinforced polyethylene terephthalate (Regenerated) [5]. 40

Figure 2-2: Variation of stress at rupture with temperature for different polyamide-6.6 composites. Material 1 is continuous fiber composite, material 2, 3 and 4 are short glass fiber composites with average fiber length of 9, 3 and 0.3 mm respectively (Regenerated) [6]. 40

Figure 2-3: Variation of tensile strength with strain rate at various temperatures for a glass fiber-epoxy resin composite. (○) 20 °C, (☐) 40 °C, (●) 60 °C, (■) 80 °C, and (△) 100 °C (Regenerated) [13]. 41

Figure 2-4: Effects of temperature and strain rate on (a) stress exponent, *n*, and, (b) stress coefficient, σ^*, of 33 wt% short glass fiber reinforced polyamide-6 in transverse direction (Regenerated) [18]. 41

Figure 2-5: Comparison of stress–strain curves for 1 mm thick specimens of short glass fiber reinforced polyamide-6.6 in different directions at RT and 130 °C [21]. 42

Figure 2-6: Effect of temperature on (a) elongation and (b) tensile strength for 60 wt% short fiber reinforced poly-phenylene sulfide composite in longitudinal and transverse directions (Regenerated) [23]. 43

Figure 2-7: Effect of temperature on normalized tensile strength of welded and unwelded 30 wt% short glass fiber reinforced nylon-6 [24]. 43

Figure 2-8: Master curve generated using time-temperature superposition principle for PBT in the transverse direction [26]. 44

Figure 2-9: Effects of aging time and temperature on relative tensile strength of polyamide-6 and polyamide-6.6 short glass fiber reinforced composites (Regenerated) [30]. 44

Figure 2-10: Variation of diffusion coefficient (*D*) with temperature for polyethylene terephthalate, PET (●) and polybutylene terephthalate, PBT (○) (Regenerated) [33]. 45

Figure 2-11: Arrhenius type plot for variation of diffusion coefficient with temperature for reinforced and unreinforced nylon-6.6 (Regenerated) [35]. 45

Figure 2-12: Stress-strain curves for un-aged, aged, and re-dried 40 wt% short carbon fiber reinforced nylon-6.6 at 20 °C (Regenerated) [35]. 46

Figure 2-13: Water absorption of polyamide-6 specimens with different fiber content weight at different temperatures [39]. 47

Figure 2-14: Effect of temperature on compressive creep behavior of discontinues glass fiber phenolic composites with fibers in transverse direction [45]. 48

Figure 2-15: Flexural creep modulus versus time curves at 121 °C under stress level of 24.1 MPa for (a) reinforced polypropylene specimens, (b) reinforced polycarbonate specimens (Regenerated) [46]. 48

Figure 2-16: Double logarithmic plots of minimum creep rate versus stress at 23 and 80 °C. PP is neat polypropylene. SA2, SA4, SA8 and SA13 are polypropylene-based composites with respectively 5, 10, 20 and 30 wt% short glass fiber content with standard fiber/matrix adhesion. EA8 and EA13 are polypropylene-based composites with respectively 20 and 30 wt% short glass fiber content with elevated fiber/matrix adhesion (Regenerated) [47]. 49

Figure 2-17: Crack speed vs. time for creep tests performed at various temperatures for short glass fiber reinforced polypropylene composite [48]. 50

Figure 2-18: Time–temperature–stress superposition master curves for several short glass fiber composites at a reference temperature of 50 °C [50]. 50

Figure 2-19: Fatigue strength master curve for polyamide-6 and polyamide-6.6 short glass fiber thermoplastic composites incorporating temperature and aging time effects [30]. 51

Figure 2-20: (a) Dependence of *S*-*N* curves on temperature, (b) representation of all fatigue data at different temperatures and frequencies by a master curve, (c) variation of slope and, (d) intercept of *S*-*N* lines with temperature for short glass fiber reinforced polyamide-6.6 [55]. 52

Figure 2-21: (a) Effect of temperature on fatigue behavior at R = 0 [57] and, (b) Influence of notches on fatigue strength at 130 °C under R = -1 condition in the longitudinal direction for short glass fiber reinforced polyamide-6.6 (Regenerated) [56]. 53

Figure 2-22: Temperature dependence of the slope *A* and intercept *B* of *S*-*N* curves for short glass fiber reinforced polyamide-6.6 at 20 Hz [58]. 54

Figure 2-23: Effect of temperature and fiber orientation on fatigue behavior of short glass fiber reinforced polyamide-6 [59]. k_1 values on the graph are reciprocals of the slope of *S*-*N* lines. 54

Figure 2-24: Equivalent stress amplitude versus fatigue life for PBT and PA6 at different temperatures in longitudinal, 18°, 45°, and transverse directions at R = -1, 0.1 and 0.3 loading conditions [61]. 55

Figure 2-25: (a) Excerpt of TMF data set (T_{min} = -40 °C) and, (b) master curve of SED range versus cycles to failure correlating TMF and isothermal smooth and notch specimen fatigue data for short glass fiber reinforced polybutylene terephthalate at different temperatures and pre-strain levels [65]. 56

Figure 2-26: Cross plot of fractional stress rupture damage against fractional fatigue damage for polyethylene pipe line component [66]. 57

Figure 2-27: Total crack velocity, (*da/dt*) total, during FCP tests of glass fiber reinforced polypropylene composites at (○) 0.1 Hz, (□) 1 Hz, and (△) 10 Hz compared with the calculated (▼) pure creep component,(*da/dt*) creep; and pure fatigue components, (*da/dt*) fatigue at (●) 0.1 Hz, (■) 1 Hz, and (▲) 10 Hz [69]. 57

Figure 3-1: (a) Isotactic structure of polypropylene [72], and (b) repeated structure unit of polyamide [94]. 72

Figure 3-2: (a) Location of specimens cut from injection molded plaques in the transverse direction (arrows indicate the injection molding direction and the dashed areas are discarded materials). (b) Specimen geometry used for the experimental study (dimensions are in mm) [78]. 73

Figure 3-3: (a) Different failure locations are shown as IGIT (Orange), OGIT (Red), and OGOT (Yellow). (b) Specimen grip locations for (1) monotonic tension and creep tests and (2) the majority of fatigue and creep-fatigue tests, and (3) the distance of the marks for the video extensometer. (Dimensions are in mm) [78]. 73

Figure 3-4: (a) Instron 8801 servo-hydraulic testing machine used for tensile, short-term creep, fatigue and creep-fatigue tests shown with computer and controller, and (b) Instron M3 creep test machine with lever arm used for long-term creep tests. 74

Figure 3-5: (a) Video extensometer used for tensile and creep tests. (b) A marked test specimen illuminated with the optical LED array. 75

Figure 3-6: Instron 3119-506 environmental chamber attached to the Instron 8801 testing machine. 75

Figure 3-7: FLIR i7 model thermal imaging camera. 76

Figure 3-8: Perkin Elmer Q800 DMA machine 76

Figure 3-9: Hitachi S-4800 scanning electron microscope. 77

Figure 4-1: Calculated tensile properties from a monotonic tension test; (a) engineering stress versus engineering strain curve, and measured properties according to ISO 527 and ASTM D638, and (b) true stress versus true plastic strain curve in log-log scale, and K and n values calculated from the fit of data. 95

Figure 4-2: Effect of temperature on tensile stress-strain curve of (a) PP-T, (b) PP-G, (c) PA66/B, (d) PA66/D, and (e) PPE/PS in the transverse direction under displacement rate of 1 mm/min. 97

Figure 4-3: Comparison of tensile stress-strain curves of (a) PP-T and PP-G, and (b) PA66/B and PA66/D at different temperatures. 98

Figure 4-4: Variation of ultimate (S_u) and yield (S_y) strength and ASTM elastic modulus (E) with temperature for (a) PP-T and PP-G, (b) PA66/B and PA66/D, and (c) PPE/PS. Hashed areas are the range for T_g 99

Figure 4-5: Variation of (a) normalized ultimate tensile strength and, (b) elastic modulus (with respect to their values at 23 °C) with temperature for PP-T, PP-G, PA66/B, PA66/D, and PPE/PS. 100

Figure 4-6: SEM pictures of fractured surface of PA66/B tensile specimens at 23 °C (a, b) and 85 °C (c, d) in dry as-molded condition. Figures b and d are from the shell layer. 101

Figure 4-7: Stress-strain curves (solid lines) and corresponding Ramberg-Osgood equation representation (dash lines) at different temperatures for (a) PP-T, (b) PP-G, (c) PA66/B, (d) PA66/D, and (d) PPE/PS in the transverse direction at displacement rate of 1 mm/min in DAM condition. 103

Figure 4-8: Effect of water absorption on tensile stress-strain curve of (a) PP-T, (b) PP-G, (c) PPE/PS, and PA66/B at testing temperature of 23 °C. [%wt of moisture absorption, immersion time, immersion temperature]. Duplicate tests were conducted for DAM condition of all the materials. 104

Figure 4-9: Stress-strain curves of PA66/B specimens aged for 14 months in the laboratory environment with different drying conditions. 105

Figure 4-10: Water absorption at 23 °C and 85 °C water, and water desorption at 85 °C in vacuumed oven for PA66/B. The curves correspond to Fick’s law. 106

Figure 4-11: Tensile stress-strain curves at different water absorption conditions showing the effect of water absorption for PA66/B at (a) 23 °C and (b) 85 °C. [% wt of moisture absorption, immersion time, immersion temperature]. Duplicate tests were conducted for DAM condition in both figures. 107

Figure 4-12: DSC thermographs of unaged and aged PA66/B. 108

Figure 4-13: Variation of ultimate tensile strength (S_u) and elastic modulus (E) with water absorption at (a) 23 °C and (b) 85 °C. Variation of normalized ultimate tensile strength and elastic modulus as a function of (c) moisture content and, (d) $M_t\, t^{0.5}$ at 23 °C and 85 °C. 109

Figure 4-14: SEM micrographs of the PA66/B fracture surface in the core layer after tensile tests of (a) DAM at 23 °C, (b) DAM at 85 °C, (c) with 5.4 wt% moisture (saturated) tested at 23 °C, (b) with 5.4 wt% moisture (saturated) tested at 85 °C, and (e) re-dried specimen after desorption of 5.4 wt% moisture tested at 23 °C. 110

Figure 4-15: SEM micrographs of the glass fiber for PA66/B on tension test fracture surface of (a) DAM at 23 °C, (b) DAM at 85 °C, (c) with 5.4 wt% moisture (saturated) at 23 °C, (b) with 5.4 wt% moisture (saturated) at 85 °C, and (e) re-dried specimen after absorption of 5.4 wt% moisture. 111

Figure 5-1: Example creep curve showing the three stages of deformation based on the change in strain vs. time. 130

Figure 5-2: Effect of temperature on creep rupture of (a) PP-T, (b) PP-G, (c) PA66/B, and (d) PPE/PS in the transverse direction. Lines are fits to experimental data. Arrows show tests that did not fail and are not included in the fits. 131

Figure 5-3: Normalized creep rupture data with tensile strength for (a) PO, PP, PP-T, and PP-G and, (b) PA66/B, PPE/PS, PBT, and PA6 at different temperatures. 132

Figure 5-4: Correlations of (a) *A* and, (b) *B* values with S_u for all the materials at different temperatures and fiber orientations. The conditions associated with the symbols are the same as those in Figure 5-3. 133

Figure 5-5: LMP master curves for (a) PO, PP, PP-T, and PP-G in the transverse direction and, (b) PA66/B, PPE/PS, PA6 in the transverse direction and for PBT in both transverse and longitudinal directions. 134

Figure 5-6: Creep strain versus time curves for (a) PP-T, (b) PP-G, (c) PA66/B, (d) PPE/PS at 85 °C in the transverse direction. 135

Figure 5-7: Creep strain versus time curves at 85 °C for (a) PO, PP, PP-T, and PP-G and for, (b) PA66/B, PPE/PS, PBT, and PA6. 136

Figure 5-8: (a) Effect of temperature on creep strain curves of PP-G under stress level of 75% of S_u. (b) Comparison of PP-T and PP-G creep strain curves at 23 °C and 85 °C under stress level of 62% of S_u. 137

Figure 5-9: Comparison of predicted creep strain curves using Findley power law model (dash lines) with experimental creep strain curves of PP-G at different stress levels in the transverse direction at (a) 23 °C, (b) 85 °C, and (c) 120 °C. 138

Figure 5-10: Minimum creep rate versus stress data with corresponding power law fits for (a) PO, (b) PP, (c) PP-T, (d) PP-G, (e) PA66/B, (f) PPE/PS, (g) PBT, and (h) PA6. 139

Figure 5-11: Minimum creep rate versus normalized stress with tensile strength data for (a) PO, PP, PP-T, and PP-G and, (b) PA66/B, PPE/PS, PBT, and PA6 at different temperatures. 140

Figure 5-12: Correlation of (a) $\dot{\varepsilon}_{\min}$ and t_R using Monkman-Grant relation and (b) $\dot{\varepsilon}_{\min}$, t_R and ε_R using modified Monkman-Grant relation, for PP-G at 23, 85 and 120 °C. 141

Figure 5-13: Correlation of $\dot{\varepsilon}_{\min}$ and t_R using Monkman-Grant relation for (a) all the studied materials. (b) Correlation of $\dot{\varepsilon}_{\min}$, t_R and ε_R using modified Monkman-Grant relation for PO, PP, PP-T, and PP-G. 142

Figure 5-14: (a) TSS procedure for generating master curve and shift factors for PP-G at 85 °C. (b) Master curves and (c) corresponding shift factor versus stress plots for PP-G at 23 and 85 °C. Comparison of predictive creep strain (dash lines) using TSS and experimental creep strain curves for PP-G for different stress levels at (d) 23 °C and (e) 85 °C. 143

Figure 5-15: Creep strain master curves of (a) PO at 23 °C and 85 °C, (b) PP at 23 °C and, (c) PP-T at 23°C and 85 °C. Normalized plot of shift factor versus stress using S_u for PO, PP, PP-T, and PP-G at 23 °C and 85 °C. 144

Figure 5-16: Predicted versus experimental time to rupture for PO, PP, PP-T, and PP-G at 23 °C and 85 °C using the TSS technique. 145

Figure 5-17: (a) Long-term (up to 40 days) creep rupture data superimposed on short-term (up to 3 days) creep rupture curve and, (b) comparison of experimental long-term creep strain (data points) and predicted creep strain curve using TSS for PP-G at 23 °C. 146

Figure 6-1: Temperature sweep DMA test results including variation of storage modulus, loss modulus, and loss tangent with temperature at frequency of 1 Hz with temperate rate of 5 °C/min for (a) PA66/B and, (b) PPE/PS. 166

Figure 6-2: Frequency sweep DMA test results including variation of storage modulus, loss modulus, and loss tangent with frequency for PP, PP-T, PP-G, PA66/B, and PPE/PS at 85 °C.. 167

Figure 6-3: Effect of cyclic frequency on the fatigue life at different *R* ratios for (a) PP at 23 °C and 85 °C, (b) PP-T at 85 °C, (c) PP-G at 23 °C, (d) PP-G at 85 °C, (e) PA66/B at 85 °C and, (f) PPE/PS at 23 °C and 85 °C. 168

Figure 6-4: (a) Cycles to failure and, (b) time to failure at a given stress amplitude for different test frequencies where the self-heating is not dominant for PP, PP-T, and PP-G at different *R* ratios. The range of test frequency is shown for each condition. 169

Figure 6-5: (a) Displacement amplitude and, (b) mean displacement values of midlife cycle and 1250th cycle for different test frequencies for PP-G at 85 °C under $R = 0.3$ loading.. 170

Figure 6-6: PP-G load-displacement hysteresis loops at midlife and at a given cycle at 85 °C for different test frequencies under (a) $R = 0.3$ and, (b) $R = -1$. 171

Figure 6-7: Variation of loss tangent with frequency under $R = 0.1$ for (a) PP, PP-T, PP-G, PA66/B, and PPE/PS at 85 °C, and (b) PP-G and PPE/PS at 23 °C, measured in fatigue tests.. 172

Figure 6-8: Failed specimen gage section pictures of PP-T, PP-G, PPE/PS, and PA66/B under fatigue test at 85 °C for $R = 0.1$ loading. Crazing occurred for PP-T, PP-G, and PPE/PS... 172

Figure 6-9: Macroscopic fracture surface at frequencies of 0.25 and 4 Hz and microscopic fracture surface at frequency of 0.25 HZ at 85 °C under $R = 0.1$ condition for (a) PA66/B and, (b) PP. In each photo the left side shows crack initiation and stable crack growth region and the right side shows fast crack growth and final fracture region. 173

Figure 6-10: SEM of the fatigue fracture surface at 85 °C for (a) PP under $R = 0.1$ loading for frequencies of 0.25 and 4 Hz and, (b) PP-G under $R = 0.3$ loading for frequencies of 0.25 and 12 Hz. More damage in matrix is seen at lower frequencies for both PP and PP-G. 174

Figure 6-11: Stress amplitude versus time to rupture fatigue test data at different frequencies for (a) PP at 23 and 85 °C under $R = 0.1$ loading, (b)

PP-T at 23 and 85 °C under R = 0.1 and 0.3 loadings and, (c) PP-G at 23, 85, and 120 °C under R = 0.1 and 0.3 loadings. 175

Figure 6-12: Larson-Miller master curves for PP at R = 0.1 and for PP-T and PP-G at R = 0.1 and 0.3. 176

Figure 7-1: Effect of temperature on fatigue behavior under R = 0.1 and 0.3 loading conditions of (a) PP-T, (b) PP-G, (c) PA66/B, and, (d) PPE/PS. 197

Figure 7-2: Comparison of fatigue S-N lines of PA66/B and PA66/D at 23 °C and 85 °C for R = 0.1 loading condition. 198

Figure 7-3: Variation of intercept A (a), normalized A values with S_u (b), and slope B (c) of S-N lines with temperature under R = 0.1 and 0.3 loading conditions. Hollow symbols and hashed symbols show R = 0.1 and R = 0.3 data, respectively. Solid lines and dashed lines are fit to R = 0.1 and R = 0.3 data, respectively. 199

Figure 7-4: SEM of fracture surface of PPE/PS under R = 0.1 loading condition with fatigue life of about 50,000 cycles at (a) 23 °C and, (b) 85 °C in the transverse to the mold flow direction. Upper part of the line is the core layer and lower part of the line is the shell layer. 200

Figure 7-5: S-N master curves for R = 0.1 and 0.3 loading conditions for (a) PA66/B and (b) PPE/PS. (c) Variation of log shift factor with reciprocal of temperature for PA66/B and PPE/PS under R = 0.1 and 0.3 conditions. Solid lines are fits for PA6 and PBT data under R = -1 and 0.1 conditions [61]. 201

Figure 7-6: Comparison of fatigue data of PP-T and PP-G at 23 °C and 85 °C under R = 0.1 loading condition. (a) Stress amplitude versus cycles to failure data. (b) Normalized maximum stress with ultimate tensile strength versus cycles to failure data. 202

Figure 7-7: Mold flow direction effect at 23 °C for PP-T (a) under tension test and (b) under fatigue test for R = 0.1 loading condition. 203

Figure 7-8: SEM micrographs of PP-T fracture surfaces tested at 23 °C under R = 0.1 loading condition in (a) transverse and, (b) longitudinal directions. A few talc particles are distinguished in the final fracture zone in each picture.

.... 203

Figure 7-9: Effect of mean stress on fatigue behavior of (a) PP-T and PP-G at 23 °C, (b) PP-T and PP-G at 85 °C, (c) PP-G at 120 °C, (d) PA66/B at 23 °C, (e) PA66/B at 85 °C, (f) PA66/B at 120 °C, (g) PPE/PS at 23 °C and, (h) PPE/PS at 85 °C. 204

Figure 7-10: Correlations of fatigue data for different stress ratios and temperatures using modified Goodman mean stress parameter for (a) PP-T, (b) PP-G, (c) PA66/B, and (d) PPE/PS........ 205

Figure 7-11: Correlations of fatigue data for different stress ratios and temperatures using Walker mean stress parameter for (a) PP-T, (b) PP-G, (c) PA66/B, and (d) PPE/PS........ 206

Figure 7-12: Comparison of γ values in the Walker equation as a function of tensile strength for PP-T, PP-G, and PA66/B at 23, 85, and 125 °C with those reported for PBT and PA6 (○) in [62] and PP (☐) and PO (△) in [180]........ 207

Figure 7-13: (a) Predicted fatigue life versus experimental fatigue life and, (b) equivalent stress amplitude versus fatigue life using general fatigue model for PP, PO, PP-T, PP-G, PA66/B, PA66/D, PPE/PS, PA6, and PBT. Purple, blue, green, and red color denote -40, 23, 85, 120 or 125 °C, respectively. A total of 540 fatigue data are included in each figure........ 208

Figure 8-1: (a) Load and temperature signals used for creep-fatigue tests, and (b) load and temperature signals used for TMF tests. 231

Figure 8-2: Original and effective stress and temperature signals for TMF modeling. 232

Figure 8-3: Fit of $\log\left[N_f \frac{(S_a - S_{l0})}{(S_u - S_a)}\right]$ versus $\log(S_a)$ data of PPE/PS for R = -1 loading condition at 85 °C. 232

Figure 8-4: Experimental fatigue data and superimposed Chaboche fatigue model for (a) PA66/B at 85 °C , (b) PA66/B at 120 °C, and (c) PPE/PS at 85 °C. Curves are Chaboche fatigue life prediction model. 233

Figure 8-5: Predicted fatigue life using Chaboche fatigue model versus experimental fatigue life for PP-T and PP-G for (a) R = 0.3 loading condition and, (b) for frequency effect data at a given stress level. 234

Figure 8-6: Effect of loading waveform (sinusoidal or triangular) on life of PP-G at different stress levels for (a) fatigue loading condition and, (b) creep-fatigue loading condition. 235

Figure 8-7: Cross plot of fractional cyclic life ratio versus hold-time life ratio (a) at 85 °C for all the studied materials and, (b) at 120 °C for PP-G and PA66/B.. 236

Figure 8-8: Prediction of the non-linear interaction for cyclic and hold-time damages for (a) PP-T at 85 °C, (b) PP-G at 85 °C, (c) PP-G at 120 °C, (d) PA66/B at 85 °C, (e) PA66/B at 120 °C, and (f) PPE/PS at 85 °C. Data points are experimental results. Curves are predictions of Chaboche model and solid line is prediction of linear damage rule. 237

Figure 8-9: Effects of frequency and hold-stress position on creep-fatigue behavior of PP-G at 85 °C. 238

Figure 8-10: Predicted blocks to failure using Chaboch model versus experimental blocks to failure for creep-fatigue interaction and TMF test conditions. 238

List of Tables

Table 3-1: Name description, contents, drying conditions, and physical and mechanical properties of materials used for experimental studies according to the listed ASTM and ISO standards in the longitudinal direction obtained from technical data sheets and Matweb website [74, 90-93]. 70

Table 3-2: Summary of materials used for the experimental study and analysis. 71

Table 4-1: Tensile properties of PP-T, PP-G, PA66/B, PA66/D and PPE/PS at different testing temperatures under displacement rate of 1 mm/min in the transverse to the mold flow direction and dry as-molded condition. 93

Table 4-2: Tensile properties of PP-T, PP-G, PA66/B, and PPE/PS in wet condition. 94

Table 5-1: Summary of creep tests results of PP-T, PP-G, PA66/B, and PPE/PS. 126

Table 5-2: Material, temperature, and fiber orientation dependent tensile properties and modeling constants. 128

Table 5-3: Material and fiber orientation dependent modeling constants. 129

Table 6-1: Summary of frequency effect test results of PP, PP-T, PP-G, PA66/B, and PPE/PS. 163

Table 6-2: Larson-Miller model constants for PP, PP-T, and PP-G. 165

Table 7-1: Summary of fatigue test results of PP-T, PP-G, PA66/B, PA66/D, and PPE/PS. 191

Table 7-2: Summary of fatigue test conditions and results for PP-T, PP-G, PA66/B, PA66/D, and PPE/PS, as well as analysis results for PP and PO. 195

Table 7-3: Summary of suggested values for α in the general fatigue model. 196

Table 8-1: Chaboche creep-fatigue interaction model constants. 227

Table 8-2: Summary of creep-fatigue interaction test conditions and results. 228

Table 8-3: Summary of TMF test conditions and experimental and predicted results using Chaboche model for PA66/B. 230

List of Nomenclature

a	crack length, Chaboche creep-fatigue interaction constant
a_{T0}	temperature shift factor
A	stress-time to rupture intercept, fatigue *S-N* line intercept, parameter relating stress amplitude to Larson-Miller parameter in fatigue, Chaboche creep model constant
A_{TMF}	TMF specific parameter
b, M_0, β	Chaboche fatigue model constants
B	stress-time to rupture slope, fatigue *S-N* line slope, parameter relating stress amplitude to Larson-Miller parameter in fatigue
C, D	parameters relating stress to minimum creep rate
C_{LMP}	Larson-Miller parameter constant
D	diffusion coefficient, damage parameter
D_c	creep damage parameter
D_f	fatigue damage parameter
D_H	hold-time damage
D_0	reference diffusion coefficient
E	elastic modulus
E_a	activation energy
E_0	reference elastic modulus
E'	storage modulus
E''	loss modulus
EL	elongation
f	cyclic frequency
G, H	parameters relating stress to Larson-Miller parameter in creep
h	specimen thickness
H_m	a parameter for evaluation of water absorption with fibers
K	Boltzman constant, strength coefficient

K_t	stress concentration factor
LMP	Larson-Miller parameter
LMP_f	Larson-Miller type fatigue parameter
m	mass of wet composite, Findley power law constant
m_d	mass of dry composite
m_{pad}	mass of dry matrix
m_1, m_2	strain rate strengthening coefficients
M	stress and temperature dependent function in Chaboche fatigue model
M_m	maximum moisture absorption
M_t	percent of water absorption
n	stress exponent, strain hardening exponent, Findley power law constant
N	number of cycles
N_C	creep life
N_f	cycles to failure
N_R	number of blocks to failure
N'_f	reduced cycles to failure
Q	activation energy
R	stress ratio, constant of gases
S	stress
S_a	stress amplitude
S_{eq}	equivalent fatigue strength
S_H	hold-time stress
S_{l0}	fatigue endurance limit
S_m	mean stress
S_{max}	maximum stress
S_{Nf}	fully-reversed fatigue strength
S_u, σ_b	ultimate tensile strength
S_y, σ_y	0.2% yield strength
SED	strain energy density

S'	effective stress
t	time
t_f	time to failure in fatigue
t_H	hold-time
t_R	time to creep rupture
T	temperature
T_g	glass transition temperature
T_m	melting temperature
T_{min}	minimum temperature
T_{max}	maximum temperature
T_0	reference temperature
$\tan \delta$	loss tangent
V^*	stress activation volume
W_d	dried specimen weight
W_w	wet specimen weight
α	general fatigue model parameter, stress and temperature dependent function
β, ζ	general fatigue model parameters
γ	mean stress parameter in Walker equation
ΔS	stress range
ε	applied strain, true strain
ε_c	creep strain
ε_e	elastic strain
ε_{max}	maximum strain
ε_M	strain at ultimate strength
ε_P	true plastic strain, plastic strain
ε_R	creep rupture strain
ε_0	instantaneous strain
$\dot{\varepsilon}$	strain rate

$\dot{\varepsilon}_0$	reference strain rate
$\dot{\varepsilon}_{c/\min}$, $\dot{\varepsilon}_{\min}$	minimum creep rate
θ	loading axis with respect to the mold flow direction
λ_1, λ_2	thermal softening coefficients
σ	applied stress, true stress
σ_m	mean stress
σ_{max}	maximum stress
σ_{b0}	reference tensile strength
σ_{l0}	fully-reversed fatigue limit
σ_R	stress at rupture
σ^*	stress coefficient
φ_S	shift factor
λ, η	Monkman-Grant relation constants
λ', η'	modified Monkman-Grant relation constants

List of Abbreviations

ABS	Acrylonitrile-Butadiene-Styrene
CCP	Creep Crack Propagation
CT	Compact Tension
CW	Cooling Water
DAM	Dry As-Molded
DMA	Dynamic Mechanical Analysis
FCP	Fatigue Crack Propagation
FEA	Finite Element Analysis
HDPE	High Density Polyethylene
HCF	High Cycle Fatigue
IP	In-Phase
ISCF	Isothermal Strain Control Fatigue
LCF	Low Cycle Fatigue
LDR	Linear Damage Rule
MCR	Minimum Creep Rate
OP	Out-of-Phase
PA	Polyamide
PBT	Polybutylene Terephthalate
PC	Polycarbonate
PET	Polyethylene Terephthalate
PMMA	Poly(methyl methacrylate)
PPA	Polyphthalamide
PPE	Polypropylene-co-Ethylene
PPS	Polyphenylene Sulfide
PS	Polystyrene

PSF	Polysulfone
PVF_2	Poly(vinylidene fluoride)
PVC	Poly(vinyl chloride)
RT	Room Temperature
SEM	Scanning Electron Microscope, Scanning Electron Microscopy
SFRPC	Short Fiber Reinforced Polymer Composite
SRP	Strain Range Partitioning
STTP	Stress-Time-Temperature Parameter
SWT	Smith-Watson-Topper
TMF	Thermo-Mechanical Fatigue
TTS	Time-Temperature Superposition
TTSS	Time-Temperature-Stress Superposition
TSS	Time-Stress Superposition
UTS	Ultimate Tensile Strain
WLF	Williams-Landel-Ferry
wt	Weight

Chapter 1

Introduction

1.1 Motivation for the Study and Objectives

Polymers and their composites are lightweight, corrosion resistant, and offer desirable mechanical properties at an economical cost in many applications, such as in the automotive industry. Short fiber reinforced and talc-filled polymer composites are developed mainly to fill the property gap between continuous fiber laminate composites widely use in the aerospace industry and unreinforced polymers mainly use for non-load bearing applications. Short fiber reinforced and talc-filled polymer composites are more easily reprocessed and are less costly, compared with long fiber composites.

Thermoset plastics contain polymers that cross-link during the curing process to form irreversible chemical bonds which makes them more resistant to high temperatures than thermoplastics. Thermoplastics have a simple molecular structure with chemically independent macromolecules. Many thermoplastic resins have an increased impact resistance to comparable thermoset composites, in addition to being reusable. Thermoplastic consumption is roughly 80% or more of the total plastic consumption and include polyamide, polypropylene, polybutylene terephthalate, polyethylene terephthalate and polystyrene groups [1, 2].

Mechanical properties of thermoplastics are significantly different at temperatures below and above glass transition temperature, T_g, which is about 0.6 of melting temperature, T_m, where the temperature is in Kelvin [3]. In addition, thermoplastic materials are viscoelastic, particularly at elevated temperatures, such as in automobiles where under the hood temperature can increase up to 130 °C because of the engine temperature and the weather condition. Due to the strong dependence of mechanical properties on temperature and a large number of applications at elevated temperatures, understanding the effect of temperature on mechanical properties of thermoplastic composites is of great importance.

Components made of thermoplastic composites are subjected to variable amplitude cyclic loading in their applications which includes cyclic, static, thermal, and combined loads, for example, hold-time periods with static stress during cyclic loading, which are schematically shown in Figure 1-1. Tensile properties as the basic material properties are still widely used in design as they can be easily obtained. They can also be used as predictors of creep and fatigue properties. Strength, stiffness, and ductility are the three main properties which can be obtained from a tensile test. Creep plays an important role in damage of polymer composites as they exhibit time-dependent behavior. Long-term creep tests are usually time consuming and expensive to conduct, therefore, developing predictive models for long-term creep predictions based on short-term creep tests are often required.

Fatigue loading occurs in most engineering applications and a great number of mechanical failures are a consequence of this type of loading. Due to the viscoelastic characteristic of polymers, time considerably influences the mechanical properties. Also, most components made of these materials are subjected to service load histories which consist of cycles with mean stress. Therefore, analysis of the fatigue behavior of these materials requires a comprehensive study to consider the influence of temperature, time or frequency, and mean stress.

The combination of creep and fatigue damage mainly at elevated temperatures and when the temperature also varies with time is typically more damaging than the addition of damage caused by each individual loading condition. Frequency, stress level, mean stress, and temperature are factors which affect the creep-fatigue interaction behavior. Since creep-fatigue and thermo-mechanical fatigue (TMF) tests are complicated and expensive to conduct, an analytical model based on pure fatigue and pure creep conditions developed for life prediction under creep-fatigue and TMF loading conditions is desirable.

The overall view of the study is shown in Figure 1-2. This includes conducting experiments to interpret behavior and develop and validate predictive empirical, analytical, and semi-analytical models for tensile, creep, fatigue, creep-fatigue, and TMF behaviors. The simple tensile properties were used to predict more complex creep and fatigue behaviors. The main part of the work was investigating combined creep-fatigue behavior, developing predictive models from pure creep and pure fatigue conditions, and validating the models with creep-fatigue and TMF test data. The main effect considered was elevated temperature, while moisture and hygrothermal effects on mechanical behavior were also investigated. The viscoelasticity of the materials was evaluated using different methods and was used to interpret some mechanical behaviors. Microstructural verifications from scanning electron microscopy of the fractured surfaces, when necessary, were also provided. Most of the experiments were conducted on a plate-type specimen in the transverse to the mold flow direction which has the inferior mechanical properties.

1.2 Outline of Dissertation

To fulfil the objectives of the study represented in the previous section, the chapters of the dissertation are organized as follows. In chapter 2, a literature review on mechanical behaviors of these materials at elevated temperatures is presented. The mechanical behaviors included consist of tensile, creep, isothermal fatigue, thermo-mechanical fatigue, and creep-fatigue interaction. Environmental effects such as moisture and aging at elevated temperatures are also included. The studies reviewed include experimental works, modeling works, and failure mechanism studies.

Chapter 3 provides a discussion on physical and mechanical characteristics of the materials considered in the study. Drying conditions, equipment, experimental methods and specimen geometry used throughout the study are briefly explained. Chapter 4 reviews tensile behavior and modeling of the studied materials. Effects of temperature, moisture, and hygrothermal aging are studied and modelled. Stress-strain curves and tensile properties as a function of temperature and moisture content are mathematically represented. Tensile properties obtained in this chapter are used as inputs for estimations of creep, fatigue, and their interaction behaviors in the following chapters.

Chapter 5 presents short-term and long-term creep behaviors at different temperatures and stress levels. Relationships for representing creep properties including creep rupture properties and creep strain are developed for short-term creep condition. Applicability of the developed models for long-term creep predictions is also evaluated. Creep properties obtained are used to explain cyclic ratcheting in fatigue and also to develop creep-fatigue interaction model in the following chapters. Chapter 6 discusses the beneficial effect of increased loading frequency on fatigue behavior of the studied materials. Viscoelastic properties are obtained and used for the interpretation of the frequency effect results and observations. Models based on time dependency of fatigue failure are developed to correlate frequency effect data.

Chapter 7 discusses isothermal fatigue behavior, including temperature and mean stress effects. Mater curves are obtained to correlate fatigue data at different temperatures and applicability of two common mean stress correction models is investigated. A general fatigue life prediction model is also applied to test data obtained under different test conditions. Chapter 8 presents creep-fatigue interaction and TMF behaviors. Chaboche non-linear creep-fatigue interaction model which has been applied to metallic materials over the years for creep-fatigue interaction and TMF life predictions, was investigated for its applicability to thermoplastic composites. In chapter 9 the main findings of the study are summarized and recommendations are provided for future studies.

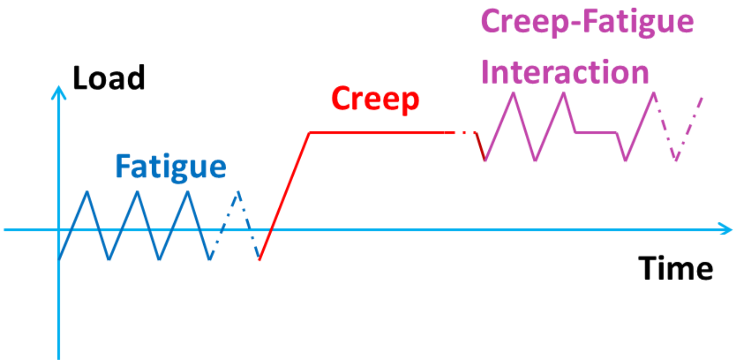

Figure 1-1: Schematic load history, including fatigue, creep, and creep-fatigue loadings.

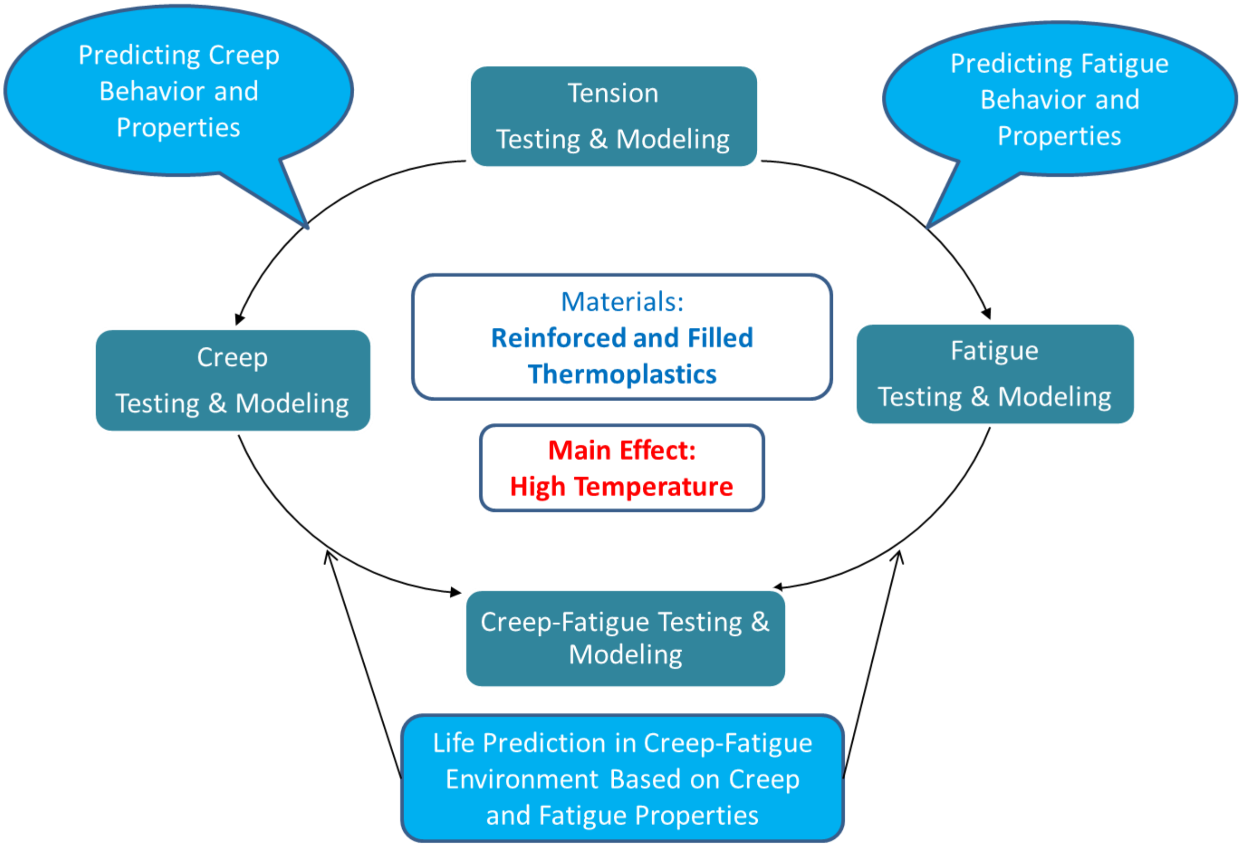

Figure 1-2: Overview of the study.

Chapter 2

Literature Review

In this chapter a review of the technical literature related to the mechanical behaviors of short fiber reinforced polymer composites at elevated temperatures is presented. A broad range of mechanical behaviors were considered consisting of tensile, creep, isothermal fatigue, thermo-mechanical fatigue, and creep-fatigue interaction. Experimental studies, modeling efforts, microstructural aspects, and failure mechanisms are included. Effects such as moisture and aging at elevated temperatures were also considered. The emphasis of the review was on mechanical properties of synthetic short fiber reinforced thermoplastic composites, mainly produced with injection molding and mostly used in automotive applications. A few studies related to neat thermoplastics and also short fiber reinforced thermosets were also included, in addition to studies on dynamic mechanical analysis (DMA) and impact properties. This literature review was published as a review paper [4].

2.1 Tensile Behavior

Tensile properties such as elastic modulus, yield strength, tensile strength, toughness and ductility are some properties that can be obtained by conducting a simple tension test and they are still widely using in design of polymeric materials. These properties for SFRPCs depend on different factors such as fiber content, strain rate, temperature, aging and moisture content. Several studies consider the effect of temperature on tensile properties of these materials.

Schultz and Friedrich [5] investigated the effects of temperature ranging between 80 °C and 120 °C and displacement rate ranging between 0.005 and 500 mm/min on tensile properties of neat and 30% by weight (30 wt%) short glass fiber reinforced polyethylene terephthalate (PET). Tensile strength and elastic modulus linearly increased with log strain rate, while they decreased as temperature increased, except at -20 °C for tensile strength where a change in failure mechanism from fiber pullout to initiation of cracks from crazes at fiber ends started. A drastic reduction in tensile strength and modulus for both reinforced and unreinforced materials were observed near T_g of matrix which was about 60 °C. SEM observations of fracture surfaces of reinforced PET were used to construct a map shown in Figure 2-1. It was concluded that at low temperatures or high strain rates, fiber pullout and matrix brittle fracture were the dominant failure mechanisms, while at elevated temperatures or low strain rates failure occurred via matrix crazing and crack propagation near the fiber ends.

Valentin et al. [6] studied the effect of temperature on tensile behavior of neat, short glass fiber reinforced (40 wt%), and continuous fiber reinforced (70 wt%) polyamide-6.6. Bending tests were performed on dried specimens in the temperature range of -40 to 140 °C to examine the effect of temperature on elastic modulus and stress at rupture. The variations of stress at rupture with temperature are shown in Figure 2-2. Short glass fiber composites with longer fiber had higher stress at rupture, while the difference was more at lower temperature. At temperatures higher than 100 °C fiber length had no effect on stress at rupture. Stress at rupture was found to obey the following equation as a function of temperature:

$$\sigma_R(T) = \sigma_R(T_0)\left[1 - B(T - T_0)\right] \tag{2.1}$$

where B is a coefficient, T_0 is the reference temperature (-40 °C), T is the temperature and σ_R is the stress at rupture. The elastic modulus was nearly constant below 55 °C, which is the T_g of polyamide-6.6. After that a gradual drop can be seen by increasing temperature.

Liello et al. [7-10] studied tensile behavior of different short glass and carbon fiber reinforced polypropylene and short carbon fiber reinforced nylon-6.6 and polycarbonate composites at different range of temperatures (20 to 110 °C) and strain rates. Dumbbell-shaped specimens cut from injection molded plaques were used. It was found that the yield stress decreased by increasing temperature for all the composites and the Eyring-type model [11] was used to relate strain rate, temperature, and yield stress as follows:

$$\dot{\varepsilon} = \dot{\varepsilon}_0 \exp -(E_a - \sigma_y V^*)/KT \tag{2.2}$$

where $\dot{\varepsilon}$ is the strain rate, σ_y is yield stress, T is temperature, E_a is activation energy, V^* is the stress activation volume, K is Boltzman constant, and $\dot{\varepsilon}_0$ is a constant. The E_a and V^* values were obtained from the graph of yield stress versus logarithm of strain rate at a constant temperature.

Miwa et al. [12-15] studied the temperature and strain rate dependencies of tensile properties of short fiber epoxy composites reinforced by glass, carbon, or hybrid glass-carbon fibers. In tensile experiments, temperature varied between 20 and 100 °C. Tensile strength increased with log strain rate and this effect slightly increased as the temperature increased for all the composites, as shown in Figure 2-3 for the glass fiber-epoxy resin composite. The same behavior was observed for the shear strength at the fiber-matrix interphase. Tensile strength and shear strength of the composites were mathematically modeled from properties of materials constituting the composites and yield shear strength at the fiber-matrix interphase at each temperature and strain rate using models developed based on the rule of mixture. Tensile strength versus strain rate master curves were developed which included temperature effect.

In the study of Gong et al. [16] a semi-empirical combining rule known as S mixing rule [17], which interpolates between upper and lower band predictions to produce a single theoretical prediction, was used to predict elastic and shear modulus of short glass and carbon fiber reinforced epoxy composites over the temperature range of -100 to 200 °C. Dynamic mechanical analysis (DMA) tests were conducted in bending and torsion modes to evaluate theoretical results. Both the Young's and shear moduli decreased with increasing temperature with a sudden change near T_g. The values for the carbon fiber reinforced composites were greater than those of glass fiber reinforced composites. In general, good agreement was observed between the experimental data and the theoretically predicted bounds for all composites over most of the temperature range studied.

In the study of Wang et al. [18] effects of temperature and strain rate on tensile behavior of reinforced polyamide-6 with 33 wt% short glass fiber were investigated. Dog bone-shaped specimens were machined from injection molded plaques in different orientations and tested at temperatures between 21 and 100 °C and strain rates of 0.05, 0.5 and 5 1/min. Both elastic modulus and tensile strength decreased with increasing temperature and increased with increasing strain rate. Elastic modulus was observed to be more temperature sensitive compared to tensile strength. There was a change in the strain rate and temperature sensitivities of tensile properties between 21 and 50 °C as a result of the T_g of the polyamide-6 matrix, which is at about 40 °C. The temperature sensitivity was much lower in the molding direction than normal to the molding direction, as the tensile properties are more fiber dependent in the molding direction. The following empirical relations were used to represent the temperature and strain rate dependencies of elastic modulus and tensile strength of composites:

$$E = E_0(\frac{\dot{\varepsilon}}{\dot{\varepsilon}_0})^{m_1} \exp\left[-\lambda_1(T - T_0)\right] \tag{2.3}$$

$$\sigma_b = \sigma_{b0}(\frac{\dot{\varepsilon}}{\dot{\varepsilon}_0})^{m_2} \exp\left[-\lambda_2(T - T_0)\right] \tag{2.4}$$

where E_0, σ_{b0}, $\dot{\varepsilon}_0$ and T_0 are reference elastic modulus, reference tensile strength, reference strain rate and, reference temperature, respectively. Two other parameters, m and λ, are defined as strain rate strengthening coefficient and thermal softening coefficient, respectively, with different values for temperature ranges below and above T_g. A two parameter temperature and strain rate dependent constitutive equation was also developed to describe the tensile stress-strain behavior of short glass fiber reinforced polyamide-6, given by:

$$\frac{d\sigma}{d\varepsilon} = E - E(\frac{\sigma}{\sigma^*})^n \tag{2.5}$$

where σ^* and n are called the stress coefficient and stress exponent, respectively. The stress exponent n, which controls the strain rate hardening effect is independent of temperature and strain rate, while the stress coefficient σ^* is both temperature and strain rate dependent, as shown in Figure 2-4 for the transversely oriented fibers.

Mouhmid et al. [19] conducted an experimental study to investigate the effect of temperature and strain rate on tensile properties of neat and 15, 30 and 50 wt% short glass fiber reinforced polyamide-6.6 at temperatures of 20, 50 and 80 °C. Young's modulus and tensile strength decreased with increasing temperature while strain at fracture increased with increasing temperature. The effect of temperature on the failure strain was much more accentuated in unreinforced material than in reinforced material. Hashemi [20] studied the effects of temperature and strain rate on tensile strength of injection molded dumbbell-shaped short glass fiber reinforced polybutylene terephthalate (PBT) at displacement rates between 0.05 and 500 mm/min and at temperatures between 23 and 100 °C. Tensile strength was found to linearly increase with increasing log of strain rate and decrease linearly with increasing temperature.

De Monte et al. [21, 22] investigated the influence of temperature on tensile behavior of 35 wt% short glass fiber reinforced polyamide-6.6 using dog bone-shaped specimens machined from injection molded plaques with different thicknesses and different fiber orientations. The behaviors of material at room and 130 °C temperatures were completely different, as can be observed from Figure 2-5. At RT, the material behaved in a brittle way with a linear elastic behavior for most of the stress-strain curve, while at 130 °C significant plastic deformation is observed. This results from increased mobility of polymer chains at 130 °C, which is much higher than T_g at 65 °C. It can also be observed that the temperature effect is similar for different orientations.

Takahashi et al. [23] studied the effect of temperature on tensile behavior of 60 wt% SiO_2 short fiber reinforced poly-phenylene sulfide, PPS. Temperature sweep dynamic mechanical analysis (DMA) was performed to obtain T_g at 90 °C. Tensile tests were conducted at 25, 80 and 125 °C in longitudinal and transverse directions. Tensile strength and elastic modulus decreased by increasing temperature and the reduction was more at the temperatures above T_g. The elongation increased by increasing temperature mainly for temperatures above T_g, as molecular chain motion of polymers intensifies above T_g. At these temperatures constraint of the matrix compared to fibers reduces, thus, elongation is governed by the properties of the matrix and the differences of elongation and the tensile strength due to the fiber orientation reduces, as can be seen in Figures 2-6(a) and (b). In the longitudinal direction fiber pullouts were observed, while in the transverse direction peeling of fibers were observed, based on SEM. The number of fiber pullouts increased with increasing temperature.

Lockwood et al. [24, 25] investigated the effect of temperature in the range of 23 to 120 °C on tensile strength of vibration welded and unwelded 30 wt% short glass fiber reinforced nylon-6. Dog bone-shaped specimens were machined from welded plaques in a way that loading direction was perpendicular to weld line and fiber orientation. The tensile strength was normalized with the tensile strength at 24 °C. The normalized tensile strength fell on a single curve for both welded and unwelded specimens with a significant decrease of 60% in normalized strength as testing temperature was increased from room temperature to 120 °C, as shown in Figure 2-7.

Mortazavian and Fatemi [26-28] studied effects of temperature and strain rate on tensile behavior of polybutylene terephthalate and polyamide-6 thermoplastics reinforced with 30 and 35 wt% short glass fibers, respectively. Tensile tests were conducted in a range of temperature between -40 and 125 °C and at a displacement rate range between 0.1 and 1000 mm/min with specimens in several mold flow directions. Tensile strength and elastic modulus linearly increased with log strain rate and non-linearly decreased with increasing temperature. Time-temperature superposition method was applied to tensile strength data at different temperatures and strain rates and a shift factor of Arrhenius type was suggested to fit tensile strength data into a master curve, as shown in Figure 2-8 for PBT in the transverse direction. Tensile fracture surface of specimens at 125 °C indicated a higher degree of matrix crazing and interfacial debonding compared with 23 °C. The effect of mold flow direction was more pronounced at 125 °C, as compared to at 23 °C.

2.2 Effects of Thermal and Hygrothermal Agings on Tensile Behavior

Changes in properties of polymers under the influence of environmental conditions such as heat, light or moisture during time is called aging. These changes can have detrimental or beneficial effects on mechanical properties, depending on aging conditions and material. Combined effect of temperature and moisture (hygrothermal) is a specific kind of aging that can have a substantial degrading effect on behavior of some polymers such as polyamide. Moisture can decrease strength and stiffness of material and temperature increases moisture absorption rate, speeding up the rate of degradation. Several studies investigated effects of thermal aging and hygrothermal aging on mechanical properties of short fiber polymer composites.

Lyons [29] studied effect of thermal aging on tensile properties of four different short glass fiber reinforced thermoplastics. The materials were polyamide-4.6 (PA4.6) and polyamide-6.6 (PA6.6) composites with respectively 30 wt% and 33 wt% short glass fiber and two different kind of 33 wt% short glass fiber reinforced polyphthalamide composites with different T_g, PPA1 with T_g = 128 °C and PPA2 with T_g = 120 °C. Dog bone-shaped specimens were used for experimental studies and aged for different durations and at different temperatures in air. Tensile test were conducted at the same temperature that was used for the isothermal aging. The secant elastic modulus at stress of 41.6 MPa, tensile strength and percent elongation (*% EL*) were measured in tensile tests and compared for different aging conditions. Isothermal aging initially increased the ultimate tensile strength and elastic modulus of these materials at lower temperatures, while it significantly decreased strength and ductility at 150 °C because of oxidation at this temperature. However, oxidation at elevated temperature increased the stiffness. A Sherby-Dorn master curve was used to relate time-temperature and stress together in creep tests.

Jia and Kagan [30] investigated effects of aging time and temperature on tensile behavior of short glass fiber (33 wt% glass) polyamides-6 and polyamide-6.6. Tests and analysis were conducted at three typical temperatures for automotive applications (-40, 23, and 121 °C). The aging was performed by keeping dry as-molded specimens in RT also placing them into 121 °C preheated chamber for 100, 500, and 1000 hours. The moisture content before and after aging was constant (0.15%), so the effect of moisture was excluded from the results. The tensile strength was found to decrease continuously as the temperature increased from -40 to 121 °C. Aging increased tensile strength of both materials mainly at 121 °C, as shown in Figure 2-9. The effect of aging on tensile strength was related to crystalline index (percentage of the volume of the polymer that is crystalline), which increases by increasing aging time.

Sinmazcelik and Yilmaz [31] investigated thermal aging effects on mechanical performance of short glass and carbon fiber reinforced composites, using injection molded PEEK specimens with 30 wt% fiber reinforcement. Thermal aging processes increased the flexural modulus, but decreased the impact properties such as toughness of the composites. Although after the aging process percent crystallinity of composites dramatically decreased, more organized crystallized structures were formed, which caused the composites to be more brittle.

Valentin et al. [6] studied kinetics of water absorption at elevated temperatures and effect of moisture content on tensile behavior of neat and glass fiber reinforced polyamide-6.6 composites. Specimens were exposed to various temperatures including 40, 70, and 90 °C under relative humidity levels of 30, 75, and 100%. The moisture absorption process was modeled using Fick's law [32] expressed as:

$$\frac{M_t}{M_m} = 1 - \frac{8}{\pi^2} \exp\left(-\left(\frac{Dt}{h^2}\right)\pi^2\right) \quad for \quad \frac{D\,t}{h^2} > 0.05 \tag{2.6}$$

$$\frac{M_t}{M_m} = \frac{4}{\pi^{1/2}}\left(\frac{Dt}{h^2}\right)^{1/2} \quad for \quad \frac{D\,t}{h^2} < 0.05 \tag{2.7}$$

In these equations, M_t is percent of water absorption expressed as:

$$M_t = \frac{W_w - W_d}{W_d} \times 100 \tag{2.8}$$

where W_d and W_w are original dried specimen weight and wet specimen weight, respectively. Also, h, t, D and M_m are specimen thickness, exposure time, diffusion coefficient, and maximum moisture absorption, respectively. Fick's model could represent all the experimental data with aging temperatures below 90 °C. Based on the humidity effect test results, it was concluded that for water absorption above 1% tensile strength and modulus reduced with increasing percent of water absorption, with greater drop for short glass fiber composites compared with continuous fiber composites, irrespective of the aging temperature.

In the study of Bastioli et al. [33] effect of water aging on behavior of polybutylene terephthalate (PBT) and polyethylene terephthalate (PET) thermoplastic composites below and above T_g was considered. The T_g of PBT and PET was reported to be 60 and 67 °C, respectively. Injection molded specimens with 30 wt% glass fiber aged at temperature range of 25 to 87 °C were used. Fick's law was used to model kinetics of water absorption at different temperatures. Variation of the diffusion coefficient with temperature is shown in Figure 2-10 for PET and PBT. Diffusion coefficient increases by increasing temperature with a sudden change of slope at T_g. It is because of the fact that above T_g there is greatly increased segmental mobility, causing a greater zone of activation. The maximum water absorbed increased as aging temperature increased, probably due to modification of crystalline-amorphous interface during absorption process. At elevated temperature, 87 °C (above T_g), a plateau of water absorption followed by an increase at sufficiently high aging time. Fracture toughness and Izod impact strength decreased with long-term aging at 87 °C because of increased amount of crystallinity. Effect of hygrothermal aging on mechanical behavior of neat and reinforced glass fiber composites for PET and PBT was observed to be the same.

Ishak and Lim [34] investigated effect of hygrothermal aging on behavior of short fiber reinforced polybutylene terephthalate at two different relative humidity, 81.2% and 100%. A relative humidity of 81.2% was obtained using saturated calcium chloride solution at 50 °C. Specimens immersed in distilled water at 100 °C to obtain 100% relative humidity. SEM was used to examine fracture surface of specimens. A slight decrease in diffusivity was observed in composites relative to neat polymer, due to distribution of fibers hindering the direct moisture diffusion. Severe decrease of elastic modulus and tensile strength was observed by increasing moisture content. A more pronounced effect of moisture was observed at 100 % relative humidity compared with 81% relative humidity, due to extensive plasticization and hydrolysis of matrix as well as degradation of fiber-matrix interface at 100% relative humidity. Hydrolysis was concluded from the presence of microvoids on the fractured surfaces and not full recovery after drying the aged specimens.

Ishak and Berry [35, 36] studied the hygrothermal aging effect on tensile and dynamic mechanical properties of short carbon fiber reinforced nylon-6.6. Injection molded specimens with 10, 20, 30 and 40 wt% fibers were aged by immersion in water at temperatures of 25, 40, 60, 80 and 100 °C. Fick's law was used to model the process of moisture absorption at different temperatures. For all the temperatures, good agreement between experimental data and Fick's law predictions was observed. The maximum or equilibrium moisture content was constant at different temperatures, while diffusion coefficient (D) increased with increasing temperature. A plot of $\ln(D)$ versus the reciprocal of water temperature is shown in Figure 2-11. Unlike what was observed in [33] for PET and PBT, there is no change in the linear variation at around T_g. A slight reduction in the diffusivity coefficient with increasing fiber volume fraction was observed because of hindrance of the direct moisture absorption into the matrix with increasing fiber volume fraction.

Stress-strain curves from tension tests for 40 wt% short carbon fiber reinforced composite at RT after different conditioning process are shown in Figure 2-12. Hygrothermal aging reduced both strength and stiffness of composite dramatically and the reduction was more at higher temperature. Full recovery of tensile properties was not obtained for reinforced composites by drying the aged specimen, while it was obtained for unreinforced specimens. It was, therefore, concluded that plasticization of matrix was a reversible phenomenon, while disruption of fiber/matrix bond and resulted microcavities were not restored after drying.

Czigany et al. [37] used acoustic emission technique and fractography to assess and compare the failure modes of short glass and carbon fiber reinforced injection-molded polyacrylamide composites. As-received (drying at 100 °C in vacuum for 8 hours), hygrothermally aged (immersing in 90 °C water for two weeks until saturation) and re-dried (drying in vacuum at 100 °C for 48 hours) specimens were used for experimental studies. For both short glass and carbon fiber reinforced polyacrylamide composites failure occurred by matrix deformation along with fiber/matrix debonding in the crack initiation range, while fiber pullout became dominant in the crack propagation range. The failure mode was very ductile for hydrothermal aged specimens at 90 °C, showing the plasticizing effect of water on composites. It was also observed that hygrothermal aging was a reversible physical process and was restored by drying.

Bergeret et al. [38] investigated the effect of moisture absorption at elevated temperatures on tensile behavior of three short glass fiber reinforced thermoplastics including polyamide-6.6 reinforced with 30 wt% short glass fiber (PA6.6), polybutylene terephthalate reinforced with 15 wt% short glass fiber (PBT), and polyethylene terephthalate reinforced with 30 wt% short glass fiber (PET). The maximum water absorption and the water absorption rate increased with increasing aging temperature due to easier diffusivity of water at higher temperatures. Significant reduction of tensile strength was also observed. Depending on the matrix, the mechanism of aging was different. PA6.6 and PBT composites showed effects of both physical aging through plasticization and chemical degradation through chain scission. PET composite did not show any evidence of plasticization. The influence of fiber coating on hygrothermal behavior and tensile properties were also studied. The maximum water uptake for long-term aging did not change, while the rate of water absorption decreased by adding specific component for coating the glass fibers. The rate of reduction of tensile strength was also decreased by improving fiber/matrix bond.

Carrascal et al. [39] investigated the hygrothermal behavior of neat and short glass fiber polyamide-6 at different temperatures (40, 50, 80 and 100 °C) with different fiber contents (0, 25 and 35 wt%) with emphasis on kinematics of water absorption. The rate of water absorption increased by increasing temperature, but the maximum capacity of water absorption did not change, as shown in Figure 2-13. Fick's law was used to predict water absorption amount during time. Since the diffusion is a thermally activated phenomenon, the diffusion coefficient D, is dependent on the temperature of absorbed water and was expressed by an Arrhenius-type law:

$$D = D_0 e^{-Q/RT} \tag{2.9}$$

where Q is the activation energy, T is temperature, R is the constant of gases and D_0 is a temperature independent constant. It was also observed that the value of D increased with increasing fiber content for all temperatures, unlike what was observed for short carbon fiber reinforced nylon-6.6 in [35]. A parameter was defined to evaluate influences of water absorption on fibers and interfacial bonding expressed as:

$$H_m = \frac{m(t) - m_d}{m_{pad}} \times 100 \tag{2.10}$$

where m_{pad} is the mass of dry polyamid-6 without reinforcement, m_d is the mass of dry composites, and $m(t)$ is the actual weight of wet specimen. Nearly identical values of this parameter were obtained for composites with different volume fractions at immersion water temperature of 40 °C, confirming no water absorption with glass.

Hassan et al. [40] studied the effect of moisture absorption on thermal, dynamic mechanical and mechanical properties of injection molded short glass fiber reinforced polyemide-6.6 with fiber volume fraction between 4% and 12%. Tensile tests were conducted on specimens in dry condition as well as saturated at 50% and 100% relative humidity. Tensile strength and elastic modulus decreased as degree of humidity increased, but ductility increased. As polymer composites absorb moisture, a hydrogen bonding between moisture and matrix forms and the interaction between polymer and fibers becomes less effective. For hygrothermaly aged specimens at elevated temperature, matrix yielding and interfacial debonding between fiber and matrix was dominant, while in dry condition a brittle matrix fracture was observed with no sign of matrix deformation.

In a study by Ghasemzadeh et al. [41] effects of thermal and hygrothermal aging on tensile properties of short glass, short flax, and short flax/glass fiber reinforced polypropylene composites were investigated. Thermal aging at 85 °C for 400 and 1028 hours increased tensile strength and elastic modulus, irrespective of fiber type and content. Thermal resistance of composites was explained by enhanced interfacial adhesion between the fibers and matrix. Hygrothermal aging at 85 °C for about 1000 hours did not noticeably affect the tensile properties of short glass and flax/glass fiber composites, while it dramatically reduced tensile strength and modulus of short flax reinforced composite. Hydrophobic and barrier character of glass fibers, even at small amounts, controlled and reduced water aging effects.

2.3 Creep Behavior

Creep, continuous deformation with time at a constant load, is a time-dependent behavior of viscoelastic materials such as polymers. Creep properties of polymeric materials are also very temperature dependent. At temperatures below T_g, segmental movement of the chains cannot occur and very little creep can take place event after a long time. As the temperature goes above T_g, both creep strain and the rate of creep increase. Most of the applications of short glass fiber reinforced polymer composites are at temperatures higher than their glass transition temperature. Therefore, creep is a major concern in design with such materials. Several studies have considered the effect of temperature on creep properties of short fiber reinforced polymers.

Cessna [42] conducted creep tests on neat and reinforced polypropylene with 10, 20, 30 and 40 wt% short glass fibers at 23 °C and 80 °C using injection molded dumbbell-shaped specimens. They applied the stress-time superposition procedure to extend short-term creep strain data for long-term creep strain predictions. Short-term creep strain versus time curves were shifted horizontally and vertically to obtain master curves and shift factors at different stress levels. Predictions for long-term creep strain were very good for 30% and 40% glass fiber reinforced specimens. The master curve and shift factors were also used to derive isothermal stress-time to rupture curves.

Gupta and Lahiri [43] investigated short-term creep behavior of unreinforced and glass fiber reinforced polypropylene. Short-term creep tests were conducted for different stress levels at the temperatures of 40, 47, and 55 °C using injection molded dumbbell-shaped specimens. Findley’s power law relationship [44] was used to represent the creep strain, ε_c, versus time curves at different temperatures and stress levels, expressed as:

$$\varepsilon_c(t) = \varepsilon_0 + mt^n \tag{2.11}$$

where ε_0 is instantaneous strain and *m* and *n* are material constants as a function of stress and temperature. It was concluded that Findley's power law could represent experimental data very well for both unreinforced and glass fiber reinforced materials at different temperatures. It was also observed that incorporation of the reinforcement in the polypropylene matrix reduced both the amount and the rate of creep strain.

Pipes et al. [45] conducted an experimental study to investigate the effect of temperature on compressive creep of discontinues glass fiber phenolic composites. Specimens with fiber orientations transverse and longitudinal to load axis were tested. Fiberglass bonds were attached to the specimens to avoid buckling. Normalized creep compliance versus time curves were used to compare different effects. It was concluded that creep resistance decreased with increasing temperature, as shown in Figure 2-14. Specimens with glass fiber in the longitudinal direction had less creep compared to specimens with fibers in the transverse direction. Time-temperature superposition principle was used to generate master curves for creep compliance versus time.

Silverman [46] compared the creep properties of different short and long chopped glass fiber reinforced thermoplastic composites at elevated temperatures (75 or 121 °C). The thermoplastics considered were acrylonitrile-butadiene-styrene (ABS), polycarbonate and polypropylene. The short glass fiber reinforced materials were injection molded from pellets prepared by mixing the resin with 40 wt% chopped glass strands. Comparison of flexural creep modulus (constant stress divided by strain) versus time curves of short and long chopped glass fiber composites showed that for long-term conditions, creep resistance of long fiber composites were better compared to short glass fiber composites for all three thermoplastics. This is shown in Figure 2-15 for polypropylene and polycarbonate composites. For ABS and polycarbonate base composites creep resistance of short glass fiber composites were better than long glass fiber composites for the initial loading period (up to 1 hour). This higher modulus for short glass fiber composites was attributed to the orientation of the short glass fibers in injection molded specimens, compared to random long glass fiber distribution in composite sheets.

Hugo et al. [47] conducted an experimental study on creep behavior of short glass fiber reinforced polypropylene. The effects of temperature, fiber content, and fiber/matrix adhesion were considered. Injection molded dumbbell-shaped specimens with 0, 5, 10, 20 and 30 wt% glass were used in temperature range of 23 to 80 °C. Some of the specimens were prepared using elevated interface adhesion to consider the effect of fiber/matrix adhesion. Minimum creep rate (MCR), which is the slope of strain-time curve in the secondary or steady state region of creep, was used as a parameter to investigate different effects. As can be seen from Figure 2-16 for the temperatures of 23 and 80 °C, plots of MCR versus stress in log-log scale result in straight lines for all conditions, represented by:

$$\dot{\varepsilon}_{c/\min} = B\sigma^{m} \tag{2.12}$$

Slope of the lines increased by increasing temperature for all the composites. Standard adhesion fibers lost their reinforcing effect at temperatures above 60 °C. It was concluded that insufficiently bond fibers lost their reinforcing role and the majority of fibers turn into potential defects, accelerating the creep and damage. Microscopy of fracture specimens showed that the prevailing damage was crazing perpendicular to the stress direction. Also crazes started preferentially at the fiber/matrix interface and was independent of the interface quality.

Pegoretti and Ricco [48] studied the effect of temperature on creep crack growth behavior of a 10 wt% short glass fiber reinforced polypropylene composite using single edge notch specimens machined from molded plaques. Creep crack propagation (CCP) at different temperatures in the range between 32 to 60 °C was obtained by applying a constant load. It was found that increasing temperature increased creep fracture process. At each temperature, as shown in Figure 2-17, the fracture propagation consisted of two stages, the first stage where crack decelerates because of crack tip blunting, followed by a stage of stable crack acceleration which ends with fracture instability.

Hadid et al. [49] developed an empirical viscoelastic model based on a simple power law model with stress-dependent parameter to represent creep strain versus time curves. Bending creep tests were conducted on neat and 43 wt% glass fiber reinforced polyamide-6.6. The basis of the model is the power law model represented in [43], with the constants of the power law model were represented by a stress-dependent function. The final form of the empirical non-linear viscoelastic model is given by:

$$\varepsilon(t) = a\sigma^{b} t^{c\exp(e,\sigma)} \tag{2.13}$$

The model has four temperature dependent constants *a*, *b*, *c* and *e*. The model could represent short-term creep strain versus time curves very well.

Chevali et al. [50] studied flexural creep behavior of nylon-6.6, polypropylene, and high density polyethylene (HDPE) discontinuous glass fiber composites in the temperature range of 23 to 120 °C. The non-linear power law model developed by Hadid et al. [49] was used to represent the experimental data. It was concluded that the non-linear empirical power model could represent experimental data very well for all the materials at different temperatures. Time-temperature-stress superposition principle was also used to obtain creep master curves and shift factors to be able to predict long-term creep strains, as shown in Figure 2-18 for all the materials at a reference temperature of 50 °C.

Houshyar et al. [51] investigated short-term creep-recovery behavior of polypropylene-co-ethylene (PPE) composites reinforced with polypropylene fibers considering effects of temperature in the range of 25 to 90 °C and fiber content. An increase in temperature resulted in higher macromolecular mobility and higher deformation during creep. Time-temperature superposition principle was used to predict long-term creep properties at different temperatures and stress levels.

Plaseied and Fatemi [52] discussed short-term (up to 100 hours) tensile creep behavior of vinyl ester polymer and its nanocomposites with 0.5% functionalized carbon nanofibers at different temperatures and stress levels. Findley's power law relationship mentioned earlier (Equation 2.11) was used to represent the creep strain versus time at different temperatures and stress levels. The constants *m* and *n* were represented by:

$$\log(m \; or \; n) = a + bT + c\sigma + d\sigma T \qquad (2.14)$$

where *a, b, c* and *d* are material constants. The model showed good predictions of creep strain versus time.

Kouadri et al. [53] studied the effect of temperature in the range of 25 to 55 °C on creep parameters and behavior of polyester reinforced with 70 wt% short glass fibers used for a storage tank. A power law model was used to represent the creep strain at different testing temperatures and stress levels, expressed as:

$$\varepsilon(t) = \varepsilon_0 + B\sigma^m t^k \qquad (2.15)$$

where *B, m* and *k* are material constants. At testing temperatures under 45 °C the primary and secondary regions of a usual creep curve were observed, while at temperatures higher than 45 °C the tertiary stage was dominant for the range of applied loading. The value of constant *m* was independent of temperature and applied stress. The value of constant *B* increased with increasing temperature approximately with a linear relation. The value of constant *k* also increased with increasing temperature with a linear relation up to 47 °C, beyond this temperature it was about constant. The change in creep behavior around 45 °C was explained by the first order transition in the matrix that results from the rotation of the lateral group along molecular polymer chain.

2.4 Isothermal Fatigue Behavior

Applications of polymeric materials in cyclically loaded components where the material should endure fatigue loading in severe environmental conditions, such as elevated temperatures, are increasing rapidly. There are several studies which considered the effect of cyclic loading on short fiber polymer composites at elevated temperatures.

Mortazavian and Fatemi [54] conducted a recent literature review on fatigue behavior of SFRPCs. The review consisted of microstructural related factors (including those related to fiber length, content, and orientation), damage development and modeling, loading conditions (including mean stress effects, cyclic creep, variable amplitude loading, and multiaxial stress effects), environmental effects (including the effects of moisture content and temperature), and fatigue of components. Cyclic deformation and softening, viscous characteristics, and dissipative response including cyclic frequency and self-heating effects, were also discussed. The emphasis of their review was on fatigue crack initiation behavior of synthetic short fiber reinforced polymer composites, mainly processed with injection molding and mostly used in automotive applications.

Jia and Kagan [30] investigated effects of aging time and temperature on tension-tension (R = 0.1) load-controlled fatigue behavior of short glass fiber (33 wt% glass) polyamides-6 and polyamide-6.6. Typical S-N curves were used to represent the experimental fatigue data. Like the tensile strength, fatigue strength decreased by increasing temperature. Aging up to 1000 hours increased fatigue strength for both materials at RT, but it did not have any effect on fatigue strength at 121 °C. The effect of aging on fatigue strength was related to crystalline index, similar to the aging effect on tensile strength, mentioned previously. This effect increased by increasing aging time. A master curve was generated to represent all fatigue data at different temperatures and for different aging conditions by normalizing fatigue data of both short glass fiber reinforced composites with tensile strength, which is shown in Figure 2-19.

Handa et al. [55] studied effect of temperature on fatigue behavior of short glass fiber reinforced polyamide-6.6 with 33 wt% glass fiber. Axial stress-controlled fatigue tests with R = 0 were conducted on injection molded specimens at different temperatures from 0 to 120 °C and at frequencies of 5, 20 and 50 Hz. Increasing temperature significantly reduced fatigue strength as shown in Figure 2-20(a). Both the slope and the intercept of S-N lines in semi-logarithmic curves indicated a linear relationship with the reciprocal of temperature. This relationship was divided into two regions by T_g, which was reported to be 57 °C. The slope and the intercept did not show any dependency on temperature at temperatures above T_g, while at temperatures below T_g the slope and the intercept increased with increasing the reciprocal of temperature as shown in Figures 2-20(c) and (d). It was concluded that the failure mechanisms were different at temperatures above and below T_g. A temperature-frequency superposition model was developed to represent all fatigue data at different temperatures and frequencies by a master curve using temperature and frequency shift factors, shown in Figure 2-20(b).

In the studies of Sonsino and Moosbrugger [56] and De Monte et al. [22, 57] effects of temperature, mean stress, and notch on constant and variable amplitude fatigue behaviors of short glass fiber reinforced polyamide-6.6 with 35 wt% glass fiber were investigated. Tests were conducted at temperatures of 22, 80, and 130 °C, with R ratios of -1 and 0 using injection molded specimens. Fatigue strength decreased significantly by increasing temperature and S-N lines at room temperature and 130 °C had about the same slopes, as shown in Figure 2-21(a). For the fatigue test conducted with maximum stress about half of ultimate tensile strength, non-zero area within hysteresis loop at 130 °C was observed, while the area of hysteresis loop at RT for the same condition was about zero. This non-linearity at high temperature was related to the fact that RT is below T_g and 130 °C was higher than T_g, which was about 60 °C. It was concluded that the notch influence almost vanished at 130 °C where S-N lines for different specimens with different notch factors were coincident, as shown in Figure 2-21(b).

Noda et al. [58] studied the effect of temperature on constant amplitude fatigue behavior of short glass fiber reinforced polyamide-6.6. Injection molded PA6.6 specimens reinforced with 33 wt% short glass fiber were used with $R = 0$ loading and frequencies of 10 and 20 Hz, and temperature in the range of 0 to 150 °C. Viscoelastic properties such as storage modulus, E', and loss tangent, tan δ, rather than the specimen surface temperature were continuously recorded during fatigue tests. Plot of the slope and the intercept of S-N lines in semi-logarithmic S-N curves versus test temperature, shown in Figure 2-22, indicate different behavior for temperatures below and above T_g. Both the slope and the intercept decreased almost linearly with increasing temperature at temperatures lower than T_g, which is about 50 °C, while the slope increased with increasing temperature and the intercept was almost constant for temperatures higher than T_g. The fatigue mechanisms were different at temperatures below and above T_g. Below T_g, microcracks propagated around fiber ends, and then cracks propagated between fiber ends in a brittle manner. Above T_g, microcracks propagated accompanied by debonding along the fiber sides and forming crack walls, after which the crack walls connected by bridging in a ductile manner.

Guster et al. [59, 60] investigated effects of temperature and fiber orientation on fatigue behavior of 50 wt% short glass fiber reinforced polyamide-6T/6I specimens with $R = 0.1$ at 50% relative humidity. Specimens were loaded parallel or perpendicular to the mold flow direction to consider fiber orientation effect. Increasing the temperature from 23 to 120 °C decreased the fatigue strength considerably. In each flow direction, the slopes of S-N curves remained nearly constant at different temperatures, as can be seen from Figure 2-23. A fatigue life assessment method was also developed for life prediction of components made of injection molded polymer composites, which takes into account fiber orientation and temperature effects.

Lockwood et al. [24, 25] studied the effect of temperature ranging between 24 and 120 °C on fatigue strength of vibration-welded and unwelded short glass fiber polyamide-6. Fatigue tests were conducted under constant amplitude loading with a stress ratio of $R = 0.1$ and within frequency range of 2 – 10 Hz. As temperature increased, fatigue strength of both welded and unwelded composites reduced. For both welded and unwelded specimens, the ratio of fatigue strength to static tensile strength was approximately 0.45, regardless of the temperature.

Mortazavian and Fatemi [61, 62] evaluated fatigue behavior of a 30 wt% short glass fiber polybutylene terephthalate and a 35 wt% short glass fiber polyamide-6, at a range of temperature between -40 to 125 °C and in different mold flow directions. Fatigue strength was significantly influenced by the temperature. A shift factor of Arrhenius type was introduced to correlate the fatigue data at different temperatures. A method was applied to estimate fully-reversed (R = -1) fatigue strength from tensile strength at different temperatures and mold flow directions, expressed as:

$$S_a = 1.08\, S_u\, (N_f)^{-0.085} \tag{2.16}$$

where S_a is stress amplitude, S_u is ultimate tensile strength, and N_f is number of cycles to failure. A fatigue life prediction model based on the strength degradation of material under constant amplitude loading was also applied to correlate fatigue data at different temperatures, stress ratios, and in different mold flow directions, as shown in Figure 2-24.

2.5 Thermo-Mechanical Fatigue and Creep-Fatigue Interaction

Some in-service components are subjected to cyclic stresses with or without a mean stress and at constant or variable elevated temperatures. These conditions can give rise to thermo-mechanical fatigue (TMF) or creep-fatigue failures. TMF is caused by a combination of cyclic mechanical and cyclic thermal loadings where both the stresses and temperature vary with time. This combination can be in-phase (IP) or out-of-phase (OP). Components and structures in high-temperature applications, for instance in their start up or shut down cycles, are often subjected to such TMF loading. Combined creep and fatigue damage can also occur, for example, hold-time periods with static stress during cyclic loading.

Damage developed by interaction of thermal and fatigue or creep and fatigue loadings in such cases may be completely different from the damage from pure thermal, fatigue, and creep situations. In most cases, the synergistic effect of combined damages are more detrimental, compared to addition of damages caused by each loading conditions separately. Although the applications of short glass fiber composites at high temperatures are rapidly increasing, there are only a small number of studies about TMF or creep-fatigue interaction behavior of short fiber composites.

Pierantoni et al. [63] simulated the behavior of a 30 wt% short glass fiber reinforced polybutylene terephthalate (PBT-GF30) under TMF loading using FEA. The goal of the study was to model the stress variations during strain-controlled TMF loading. The experimental procedure consisted of performing TMF tests in temperature ranges of -40 °C to 40 °C and -40 °C to 120 °C on smooth and sharply notched ($K_t = 9.8$) specimens. A pre-strain was applied, then heating-up and cooling-off steps were started, until failure of the specimen. As the total strain during the test was constant, variation of thermal strain caused variation of mechanical strain, therefore, both thermal and mechanical cycles were introduced in the test specimen. Two models were used to reproduce the stress profile during TMF tests using FEA software, an isotropic linear elastic model and a linear viscoelastic model. For the linear elastic model, elastic modulus and Poisson’s coefficient at different temperatures are required. The linear viscoelastic model requires viscoelastic material properties measured from dynamic mechanical analysis (DMA). The temperature dependency of the constants and properties were modeled using time-temperature superposition principal. Comparison of stress profiles obtained from these two models and experimental results showed that the linear elastic model was suitable only at low stress levels and low pre-strain values, because the model could not capture the stress relaxation at high pre-strain loading conditions. The stress profile resulted from linear viscoelastic model calibrated with DMA, were in good agreement with experimental data for different conditions for both plain and notched specimens and for low and high pre-strain levels.

Schaaf et al. [64] investigated the mechanisms of damage at the microscopic scale for the TMF tests described in [63]. In addition to TMF tests, some isothermal strain-controlled fatigue tests (ISCF) were also conducted on plain and notched specimens. Investigation of fracture surface of rupture specimens under TMF loading using SEM showed that typical isothermal fatigue failure mechanisms also occur under TMF loading, including initiation of damage at fiber ends, growth along fiber and matrix interface, and fiber pullout. Similarity between fracture surfaces of TMF sharply notched specimens ($K_t = 9.8$) and isothermal fatigue condition showed that the temperature at which the dominant failure mechanisms occur under TMF was the minimum temperature and the damage mechanism was independent of the maximum temperature.

Schaaf et al. [65] used the conclusions of the studies in [63, 64] to develop a methodology to predict lives for SFRPCs under TMF loading. A summary of TMF test results are presented in Figure 2-25(a), as a fatigue life plot in terms of normalized stabilized maximum nominal stress during TMF cycling. Increasing pre-strain, maximum temperature, and notch factor values caused a decrease in fatigue life. The theoretical methodology started with modeling the anisotropy of the material. A finite volume energy approach based on strain energy density (SED) was then used to correlate the ISCF test data with different notch factors and TMF test data with ISCF data at minimum temperature at which the dominant damage occurred [63]. The correlation was very good for the three different notch types, the three different temperature ranges, and the three of the pre-strain levels (30%, 50% and 80% of UTS). The test data with pre-strain level of 10% of UTS were not correlated with the other data, because plastic overloads did not occur in this case. To correlate all the data for all pre-strain levels, a TMF specific parameter (A_{TMF}) was introduced which was determined by some TMF tests at low pre-strain levels. TMF master curve with all the experimental data is shown in Figure 2-25(b).

Bowman and Barker [66] examined effect of creep-fatigue loading condition on a polyethylene pipeline component experimentally. Stress-controlled tests were done on an injection molded 90° Tee type pipeline component by applying cyclic waveforms with different hold-times. The Tee system was filled with tapped water with constant temperature of 79.5 °C. A trapezoidal loading profile that had elements of fatigue and constant stress loading was used. The experimental data were presented using a creep-fatigue damage curve by considering the concept of fractional damage. Based on this concept, creep damage and fatigue damage are expressed as fractions of time or cycles to failure of creep-fatigue test in relation to time or cycles to failure in pure creep or pure fatigue condition. Similar to most metallic materials, a non-linear creep-fatigue interaction behavior was observed, as shown in Figure 2-26. The creep and fatigue elements of the trapezoidal loading profile interacted synergistically to accelerate damage accumulation, therefore, the linear damage rule is non-conservative in this case.

Crowther et al. [67] investigated effect of interaction between static and dynamic loadings for glass reinforced plastics which were employed in the cooling water (CW) system of coastal power stations. The CW systems were exposed to an aggressive environment, sea water at temperature up to 40 °C, and to a complex loading pattern consisting of a background static load superimposed on sinusoidal variations and periodic unloads. The material used was a combination of layup of mixed chopped-strand mat and woven-roving in polyester with overall fiber volume fraction of 36 wt%. Tests were conducted using both dry and wet specimens to consider the effect of environment. It was concluded that there is a boundary frequency above which failure is determined solely by the number of stress cycles (fatigue damage) and below which failure is determined by time at load (creep damage). Besides, creep-fatigue interaction was seen to be detrimental at lower frequencies.

Pegoretti and Ricco [68-70] studied synergistic fatigue and creep crack growth processes in glass fiber reinforced polypropylene composites. They investigated effects of frequency and fiber content on creep-fatigue crack propagation process. Single edge notch specimens machined from molded plaques were used for experimental studies. The fatigue crack propagation (FCP) resistance of the composites was found to improve as the fiber weight fraction increased. Increasing frequency up to a certain limit caused a dramatic increase in fatigue life. To explain the effect of frequency on fatigue life, FCP was considered to be composed of two components, one due to a pure fatigue process, and the other due to viscoelastic creep as suggested in [71]. The mathematical formulation, assuming linear damage summation, can be expressed as follow:

$$\left(\frac{da}{dN}\right)_{total} = \left(\frac{da}{dN}\right)_{fatigue} + \left(\frac{da}{dN}\right)_{creep} = \left(\frac{da}{dN}\right)_{fatigue} + \left(\frac{da}{dt}\right)_{creep}\frac{dt}{dN} \qquad (2.17)$$

where *dt/dN* is the time period, which can be expressed as the inverse of test frequency (*1/f*). The pure fatigue and pure creep crack growth rates were obtained by plotting the total fatigue crack growth rate versus inverse of test frequency at different stress intensity factor ranges. According to this procedure, as shown in Figure 2-27, it was concluded that for low test frequency (0.1 and 1 Hz) the role of creep crack growth is predominant, while for high frequency (10 Hz) creep and fatigue crack growth became comparable, giving about the same contribution to the overall crack rate. Comparison of FCP obtained in this study with CCP data obtained in [48] indicated that FCP at low frequencies (0.1 and 1 Hz) were substantially equivalent to an isothermal CCP at 45 °C. This temperature, which is higher than test temperature (23 °C), was related to the crack tip temperature which is known to be higher than the test temperature.

2.6 Summary

Short fiber polymer composites are cost effective, lightweight, and corrosion resistant with sufficient strength for many applications. Many applications of short fiber polymer composites are at elevated temperatures, while mechanical behavior of these materials is considerably temperature dependent. This review compiled the information from technical literature on tensile, creep, isothermal fatigue, thermo-mechanical fatigue, and creep-fatigue interaction behaviors of short fiber reinforced polymer composites at elevated temperatures.

Elastic modulus and tensile strength decrease and ductility increases with increasing temperature, with an abrupt change near T_g. The temperature sensitivity is lower in the mold flow direction, as compared to the normal to the mold flow direction. Empirical relations have been developed to represent the temperature and strain rate dependencies of the tensile properties. At temperatures below T_g or at high strain rates, fiber pullout and matrix brittle fracture are dominant failure mechanisms, while at temperature above T_g or low strain, failure occurs via matrix crazing and crack propagation near the fiber ends.

Thermal aging can have detrimental or beneficial effects on tensile properties of short fiber polymer composites, depending on aging time, aging temperature, and material. Aging affects the crystalline index and also the structure of crystals in thermoplastics. The main consequence of the water uptake in hygrothermal aging is plasticization of matrix. The rate of water absorption increases by increasing temperature, but the maximum capacity of water absorption does not change. As polymer composites absorb moisture, hydrogen bonding between moisture and matrix forms and the interaction between polymer and fibers becomes less effective. As a result, the matrix cannot transfer the load to a sufficient length of fibers, less fiber breakage occurs, and ductility increases.

Creep resistance and rupture strength decrease with increasing temperature. Time-temperature-stress superposition procedure has been used for extending short-term creep data for long-term creep predictions in most of the studies. Power law models, such as Findley's power law are widely used to represent creep strain curve for a wide range of temperatures and stress levels. Microscopy of the fracture specimens shows that the prevailing creep damage is crazing perpendicular to the stress direction. Crazes start preferentially at the fiber/matrix interface and the craze inducing activity of fibers is independent of the interface quality.

Fatigue strength decreases with increasing temperature. Both the slope and the intercept of S-N lines in semi-logarithmic curves decrease nearly linearly with increasing temperature below T_g. Below T_g, microcracks propagate around fiber ends, followed by crack propagation between fiber ends in a brittle manner. Above T_g, microcracks propagate accompanied by debonding along the fiber length, forming crack walls, after which the crack walls connect by bridging in a ductile manner. Non-linearity of cyclic deformation behavior because of plasticity and viscoelasticity is observed at temperatures higher than T_g, where the area within the hysteresis loops is higher compared to that at the same condition and at temperatures lower than T_g. Notch influence on fatigue behavior nearly vanishes at elevated temperatures.

Investigation of fracture surface of failed specimens under TMF loading shows that typical isothermal fatigue failure mechanisms also occur under TMF loading. This includes initiation of damage at fiber ends, crack growth along fiber and matrix interface, and fiber pullout. The temperature at which the dominant failure mechanism occurs under TMF for sharply notched specimens is the minimum temperature and the damage mechanism is independent of the maximum temperature. Strain energy density range has been found to correlate ISCF and TMF experimental data.

Creep-fatigue damage curve by considering the concept of fractional damage has been used to represent experimental creep-fatigue interaction data. Based on this concept, creep damage and fatigue damage are expressed as fractions of time or cycles to failure in relation to time or cycles to failure under pure creep or pure fatigue condition. However, similar to most metallic materials, a non-linear creep-fatigue interaction behavior is typically observed. The creep and fatigue damages interact synergistically to accelerate damage accumulation, therefore, the linear damage rule is non-conservative under such conditions.

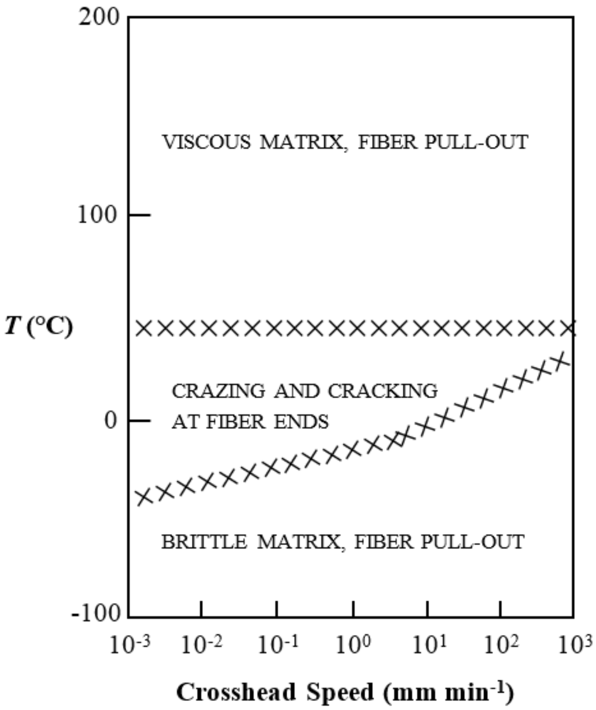

Figure 2-1: Failure behavior map for a short glass fiber reinforced polyethylene terephthalate (Regenerated) [5].

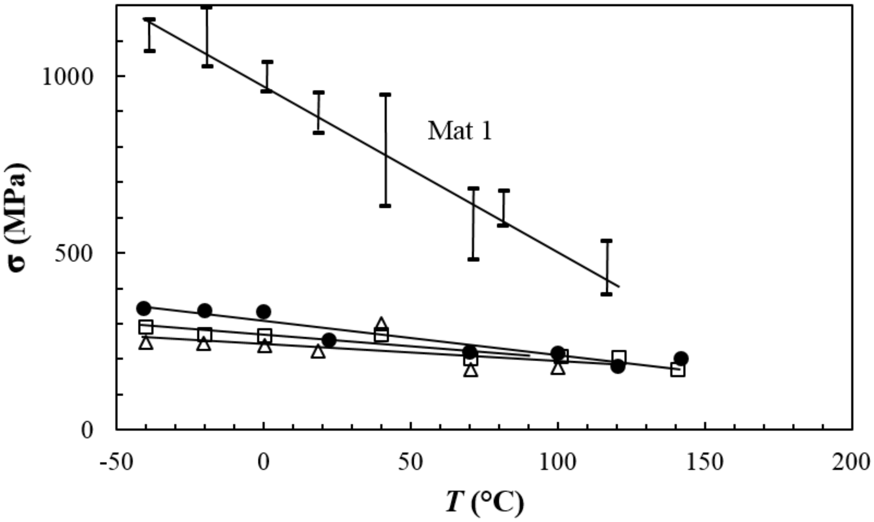

Figure 2-2: Variation of stress at rupture with temperature for different polyamide-6.6 composites. Material 1 is continuous fiber composite, material 2, 3 and 4 are short glass fiber composites with average fiber length of 9, 3 and 0.3 mm respectively (Regenerated) [6].

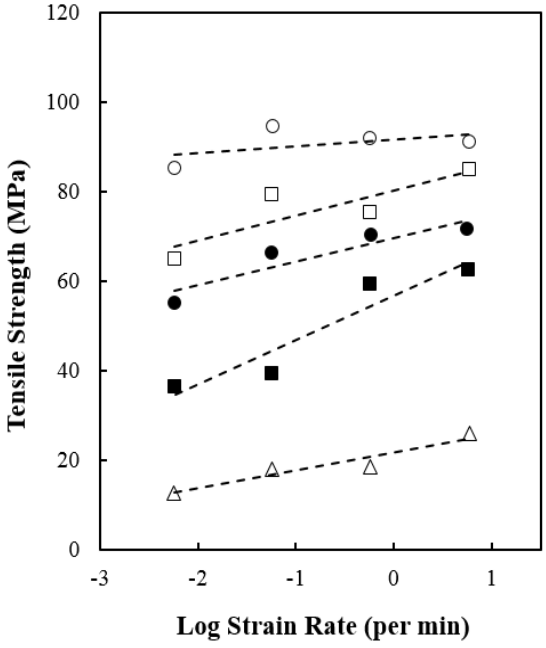

Figure 2-3: Variation of tensile strength with strain rate at various temperatures for a glass fiber-epoxy resin composite. (○) 20 °C, (□) 40 °C, (●) 60 °C, (■) 80 °C, and (△) 100 °C (Regenerated) [13].

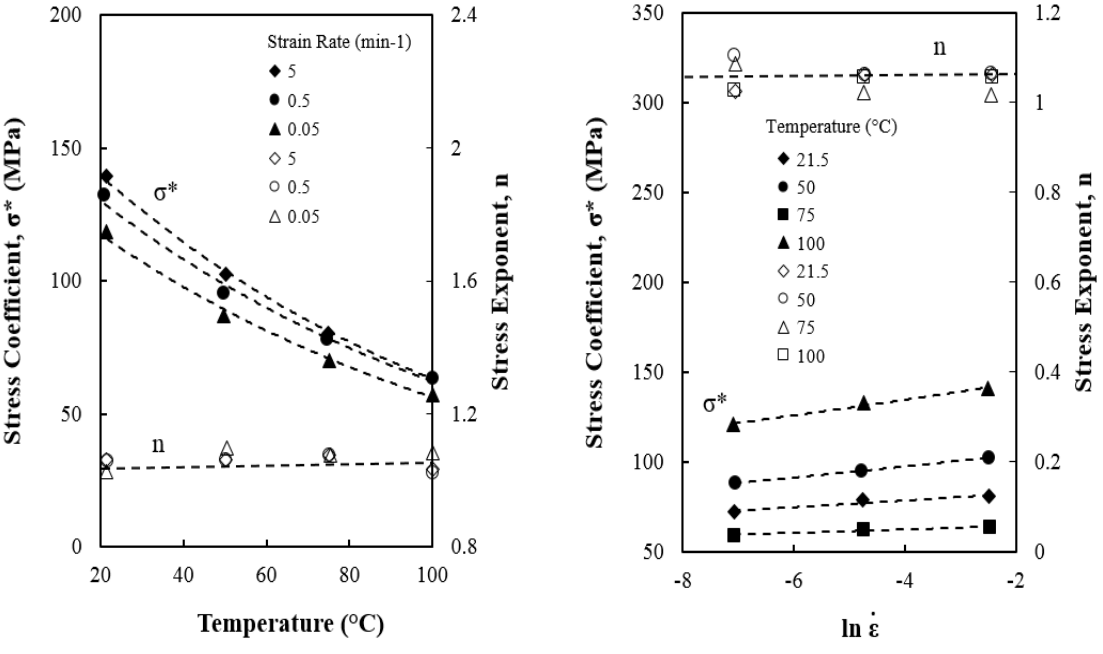

(a) (b)

Figure 2-4: Effects of temperature and strain rate on (a) stress exponent, *n*, and, (b) stress coefficient, *σ**, of 33 wt% short glass fiber reinforced polyamide-6 in transverse direction (Regenerated) [18].

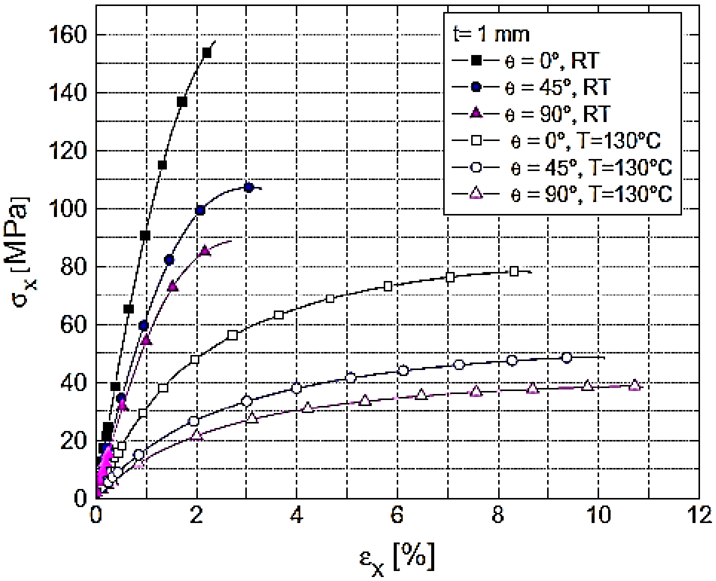

Figure 2-5: Comparison of stress–strain curves for 1 mm thick specimens of short glass fiber reinforced polyamide-6.6 in different directions at RT and 130 °C [21].

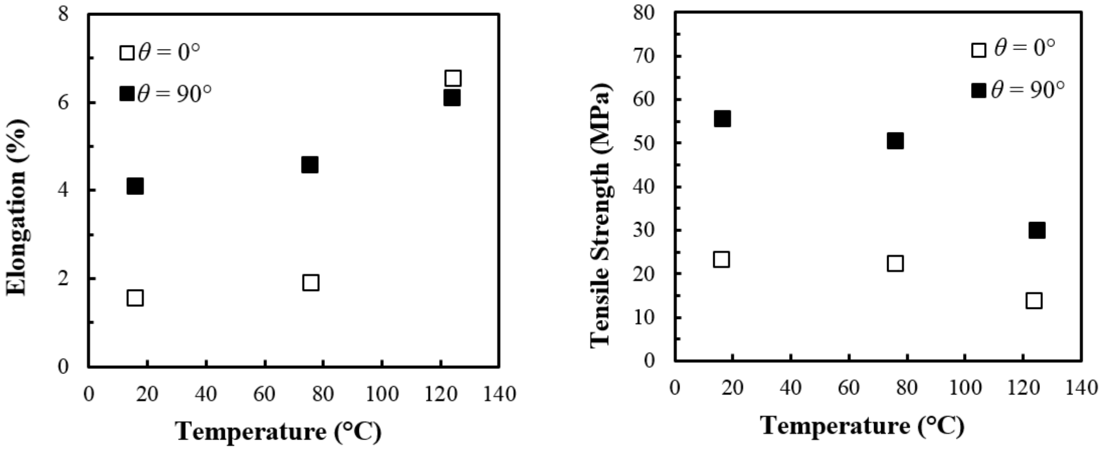

(a) (b)

Figure 2-6: Effect of temperature on (a) elongation and (b) tensile strength for 60 wt% short fiber reinforced poly-phenylene sulfide composite in longitudinal and transverse directions (Regenerated) [23].

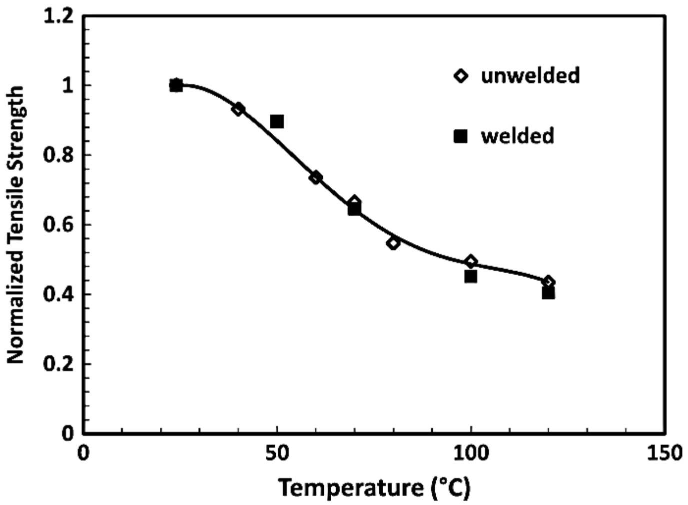

Figure 2-7: Effect of temperature on normalized tensile strength of welded and unwelded 30 wt% short glass fiber reinforced nylon-6 [24].

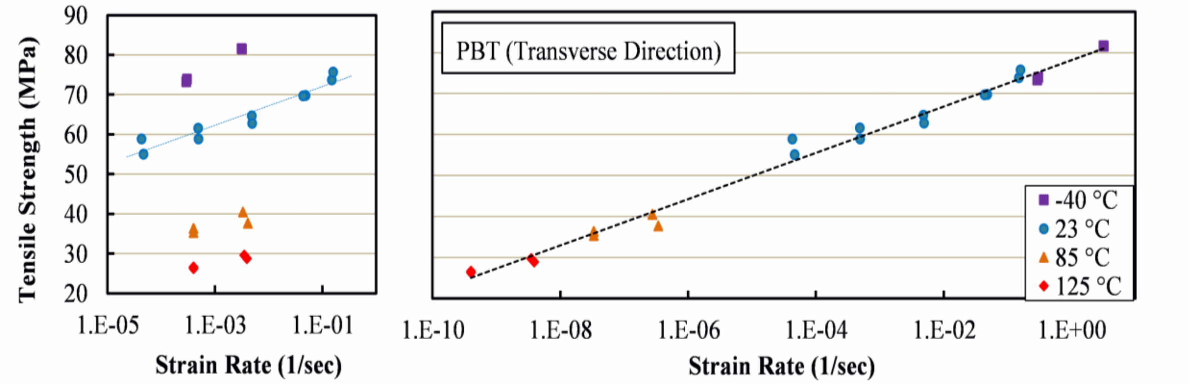

Figure 2-8: Master curve generated using time-temperature superposition principle for PBT in the transverse direction [26].

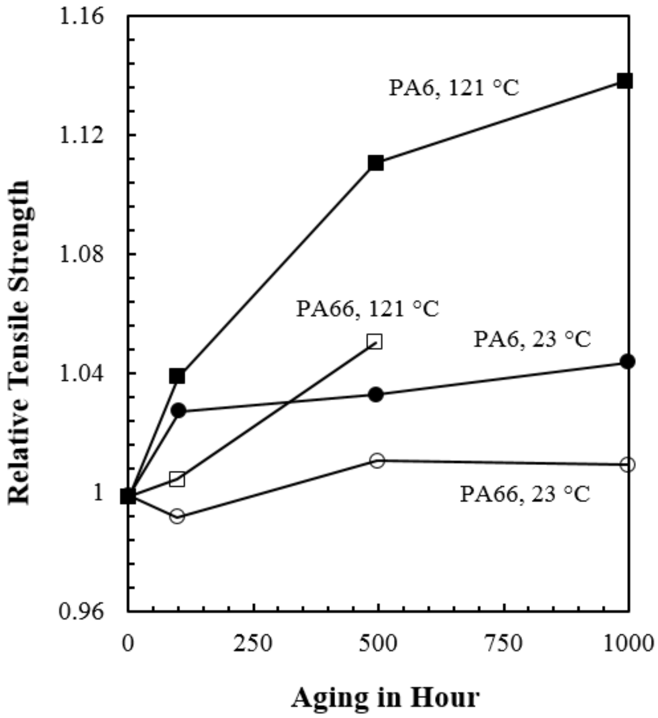

Figure 2-9: Effects of aging time and temperature on relative tensile strength of polyamide-6 and polyamide-6.6 short glass fiber reinforced composites (Regenerated) [30].

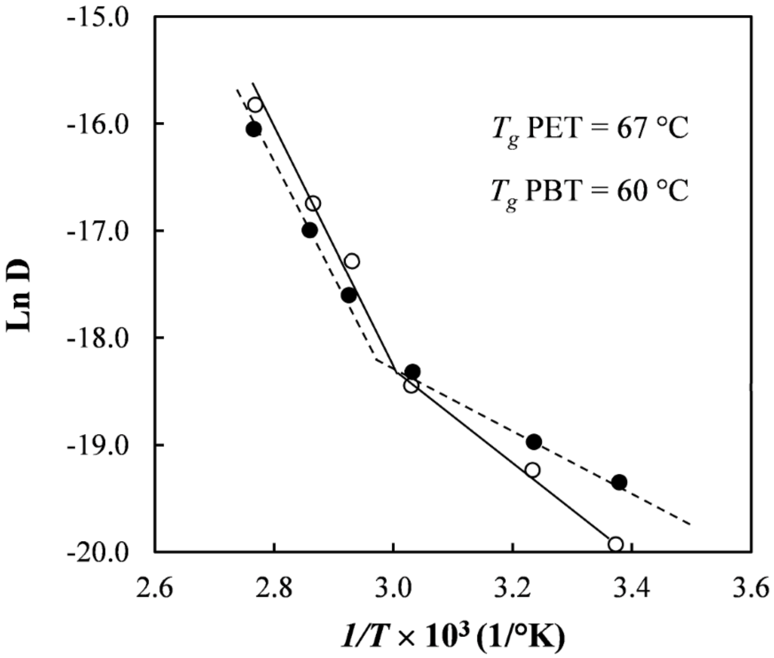

Figure 2-10: Variation of diffusion coefficient (*D*) with temperature for polyethylene terephthalate, PET (●) and polybutylene terephthalate, PBT (○) (Regenerated) [33].

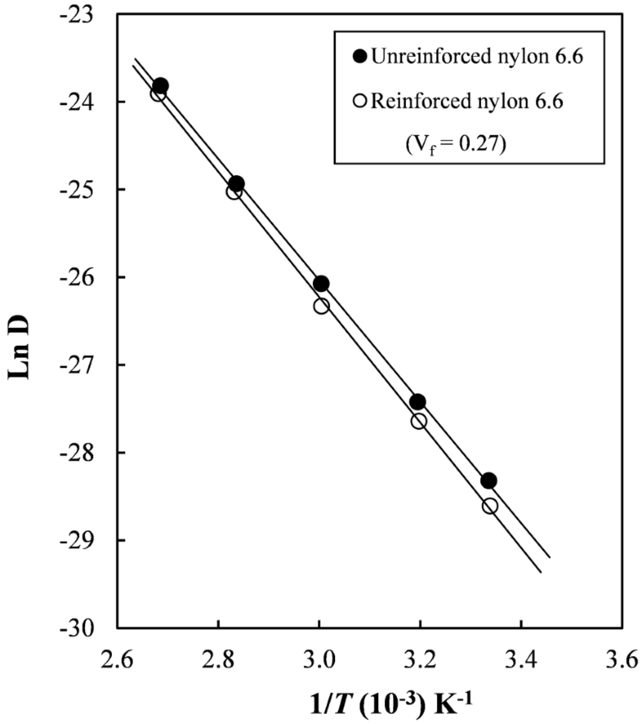

Figure 2-11: Arrhenius type plot for variation of diffusion coefficient with temperature for reinforced and unreinforced nylon-6.6 (Regenerated) [35].

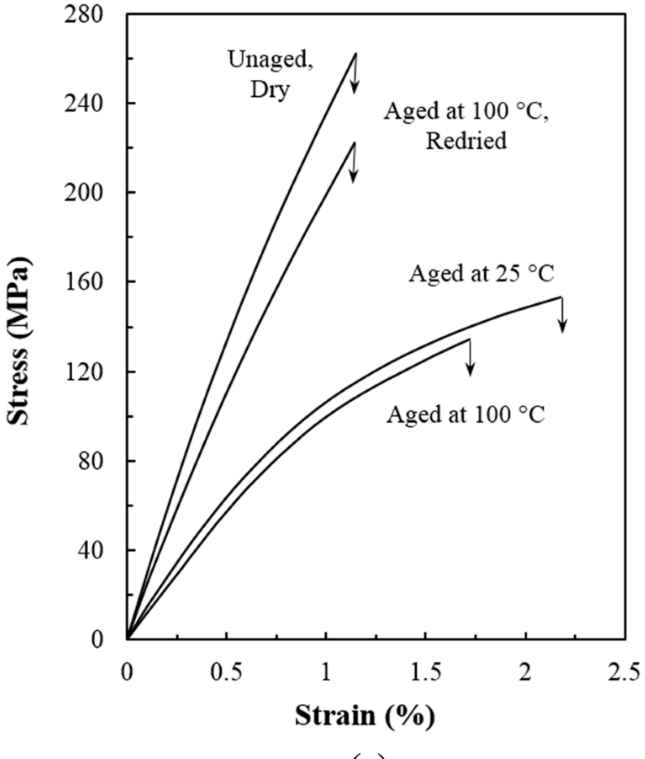

(a)

Figure 2-12: Stress-strain curves for un-aged, aged, and re-dried 40 wt% short carbon fiber reinforced nylon-6.6 at 20 °C (Regenerated) [35].

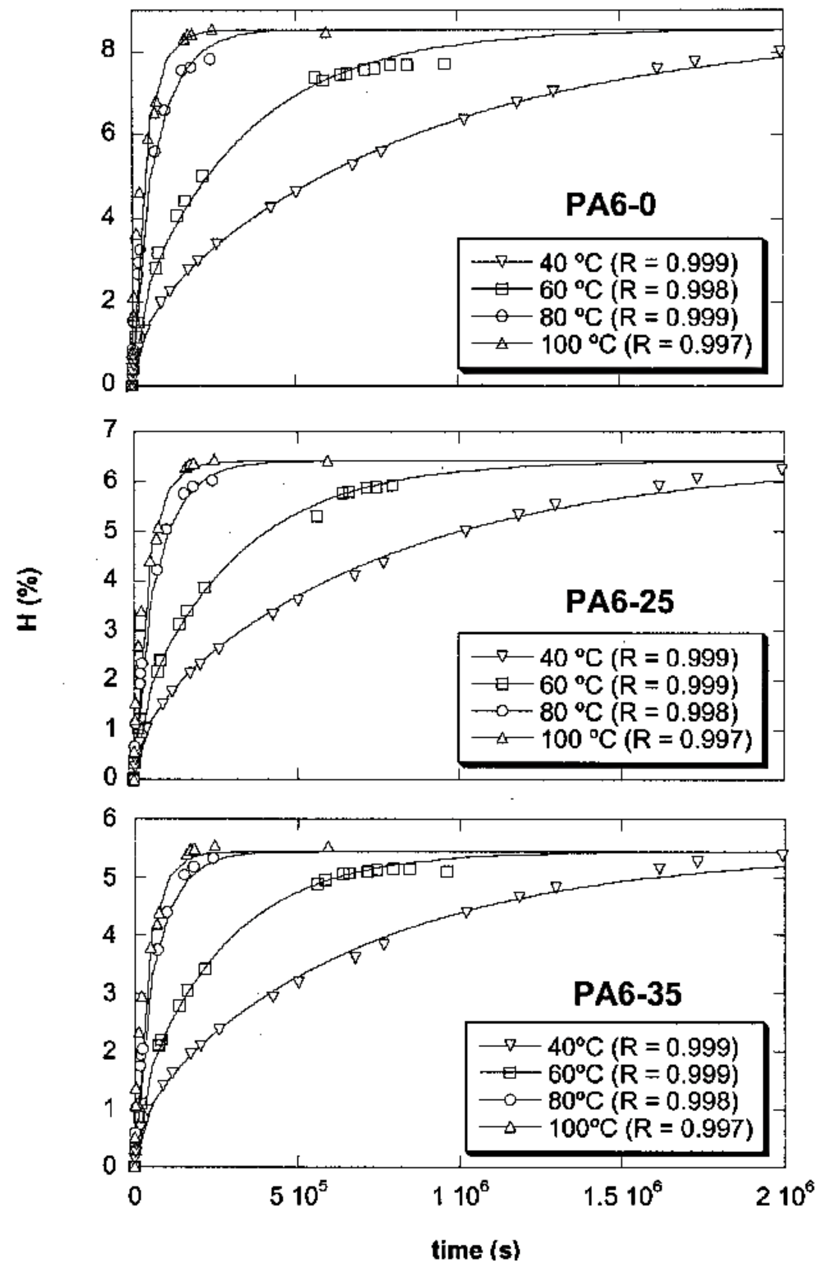

Figure 2-13: Water absorption of polyamide-6 specimens with different fiber content weight at different temperatures [39].

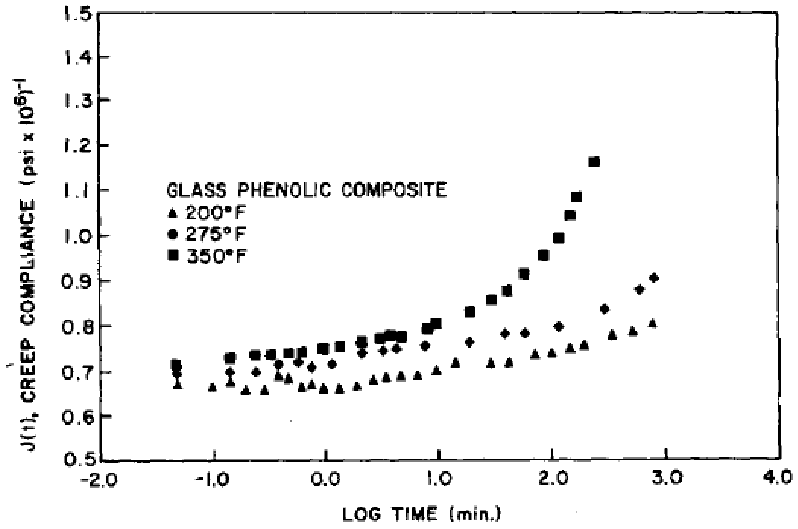

Figure 2-14: Effect of temperature on compressive creep behavior of discontinues glass fiber phenolic composites with fibers in transverse direction [45].

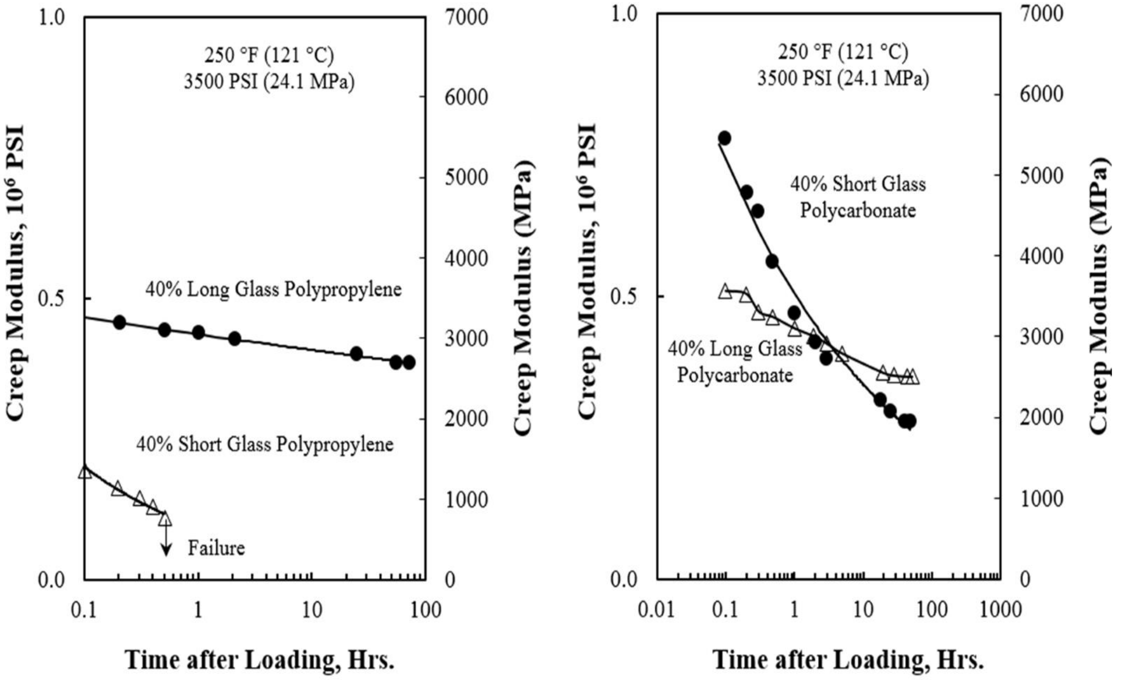

(a) (b)

Figure 2-15: Flexural creep modulus versus time curves at 121 °C under stress level of 24.1 MPa for (a) reinforced polypropylene specimens, (b) reinforced polycarbonate specimens (Regenerated) [46].

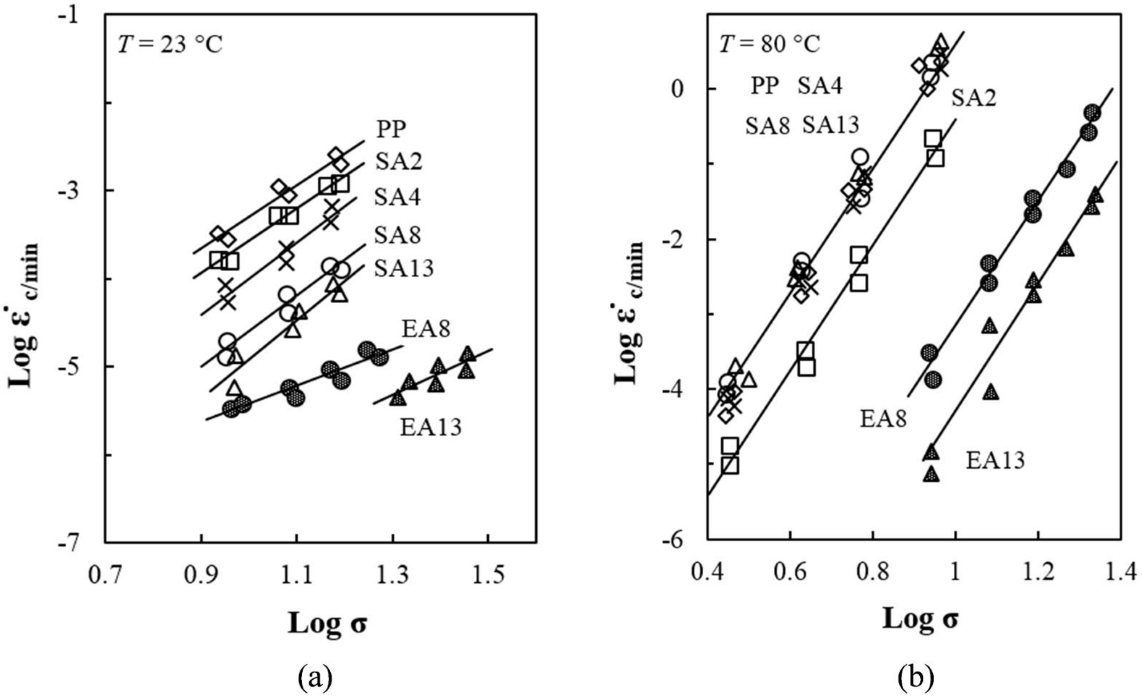

Figure 2-16: Double logarithmic plots of minimum creep rate versus stress at 23 and 80 °C. PP is neat polypropylene. SA2, SA4, SA8 and SA13 are polypropylene-based composites with respectively 5, 10, 20 and 30 wt% short glass fiber content with standard fiber/matrix adhesion. EA8 and EA13 are polypropylene-based composites with respectively 20 and 30 wt% short glass fiber content with elevated fiber/matrix adhesion (Regenerated) [47].

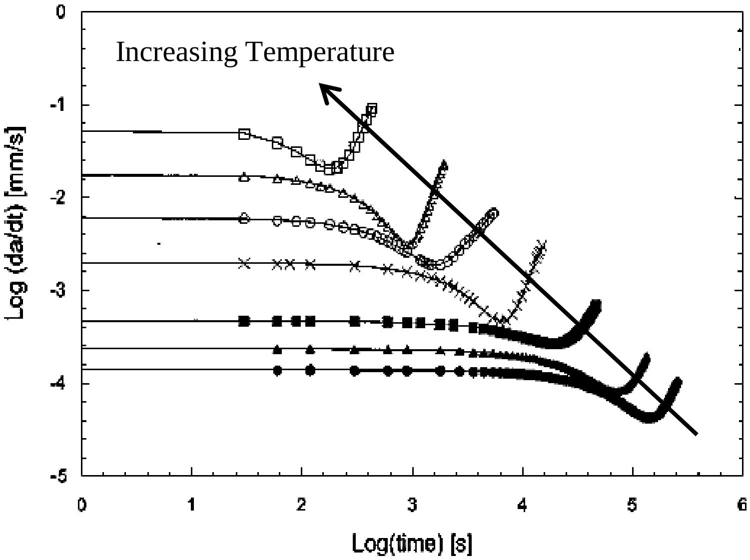

Figure 2-17: Crack speed vs. time for creep tests performed at various temperatures for short glass fiber reinforced polypropylene composite [48].

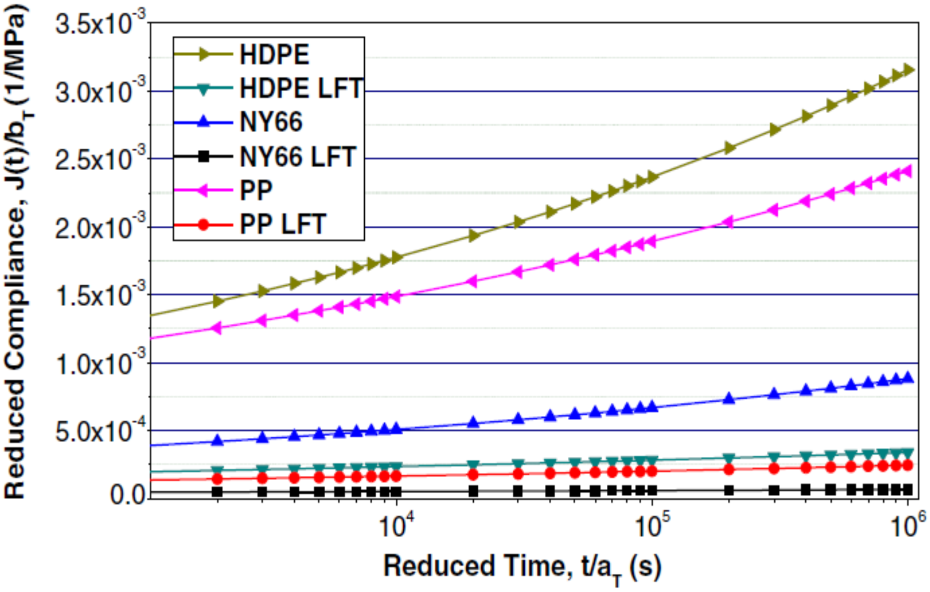

Figure 2-18: Time–temperature–stress superposition master curves for several short glass fiber composites at a reference temperature of 50 °C [50].

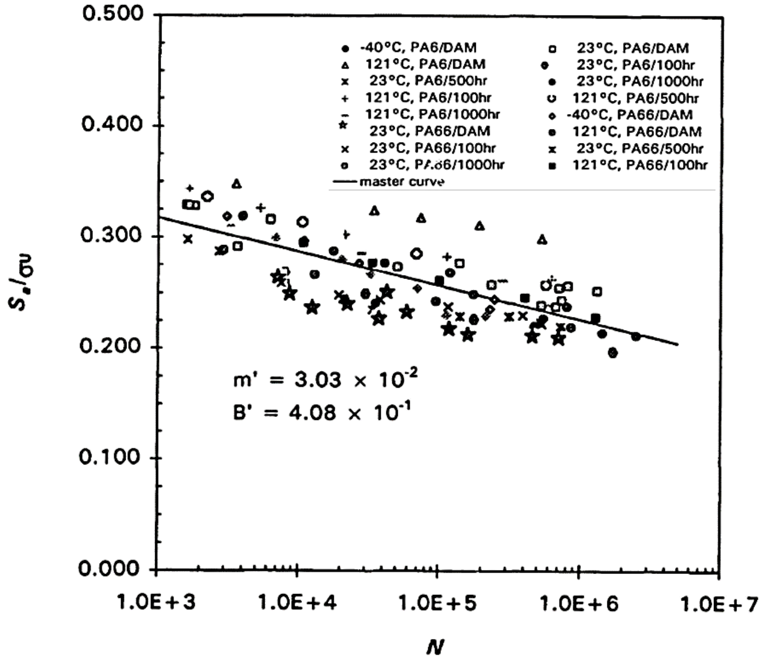

Figure 2-19: Fatigue strength master curve for polyamide-6 and polyamide-6.6 short glass fiber thermoplastic composites incorporating temperature and aging time effects [30].

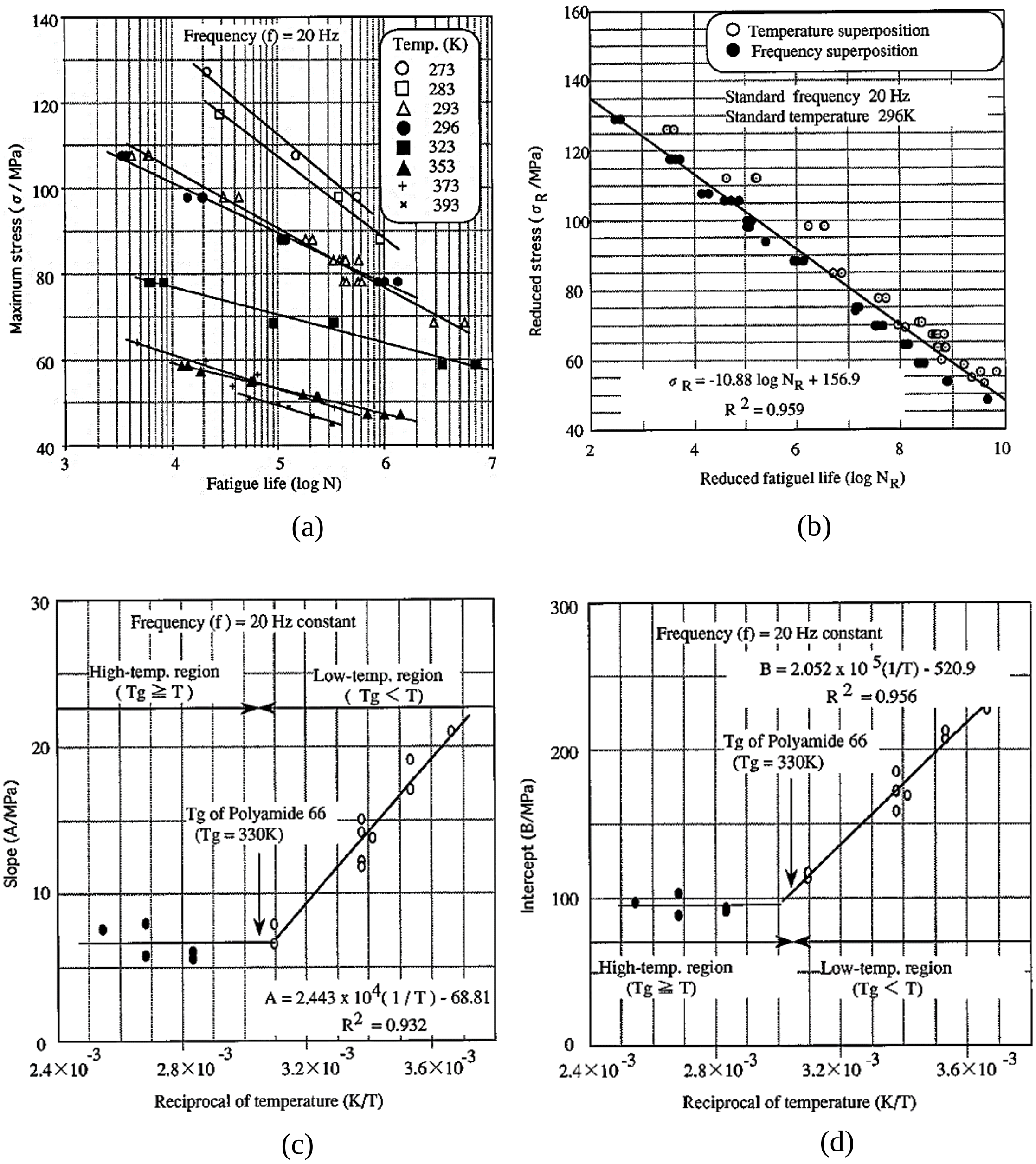

(a) (b)

(c) (d)

Figure 2-20: (a) Dependence of *S-N* curves on temperature, (b) representation of all fatigue data at different temperatures and frequencies by a master curve, (c) variation of slope and, (d) intercept of *S-N* lines with temperature for short glass fiber reinforced polyamide-6.6 [55].

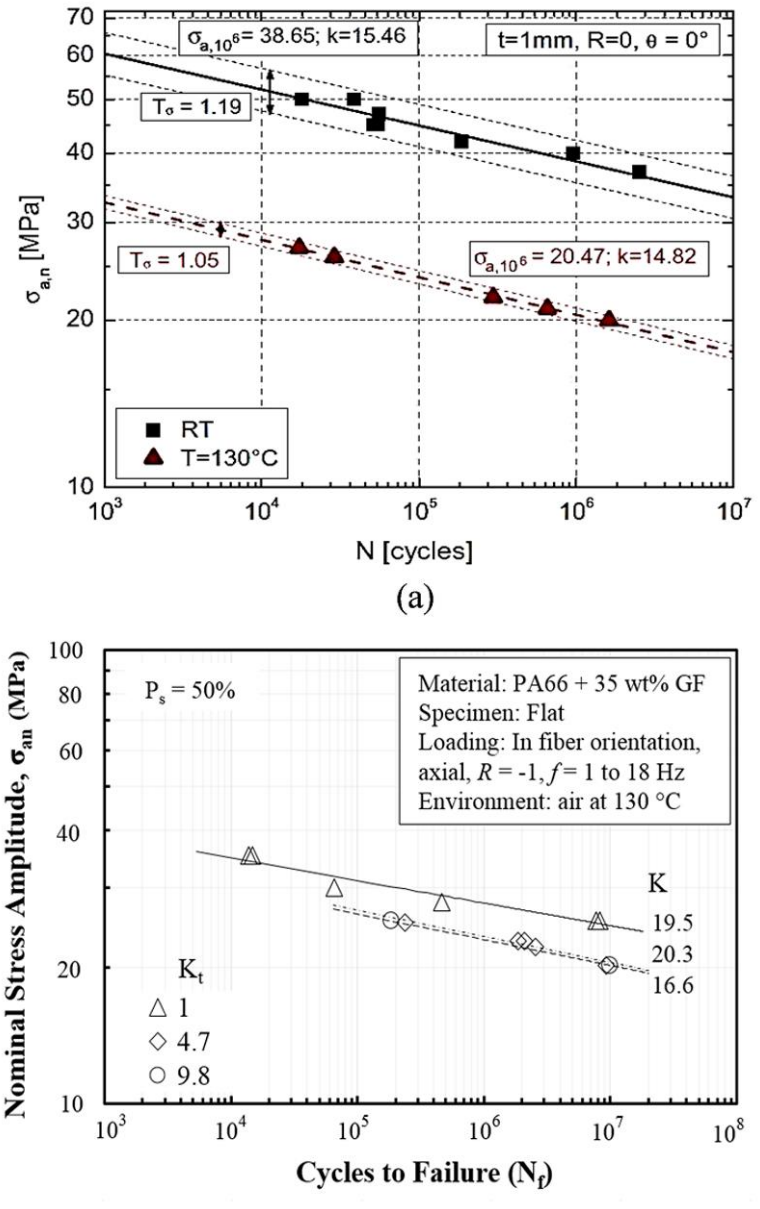

(a)

(b)

Figure 2-21: (a) Effect of temperature on fatigue behavior at *R* = 0 [57] and, (b) Influence of notches on fatigue strength at 130 °C under *R* = -1 condition in the longitudinal direction for short glass fiber reinforced polyamide-6.6 (Regenerated) [56].

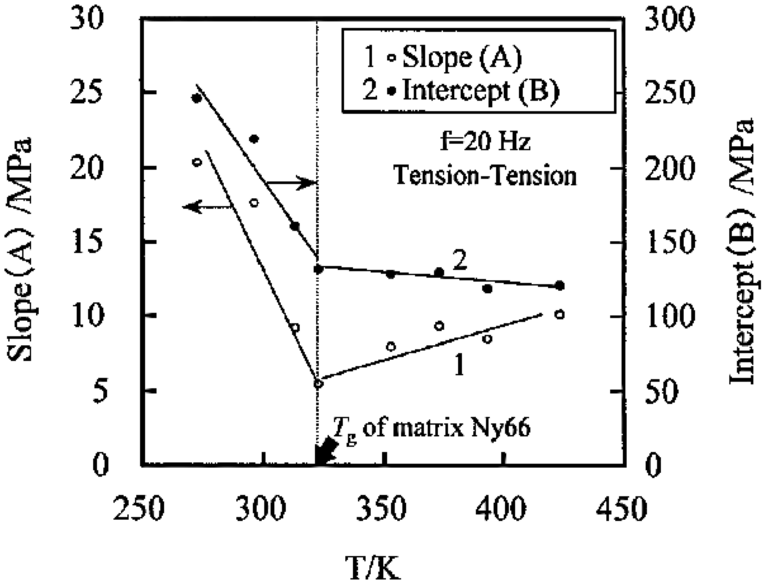

Figure 2-22: Temperature dependence of the slope *A* and intercept *B* of *S-N* curves for short glass fiber reinforced polyamide-6.6 at 20 Hz [58].

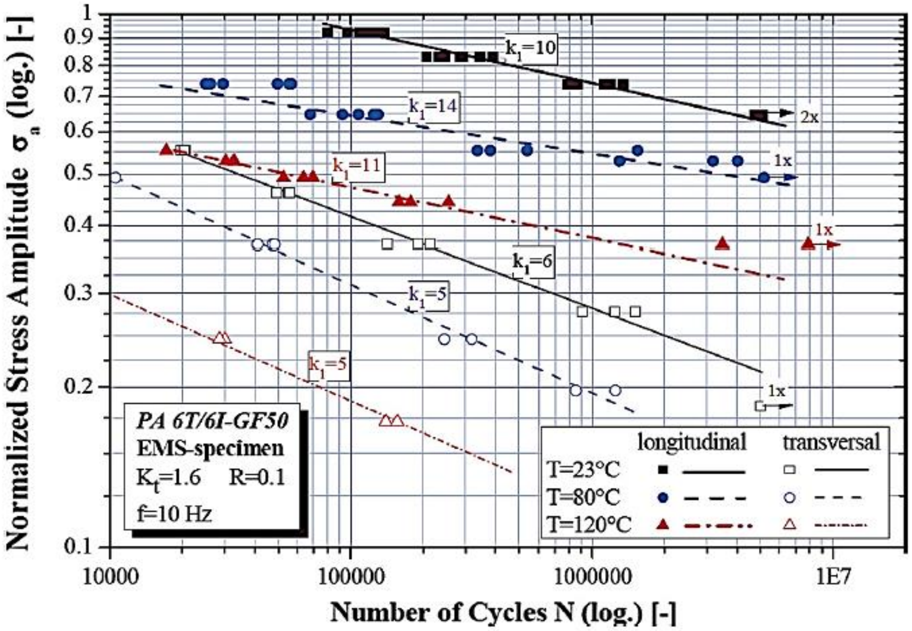

Figure 2-23: Effect of temperature and fiber orientation on fatigue behavior of short glass fiber reinforced polyamide-6 [59]. k_1 values on the graph are reciprocals of the slope of *S-N* lines.

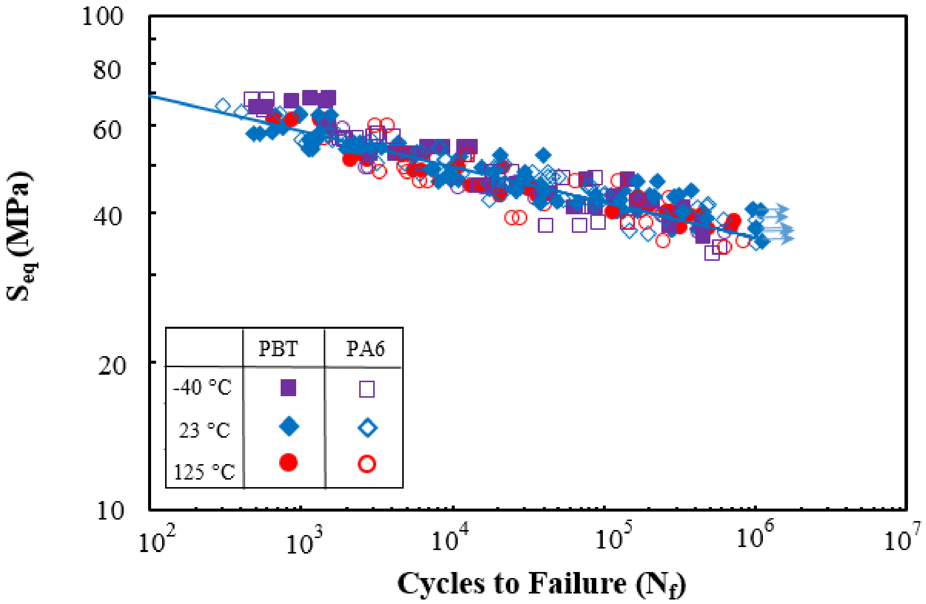

Figure 2-24: Equivalent stress amplitude versus fatigue life for PBT and PA6 at different temperatures in longitudinal, 18°, 45°, and transverse directions at R = -1, 0.1 and 0.3 loading conditions [61].

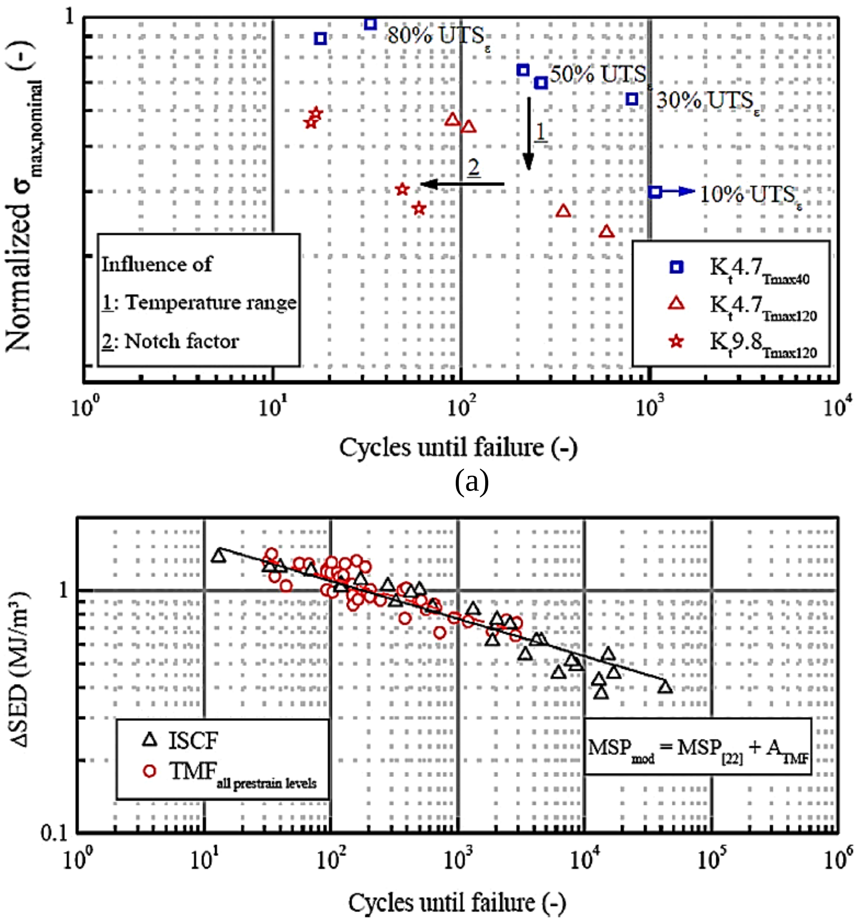

(a)

(b)

Figure 2-25: (a) Excerpt of TMF data set (T_{min} = -40 °C) and, (b) master curve of SED range versus cycles to failure correlating TMF and isothermal smooth and notch specimen fatigue data for short glass fiber reinforced polybutylene terephthalate at different temperatures and pre-strain levels [65].

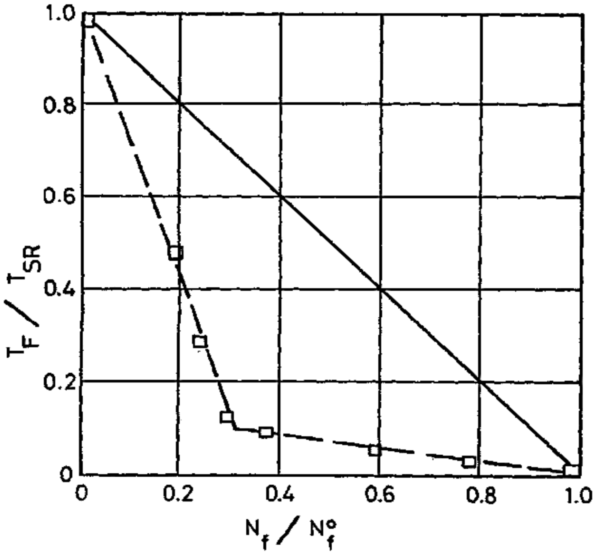

Figure 2-26: Cross plot of fractional stress rupture damage against fractional fatigue damage for polyethylene pipe line component [66].

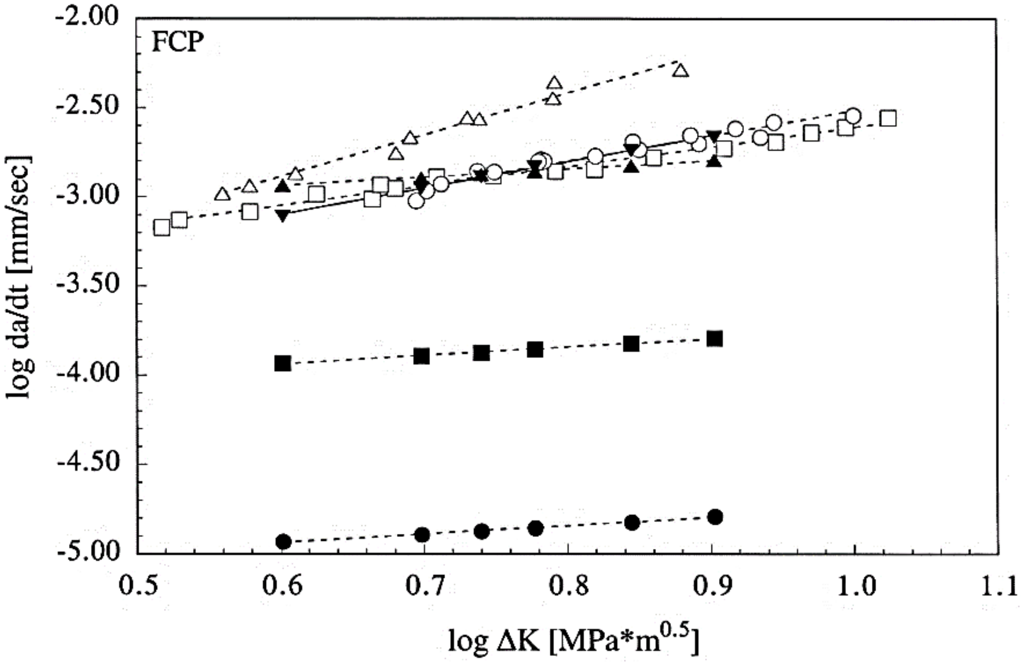

Figure 2-27: Total crack velocity, (*da/dt*) total, during FCP tests of glass fiber reinforced polypropylene composites at (○) 0.1 Hz, (□) 1 Hz, and (△) 10 Hz compared with the calculated (▼) pure creep component,(*da/dt*) creep; and pure fatigue components, (*da/dt*) fatigue at (●) 0.1 Hz, (■) 1 Hz, and (▲) 10 Hz [69].

Chapter 3

Experimental Program and Procedures

In this chapter physical and mechanical characteristics of composites considered for the study are described. Specimen preparation procedures are discussed and characteristics of the optimal specimen geometry for the experimental study are presented. Testing equipment and procedure for tensile, creep, fatigue and creep-fatigue experiments are also explained.

3.1 Material Fabrication and Descriptions

Five different thermoplastic composites were used for experimental studies, one talc-filled and four short glass fiber reinforced thermoplastic composites. Thermoplastic resins were polypropylene, polyamide-6.6, and modified polyphenylene ether and polystyrene. A summary of the materials including their full name, supplier, contents, drying conditions, and physical and mechanical properties in the longitudinal direction according to different ASTM and ISO standards is presented in Table 3-1. In the following sections more detailed information about the materials are presented.

3.1.1 40 wt% talc-filled polypropylene (PP-T) and 30 wt% short glass fiber reinforced polypropylene (PP-G)

Polypropylene is a semi-crystalline thermoplastic polymer with excellent and desirable physical and mechanical properties when used in room-temperature applications and has a wide variety of applications including non-load bearing usages such as packaging and engineering usages such as automotive components. From the simple chemical formula of propylene ($CH_2 = CH\text{-}CH_3$) different subfamilies can be obtained according to polymerization process, the use of co-monomers, blending with elastomers, and the use of reinforcements. Homopolymers including isotactic (crystallizable) and atactic (noncrystallizable) polypropylene are obtained from polymerization of propylene alone [1]. Isotactic polypropylene with the structure shown in Figure 3-1 has the engineering applications.

Copolymers of propylene are obtained by polymerization with another olefin or ethylene. The copolymers have better mechanical behavior at low temperature and are more impact resistant but less rigid than the homopolymers [72]. Melting temperature and glass transition temperature of isotactic polypropylene are reported to be about 160 °C and 0 °C, respectively [73]. Reinforcements such as fibers increase both mechanical and thermal properties of polypropylene, including strength, elastic modulus, heat deflection temperature, creep resistance, and even impact strength. Fillers, such as talc and calcium carbonate are often used as extenders, thus reducing the final material cost. However, some improvements in stiffness and impact can be obtained with these materials [1].

Most of the fillers and reinforcements are polar in nature. Polarity refers to a separation of electric charge leading to a molecule or its chemical groups having an electric dipole or multipole moment. Polypropylene, on the other hand, is nonpolar. Therefore, poor adhesion between polypropylene resin and filler or fiber is a problem in polypropylene-based composites. Surface treatment of fibers and fillers is the most commonly used procedure of overcoming this weakness.

PP-T and PP-G are isotactic polypropylene composites which are filled with 40 wt% talc and reinforced with 30 wt% short glass fibers, respectively. Thermylene is the trade name for PP-T and PP-G, and the main application of both is in the automotive industry, mainly in electric parts. Also, PP-T and PP-G with a specific chemical coupling technology between filler or fiber and resin were heat stabilized for higher temperature applications [74].

PP-T and PP-G were injection molded into rectangular plaques with dimensions of 2.8 × 100 × 200 mm. Some basic physical and mechanical properties of PP-T and PP-G are summarized in Table 3-1.

3.1.2 30 wt% short glass fiber reinforced polyamide-6.6 (PA66/B and PA66/D)

Polyamides also known as nylons are semi-crystalline thermoplastics. They can be homopolymers of an amino acid or copolymers of a diamine and a diacid. The repeat unit structure of polyamide is shown in Figure 3-1(b). There are many different types of polyamides depending on the starting monomers used in the polymerization process. Polyamides are typically identified by two numbers (for example polyamide-6.6 or polyamide 6). The first number refers to the number of carbons in diamine monomer, and the second number refers to the number of carbons in diacid monomer [75]. Polyamides are often reinforced with mineral fillers, glass or carbon fibers, and modified with specific additives (elastomers) to improve impact behavior, tribological properties, etc.

Polyamides are thermoplastics with relatively high strength, stiffness and impact properties, and good low-temperature mechanical behavior and are resistance to oils. However, they are sensitive to ultraviolent light, high energy radiation, and chemical environments, including oxygen and moisture, and these factors may substantially influence their properties.

The degree of water absorption is strongly dependent on the number of polar groups in polymer chains, the degree of crystallinity, and the temperature. Polyamides with either fewer carbon atoms (higher polarity) between amides, or lower degree of crystallinity (higher diffusion due to larger amorphous region) absorb more moisture [76]. Rate of diffusion is significantly related to the temperature [1]. At temperatures above T_g, molecular segments have significant mobility and, as a result, there is appreciable free volume in polymer mass which makes diffusion easier. However, at temperatures below T_g less mobility and diffusivity are observed. The moisture in polyamide acts as a plasticizer that reduces the entanglement and bonding between molecules, therefore, increases their volume and mobility. The increase in moisture may cause profound changes in a material behavior under load; it reduces strength, stiffness, and natural frequency, while increasing energy absorption and ductility in the material.

Polyamide-6.6 is a copolymer of hexamethylenediamine (C6 diamine) and adipic acid (C6 diacid) and is the oldest, the best known, with probably more than 70% of the total polyamide consumption, and also is among the cheapest of them which has engineering applications [1]. T_g of polyamide 6.6 is related to degree of crystallinity and method and rate used for measuring this temperature. Dried polyamide 6.6 has a glass transition temperature of close to 50 °C and melting temperature of about 260 °C.

PA66/B and PA66/D are 30 wt% short glass fiber reinforced polyamide-6.6 composites from two different supplier, BASF and DuPont, respectively. PA66/B and PA66/D composites were processed into rectangular plaques with dimensions of 2.8 × 100

× 200 mm using injection molding. Processing was done at the melt temperature of between 280 to 305 °C and mold temperature of 80 to 90 °C. Some basic physical and mechanical properties of PA66/B and PA66/D are summarized in Table 3-1.

3.1.3 20 wt% short glass fiber reinforced polyphenylene ether and polystyrene (PPE/PS)

Polyphenylene ether (PPE) are ethers like polyoxymethylene where an aromatic unit replaces the methylene group leading to — (—C_6H_4—O—)$_n$— structure [1]. PPE is usually used in the form of alloys with other resins such as high-impact polystyrene which is the most used, polyamides, and polyetherimide. PPEs are used in technical parts because of the good price/performance ratios for mechanical and electrical properties, good creep behavior, low moisture uptake, good heat and low-temperature behaviors, and good dimensional stability.

This blend of polyphenylene ether and high impact polystyrene is an amorphous thermoplastic and known as Noryl. The two polymers compatibility in Noryl resin is due to the presence of a benzene ring in the repeat units of both chains. Noryl has both the inherent benefits of PPE and polystyrene (excellent dimensional stability, good processibility, and low specific gravity). Noryl has a T_g of close to 100 °C and melting temperature of about 320 °C.

PPE/PS is 20 wt% short glass fiber reinforced modified polyphenylene ether and polystyrene resin. It is known as a fire retardant material with high glass transition and melting temperatures which is specifically used in electronics and electrical equipment in the auto industry. PPE/PS composite in this project was processed into rectangular plaques with dimensions of 2.8 × 100 × 200 mm using injection molding. Processing was done at the melt temperature of between 300 to 325 °C and mold temperature of 80 to 110 °C. Some basic physical and mechanical properties of PPE/PS are summarized in Table 3-1.

3.1.4 PP, PO, PA6, and PBT from previous works

Some additional tests and analysis were performed on the materials in studies of Mellott [77] and Mortazavian [78]. PP is the neat thermoplastic and is an impact polypropylene copolymer. PO is a talc-filled composites and is a polypropylene-elastomer blend (a thermoplastic polyolefin) with 25% by weight (25 wt%) elastomer and 35 wt% talc. More information about PP and PO can be found in [77]. Polybutylene terephthalate with 30 wt% glass fibers (here referred to as PBT), and polyamide-6 containing 35 wt% glass fibers and about 10 wt% rubber impact modifier (here referred to as PA6) are materials from the study of Mortazavian [78]. Specimen thickness for these materials was 3.8 mm. A summary of the materials used in the experimental study including their T_g and T_m is given in Table 3-2.

3.2 Material Storage, Drying Conditions, Specimen Geometry, and Preparation

The composite materials were injection molded into plaques with dimensions mentioned in the previous sections at General Motors. Material plaques were stored in plastic zip bags with some amount of desiccant and were kept in constant laboratory condition of 23 °C to preserve dry as-molded condition before specimen preparation.

Five Rectangular strips with width of 25 cm were cut from each material plaques in 90° with respect to the mold flow direction, as shown in Figure 3-2(a), using a band saw. The top and the bottom of each plaque were removed and discarded in order to avoid any end effects of molding process.

The same specimen geometry used in the studies of Mellott [77] and Mortazavian [78] for conducting tensile, creep, and fatigue tests, shown in Figure 3-2(b) was also used in this study. A generous curve in the transition from the gage section to the gripping area was provided in order to have a low stress concentration (K_t = 1.05). A relatively large section in the gage area was provided to allow marking the specimen for tracking strain and recording temperature rise. Different failure locations were defined according to finite element analysis performed on the test specimen under a simple tension load, as shown in Figure 3-3(a). The gripping position for tension, creep, fatigue, and creep-fatigue tests and also the defined gage section for measuring strain for those tests are shown in Figure 3-3(b).

The specimens were machined from cut strips using a CNC milling machine. Dimensional and symmetrical accuracy of specimens were evaluated using an optical comparator. Accepted specimens were inspected for scratches and defects and were stored in sealed bags with desiccants prior to testing.

All the specimens were dried before testing to preserve the dry as-molded condition and exclude moisture effect. PA66/B and PA66/D specimens were dried for 24 hours at 80 °C and PPE/PS specimens were dried for 4 hours at 100 °C in a vacuum chamber. PO, PP, PP-T, and PP-G specimens were dried for 4 hours at 80 °C and PBT and PA6 specimens were dried for 6 hours at 120 °C and 80 °C, respectively, in a regular chamber. All the specimens were kept in a desiccator prior to testing.

3.3 Testing Equipment

Most of the tests, including tensile, short-term creep, fatigue, and creep-fatigue tests were conducted using an Instron 8801 servo-hydraulic testing machine powered by a hydraulic pump, which is shown in Figure 3-4(a). A pair of 5 kN pneumatic grips which are suitable for testing polymers at low and elevated temperatures were used for gripping specimens. Load cell with capacity of 10 kN was used to measure the applied load to the specimen. The machine was controlled by an Instron Fast Track 8800 controller. Display and acquisition of data were done on a personal computer using Instron software. An Instron M3 creep machine was used to conduct long-term creep tests, as shown in Figure 3-4(b). Lever arm with dead weight was used to apply the constant load.

The Instron Bluehill software was used for both tension and creep tests. Tension tests were performed in displacement-controlled mode and creep tests were conducted under load-controlled mode. Fatigue tests were performed under load-controlled condition utilizing the Instron SAX software. Creep-Fatigue tests were conducted in load-controlled mode using Instron Waveform software.

A strain-gaged specimen was used to check the alignment of the load train prior to testing following ASTM E1012 [79]. Eight strain gages were attached to an aluminum flat specimen which was precisely machined according to the specimen geometry utilized for testing (see Figure 3-2(b)). The alignment specimen was gripped in the machine and similar stress levels as test conditions were applied. A software calculated the percent bending due to eccentricity and tilt. An alignment fixture was used to reduce the percent bending within 5% according to ASTM E1012 [79].

An Instron video extensometer was used to measure the strain values under tensile and creep tests, which is shown in Figures 3-5(a) and (b). Two dots with a consistent distance of 8 mm were marked using special markers on the specimen gage section prior to testing. The distance between these two points and the resultant strain were automatically measured during the test. The video extensometer has the capability of measuring large strains and as it is a non-contact extensometer, it does not have the drawbacks of contact extensometers such as attachment issues or weight. The video extensometer can easily measure the strain at elevated temperatures as it is outside of the chamber.

An environmental chamber with an operating temperature range between -70 °C to 350 °C with the accuracy of ±1 °C was utilized to conduct tests at elevated temperatures, as shown in Figure 3-6. This chamber employs an electronic heating element to increase the temperature and with a continuous working fan maintaining the temperature constant inside the chamber.

The amount of temperature rise as well as a visual profile of temperature in specimen gage section during fatigue and creep-fatigue tests were measured using a thermal imaging camera of the type FLIR, model i7, which is shown in Figure 3-7.

Dual cantilever dynamic mechanical analysis (DMA) tests were conducted using a Perkin Elmer Q800 DMA machine, which is shown in Figure 3-8. The rectangular specimens cut from the plaques were used for DMA tests. A Hitachi S-4800 scanning electron microscope (SEM), which is shown in Figure 3-9, was used to investigate the fracture surface of failed specimens in microscopic scale. The specimens were coated with gold before doing scanning electron microscopy.

3.4 Testing Procedures

Monotonic tension tests were performed under displacement-controlled mode according to the ISO 527 [80] and ASTM D638 [81] test standards. Specimens were gripped in locations shown in Figure 3-3(b). Different tensile properties including tensile strength, 0.2% yield strength, elastic modulus, strain at tensile strength, strength coefficient, strain hardening exponent, and elongation were determined from each test.

Short-term creep tests were performed using Bluehill testing software. Specimens were gripped in the same location as the monotonic tension tests and a constant tensile load was applied to the specimen. Long-term tests were conducted using the same specimens for short-term tests, but screws and nuts were used for gripping them in the creep testing machine. Stress levels correspond to rupture time between 0.1 to 72 hours were selected for short-term testing, while the rupture time for long-term tests were up to 1 month. Axial strain was measured during testing using the video extensometer for short-term tests and high resolution pictures were used to measure strain for long-term tests. Testing procedures were based on the ASTM D2990 [82] and ISO-899 [83] standards for tensile creep testing.

Load-controlled fatigue tests were performed using the Instron SAX software. Tests were performed under sinusoidal waveform in a range of cyclic frequency between 0.125 to 20 Hz depending on the material, the test temperature, the stress ratio, and the stress level. Temperature of the gage section was monitored during room temperature tests to consider the self-heating effect. Displacement values were recorded during tests. The displacement amplitude, which is directly related to the strain amplitude of the specimen gage section, was used to evaluate the magnitude of cyclic softening. Similarly, the mean displacement, which is directly related to the mean strain in the specimen gage section, was used to evaluate the magnitude of cyclic creep. Specimens were typically griped in region (2) indicated in Figure 3-3(b). In some of fully-reversed tests, specimens were gripped in a shorter length to avoid specimen buckling during the compression part of the cycle.

Four stress amplitude levels correspond to fatigue life between 10^3 and 10^6 cycles were selected for testing. Specimen fracture was selected as failure criterion and if specimen did not fracture before 10^6 cycles, the test was manually stopped and was considered as a run out test. Three different failure regions around the specimen gage were defined, which are shown in Figure 3-3(a). Specimens breaking in 10 mm gage section (IGIT) and in 3 mm outside of the gage section (OGIT) are defined as valid tests. Specimens breaking outside of these two regions were identified as invalid tests (OGOT). ASTM standard D7791 [84] which is a recent and brief standard for fatigue testing of polymers, was considered in the experimental study.

Creep-fatigue tests were conducted in load-controlled mode using trapezoidal stress signals. The gripping positions of the specimens were the same as those of fatigue tests. Instron Waveform software was used to generate different signals which could have different amounts of creep damage and fatigue damage in each test. There is no standard test method for conducting creep-fatigue test of polymeric materials, therefore, ASTM E2714 [85] which is for metallic materials was used, where appropriate.

Dynamic mechanical analysis (DMA) tests in temperature sweep and in frequency sweep modes were performed using a dual cantilever DMA machine based on ASTM D7028, ASTM D5418 and ASTM D4065 standard test methods [86-88]. A rectangular plate-type specimen geometry with dimensions of 13 × 60 mm with the mentioned plaques thickness for each material was used. Temperature sweep DMA tests were conducted in temperature range between 25 to 150 °C. Frequency of applied cyclic load was 1 Hz. The DMA frequency sweep tests were conducted in the frequency range of 0.1 to 75 Hz at 85 °C. Differential scanning calorimetry (DSC) tests were also performed for some of the materials based on ASTM D3418 standard test method [89]. DMA and DSC tests were conducted to evaluate viscoelastic behavior and to obtain the glass transition temperature (T_g).

Table 3-1: Name description, contents, drying conditions, and physical and mechanical properties of materials used for experimental studies according to the listed ASTM and ISO standards in the longitudinal direction obtained from technical data sheets and Matweb website [74, 90-93].

Material	**PP-T**			**PP-G**			**PA66/B**		**PA66/D**			**PPE/PS**
Contents	**40% Talc-60% Polypropylene**			**30% Glass-70% Polypropylene**			**30% Glass-70% Polyamide66**		**30% Glass-70% Polyamide66**			**20% Glass-80% PPE+PS***
	Technical Data Sheet		**Matweb**	**Technical Data Sheet**		**Matweb**	**Technical Data Sheet**	**Matweb**	**Technical Data Sheet**			**Technical Data Sheet**
									DAM	**%50 RH**		
Tensile Strength	ASTM D638 35 MPa	ISO 527 31 MPa	ASTM D638 29.6 MPa	ASTM D638 81 MPa	ISO 527 85 MPa	ASTM D638 82.7 MPa	ISO 527 179 MPa	ISO 527 190 MPa	ISO 527 195 MPa	ISO 527 130 MPa		ASTM D638 106 MPa
Elongation	-		ASTM D638 8%	-		ASTM D638 3%	ISO 527 2.6%	ISO 527 3%	ISO 527 3.3%	ISO 527 5%		ASTM D638 5%
Tensile Modulus	-		-	-		-	-	ISO 527 10 GPa	ISO 527 10 GPa	ISO 527 7.2 GPa		-
Flexural Modulus	ASTM D790 2.5 GPa	ISO 178 3.8 GPa	ASTM D790 3.38 GPa	ASTM D790 5.3 GPa	ISO 178 6 GPa	ASTM D790 5 GPa	ISO 178 8.73 GPa	ISO 178 8.6 GPa	-	-		ASTM D790 5.7
Tensile Creep Modulus	-		-	-		-	-	-	-	ISO 899 1 Hour 6.8 GPa	ISO 899 1000 Hour 5.1 GPa	-
Melting Temperature	165 °C		-	165 °C		-	ISO 3146 260 °C	ISO 3146 280-300 °C	ISO 11357 262 °C	-		300-325 °C
Specific Gravity	ISO 1183 1.26 gr/cm3		ASTM D792 1.24 gr/cm3	ISO 1183 1.14 gr/cm3		ASTM D792 1.13 gr/cm3	ISO 1183 1.36 gr/cm3	ISO 1183 1.36 gr/cm3	ISO 1183 1.37 gr/cm3			ASTM D792 1.23 gr/cm3
Drying Condition	**3 Hours @ 80 °C**			**3 Hours @ 80 °C**			**4 Hours @ 80 °C (Vacuum)**		**4 Hours @ 80 °C (Vacuum)**			**4 Hrs @ 120 °C (Vacuum)**
Full name and company	**[P-40TC-8100] –ASAHI KASEI**			**[P6-30FG-0600] –ASAHI KASEI**			**[A3WG6 BK 00564] – BASF**		**[70G30HSLR NC010] – DuPont**			**[SE1GFN2] – Sabic**

*PPE: Polyphenylene ether & PS: Polystyrene

Table 3-2: Summary of materials used for the experimental study and analysis.

Material Designation	**Polymer Matrix**	**Reinforcement**	**T_m (°C)**	**T_g (°C)**
PO	Polypropylene + 25 wt% Rubber	30 wt% Talc	>120	<-10
PP	Impact Polypropylene	None	170	4
PP-T	Polypropylene	40 wt% Talc	165	11
PP-G	Polypropylene	30 wt% Short Glass Fiber	165	23
PA66/B	Polyamid-6,6 (BASF)	30 wt% Short Glass Fiber	260	55
PA66/D	Polyamid-6,6 (DuPont)	30 wt% Short Glass Fiber	260	55
PPE/PS	Polyphenylene ether +Polystyrene	20 wt% Short Glass Fiber	325	135
PBT	Polybutylene terephthalate	30 wt% Short Glass Fiber	255	50
PA6	Polyamide-6 + 10% Rubber	35 wt% Short Glass Fiber	220	40

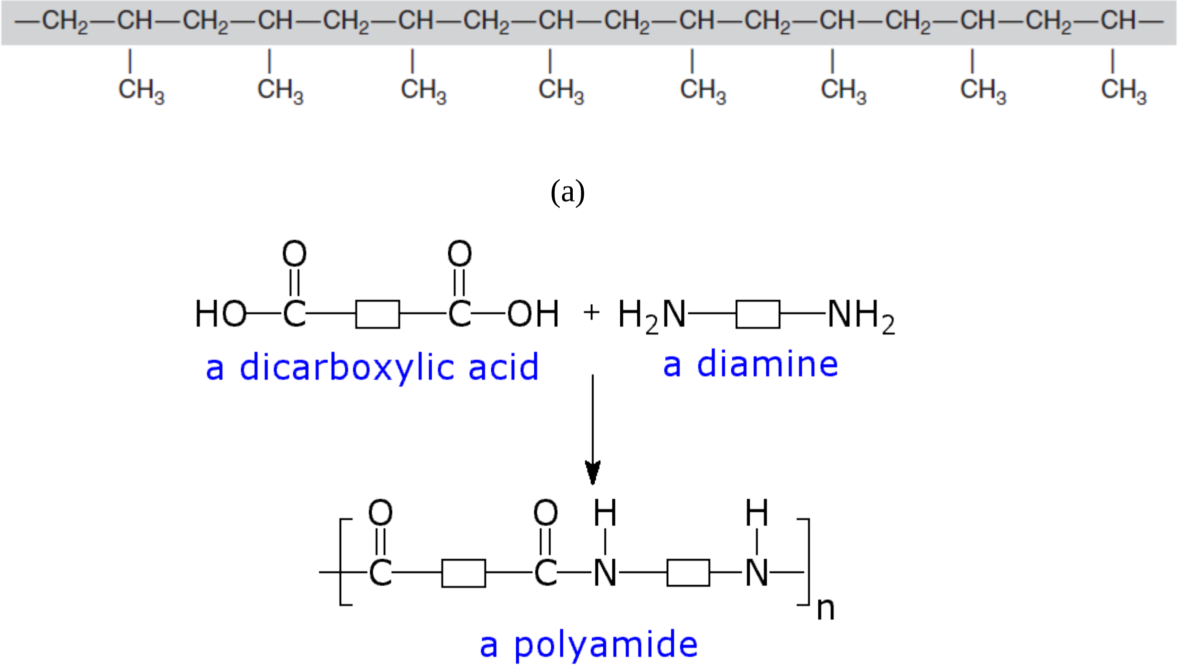

(a)

(b)

Figure 3-1: (a) Isotactic structure of polypropylene [72], and (b) repeated structure unit of polyamide [94].

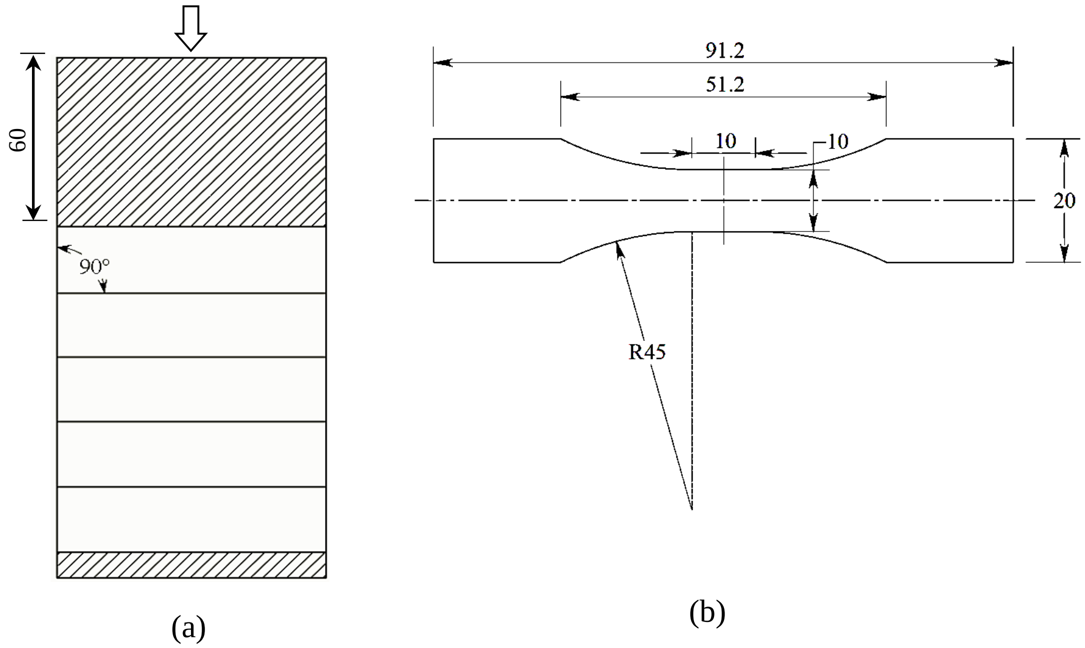

Figure 3-2: (a) Location of specimens cut from injection molded plaques in the transverse direction (arrows indicate the injection molding direction and the dashed areas are discarded materials). (b) Specimen geometry used for the experimental study (dimensions are in mm) [78].

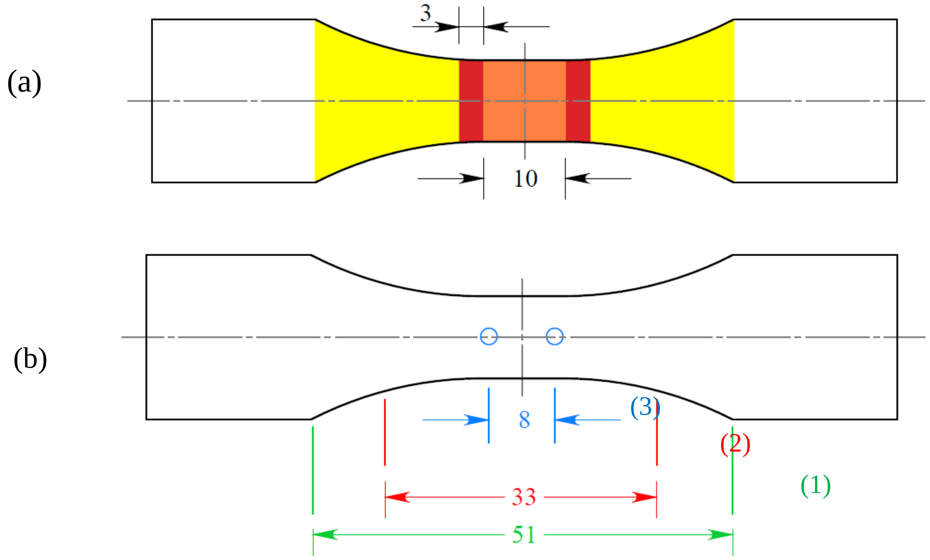

Figure 3-3: (a) Different failure locations are shown as IGIT (Orange), OGIT (Red), and OGOT (Yellow). (b) Specimen grip locations for (1) monotonic tension and creep tests and (2) the majority of fatigue and creep-fatigue tests, and (3) the distance of the marks for the video extensometer. (Dimensions are in mm) [78].

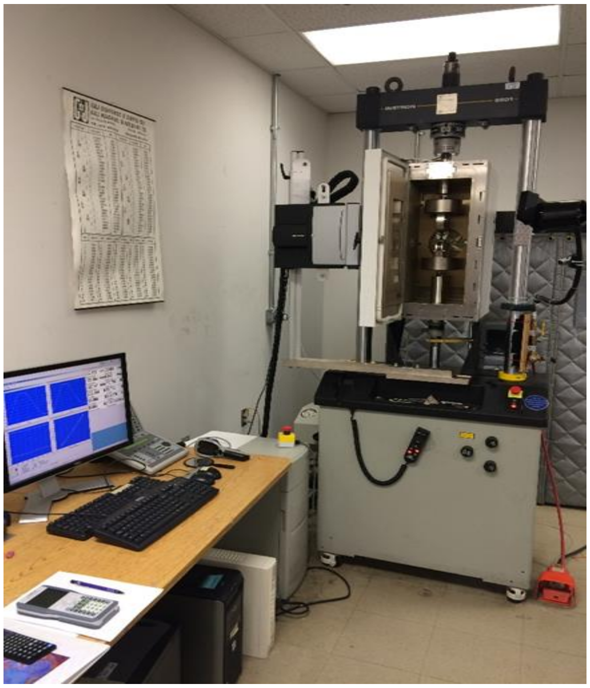

(a)

(b)

Figure 3-4: (a) Instron 8801 servo-hydraulic testing machine used for tensile, short-term creep, fatigue and creep-fatigue tests shown with computer and controller, and (b) Instron M3 creep test machine with lever arm used for long-term creep tests.

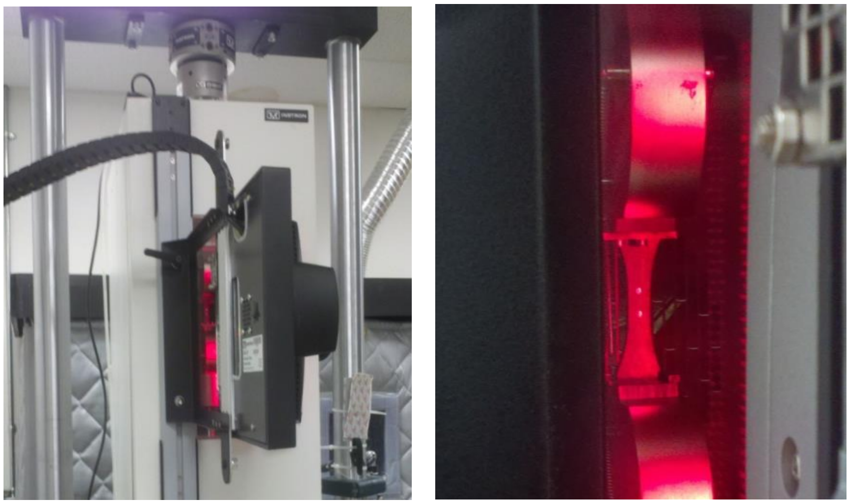

(a) (b)

Figure 3-5: (a) Video extensometer used for tensile and creep tests. (b) A marked test specimen illuminated with the optical LED array.

Figure 3-6: Instron 3119-506 environmental chamber attached to the Instron 8801 testing machine.

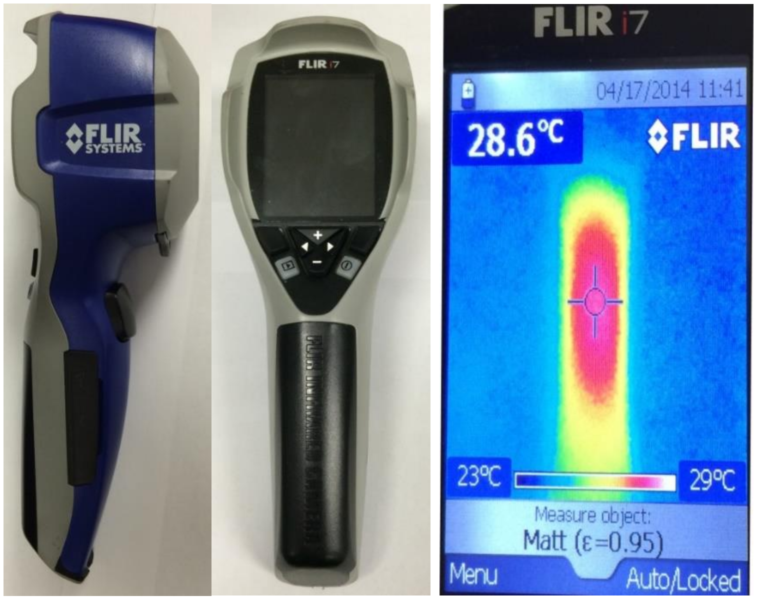

Figure 3-7: FLIR i7 model thermal imaging camera.

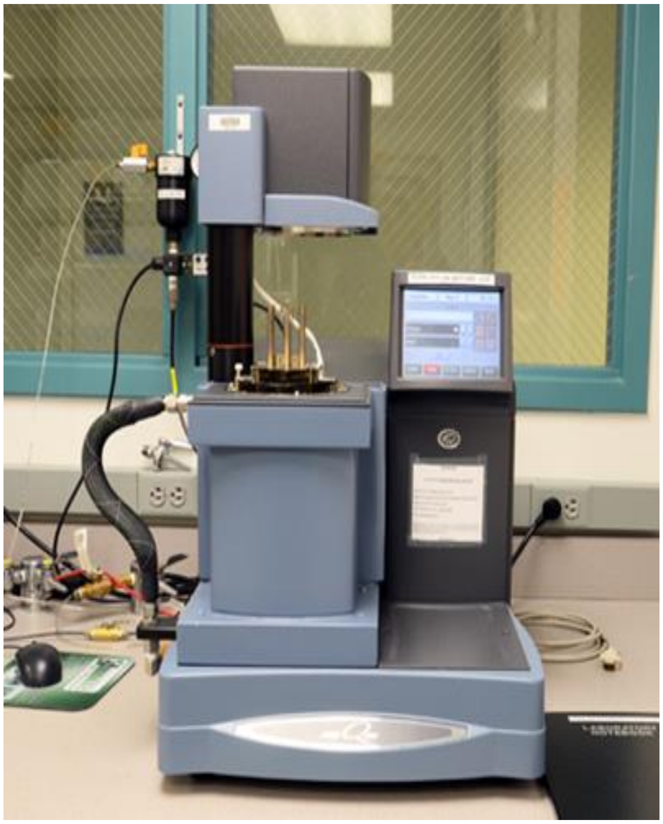

Figure 3-8: Perkin Elmer Q800 DMA machine.

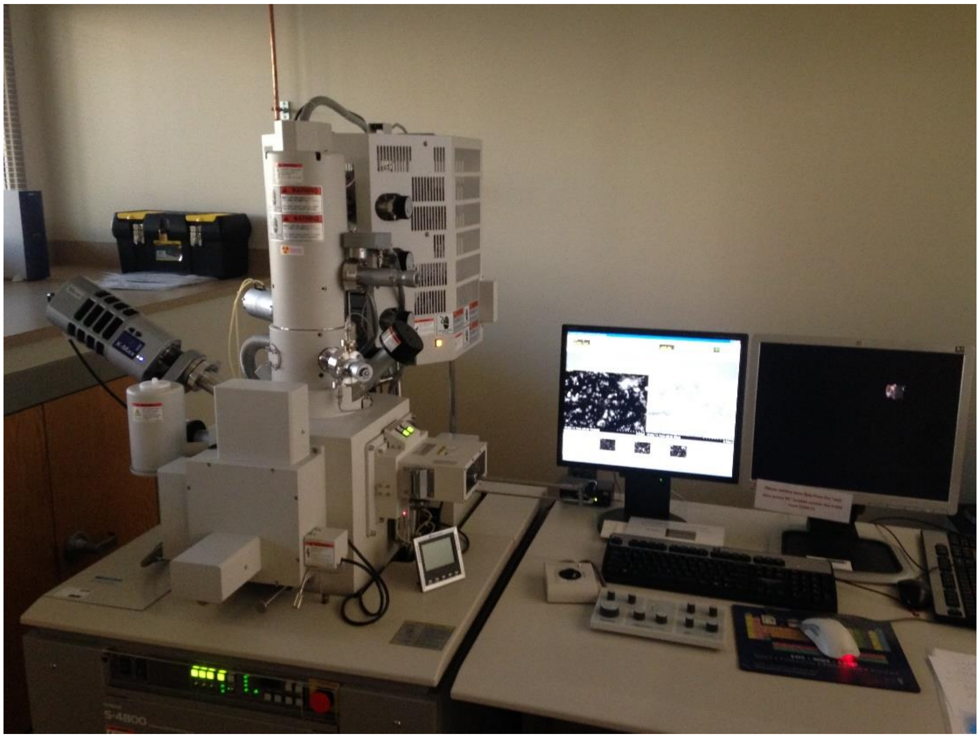

Figure 3-9: Hitachi S-4800 scanning electron microscope.

Chapter 4

Tension Test Results and Analysis

In this chapter effects of temperature, moisture, and hygrothermal aging on tensile properties of studied materials are investigated. To investigate the effect of temperature, tension tests were conducted at 23 °C, 85 °C, and 120 °C for PP-T, PP-G, and PPE/PS and at these temperatures in addition to at 150 °C for PA66/B and PA66/D. To consider the hygrothermal aging effect on tensile properties, PP-T, PP-G, PPE/PS, and PA66/B specimens were immersed in 85 °C water for 4 days (saturation time for PA66/B in 85 °C water), then tested at 23 °C. In addition to the aforementioned conditions, to investigate the kinematics of water absorption and assess the effect of water absorption on tensile properties of PA66/B, specimens were immersed in 23 °C water for a duration between one day to 140 days and in 85 °C water for a duration of a few hours up to 6 days. Scanning electron microscopy was also performed on fracture surfaces to study the moisture effect at the microstructural level. Tensile properties obtained in this chapter were used as inputs for estimations of creep, fatigue, and creep-fatigue interaction behaviors in the following chapters. Results and analysis presented in this chapter were published in [95].

4.1 Introduction

Tensile properties as the basic material properties are still widely used in design. A simple tension test provides valuable information about stiffness, strength, toughness, and ductility of a material. Fiber content, length, diameter, and direction can affect tensile properties of polymer composites. These aspects have been studied in previous studies, such as in [28, 96].

Tensile strength and elastic modulus of thermoplastic composites have been observed to decrease with increasing temperature, with a sudden drop near T_g [21, 27]. Strain at fracture increases with increasing temperature, particularly at temperatures above T_g, as molecular chain motion of polymers intensifies. This effect is much more accentuated in unreinforced materials than in reinforced materials [19]. The temperature dependency of tensile properties is generally matrix dominance when loaded in the normal to the molding direction than when loaded in the molding direction. Tensile properties are more fiber dependent in the molding direction and temperature sensitivity of them is less [27]. Under tensile loading, fiber pullout and matrix brittle fracture are the dominant failure mechanisms at low temperatures or high strain rates, while failure occurs via matrix crazing and crack propagation near the fiber ends at elevated temperatures or low strain rates [5]. Time-temperature dependency of tensile properties has been modeled using empirical models [9].

Kinetics of water absorption of polymers and their composites has also been studied considering the effects of temperature, thickness, mold flow direction and reinforcement content. In most cases, water absorption process has been reported to follow Fick's law [97-99], however, exceptions at some conditions have also been reported [6, 98, 100]. For example, at elevated temperatures where thermal aging, oxidation and leaching are important, more deviation from Fick's law has been observed [6].

Nearly all polymers absorb moisture and the amount of water uptake depends on the polymer composition. For example, polyamide groups are highly sensitive to moisture because of their polar structure. The rate of water absorption increases with increasing temperature, with a sudden change near T_g, while the maximum water uptake is constant [97]. Increasing temperature enhances segmental mobility which results in greater zone of activation, therefore, the rate of water absorption increases. In polymer composites only the resin typically absorbs moisture, but the fiber/matrix interface can change the rate of water absorption [101].

A significant reduction in T_g and a slight increase in crystallinity of the materials has been observed with increasing the amount of water absorption [6]. Tensile strength and elastic modulus reduce significantly with increasing percent of water absorption [36, 97, 101]. The reduction is lower for composites with enhanced fiber/matrix bond [101]. This effect has been related to plasticization of the matrix and weakness of fiber and matrix interface due to the water absorption.

There are inconsistent reports in the literature about the recovery of water absorption effect on materials properties. Some studies suggest that the water absorption process is a physical phenomenon and can be recovered with desorption of water [6, 97], while in some other studies full recovery has not been obtained with complete drying of aged specimens [34, 35]. The nature of moisture attack plays an important role in recovery of the mechanical properties. For example, in polyamide composites the plasticization effect of water on the resin is a reversible physical process, however, for PBT hydrolysis of ester groups with moisture is an irreversible chemical process [101]. In addition, exposure of glass fibers to water can result in a chemical reaction. Therefore, composites without a coupling agent where fibers are not protected from diffusion of water do not show recoverability of mechanical properties with complete drying, while for composites with treated fibers full recovery has been reported [102].

4.2 Tensile Properties

The tensile properties for duplicate tests for each material at different temperature for dry as-molded conditions are listed in Table 4-1. These include strain rate, the 0.2% offset yield strength (S_y), ultimate strength (S_u), strain at ultimate strength (ε_M), and elastic modulus (E). Elastic modulus has different definitions in ASTM-D638 [81] and ISO-527 [80], therefore, it was measured based on both methods. According to ASTM-D638, elastic modulus is defined as the slope of fitted line to the elastic part of stress-strain curve. Based on ISO-527, elastic modulus is defined as the slope of fitted line to the part of stress-strain curve within 0.0005 to 0.0025 mm/mm strain. Tensile properties and their definitions are shown in Figure 4-1(a). The tensile properties and aging conditions for the moisture study are listed in Table 4-2.

The Ramberg-Osgood relation has been shown [77, 78] to represent stress-strain curves of polymeric materials very well. This model was also used in this study to represent stress-strain curves of the materials, given in the following form:

$$\varepsilon = \frac{\sigma}{E} + (\frac{\sigma}{K})^{\frac{1}{n}} \tag{4.1}$$

where K is the strength coefficient and n is the strain hardening exponent. These properties were obtained based on ASTM E646 test standard for metallic sheet materials [103] from a fit of true stress (σ) versus true plastic strain (ε_p) in log-log scale in the form of:

$$\sigma = K(\varepsilon_P)^n \tag{4.2}$$

An example of this fit is shown in Figure 4-1(b). *K* and *n* values are also listed in Table 4-1.

4.3 Temperature Effect

Stress-strain curves are considerably influenced by temperature for all the materials, as shown in Figure 4-2. Large deformations were observed for PP-T and PP-G at 85 °C and 120 °C and PP-T specimens became gummy at these temperatures. As can be seen in Figure 4-2, PA66/B and PA66/D at 23 °C behave in a brittle way, as their response show linear elastic behavior for a large portion of the stress-strain curve. At elevated temperatures these materials behave in a ductile manner with significant plastic deformation. Strain at rupture increases with increasing temperature from 23 °C to 85 °C and remains constant up to 150 °C. For PPE/PS, the behavior is different from the other studied materials, where a reduction in strain at rupture is observed with increasing temperature. Since the tested temperatures are lower than T_g, which is 135 °C, more stability in deformation is observed with increasing temperature.

Comparison between tensile stress-strain curves of PP-T and PP-G at different temperatures is shown in Figure 4-3(a). The plastic deformation of PP-G is less than PP-T at all temperatures, related to the strengthening effect of glass fibers. PA66/B has somewhat lower tensile strength than PA66/D, mainly at elevated temperatures as can be seen in Figure 4-3(b) (98% at 23 °C and 91% at elevated temperatures). However, their elastic moduli at different temperatures are almost the same.

Variations of S_u, S_y, and E with temperature are shown in Figure 4-4 for all the materials. A linear reduction in tensile properties with temperature is observed for PP-T, PP-G, and PPE/PS. For these materials T_g is not in the range of studied temperatures. However, for PA66/B and PA66/D, two different slopes can be identified for variations of strength and stiffness at temperatures near and above T_g. The reduction is more significant with increasing temperature from 23 to 85 °C, as compared to the reduction from 85 to 150 °C.

The strength (S_u and S_y values) of PP-G are higher than PP-T at all temperatures due to the strengthening effect of the glass fibers. The stiffness (E value) of PP-T is higher than PP-G at 23 °C, equal to PP-G at 85 °C, and less than PP-G at 120 °C. The main reason for incorporating talc in polymers is to increase the stiffness. The degree of rigidity depends on the filling level, aspect ratio (diameter to thickness) and fineness of the talc [72]. Talc has relatively high stiffness and increases the crystallinity index of the composite [72], therefore, increases the stiffness of polypropylene. For PP-T at elevated temperatures (85 °C and 120 °C), the polypropylene matrix becomes gummy, results in reduction of bonds between talc and matrix, therefore, talc loses its strengthening effect on stiffness.

Addition of talc decreases the tensile strength, as compared to neat polypropylene [104, 105] due to its stress concentration effect. It also has a weak interfacial bond with polypropylene and creates voids and areas for damage initiation in polypropylene matrix, therefore, reduces the strength and the reduction increases with increasing the talc content.

The sensitivity of strength and stiffness to temperature can be compared for all the materials using Figure 4-5, which shows the variation of normalized S_u and E with respect to their values at 23 °C with temperature. Effect of temperature on strength of both PP-T and PP-G is the same. This indicates the dominancy of the matrix in temperature dependency on strength. Temperature sensitivity of stiffness is higher for PP-T, as compared to PP-G. Temperature sensitivity of elastic modulus for PPE/PS is much less compared to other materials. This material has an amorphous matrix which behaves glassy below T_g where secondary bonds determine elastic properties and are less affected by a change in temperature [106].

Temperature effect on tensile fracture surface was investigated microstructurally using SEM pictures for PA66/B, as shown in Figure 4-6 at 23 °C and 85 °C. Core and shell layers which have fibers in the longitudinal and transverse directions, respectively, can be observed distinctively at both 23 °C and 85 °C (Figures 4-6(a) and (c)). Damage in the core layer is different from that of shell layer at both temperatures, since there are more fibers in the core layer resulting from the injection molding process. Stress concentrations at the tip of fibers, which are longitudinally oriented, cause more damage to the matrix. A brittle fracture surface is observed at 23 °C and many fiber pullout regions, which are typical indication of brittle failure in short fiber composites, can be seen in Figure 4-6(a), mainly in the core layer. The flaky matrix with some deboned fibers and also regions of fiber pullouts can be seen in Figure 4-6(b), which is for the shell layer at 23 °C. At 85 °C, a combined ductile and brittle failure is observed in Figure 4-6(c), related to damage initiation zone and final fracture surface, respectively.

A significant plastic deformation incorporated with matrix crazing with fibrils structure can be seen in the upper side of Figure 4-6(c), showing the damage initiation side. Brittle failure on the lower right side and the remainder of the fracture surface are also observed in Figure 4-6(c). A significant plastic zone, mainly at the fiber ends along with aligned fibers in the loading direction, because of weak fiber/matrix bond due to the plastic deformation can be seen in Figure 4-6(d), which is for the shell layer of the damage initiation zone at 85 °C. A similar behavior is expected for PP-T and PP-G at room and at elevated temperatures. However, for PPE/PS a more brittle failure zone of fracture is expected at all the tested temperatures, since they are all below T_g.

The Ramberg-Osgood relation presented by Equation 4.1 was used to represent the stress-strain curves up to ultimate tensile strength of the studied materials at all temperatures. As can be seen in Figure 4-7, this relation can represent the true stress-true strain curves of all the materials very well. Variation of strength coefficient, K, with temperature was observed to be very similar to the variations of tensile strength and elastic modulus with temperature. A uniform trend for variation of strain hardening exponent, n, with temperature was not observed. For PP-T, PA66/B, and PA66/D strain hardening exponent increased with increasing temperature, while for PP-G and PPE/PS the opposite trend was observed.

4.4 Moisture and Hygrothermal Effects

Hygrothermal aging effect on tensile properties of PP-T, PP-G, and PPE/PS was observed to be much less than PA66/B, as shown in Figure 4-8. Polypropylene because of its non-polar structure is much less sensitive to moisture, as compared to polyamide [72]. Hygrothermal aging affected the tensile strength, elastic modulus (mainly for PP-T), and the strain at failure for PP-T and PP-G, which can be seen in Figures 4-8(a) and (b). About 7% and 4% reduction in tensile strength with water absorption was observed for PP-T and PP-G, respectively, with respect to DAM condition.

PPE/PS specimen absorbed 0.21 wt% with immersion in 85 °C water for four days. A small reduction of elastic modulus (about 4 %) and larger reduction of tensile strength (about 17%) was observed for PPE/PS with hygrothermal aging, as can be seen in Figure 4-8(c). Since PPE/PS matrix is amorphous, a small water absorption causes a more significant reduction in tensile strength, as compared to PP-T and PP-G, and even PA66/B with the same amount of water absorption.

PA66 specimen absorbed 5.4% moisture with immersion in 85 °C water for four days which is much higher, as compared to the other studied materials. Reduction in elastic modulus and tensile strength were obtained to be 49% and 62%, respectively. Polyamide is a semi-crystalline polymer for which polar amide groups form most of its crystalline regions [76]. The electrons shared between some atoms are not shared equally, resulting in regions of slight positive and slight negative charges in the polymer chain. When water molecules come into contact with polyamide, weak bonds form, and water molecules diffuse through the material forcing polymer chains apart, causing swelling. Water is absorbed only in the amorphous phase, while crystalline regions resist being pulled apart. This is because the bonds between the amide groups are stronger than the attraction to water, therefore, water acts as a plasticizer rather than a solvent. The separation of polymer chains reduces the polar attraction between chains and allows for increased chain mobility, resulting in diminished mechanical properties such as strength and stiffness.

The polarity of polyamides also causes a strong bond with reinforcements such as glass, which is also polar. In addition, a silane coupling agent is usually used to increase the interface adhesion between glass fiber and matrix such as polyamide and to protect the interface region from water damage [102, 107]. Since tensile properties of PA66/B were much more affected by moisture absorption, as compared to the other studied materials, a more comprehensive moisture study was conducted for it.

4.5 Moisture Absorption of PA66/B

As received or dry as-molded (DAM) PA66/B specimens after molding process were kept in the laboratory environment which has average of 20% RH with ±10% variation and temperature of 23 °C with ±2 °C variation. The %wt of moisture absorption was periodically measured by weighting the specimens and calculated as:

$$M_t = \frac{W_w - W_d}{W_d} \times 100 \tag{4.3}$$

where W_d and W_w are DAM specimen and wet specimen weight, respectively. M_t values were obtained to be 0.65 wt% after one year, 0.75 wt% after 14 months, and 1.45 wt% after two years. As observed previously for hygrothermally aged specimens, this amount of moisture absorption can dramatically affect the mechanical properties. To achieve DAM condition, moisture should be desorbed completely. Full recovery of tensile properties were obtained by drying the 14 months aged specimen at 80 °C for 24 hours in a vacuum chamber, as shown in Figure 4-9. Full water desorption was not obtained by drying in a regular chamber.

PA66/B specimens were immersed in 23 °C and 85 °C water for different durations and %wt of water absorption was measured based on Equation 4.3. Fick’s law is the most commonly used approach to model single free-phase diffusion [32] and predicts that the %wt of absorbed fluid increases linearly with square root of time, and then gently slows until it reaches a plateau (saturation). The simplest form of the model can be expressed in two regions as [108]:

$$\frac{M_t}{M_m} = \frac{4}{\pi^{1/2}} \left[\frac{D\,t}{h^2} \right]^{1/2} \quad \text{for} \quad \frac{D\,t}{h^2} < 0.05 \tag{4.4}$$

$$\frac{M_t}{M_m} = 1 - \frac{8}{\pi^2} \exp\left[- \left[\frac{D\,t}{h^2} \right] \pi^2 \right] \quad \text{for} \quad \frac{D\,t}{h^2} > 0.05 \tag{4.5}$$

where t is time, h is the thickness of the specimen, D is the diffusion coefficient, and M_m is the maximum water absorption. D values can be obtained at each temperature from the fit of Equation 4.4 to the initial linear portion of the moisture uptake curve.

Figure 4-10 shows the %wt of water uptake as a function of time at immersion temperatures of 23 and 85 °C and the corresponding Fick's model predictions. Each data point is the average weight of three different specimens. At both temperatures, good agreement is observed between experimental results and Equations 4.4 and 4.5, which confirms the Fickian behavior of PA66/B. M_m value is 5.4% at 23 °C and 85 °C, indicating M_m is independent of immersion temperature. D values were obtained to be 3×10^{-13} and 1.3×10^{-11} (m^2/s) at 23 °C and 85 °C, respectively, indicating that unlike M_m, diffusion coefficient is highly influenced by immersion temperature. Due to higher mobility of polymer chains at elevated temperatures, the rate of water absorption increases dramatically. Obtained M_m and D values are in agreement with values reported by Ishak and Berry [35] for 30 wt% short carbon fiber reinforced polyamide-6.6, suggesting that glass or carbon do not affect the water uptake process.

For polymers and polymer composites, diffusion coefficient D has been related to the immersion temperature by an Arrhenius type relationship [101], given by:

$$D = D_0 \exp\left(\frac{-E_a}{RT}\right) \tag{4.6}$$

where D_0 is the pre-exponential coefficient, R is the gas constant (8.31 J/mol K), E_a is the activation energy, and T is the absolute temperature in Kelvin. Values of D_0 and E_a were reported to be 8.5×10^{-3} m^2/s and 58.65 kJ/mol, respectively for short carbon reinforced polyamide-6.6 composite [35]. Using Equation 4.6 with these constants results in reasonable values for D at 23 °C and 85 °C (3.6×10^{-13} m^2/s and 2.3×10^{-11} m^2/s, respectively). Broudin et al. [109] mentioned that the Arrhenius equation is accurate for the glassy state of polymer ($T<T_g$), but for rubbery state ($T>T_g$) a more complicated behavior should be considered. Therefore, more variation at 85 °C is expected. Estimated D values can be used with Equations 4.4 and 4.5 and the fact that maximum water uptake is constant at different temperatures (5.4% for PA66/B), to predict the amount of absorbed moisture at different temperatures and time.

As mentioned earlier, water molecules diffuse through the PA66/B specimens, forcing polymer chains apart, causing swelling of the polyamide. Comparison of the dimensions of the specimens before and after immersion in water showed 4% increase in thickness and 0.1 % increase in width at both 23 °C and 85 °C for the saturated condition. These are in agreement with data reported by Thomason and Porteus [110]. As the fibers are oriented in the transverse to the mold flow direction, dimension change in width should be less, since the fibers which are along the width, prevent movement of the polymer resin. One specimen after 130 days immersion in 23 °C water with saturated water content of 5.4 wt% was dried in vacuum chamber at 85 °C. The water desorption during time, similar to water absorption, follows Fick's model, as shown in Figure 4-10. After four days, full drying was obtained.

4.6 Effect of Water Absorption on Tensile Properties of PA66/B

Tensile test were conducted on aged specimens at 23 °C and hygrothermally aged specimens at 85 °C at temperature the same as that of immersion temperature. Stress-strain curves with different moisture contents tested at 23 °C and 85 °C are shown in Figure 4-11. Tensile strength, elastic modulus, and strain at failure are considerably influenced by the amount of absorbed water. T_g of polyamide-6.6 decreases considerably with increasing moisture content and can reach to 0 °C from about 55 °C [109]. At 23 °C, for aged specimens with T_g higher than 23 °C strain at failure is similar to that of DAM condition, but for aged specimens with T_g lower than 23 °C strain at failure increased (see Figure 4-11(a)). At 85 °C, which is above T_g, because of post-crystallization [98] a reduction in strain at failure is observed, compared to DAM condition (see Figure 4-11(b)).

Comparison of stress-strain curves of conditioned specimens in the laboratory environment, shown in Figure 4-9 (aging time of 14 months), with stress-strain curve of conditioned specimens at 23 °C water, shown in Figure 4-11(a) (aging time of 4 days) shows that in addition to %wt of absorbed moisture, aging time has also affected the mechanical behavior.

The stress-strain curve of re-dried specimen after immersion for 130 days in 23 °C water, shown in Figure 4-11(a), indicates that water desorption in addition to recoverability, somewhat increases both stiffness and strength of the PA66/B. The percentage of crystallinity of DAM and re-dried PA66/B, obtained from DSC thermograms shown in Figure 4-12, were obtained to be 25.9% and 27.1%, respectively. Narrower melting peak for the aged specimen shows formation of more organized crystalline structure, as compare to the DAM specimen. This increase in crystallinity resulted in the increase of both stiffness and strength, which was also reported in [6, 111].

Exponentially decaying fit with %wt of absorbed water was used for tensile strength and elastic modulus at both 23 and 85 °C, as shown in Figures 4-13(a) and (b). Additional reduction of strength and stiffness after 4 %wt water absorption, which is the point of transition from linear to exponential form in Fick's model at both temperatures is nearly negligible. Normalized tensile strength and elastic modulus with respect to their values in DAM condition is used to compare the water aging effects at 23 °C and 85 °C, as shown in Figure 4-13(c). It can be seen that the effect of water aging on S_u and E is almost the same at both temperatures.

The water aging effect on strength and stiffness were significantly more at 23 °C, as compared to 85 °C, as can be seen in Figure 4-13(c). The aging time is much less at 85 °C compared to 23 °C (22 times less for saturated condition). When the factor of time is combined with %wt of water absorption in the form $M_t\, t^{0.5}$, a good correlation of both strength and stiffness at both 23 °C and 85 °C is obtained, as can be seen in Figure 4-13(d). An exponentially decaying curve is obtained up to the transition point mentioned earlier (i.e. from linear to exponential form in Fick's model). After this point the tensile properties remain constant. The equation of the fit is expressed as:

$$\frac{X}{X_0} = 0.904\, e^{-0.004 M_t t^{0.5}} \tag{4.7}$$

where X can be S_u or E and X_0 is the S_u or E in DAM condition.

Figure 4-14 shows SEM micrographs of fracture surfaces of the core layer of DAM specimens tested at 23 °C and 85 °C, aged specimens tested at 23 °C and 85 °C, and a re-dried specimen after saturation in 23 °C water. Specimens were cut transverse to the mold flow direction, therefore, the orientation of the majority of fibers in the core layer are perpendicular to the fracture plane due to the core-shell morphology [28]. Matrix cracking with no evidence of matrix deformation along with fiber pullouts, indicating brittle failure of the specimen, are observed for DAM specimen tested at 23 °C (Figure 4-14(a)). Significant plastic deformation of the matrix, mainly at fiber tips due to stress concentration, is observed at 85 °C for DAM condition (Figure 4-14(b)). For the aged specimens, matrix yielding and plastic deformation illustrating the physical damage of the matrix, and debonding between fiber and matrix (mainly at 85 °C) which results in an increase in deformation, are evident (Figures 4-14(c) and (d)). Fracture surface of the re-dried specimen shows brittle failure, similar to that of the DMA specimen at 23 °C and a strong fiber/matrix interface is observed (Figure 4-14(e)).

In order to illustrate the effect of water aging and re-drying on fiber/matrix interface, SEM micrographs of the fiber in the fracture surface in different conditions are shown in Figure 4-15. For DAM specimens tested at 23 °C and 85 °C, an excellent bond between fiber and matrix are observed (Figures 4-15(a) and (b)). Continuous cover of fiber by matrix at 23 °C and significant plastic deformation and fibrils of matrix at the tip of fiber at 85 °C are indications of brittle and ductile failures, respectively [112]. Diffused water at 85 °C affected the interface between fiber and matrix (Figure 4-15(d)). A nearly clean fiber with small retention of the matrix on it, reveals drastic damage at fiber/matrix interface with hygrothermal effect (Figure 4-15(d)). Finally, for the re-dried water aged specimen at 23 °C, a very good bond can be seen (Figure 4-15(e)), which confirms recoverability of water aging at 23 °C with complete drying.

Table 4-1: Tensile properties of PP-T, PP-G, PA66/B, PA66/D and PPE/PS at different testing temperatures under displacement rate of 1 mm/min in the transverse to the mold flow direction and dry as-molded condition.

Mat.	**Temp. (°C)**	**Strain Rate (1/sec)**	**0.2% Offset Yield Strength (MPa)**	**Ultimate Strength (MPa)**	**Strain at Ultimate Strength (mm/mm)**	**Elastic Modulus (ISO) (GPa)**	**Elastic Modulus (ASTM) (GPa)**	***K* (MPa)**	***n***
PP-T	23	$5\ (10^{-4})$	21.1	29.6	0.023	3.90	4.40	59.5	0.157
	23	$5\ (10^{-4})$	21.3	29.2	0.021	4.29	4.10	58.4	0.152
	85	$2\ (10^{-4})$	7.4	13.8	0.039	1.32	1.60	34.4	0.233
	85	$2\ (10^{-4})$	7.7	13.7	0.041	0.94	1.50	32.6	0.221
	120	$2\ (10^{-4})$	3.25	7.5	0.056	0.56	0.65	20.2	0.278
	120	$2\ (10^{-4})$	3.43	7.8	0.049	0.57	0.70	21.0	0.272
PP-G	23	$4\ (10^{-4})$	27.7	47.1	0.041	3.53	3.46	111	0.209
	23	$4\ (10^{-4})$	28.5	46.6	0.041	2.90	3.43	101	0.191
	85	$6\ (10^{-4})$	12.1	21.6	0.067	1.40	1.40	39.5	0.172
	85	$6\ (10^{-4})$	12.4	21.9	0.065	1.55	1.63	42.3	0.180
	120	$7\ (10^{-4})$	6.2	12.0	0.140	0.79	0.93	20.7	0.174
	120	$7\ (10^{-4})$	5.9	11.8	0.150	0.95	1.00	20.5	0.181
PA66/B	23	$4\ (10^{-4})$	67.7	105.4	0.036	4.50	5.30	258	0.198
	23	$4\ (10^{-4})$	71.2	102.4	0.032	5.11	5.20	246	0.185
	85	$4\ (10^{-4})$	25.2	58.1	0.085	2.30	2.27	136	0.245
	85	$4\ (10^{-4})$	26.1	59.5	0.085	2.14	2.22	143	0.250
	120	$4\ (10^{-4})$	19.5	47.2	0.089	1.52	1.60	121	0.269
	120	$4\ (10^{-4})$	20.1	46.3	0.090	1.66	1.53	106	0.238
	150	$4\ (10^{-4})$	16.8	40.2	0.081	1.42	1.47	91.0	0.248
	150	$4\ (10^{-4})$	18.1	40.0	0.088	1.46	1.53	92.5	0.242
PA66/D	23	$4\ (10^{-4})$	74.7	106.6	0.034	5.59	5.32	229	0.166
	23	$4\ (10^{-4})$	73.3	106.7	0.032	5.94	5.87	255	0.187
	85	$4\ (10^{-4})$	25.7	61.0	0.086	1.29	2.40	155	0.272
	85	$4\ (10^{-4})$	25.2	59.8	0.094	1.93	2.00	146	0.259
	120	$4\ (10^{-4})$	21.6	50.3	0.108	1.66	1.70	111	0.241
	120	$4\ (10^{-4})$	20.2	49.6	0.094	1.44	1.67	120	0.263
	150	$4\ (10^{-4})$	18.2	44.6	0.089	1.58	1.53	108	0.262
	150	$4\ (10^{-4})$	17.5	43.1	0.101	1.39	1.47	105	0.268
PPE/PS	23	$4\ (10^{-4})$	52.4	71.2	0.031	4.60	4.40	139	0.147
	23	$4\ (10^{-4})$	52.7	70.5	0.032	4.40	4.50	133	0.139
	85	$3\ (10^{-4})$	38.2	46.3	0.024	3.80	4.00	73.7	0.098
	85	$3\ (10^{-4})$	40.8	46.8	0.020	3.80	4.00	69.3	0.075
	120	$4\ (10^{-4})$	22.4	29.9	0.023	3.80	3.50	55.2	0.131
	120	$4\ (10^{-4})$	22.8	30.7	0.017	3.50	3.40	57.5	0.124

Table 4-2: Tensile properties of PP-T, PP-G, PA66/B, and PPE/PS in wet condition.

Mat.	**Drying Condition Before Immersion**	**Immersion Time (Hrs)**	**Immersion Temp. (°C)**	**% wt Moisture Absorbed**	**Testing Temp. (°C)**	**Ultimate Strength (MPa)**	**Strain at Ultimate Strength (mm/mm)**	**0.2% Offset Yield Strength (MPa)**	**Elastic Modulus (ISO) (GPa)**	**Elastic Modulus (ASTM) (GPa)**
PP-T	80 °C, R*, 4 Hrs	96	85	0.11	23	27.3	0.026	18.4	3.57	4.00
PP-G	80 °C, R, 4 Hrs	96	85	0.20	23	43.6	0.034	23.3	3.24	3.43
PA66/B	80 °C, R, 4 Hrs	-	-	-	23	103.2	0.039	71.2	5.40	5.20
	80 °C, R, 24 Hrs	-	-	-	23	94.9	0.045	57.5	5.50	5.00
	80 °C, R, 4 Hrs	-	-	-	23	89.6	0.050	52.0	5.31	5.00
	80 °C, V**, 24 Hrs	-	-	-	23	105.5	0.035	69.8	5.28	5.33
	80 °C, V, 4 Hrs	-	-	-	23	97.5	0.039	58.1	5.52	5.33
	80 °C, V, 12 Hrs	-	-	-	23	103.2	0.036	65.7	5.86	5.66
	80 °C, R, 4 Hrs	96	23	1.45	23	73.4	0.056	42.5	4.00	3.90
	80 °C, R, 4 Hrs	96	23	1.45	23	74.7	0.050	42.4	4.00	3.90
	80 °C, V, 24 Hrs	96	23	1.45	23	83.2	0.029	59.0	4.32	4.50
	80 °C, V, 24 Hrs	288	23	2.21	23	74.4	0.033	44.4	3.90	4.20
	80 °C, V, 24 Hrs	816	23	3.70	23	58.5	0.049	31.4	2.86	2.75
	80 °C, V, 24 Hrs	1200	23	4.5	23	54.25	0.080	25.9	2.2	2.25
	80 °C, V, 24 Hrs	3120	23	5.4	23	53.2	0.081	24.5	2.2	2.2
	80 °C, V, 24 Hrs	3120	23	5.4	23	110.5	0.033	78.5	6.4	6.5
	80 °C, V, 24 Hrs	7	85	2.38	85	48.9	0.077	21.9	1.87	1.97
	80 °C, V, 24 Hrs	31	85	4.31	85	39.0	0.086	17.7	1.60	1.62
	80 °C, V, 24 Hrs	144	85	5.07	85	38.2	0.076	17.4	1.61	1.62
PPE/PS	100 ^{0}C, V, 4 Hrs	96	RT	0.00	23	64.5	0.022	51.5	4.50	4.50
	100 ^{0}C, V, 4 Hrs	96	85	0.21	23	59.3	0.031	50.1	3.91	4.20

*R: Regular Chamber, **: Vacuum Chamber

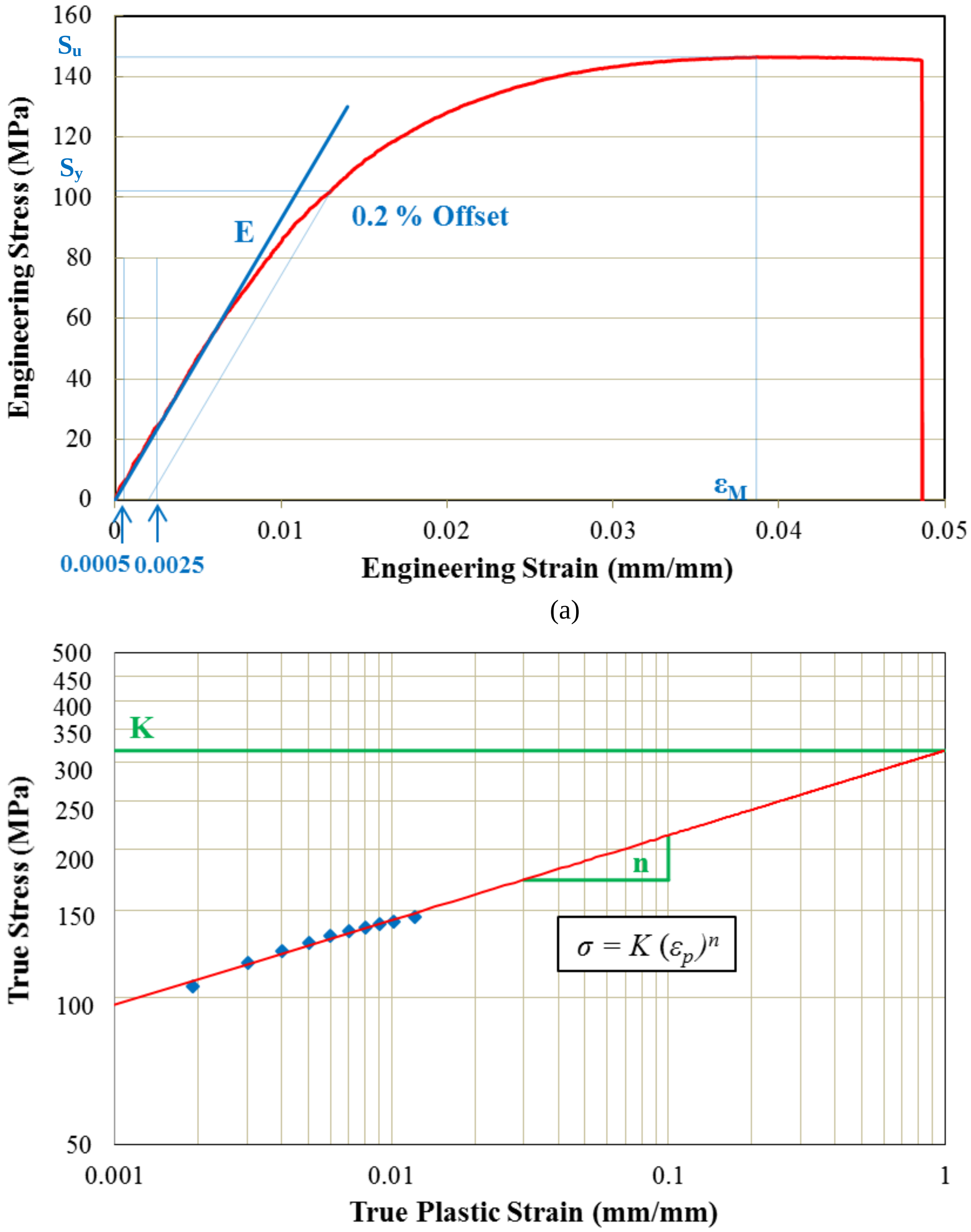

(a)

(b)

Figure 4-1: Calculated tensile properties from a monotonic tension test; (a) engineering stress versus engineering strain curve, and measured properties according to ISO 527 and ASTM D638, and (b) true stress versus true plastic strain curve in log-log scale, and *K* and *n* values calculated from the fit of data.

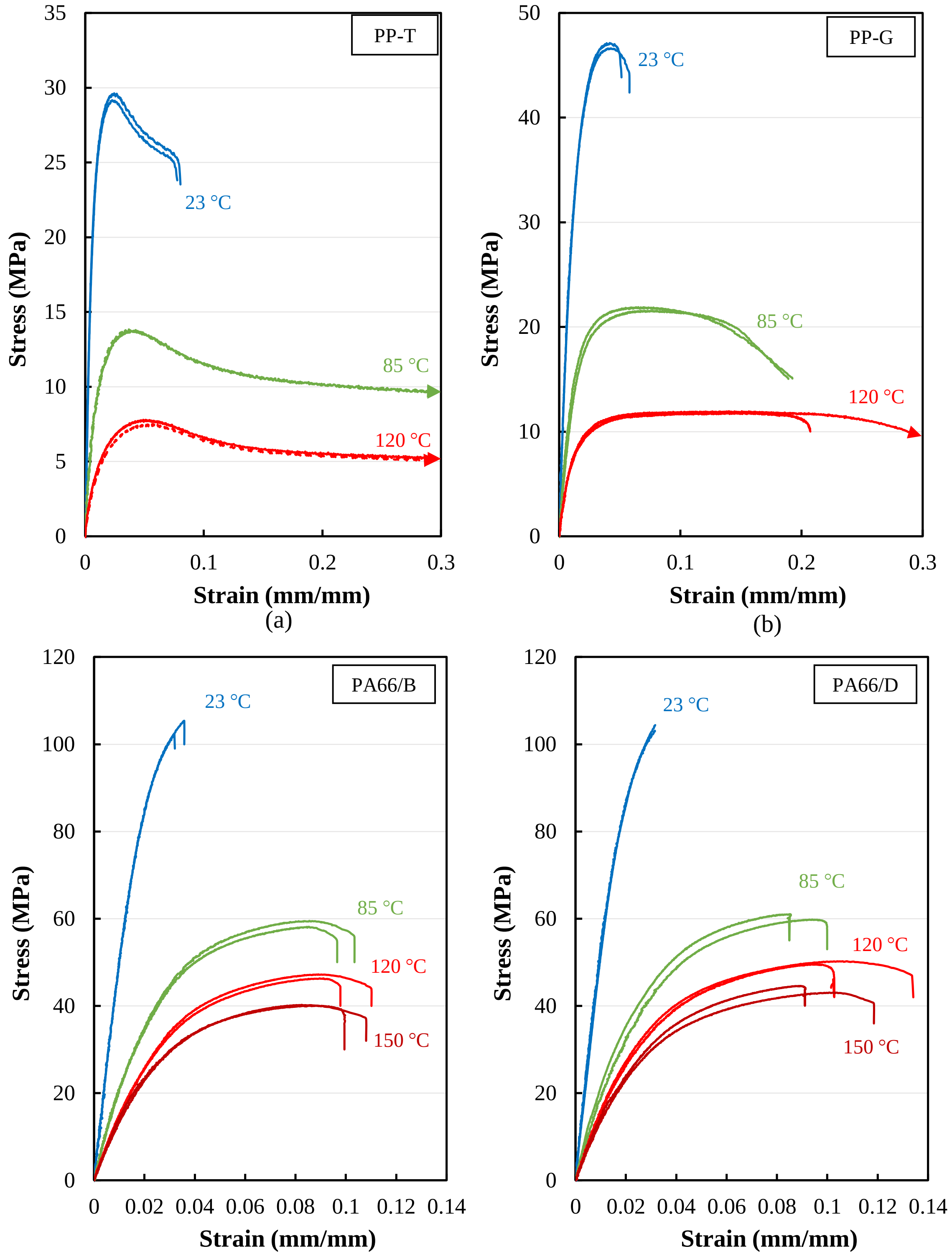
PP-T
Stress (MPa)
Strain (mm/mm)
0
5
10
15
20
25
30
35
0
0.1
0.2
0.3
23 °C
85 °C
120 °C
PP-G
Stress (MPa)
Strain (mm/mm)
0
10
20
30
40
50
0
0.1
0.2
0.3
23 °C
85 °C
120 °C
PA66/B
Stress (MPa)
Strain (mm/mm)
0
20
40
60
80
100
120
0
0.02
0.04
0.06
0.08
0.1
0.12
0.14
23 °C
85 °C
120 °C
150 °C
PA66/D
Stress (MPa)
Strain (mm/mm)
0
20
40
60
80
100
120
0
0.02
0.04
0.06
0.08
0.1
0.12
0.14
23 °C
85 °C
120 °C
150 °C

(a)

(b)

(c)

(d)

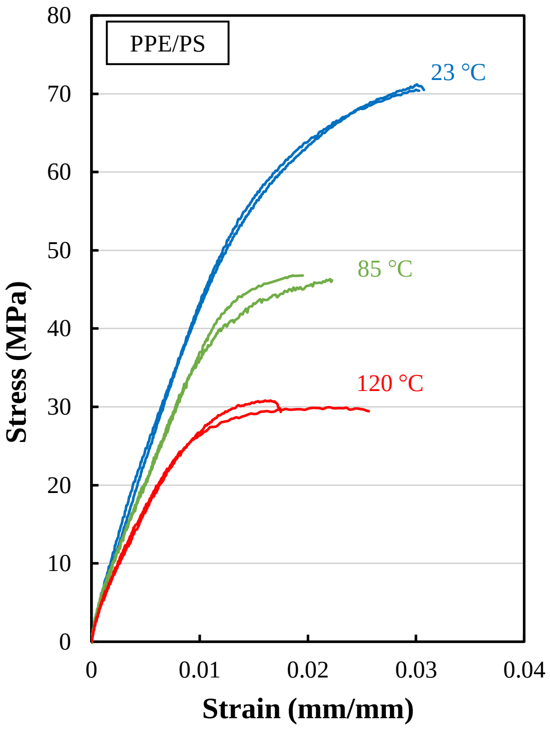

(e)

Figure 4-2: Effect of temperature on tensile stress-strain curve of (a) PP-T, (b) PP-G, (c) PA66/B, (d) PA66/D, and (e) PPE/PS in the transverse direction under displacement rate of 1 mm/min.

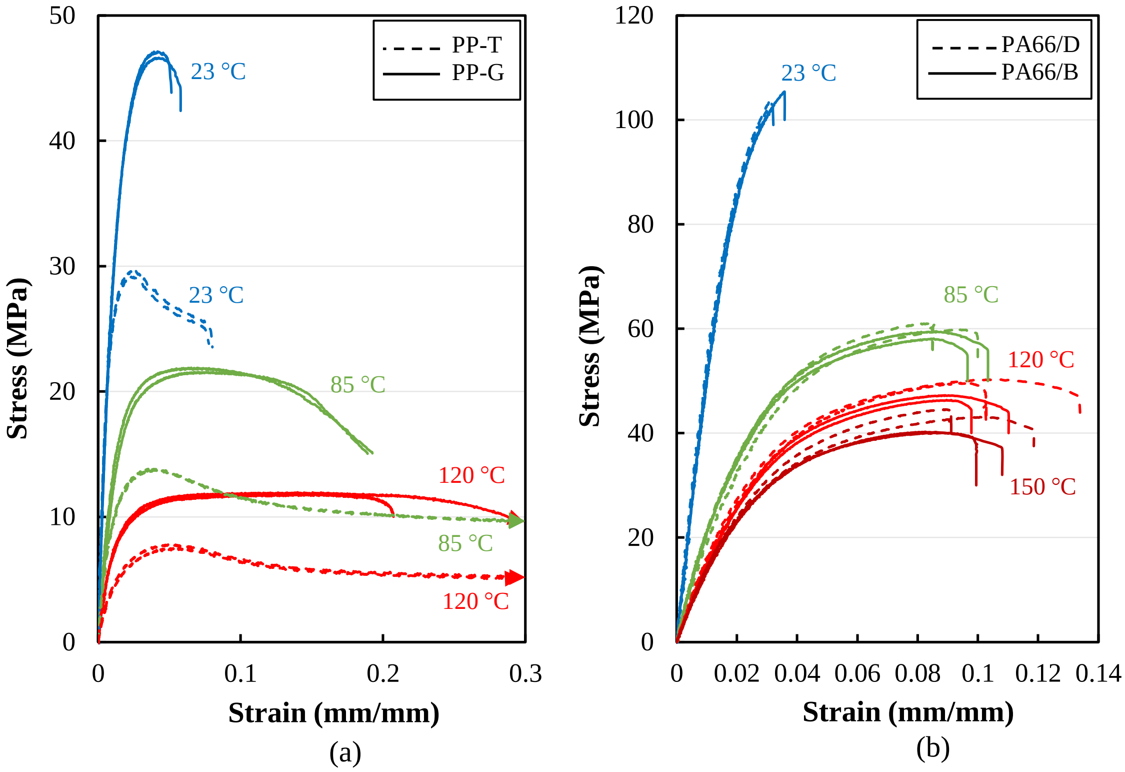

Figure 4-3: Comparison of tensile stress-strain curves of (a) PP-T and PP-G, and (b) PA66/B and PA66/D at different temperatures.

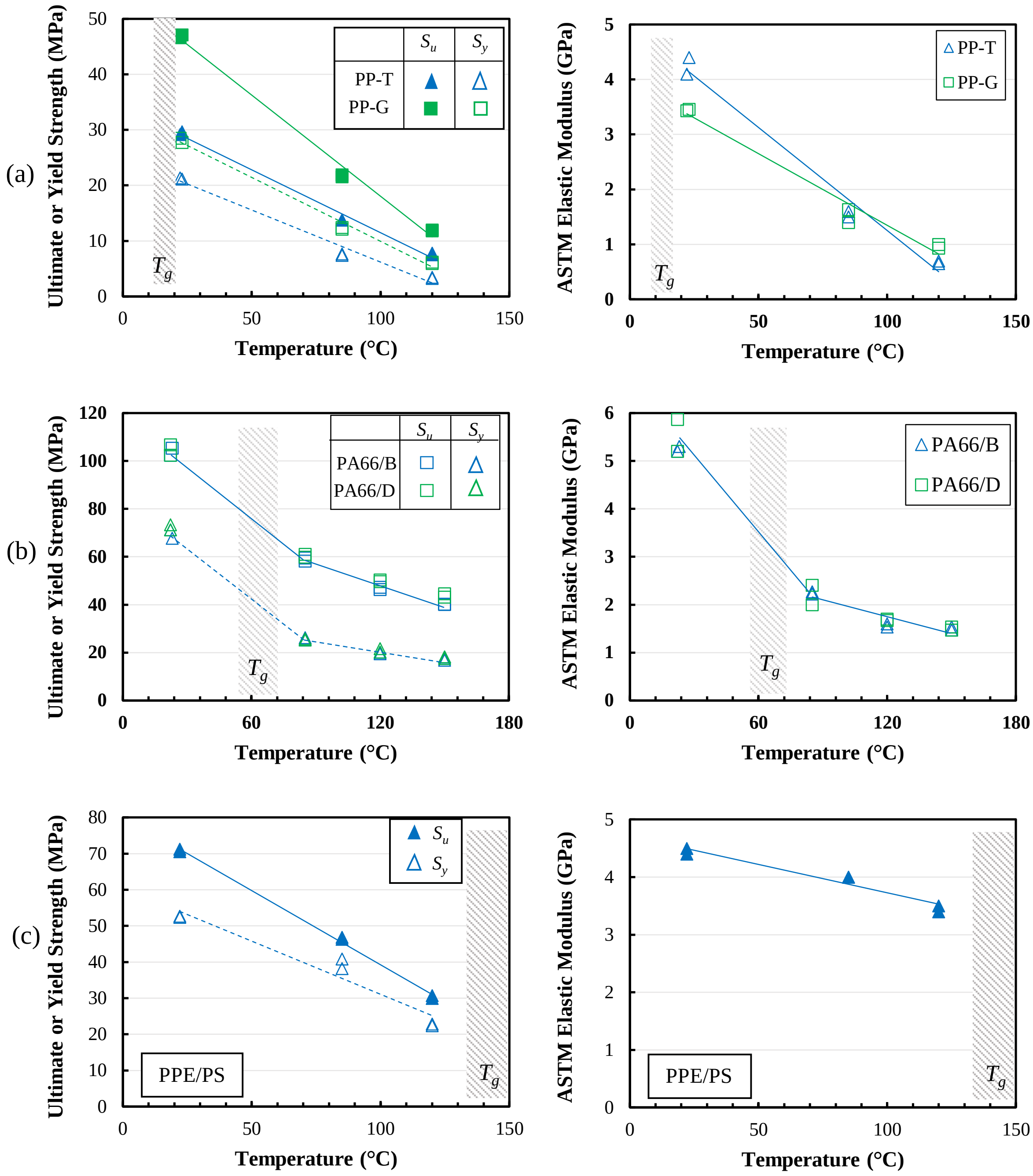

Figure 4-4: Variation of ultimate (S_u) and yield (S_y) strengths and ASTM elastic modulus (E) with temperature for (a) PP-T and PP-G, (b) PA66/B and PA66/D, and (c) PPE/PS. Hashed areas are the range for T_g.

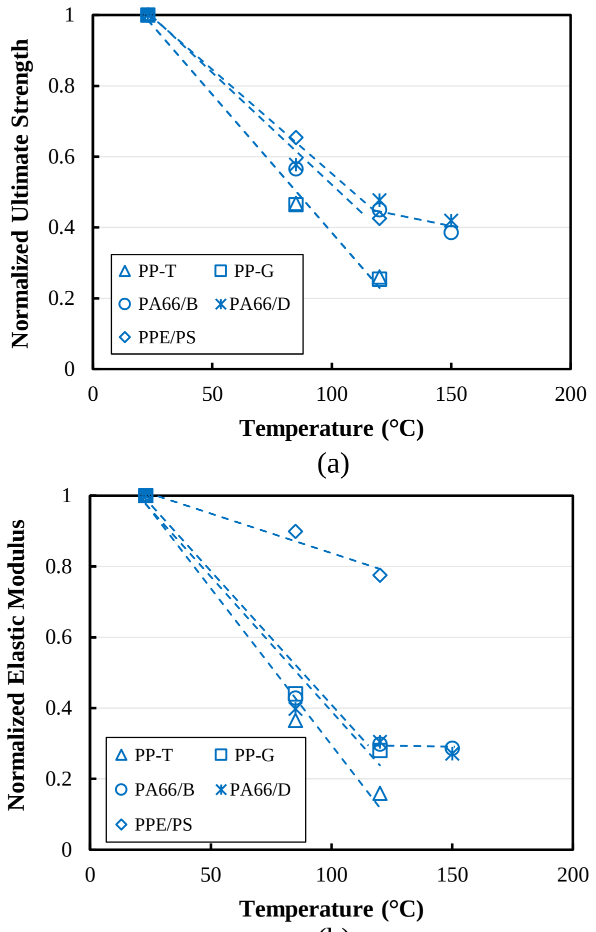

(a)

(b)

Figure 4-5: Variation of (a) normalized ultimate tensile strength and, (b) elastic modulus (with respect to their values at 23 °C) with temperature for PP-T, PP-G, PA66/B, PA66/D, and PPE/PS.

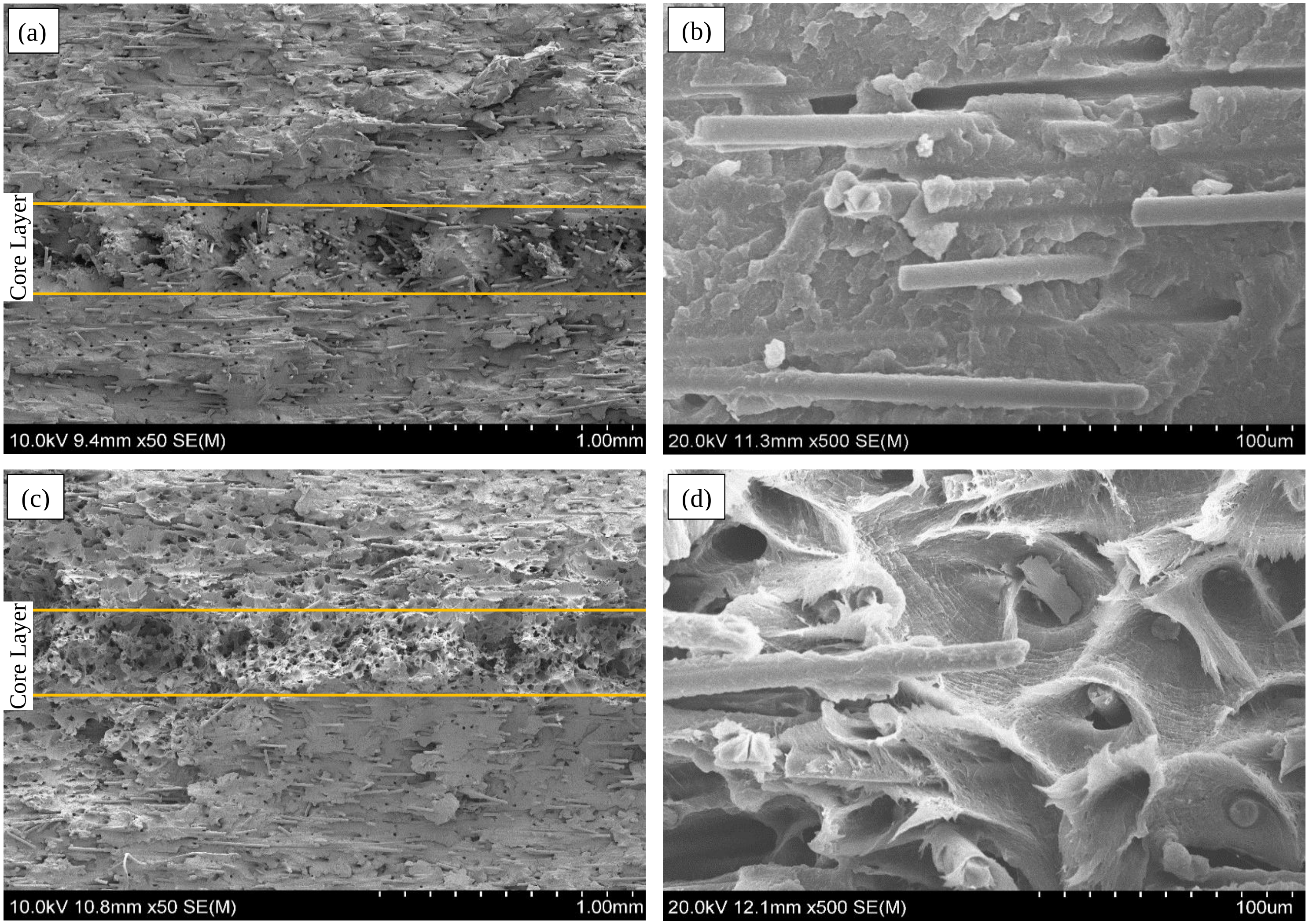

Figure 4-6: SEM pictures of fractured surface of PA66/B tensile specimens at 23 °C (a, b) and 85 °C (c, d) in dry as-molded condition. Figures b and d are from the shell layer.

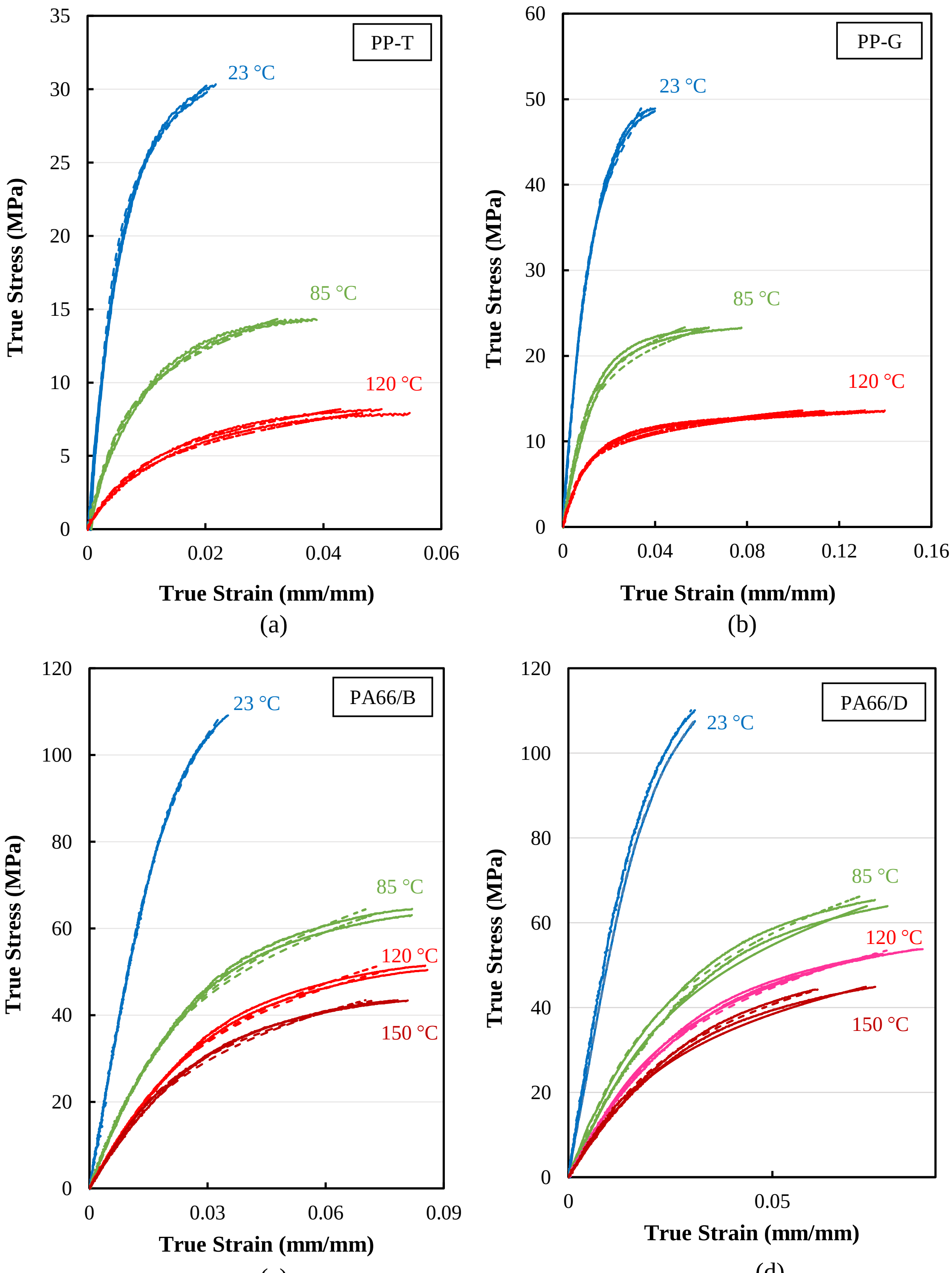
PP-T
23 °C
85 °C
120 °C
True Stress (MPa)
True Strain (mm/mm)
0
5
10
15
20
25
30
35
0
0.02
0.04
0.06
PP-G
23 °C
85 °C
120 °C
True Stress (MPa)
True Strain (mm/mm)
0
10
20
30
40
50
60
0
0.04
0.08
0.12
0.16
PA66/B
23 °C
85 °C
120 °C
150 °C
True Stress (MPa)
True Strain (mm/mm)
0
20
40
60
80
100
120
0
0.03
0.06
0.09
PA66/D
23 °C
85 °C
120 °C
150 °C
True Stress (MPa)
True Strain (mm/mm)
0
20
40
60
80
100
120
0
0.05

(a) (b)

(c) (d)

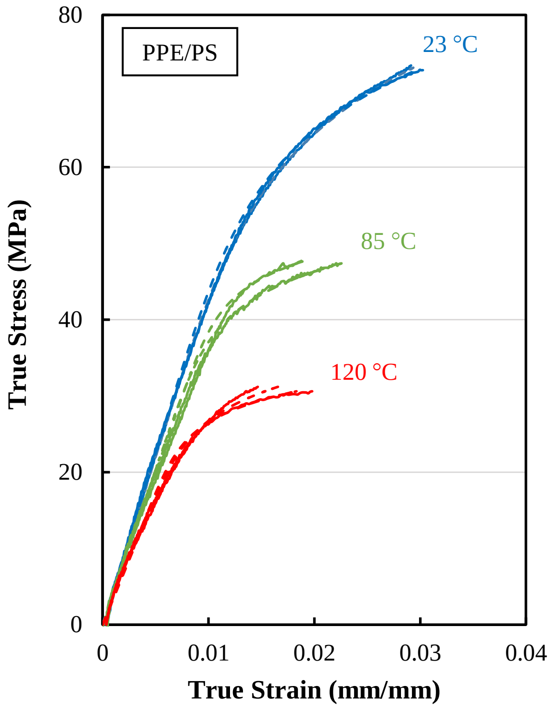

(e)

Figure 4-7: Stress-strain curves (solid lines) and corresponding Ramberg-Osgood equation representation (dash lines) at different temperatures for (a) PP-T, (b) PP-G, (c) PA66/B, (d) PA66/D, and (d) PPE/PS in the transverse direction at displacement rate of 1 mm/min in DAM condition.

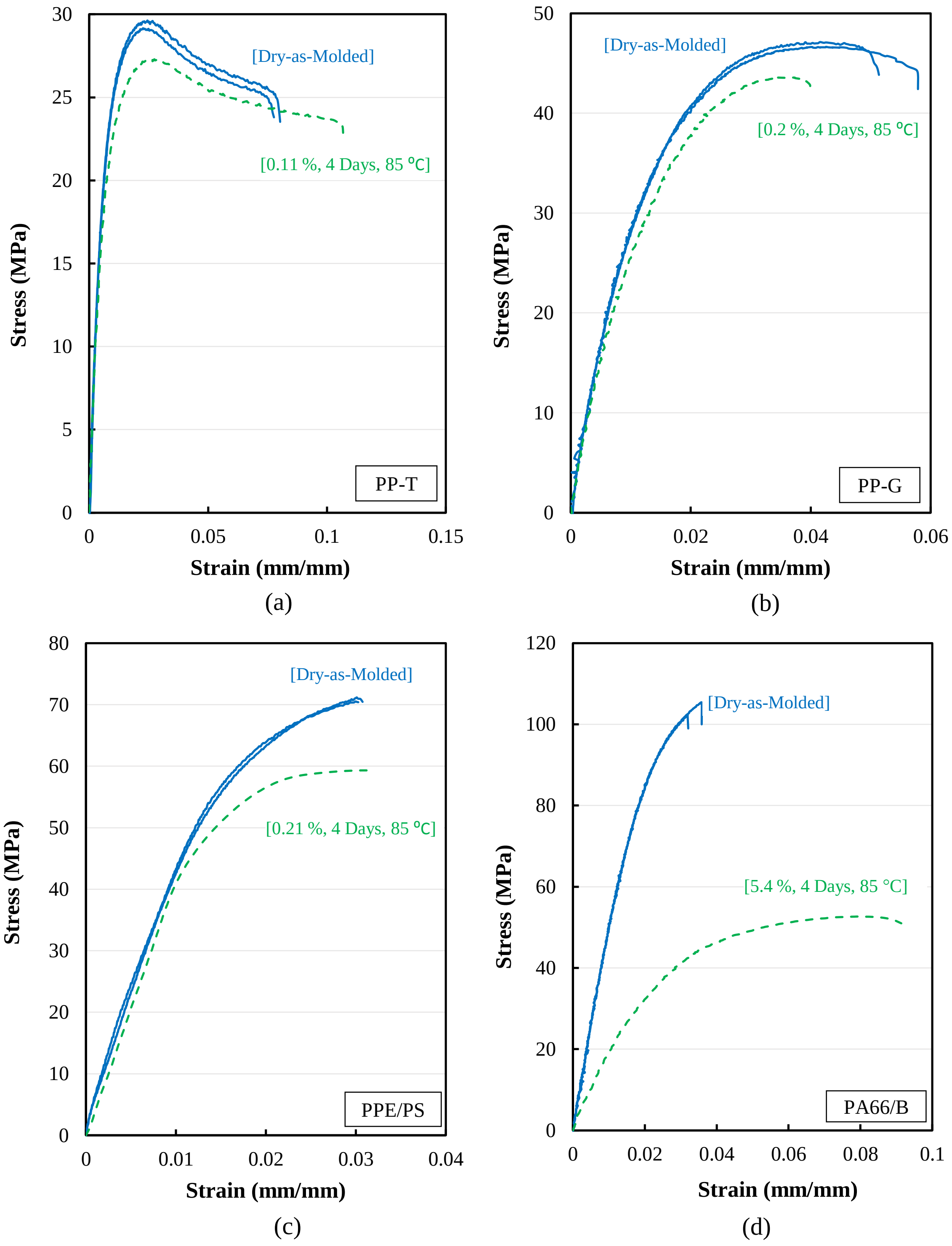

(a)

(b)

(c)

(d)

Figure 4-8: Effect of water absorption on tensile stress-strain curve of (a) PP-T, (b) PP-G, (c) PPE/PS, and PA66/B at testing temperature of 23 °C. [%wt of moisture absorption, immersion time, immersion temperature]. Duplicate tests were conducted for DAM condition of all the materials.

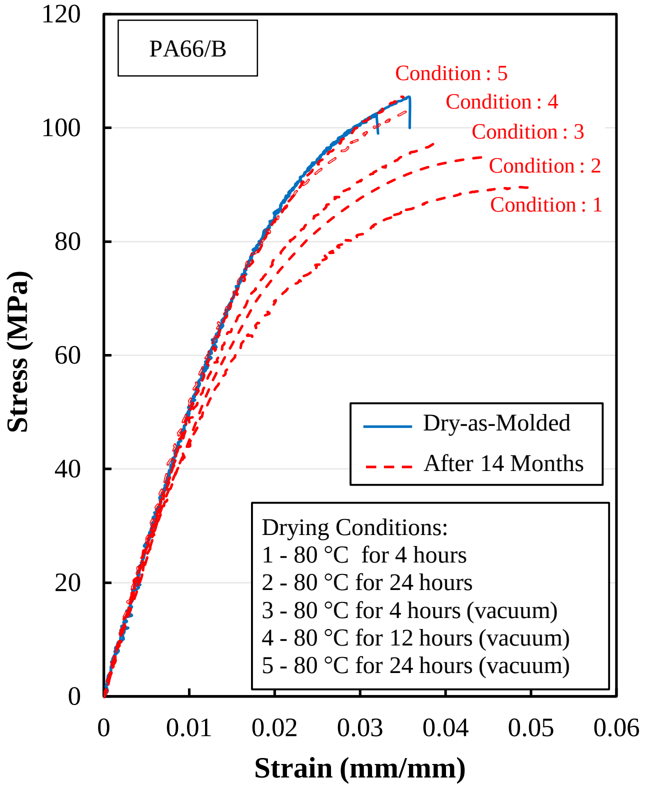

Figure 4-9: Stress-strain curves of PA66/B specimens aged for 14 months in the laboratory environment with different drying conditions.

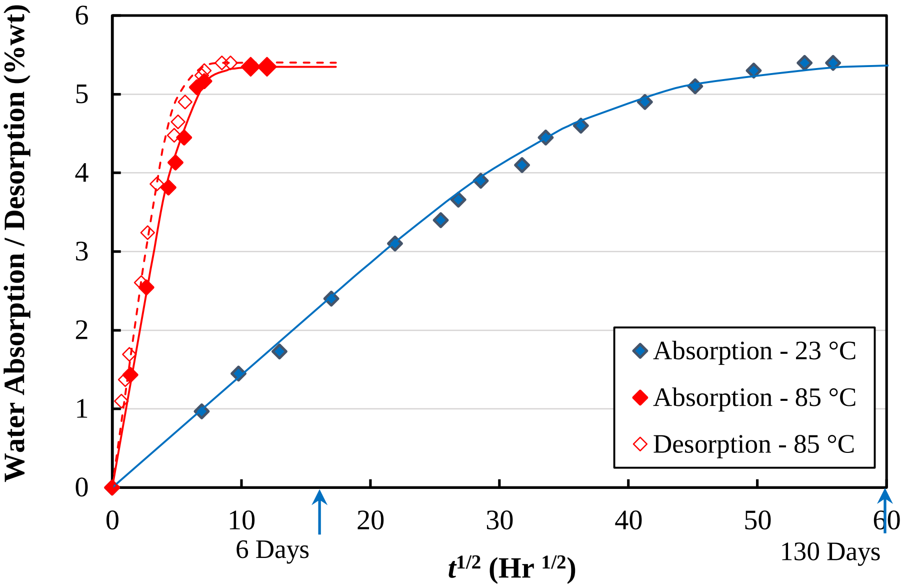

Figure 4-10: Water absorption at 23 °C and 85 °C water, and water desorption at 85 °C in vacuumed oven for PA66/B. The curves correspond to Fick's law.

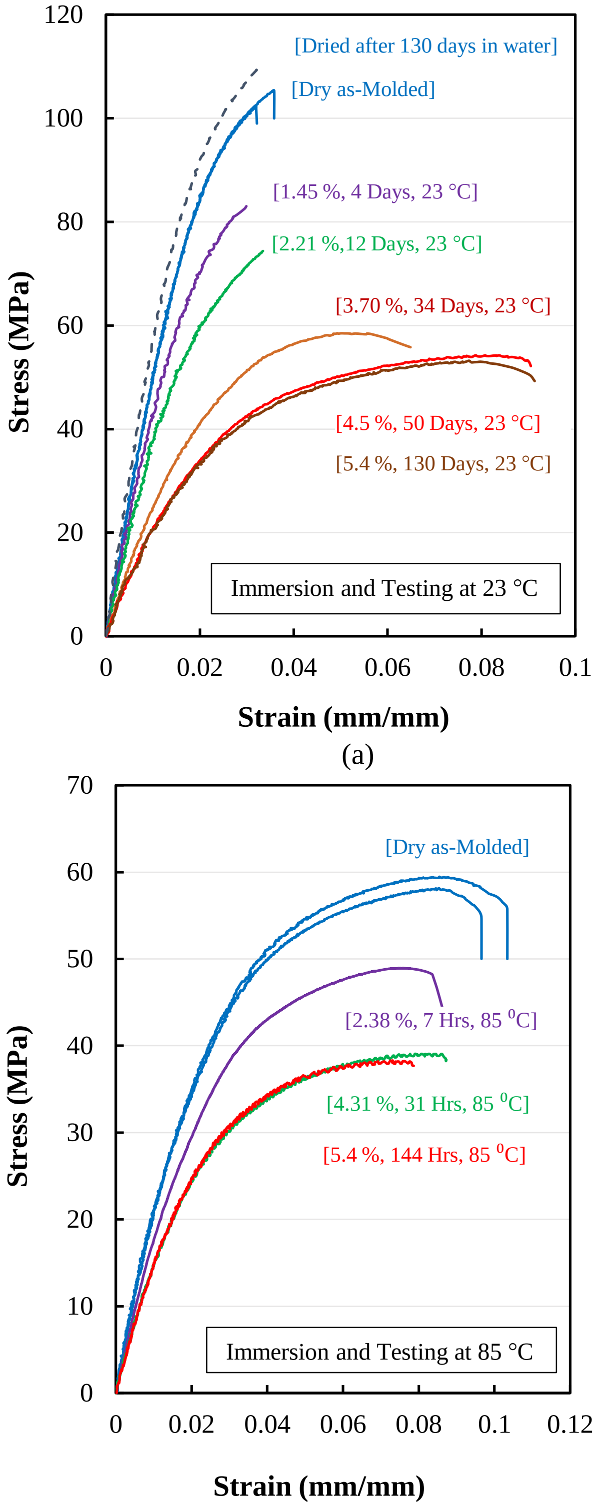

(a)

(b)

Figure 4-11: Tensile stress-strain curves at different water absorption conditions showing the effect of water absorption for PA66/B at (a) 23 °C and (b) 85 °C. [% wt of moisture absorption, immersion time, immersion temperature]. Duplicate tests were conducted for DAM condition in both figures.

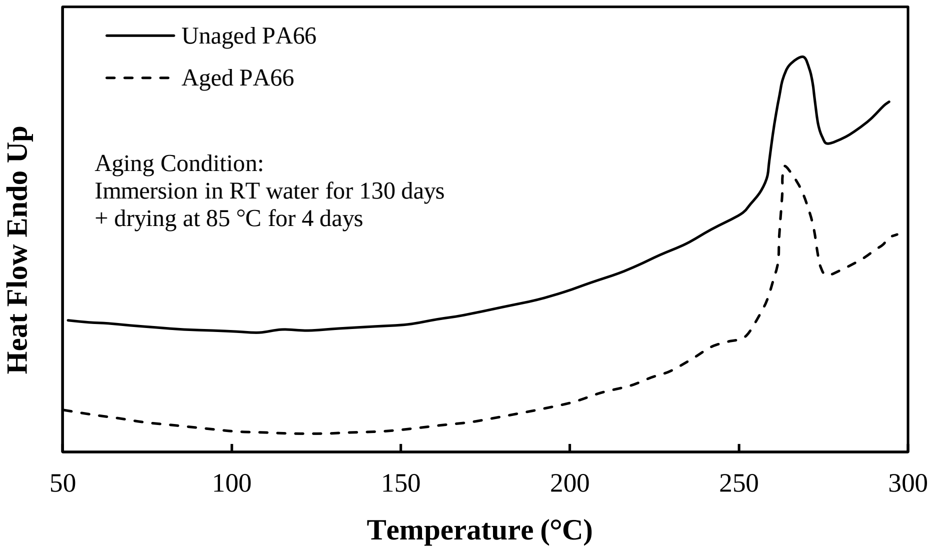

Figure 4-12: DSC thermographs of unaged and aged PA66/B.

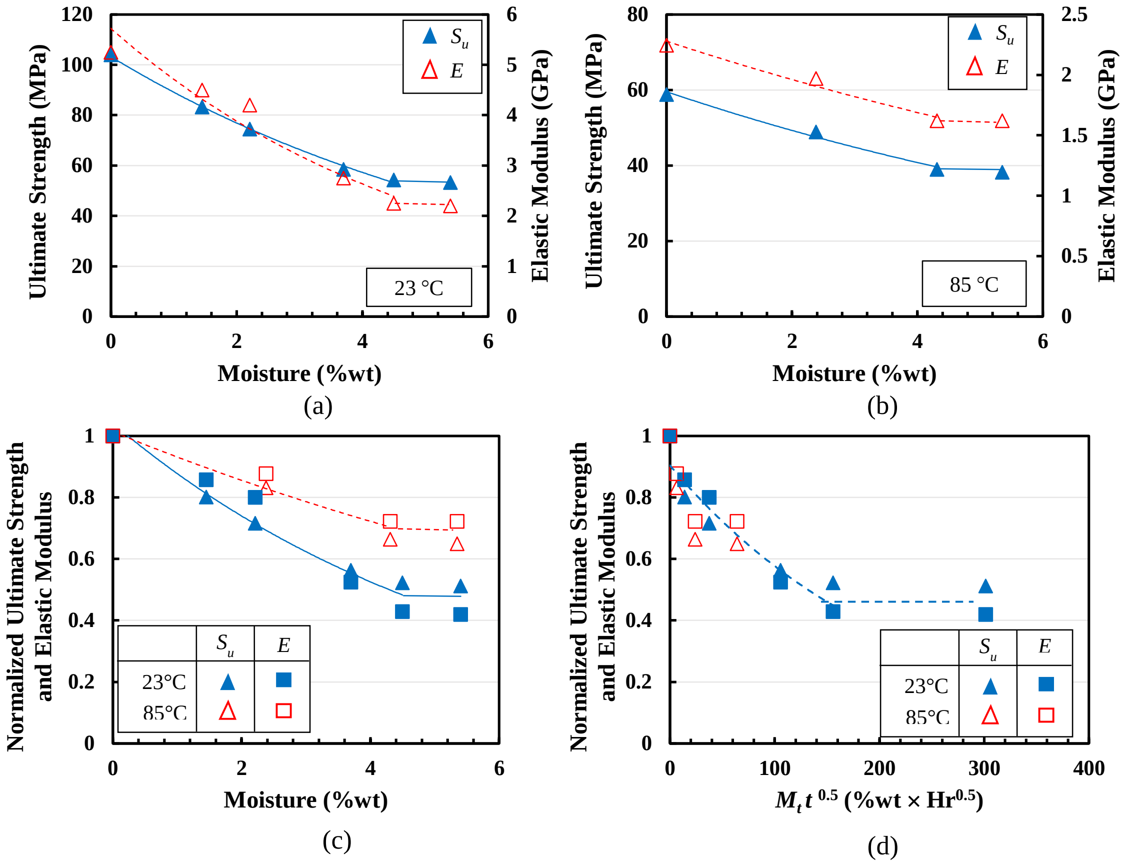

(a)

(b)

(c)

(d)

Figure 4-13: Variation of ultimate tensile strength (S_u) and elastic modulus (E) with water absorption at (a) 23 °C and (b) 85 °C. Variation of normalized ultimate tensile strength and elastic modulus as a function of (c) moisture content and, (d) $M_t t^{0.5}$ at 23 °C and 85 °C.

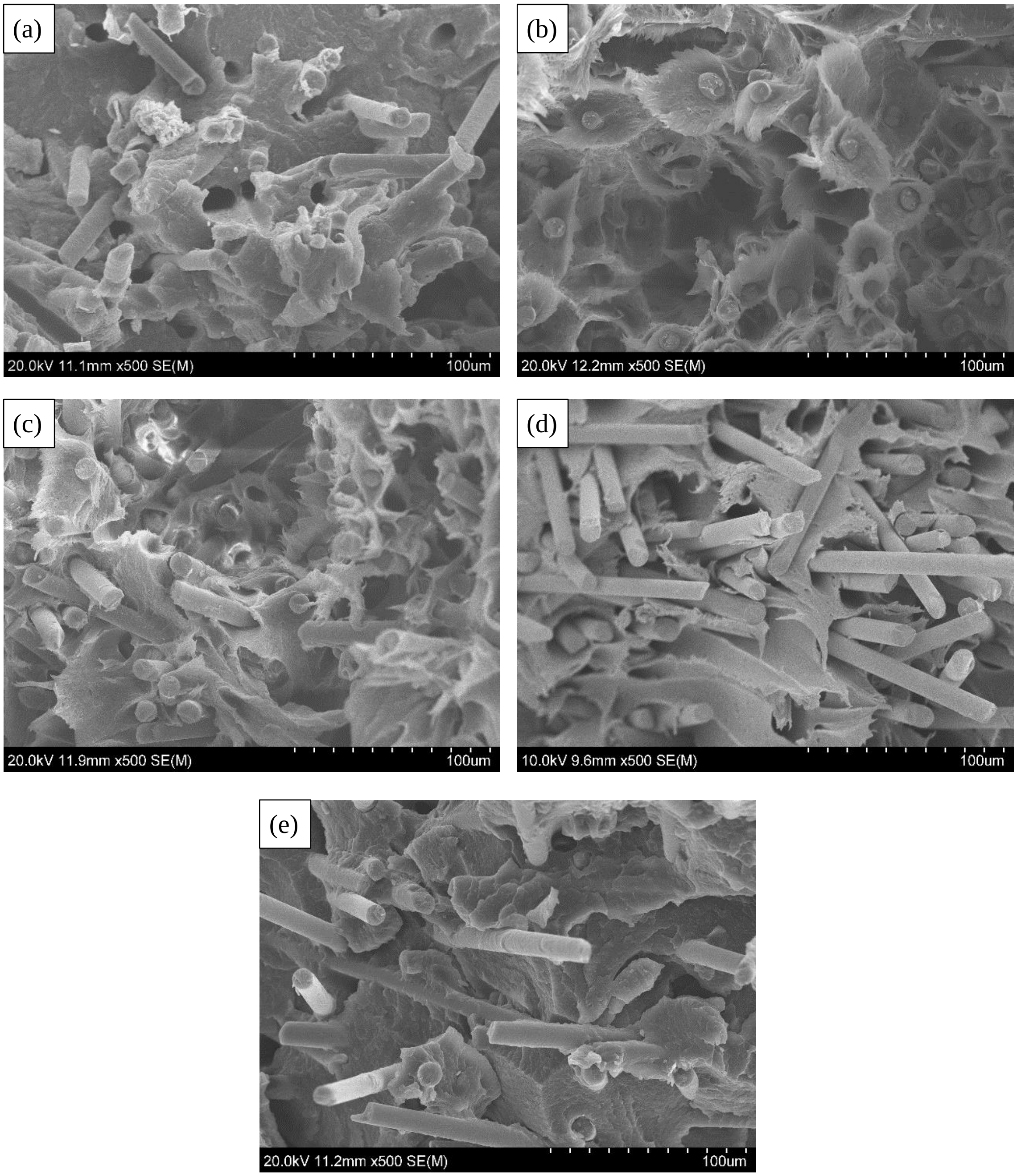

Figure 4-14: SEM micrographs of the PA66/B fracture surface in the core layer after tensile tests of (a) DAM at 23 °C, (b) DAM at 85 °C, (c) with 5.4 wt% moisture (saturated) tested at 23 °C, (b) with 5.4 wt% moisture (saturated) tested at 85 °C, and (e) re-dried specimen after desorption of 5.4 wt% moisture tested at 23 °C.

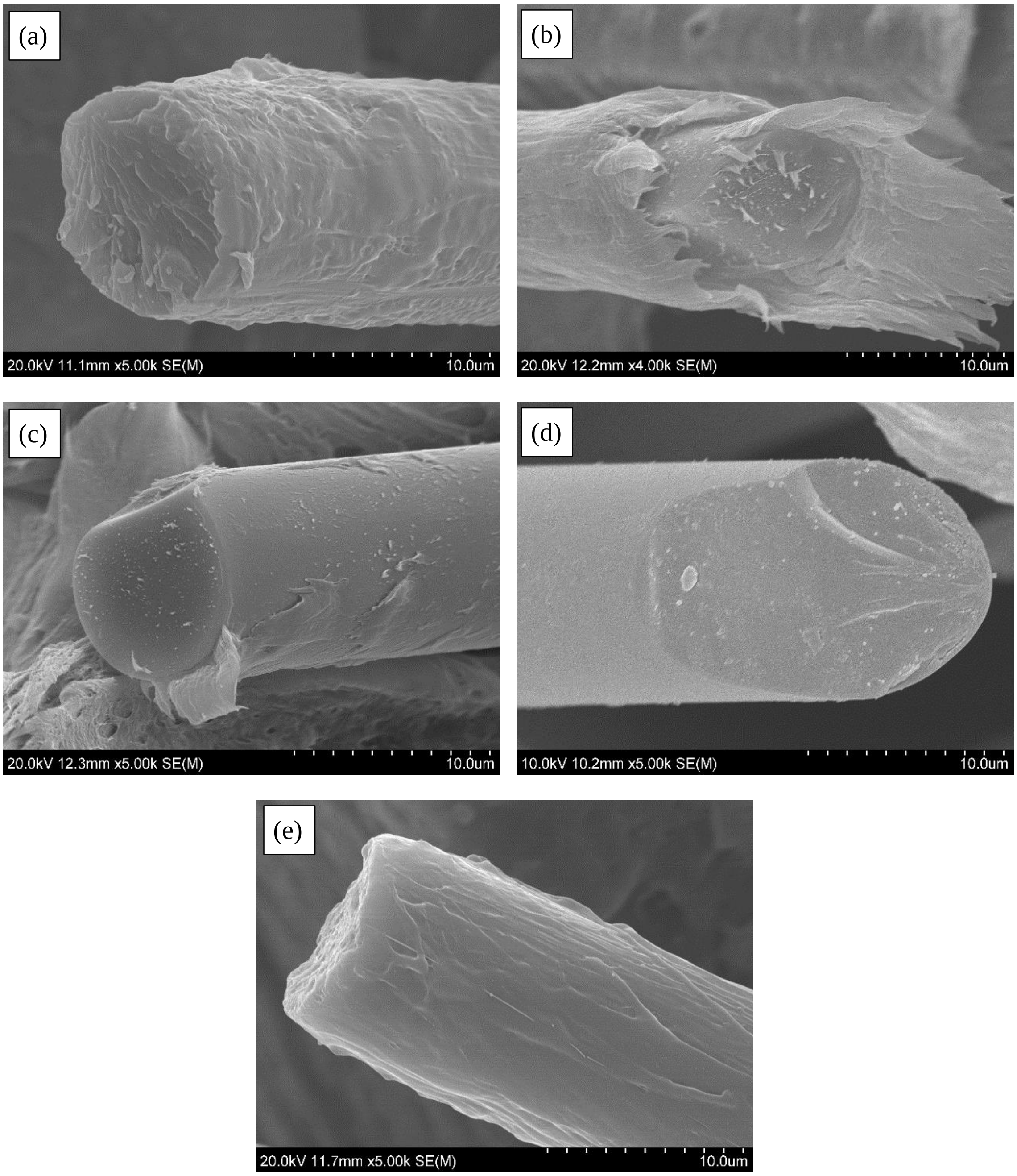

Figure 4-15: SEM micrographs of the glass fiber for PA66/B on tension test fracture surface of (a) DAM at 23 °C, (b) DAM at 85 °C, (c) with 5.4 wt% moisture (saturated) at 23 °C, (b) with 5.4 wt% moisture (saturated) at 85 °C, and (e) re-dried specimen after absorption of 5.4 wt% moisture.

Chapter 5

Creep Test Results and Analysis

In this chapter creep behavior of PP-T, PP-G, PA66/B, and PPE/PS is investigated. Creep tests were conducted at 23 °C and 85 °C for PP-T and PPE/PS and at these temperatures in addition to at 120 °C for PP-G and PA66/B under different stress levels. Empirical fits were used to represent creep rupture data and relate minimum creep rate (MCR) data to the applied stress. Larson-Miller parameter was used to correlate creep rupture data and a power law model was used to represent experimental creep strain curves. Semi-empirical models were used to correlate minimum creep rate, time to rupture, and strain at rupture together. Creep strain master curves and the corresponding shift factor versus stress curves were developed using short-term creep data according to the time-stress superposition (TSS) method. A small number of long-term creep tests were also conducted to verify the capability of the developed models for long-term creep predictions based on short-term creep data. Results of creep tests for PO and PP [77] and PA6 and PBT [78] were used for some additional analysis and comparisons with experimental results of PP-T, PP-G, PA66/B, and PPE/PS. Experimental results and analysis presented in chapter were published in [113].

5.1 Introduction

Polymeric materials are typically subjected to loading and environmental conditions causing creep deformation. This time-dependent behavior results in molecular rearrangement, the degree of which depends on factors including the type of material, magnitude of the stress, temperature, and time.

For a linear viscoelastic material under creep condition, the applied stress is proportional to the strain response at a given time, independent of the stress. For viscoelastic creep, the behavior exhibits non-linearity at large strains. While linear viscoelastic behavior is represented using physical based constitutive equations, such as Maxwell model, constitutive equations for non-linear creep or other viscoelastic behaviors are much more complex. As a results, they require a large number of functions with higher order stress terms with a large number of material constants and are typically empirical in nature [114].

When a constant load is applied on the specimen, an initial elongation occurs which is known as instantaneous strain, ε_0. This is followed by a rapidly decreasing deformation rate known as the primary stage, followed by a steady-state linear deformation stage, known as the secondary creep stage, for which the experimental data is typically of most interest. The final stage involves rapid deformation at an accelerated rate known as tertiary deformation, ultimately leading to the specimen rupture. Some materials do not have the secondary stage, while tertiary creep only occurs at high stresses and for ductile materials [82]. The three stages of creep curve are shown in Figure 5-1. Instantaneous creep strain, ε_0, can consist of elastic (ε_e) and plastic (ε_p) strain depending on the level of the applied load or stress and can constitute a considerable fraction of the total strain.

While creep in metallic materials occurs only at elevated temperatures, creep of polymers can be significant at any temperature. Therefore, creep or relaxation are major concerns in using polymer and polymer composites in structural applications. Long-term creep deformation and strength applicable to service condition are normally obtained by extrapolation of short-term test data obtained under accelerated testing conditions, such as higher temperature, stress, and humidity by using prediction models.

A number of studies in the literature have investigated creep behavior of neat polymers including damage mechanism [115], non-linear creep behavior and modeling [116], superposition methods for long-term creep predictions considering environmental effects [117-119], and creep rupture behavior and predictions [120, 121]. The studies related to creep behavior and modeling of short fiber reinforced polymer composites (SFRPCs) at elevated temperatures were summarized in chapter 2. Time-temperature-stress superposition (TTSS) procedure has been used for extending short-term creep data for long-term creep predictions. Empirical power law models have been widely used to represent non-linear creep strain curves for a wide range of temperatures and stress levels. Prevailing creep damage is crazing perpendicular to the stress direction where crazes start mainly at the fiber/matrix interface independent of the interface quality.

Seltzer et al. [122], studied creep behavior of injection molded polyamide-6 organoclay nanocomposite using dynamic mechanical analysis (DMA) in the cantilever-bending mode. Specimens were conditioned by immersion in 70 °C water to reach the saturation condition. It was observed that adding organoclay increased both initial creep and time-dependent creep resistant due to constraining effect on the movement of polymer matrix chains. However, addition of organoclay above 3.3 volume% did not further improved the creep resistant. This was attributed to the modification of the polyamide-6 morphology in the nano-scale.

5.2 Creep Properties

Creep tests began with a loading ramp between 1 to 5 seconds. Short-term tests lasted on the order of about one hour to three days. A limited number of longer time creep tests (up to about 40 days) were also conducted for PP-G. Two repeat tests were conducted for most of the conditions. Creep strain during the test and time to rupture were measured for each test. A summary of creep tests and properties for duplicate tests for each material at different temperatures is listed in Table 5-1. These include time to rupture (t_R), minimum creep rate (MCR), instantaneous strain (ε_0), rupture strain (ε_R), and elastic modulus (E) for the startup ramp. Creep properties and their definitions are shown in Figure 5-1.

5.3 Creep Rupture Data and Modeling

Stress versus time to rupture data for the materials at different temperatures are plotted in Figure 5-2. Tests that did not fail (run-outs) are not included in the fits, however, the data points are shown in the plots. A significant effect of temperature is observed for all the materials, as expected. To be able to compare the creep rupture behavior of the materials together, stress versus time to rupture data in Figure 5-3 are normalized with the corresponding ultimate tensile strength, S_u, obtained from tension tests conducted at a displacement rate of 1 mm/min. The data for PO, PP, PP-T, and PP-G are shown in Figure 5-3(a), while the data for PA66/B, PPE/PS, PBT, and PA6 are shown in Figure 5-3(b). The second group of materials are more creep resistant than the first group, and the T_g of the second group is also higher than the first group. PO, PP, PP-T, and PP-G data at 23 °C are correlated very well by normalizing with tensile strength. Normalizing with tensile strength also correlates all the creep rupture data of the second group very well, except for PPE/PS data at 85 °C (see Figure 5-3(b)).

T_g and T_m of PO are lower than those of PP, PP-T, and PP-G, therefore, more temperature sensitivity in creep rupture behavior of PO is expected. The mechanism of creep damage of polypropylene, which is mainly due to the crazes perpendicular to the stress direction, remains unchanged in the presence of reinforcement. PPE/PS has an amorphous matrix, while PA66/B, PBT, and PA6 have a semi-crystalline matrix. Also, percent weight of short glass fiber reinforcement for PPE/PS is lower, as compared to the other SFRPCs, therefore, creep rupture behavior of PPE/PS is more temperature dependent. A craze type failure was observed for PPE/PS specimens, while no evidence of crazing even at elevated temperatures was observed for PA66/B, PBT, and PA6.

A power fit was utilized to represent the creep rupture experimental data in the form of:

$$S = A(t_R)^B \tag{5.1}$$

where S is the applied stress level, t_R is the time to rupture in hours, A is the intercept at t_R = 1, and B is the slope of the fitted line. A and B are temperature and orientation dependent constants and their values for all the materials at different temperatures are reported in Table 5-2. Correlations of A and B values with S_u are shown in Figure 5-4 and expressed by the following equations:

$$A = 0.85 S_u \qquad \text{with } R^2 = 0.99 \tag{5.2}$$

$$B = -0.44(S_u)^{-0.66} \qquad \text{with } R^2 = 0.8 \tag{5.3}$$

These correlations can be used to estimate creep rupture properties of thermoplastics and thermoplastic composites at different temperatures and in different mold flow directions.

Different correlative parameters based on the Arrhenius rate equation [123] which relate temperature and time to rupture together have been developed over the years. Larson-

Miller [124], Manson-Haferd [125], Sherby-Dorn [126], Manson-Succop [127], and Manson- Muralidharan [128] are some of these parameters. Larson-Miller Parameter (LMP) has become the most widely used because of its simplicity. Comparison of correlations with different parameters did not show considerable differences based on the experimental data in this study. This parameter is expressed in the following form:

$$\mathrm{LMP} = \frac{(T + 273)\,(\log t_R + C_{LMP})}{1000} \tag{5.4}$$

where T is the temperature in °C, t_R is time to rupture in hours, and C_{LMP} is a constant. C_{LMP} value was determined by fitting a line to log t_R versus $1/T$ data for a given material and stress level. Intersection of the lines for different stress levels at $1/T = 0$ defines the value of constant C_{LMP}.

Larson-Miller master curves for all the materials are shown in Figure 5-5. As can be seen, the correlations are very good. The power law fit is used to represent master curves in the following form:

$$S = G\,(\mathrm{LMP})^{H} \tag{5.5}$$

where S is stress in MPa, and G and H are material constants which are listed in Table 5-3. The Larson-Miller creep parameter can be used for long-term creep-rupture predictions at different temperatures, provided that stress should be in the range of test stresses [129].

5.4 Creep Strain-Time Behavior and Predictions

Creep strain versus time curves for PP-T, PP-G, PA66/B, and PPE/PS at 85 °C are shown in Figure 5-6. As can be seen, creep strain increases by increasing stress level as expected. Comparison of creep strain versus time curves at 85 °C in the transverse direction at several stress levels are shown in Figure 5-7. For PO, PP, PP-T and PP-G the third stage of creep is an important portion of the creep curve (see Figure 5-7(a)), while for the other materials it is a small portion of the creep curve (see Figure 5-7(b)). Creep strain of PA6 is considerably higher than PA66/B, PPE/PS, and PBT (see Figure 5-7(b)), due to the effect of elastomer additive (10 %wt).

An increase in temperature results in higher macromolecular mobility, therefore, higher creep deformation for all the materials, as expected. An example of this is shown in Figure 5-8(a) for PP-G at a stress level of 75% of S_u. Creep curves of PP-T and PP-G are similar at both 23 °C and 85 °C, as shown in Figure 5-8(b). This indicates that the type of reinforcement (talc or short glass fiber) has the same effect on creep deformation of polypropylene, similar to that observed for creep rupture behavior. Reinforcement or filler does not change the creep mechanism and only results in improved creep strength (i.e. reduction of both creep strain and rate), as compared to the neat polymer [130].

Several empirical power law models have been proposed to describe the non-linear creep deformation behavior of polymeric materials. Some of these models were reviewed in [52] and [131]. The power law models have evolved over the years in order to be applicable to a wider range of temperatures, stress levels, and polymeric materials [49, 50, 53]. The Findley power law model [44] has become a widely used model for describing creep deformation of polymers and their composites and is given by:

$$\varepsilon_c = \varepsilon_0 + mt^n \tag{5.6}$$

where ε_c is creep strain, n is a temperature dependent material constant, and m is both stress and temperature dependent constant. m is the intercept and n is the slope of the fitted line in the log-log plot of (ε_c- ε_0) versus time. n values are reported in Table 5-2 for different temperatures with t and ε_c in hour and %, respectively. n is nearly constant for PP, independent of temperature, but for talc-filled and short glass fiber reinforced materials, larger variation with temperature is observed. Temperature independency of *n* for neat polymers [43, 132] and temperature dependency for filled and reinforced polymers [133] have also been reported in the literature.

Values of ε_0 can be estimated using Remberg-Osgood equation, which was used in previouse chapter to model the tensile stress-strain behavior of the studied materials. In order to find the variation of constant *m* with stress, the following equation, which was suggested by Hadid et al. [131], was used:

$$m = a\,S^b \tag{5.7}$$

where *a* and *b* are material constants and their values are reported in Table 5-2.

Predictive creep curves using Equations 5.6 and 5.7 for PP-G at different temperatures are presented in Figure 5-9. It can be seen that the Findley model is reasonably accurate in representing the short-term creep strain curves of PP-G. Similar predictions were observed for other materials at different stress levels and temperatures.

5.5 Minimum Creep Rate Data and Correlations

Minimum creep rate, $\dot{\varepsilon}_{\min}$, is the slope of the portion of creep vs. time diagram corresponding to secondary creep and is an important parameter widely used for creep design of many components. Norton power law [134, 135] is used to relate minimum creep rate to stress as:

$$\dot{\varepsilon}_{\min} = C\,(S)^D \tag{5.8}$$

where *C* and *D* are material, temperature, and orientation dependent constants, with values reported in Table 5-2 with *S* and $\dot{\varepsilon}_{\min}$ in MPa and %/hours, respectively. Figure 5-10 shows

$\dot{\varepsilon}_{\min}$ versus stress data and the corresponding Norton power law fits at different temperatures for all the materials in log-log plots. As can be seen, $\dot{\varepsilon}_{\min}$ increases with increasing temperature and stress level for all the materials. Minimum creep rate versus normalized stress using S_u data are shown in Figure 5-11. The data for PO, PP, PP-T, and PP-G are shown in Figure 5-11(a), while the data for PA66/B, PPE/PS, PBT and PA6, are shown in Figure 5-11(b). Similar to what was observed for creep rupture data (Figure 5-3), PO, PP, PP-T, and PP-G data at 23 °C are correlated very well by normalizing with tensile strength. Also, normalizing with tensile strength correlates all the minimum creep rate data of the second group very well, except for PPE/PS data at 85 °C (see Figure 5-11(b)).

PA66/B, PPE/PS, PBT, and PA6 exhibit small primary and tertiary creep stages and the secondary creep stage is the main part of the creep strain curve, particularly for tests conducted at lower stress levels. Therefore, for these conditions creep strain can be estimated with a linear line with its slope and intercept to be $\dot{\varepsilon}_{\min}$ and ε_0, respectively, where ε_0 can be estimated using Ramberg-Osgood relation, explained earlier.

The Monkman-Grant relationship [136] has been widely applied to metallic materials. It relates time to rupture, t_R, to the minimum or secondary creep rate, $\dot{\varepsilon}_{\min}$, given by:

$$\dot{\varepsilon}_{\min}^{\lambda} t_R = \eta \tag{5.9}$$

where λ and η are material constants with their values reported in Table 5-3 for all the materials, with t_R and $\dot{\varepsilon}_{\min}$ in hours and %/hours, respectively. The correlations of PP-G data at 23 °C, 85 °C, and 120 °C using this relationship is shown in Figure 5-12(a).

As can be seen, the correlation are reasonable and similarly good correlations were obtained for the other studied materials. λ and η were found to be fiber orientation independent for PBT. Correlations of all data using a single fit by Monkman-Grant relationship is shown in Figure 5-13(a), expressed as:

$$\dot{\varepsilon}_{\min}^{0.86} t_R = 2.65 \qquad \text{with } R^2 = 0.78 \tag{5.10}$$

A modified version of Monkman-Grant relation was suggested by Dobes and Milicka [137] which also includes strain at rupture, ε_R, in the correlations. This model is suitable for materials exhibiting small secondary creep and large tertiary creep stage and is represented by the following form:

$$\dot{\varepsilon}_{\min}^{\lambda'} (t_R / \varepsilon_R) = \eta' \tag{5.11}$$

where the material constants λ' and η' are reported in Table 5-3 with t_R and $\dot{\varepsilon}_{\min}$ in hours and %/hours, respectively. As mentioned earlier, a significant portion of creep curves of PO, PP, PP-T, and PP-G is in the third stage of creep and strain at rupture cannot be obtained using minimum creep rate predictions (Equation 5.9), therefore, Equation 5.11 is valuable when strain at rupture is needed for these materials.

As can be seen in Figure 5-12(b), correlations of data using the modified Monkman-Grant relation is very good for PP-G and similar good correlations was also obtained for PO, PP, and PP-T. λ' is suggested to be unity for most metallic materials [138]. For PO, PP, and PP-G, λ' values are near to unity and is 0.68 for PP-T. A single fit using Equation 5.11 for PO, PP, PP-T, and PP-G is shown in Figure 5-13(b), expressed by:

$$\dot{\varepsilon}_{\min}^{0.89} (t_R / \varepsilon_R) = 0.41 \qquad \text{with } R^2 = 0.92 \tag{5.12}$$

5.6 Long-Term Creep Tests and Predictions

5.6.1 Time-stress superposition principle for long-term creep predictions

Creep tests usually take a long time and are tedious and expensive to conduct, therefore, predictive methods for long-term creep properties based on short-term data are of great interest. Accelerated or short-term tests can be conducted at elevated temperatures or under higher stress levels. Time-temperature superposition (TTS) is a well-known procedure frequently applied either to determine the temperature dependence of the viscoelastic behavior of polymeric materials, or to expand the time regime at a given temperature at which the material behavior is studied from a reference condition. This procedure is developed for prediction of linear viscoelastic properties of homogeneous polymers and may not be accurate when applied to semi-crystalline polymers [131]. In addition, the change of temperature causes a variation of the volume of the material, and consequently material density change. Due to these limitations, applying this method to experimental data of thermoplastic composites may result in inaccurate predictions.

In an analogous manner to the TTS procedure, a time-stress superposition (TSS) approach has been developed which is used for prediction of viscoelastic properties at lower stress levels (long-term creep) from shifting the resultant data at higher stress levels (short-term creep) at a constant temperature. This method was been applied successfully for thermoplastic and their composites [139, 140] and is expressed in the following form for creep strain:

$$\varepsilon(S_1, t) = \varepsilon(S_2, \frac{t}{\varphi_S}) \tag{5.13}$$

where S_1 and S_2 are applied stresses and φ_S is the stress shift factor. This method was successfully applied to creep strain data of PO, PP, PP-T, and PP-G at 23 °C and 85 °C, while the shifting method was not successful at 120 °C for PP-G and 125 °C for PO and PP. Therefore, it appears that there is a temperature limit for TSS principle, like the limit for Williams-Landel-Ferry (WLF) equation which is used to relate temperature shifting factor to temperature in TTS, and is valid for the temperature range between T_g and T_g+100 °C [141].

The creep master curve and corresponding shift factors were obtained by shifting the short-time (about an hour) creep strain curves along the time axis with respect to the reference curve at each stress level and each temperature. The TSS procedure is shown in Figure 5-14(a) for PP-G at 85 °C for a reference stress of 11 MPa. The master curves and corresponding shift factors versus stress in a log-log plot are shown in Figures 5-14(b) and (c) for PP-G at 23 °C and 85 °C. A line was fitted to shift factors versus stress data in a log-log plot, the same as that in the study of Hadid et al. [131].

As mentioned earlier, only the first one hour data of creep strain curves were used to generate the master curves and shift factors. It can be seen from Figures 5-14(d) and (e) that the prediction of creep strain curves using TSS are very good and better than the Findley model (see Figure 5-9) for PP-G at 23 °C and 85 °C for different stress levels. Similar good predictions were obtained for PO, PP, and PP-T. The creep strain master curves for PO and PP-T at 23 °C and 85 °C and for PP at 23 °C and the corresponding shift factors versus normalized stress with S_u data are shown in Figure 5-15. It can be seen that the shift factor versus normalized stress data are correlated at 23 °C for PO, PP, PP-T, and PP-G. At 85 °C, however, PO data are not correlated with PP-T and PP-G.

Obtained time to rupture of the master curve at the reference stress levels can be shifted using shift factors at each stress level to predict time to ruptures at other stress levels. As can be seen in Figure 5-16, nearly all the data predicted using this procedure are within a factor of 2 of experimental data, indicating the capability of TSS method in prediction of creep rupture data.

5.6.2 Experimental results versus predictions

To evaluate the applicability of predictive models for long time creep condition, which is of interest in real applications, a limited number of long-term (up to 40 days) creep tests were conducted for PP-G at 23 °C. As shown in Figure 5-17(a), 10 days and 40 days creep rupture data of PP-G at 23 °C are consistent with the extrapolated creep rupture curve fitted to short-term creep test data. The Larson-Miller model (Equations 5.4 and 5.5) predicts the time to ruptures at 23 °C for PP-G to be 197 and 720 hours for the stress levels of 25.5 and 23 MPa, respectively. As compared with the experimental time to rupture of 273 and 1304 hours, the predictions are within a factor of less than two. The predicted time to rupture data for the two stress levels using TSS included in Figure 5-16, indicates that predictions for long-term tests are also in the scatter band of two.

The TSS method developed using the first one hour creep strain curves of short-term tests not only can predict the creep strain of the rests of those tests, but can also be used for predictions at other stress levels. As can be seen in Figure 5-17(b), the creep strain predictions for long-term tests are very good for both stress levels of 25.5 and 23 MPa. For long-term creep predictions, Findley [142] suggested that the constants of the power law model can be obtained from the early creep strain data. The Findley power law predictions were not as good as those based on TSS, however.

The calculated minimum creep rate of long-term tests from experimental data are 0.011 and 0.0021 %/hour for tests conducted under stress levels of 25.5 and 23 MPa, respectively. Predicted minimum creep rate values from Equation 5.9 are 0.014 and 0.0037 %/hour and from Equation 5.11 are 0.015 and 0.0013 for tests conducted under stress levels of 25.5 and 23 MPa, respectively. Comparisons between experimental and predictive minimum creep rate values show that the minimum creep rate correlations based on short-term creep data give acceptable predictions for long-term tests.

As thermal and hygrothermal aging affect the mechanical behavior of some polymers and polymer composites in a beneficial or a detrimental way [4], they can cause error for long-term creep predictions based on short-term creep data. To overcome this issue, short-term creep tests can be conducted on already aged specimens or aging effects can be incorporated in the generated TSS master curves by additionally shifting the curves according to specimen aging times [118, 119].

Table 5-1: Summary of creep tests results of PP-T, PP-G, PA66/B, and PPE/PS.

Temp. (°C)	**Stress (MPa)**	S/S_u	**Time to Rupture (Hrs)**	**MCR (% / Hrs)**	ε_0 **(%)**	ε_R **(%)**	E **(MPa)**	**Failure Location**
PP-T								
23	23.5	0.80	0.69	3.24	0.64	5.07	5167	OGIT
23	22	0.75	3.57	0.49	0.54	7.07	4867	IGIT
23	22	0.75	3.32	0.58	0.52	8.50	4800	OGIT
23	20	0.68	13.5	0.23	0.47	-	4800	IGIT
23	20	0.68	20.1	0.15	0.48	-	4867	OGIT
23	19	0.65	53.5	0.06	0.39	-	4933	IGIT
23	18.5	0.63	100	-	0.31	-	4850	N Break
85	9	0.65	1.78	1.15	0.76	13.1	1567	IGIT
85	9	0.65	1.71	1.20	0.73	12.9	1633	OGIT
85	8.5	0.62	4.55	0.40	0.68	15.6	1533	IGIT
85	8.5	0.62	4.97	0.35	0.69	-	1500	IGIT
85	7.8	0.56	24.9	0.07	0.63	-	1567	IGIT
85	7.8	0.56	30.2	0.06	0.6	-	1600	IGIT
85	7.6	0.55	44.1	0.03	0.58	-	1600	IGIT
85	7.4	0.53	112	0.02	0.55	-	1567	OGIT
PP-G								
23	40	0.85	0.26	10.8	1.59	5.95	3567	IGIT
23	37	0.80	1.40	1.80	1.38	5.43	3650	IGIT
23	35	0.75	3.36	-	1.21	-	3833	IGIT
23	35	0.75	3.35	0.72	1.26	5.01	3767	OGIT
23	32	0.68	11.7	0.39	1.11	-	3600	IGIT
23	32	0.68	9.31	0.32	1.21	6.33	3467	IGIT
23	29	0.62	65.9	-	0.81	-	4000	IGIT
23	29	0.62	53.4	0.14	0.99	-	3333	OGIT
85	18	0.80	0.24	35.1	1.43	13.1	1600	OGIT
85	16	0.75	0.84	9.70	1.17	13.1	1667	OGIT
85	13	0.60	6.85	-	1.06	-	1700	IGIT
85	13	0.60	10.4	0.90	0.88	14.1	1633	IGIT
85	12	0.55	19.4	0.47	0.79	-	1700	IGIT
85	12	0.55	19.0	0.36	0.89	-	1700	IGIT
85	11	0.50	47.0	0.11	0.75	-	1700	IGIT
85	11	0.50	39.9	0.14	0.71	-	1733	OGIT
120	9	0.75	1.15	11.3	1.08	17.8	1250	IGIT
120	9	0.75	1.01	14.3	1.04	19.4	1150	IGIT
120	7.5	0.63	5.51	1.19	0.98	15.5	1100	IGIT
120	7.5	0.63	6.58	1.04	0.99	15.1	1100	IGIT
120	6.5	0.55	19.0	0.12	0.83	-	1050	IGIT
120	6.5	0.55	18.3	0.17	0.78	-	1100	OGIT
120	5.5	0.46	72.4	0.02	0.61	-	1100	IGIT
120	5.5	0.46	83.6	-	0.59	-	1180	OGIT

Table 5-1(cont'd): Summary of creep tests results of PP-T, PP-G, PA66/B, and PPE/PS.

Temp. (°C)	**Stress (MPa)**	S/S_u	**Time to Rupture (Hrs)**	**MCR (% / Hrs)**	ε_0 **(%)**	ε_R **(%)**	E **(MPa)**	**Failure Location**
				PA66/B				
23	93	0.89	0.14	-	1.82	-	5833	IGIT
23	93	0.89	2.90	0.37	1.7	4.35	6000	IGIT
23	93	0.89	0.70	1.82	1.79	4.28	5967	OGIT
23	88	0.85	3.60	0.25	1.77	4.57	5833	IGIT
23	88	0.85	7.20	0.16	1.69	-	5933	IGIT
23	84	0.81	38.6	0.10	1.62	-	5933	OGIT
23	84	0.81	26.6	0.12	1.51	-	6033	IGIT
23	78	0.75	75.0	0.08	1.31	-	6067	N Break
85	51	0.87	0.90	1.94	2.48	7.58	3067	IGIT
85	50	0.85	1.80	0.95	2.36	6.87	3167	IGIT
85	50	0.85	4.50	0.25	2.13	5.85	2900	IGIT
85	48	0.82	9.70	-	2.03	-	3067	IGIT
85	48	0.82	15.3	0.18	2.18	-	3067	OGIT
85	47	0.80	25.0	0.16	2.02	-	2967	IGIT
85	47	0.80	32.8	0.10	1.86	-	3067	IGIT
85	46	0.78	74.0	0.08	1.93	-	2900	IGIT
120	40	0.86	0.80	2.70	2.95	8.41	1680	IGIT
120	40	0.86	5.10	0.54	2.54	7.96	1760	IGIT
120	40	0.86	1.42	1.15	2.78	7.37	1800	OGIT
120	37	0.80	22.9	0.28	2.25	-	1760	IGIT
120	37	0.80	5.80	0.31	2.44	7.18	1720	IGIT
120	37	0.80	6.36	0.24	2.43	7.66	1760	OGIT
120	36	0.77	41.0	-	-	-	-	IGIT
120	35	0.75	75.0	-	1.70	-	1920	N Break
				PPE/PS				
23	60	0.85	0.40	0.76	1.48	2.85	4900	OGIT
23	58	0.82	0.90	0.43	1.42	2.70	4700	IGIT
23	56	0.80	3.50	0.20	1.27	2.54	4870	IGIT
23	56	0.80	3.80	0.25	1.25	3.14	4800	IGIT
23	56	0.80	6.40	0.20	1.25	-	4870	IGIT
23	53	0.75	22.3	0.07	1.18	-	4870	OGIT
23	53	0.75	51.0	0.09	1.24	-	4900	IGIT
23	53	0.75	25.7	0.09	1.23	-	4870	OGIT
85	35	0.90	1.30	0.86	0.90	3.11	4170	IGIT
85	35	0.90	1.20	0.75	1.00	2.70	4170	IGIT
85	32	0.82	6.40	0.20	0.84	2.90	4200	IGIT
85	32	0.82	7.50	0.22	0.82	2.89	4100	IGIT
85	30	0.77	17.8	0.04	0.79	-	4270	OGIT
85	30	0.77	27.8	0.04	0.76	-	4100	IGIT
85	28	0.72	83.6	0.05	0.72	-	4070	OGIT
85	28	0.72	98.0	0.06	0.66	-	4000	OGIT

Table 5-2: Material, temperature, and fiber orientation dependent tensile properties and modeling constants.

Material	**Direction**	**Temp. (°C)**	**S_u (MPa)**	**E (MPa)**	**A**	**B**	**C**	**D**	**n**	**a**	**b**
PO	T	23	14.7	2123	11.7	-0.076	4E-15	14.3	0.500	2E-6	6.33
	T	85	4.1	670	2.7	-0.133	4E-5	12.5	0.450	2E-2	6.29
	T	125	2.1	350	1.0	-0.219	2E1	8.6	0.410	2E1	6.89
PP	T	23	22.3	1630	21.8	-0.070	1E-15	12.2	0.400	1E-5	4.50
	T	85	9.5	566	6.8	-0.125	7E-9	10.6	0.420	9E-4	4.69
	T	125	5	282	3.1	-0.205	3E-5	9.8	0.410	1E-1	3.20
PP-T	T	23	29.4	4200	23.3	-0.052	4E-23	16.6	0.438	1E-9	6.73
	T	85	13.7	1550	9.23	-0.051	1E-19	19.9	0.318	1E-5	5.56
PP-G	T	23	46.8	3446	37.3	-0.062	1E-20	12.9	0.375	5E-8	5.00
	T	85	21.7	1516	15.8	-0.094	2E-13	11.4	0.600	8E-9	7.55
	T	120	11.9	966	9.1	-0.116	2E-12	13.3	0.762	1E-8	9.51
PA66/B	T	23	104.7	5250	91.9	-0.026	3E-31	15.4	0.237	1E-11	5.71
	T	85	58.8	2250	51.0	-0.025	5E-52	30.1	0.182	2E-11	6.62
	T	120	46.7	1550	40.0	-0.028	8E-34	20.7	0.206	6E-11	6.82
PPE/PS	T	23	70.8	4400	58.2	-0.027	1E-32	17.9	0.288	2E-15	8.39
	T	85	39.5	4000	35.3	-0.052	5E-20	12.4	0.343	4E-9	5.54
PBT	T	85	35.5	2300	31.2	-0.023	5E-63	41.6	-	-	-
	T	125	26.5	1830	22.0	-0.036	2E-35	25.6	-	-	-
	L	85	64	4600	55.5	-0.017	7E-53	30.0	-	-	-
	L	125	48.5	3380	41.8	-0.023	1E-59	36.3	-	-	-
PA6	T	85	46.5	1800	38.7	-0.049	3E-62	38.4	-	-	-
	T	125	37	1300	32.3	-0.022	3E-53	34.6		-	-

Table 5-3: Material and fiber orientation dependent modeling constants.

Material	**Direction**	C_{LMP}	G	H	λ	η	λ'	η'
PO	T	40	4.92E9	-8.03	0.60	4.0	0.90	0.53
PP	T	31	2.66E7	-6.36	0.92	4.5	1.12	0.46
PP-T	T	42	4.90E6	-4.86	1.00	2.1	0.68	0.27
PP-G	T	26	1.75E6	-5.24	0.83	5.3	0.91	0.50
PA66/B	T	55	3.41E5	-2.95	1.35	1.7	-	-
PPE/PS	T	32	4.07E4	-2.90	1.68	0.4	-	-
PBT	T	50	4.24E5	-3.30	1.00	0.6	-	-
	L	60	2.34E5	-2.72	//	//	-	-
PA6	T	22	1.6E3	-1.80	0.82	1.2	-	-

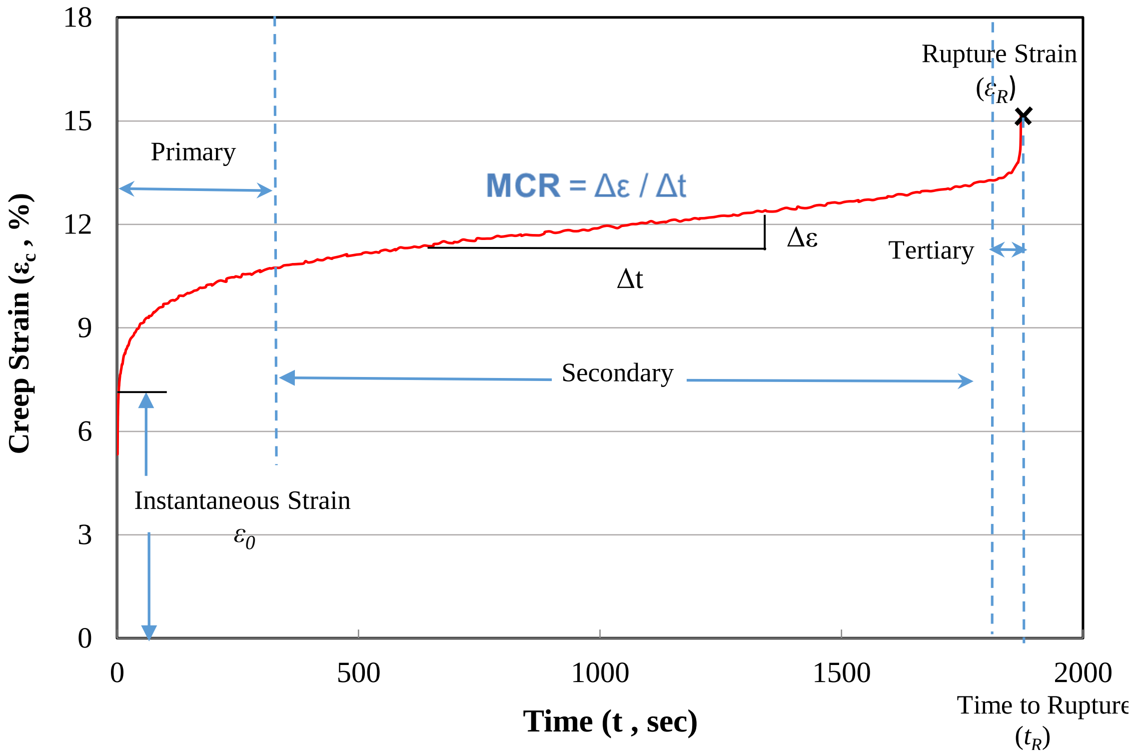

Figure 5-1: Example creep curve showing the three stages of deformation based on the change in strain vs. time.

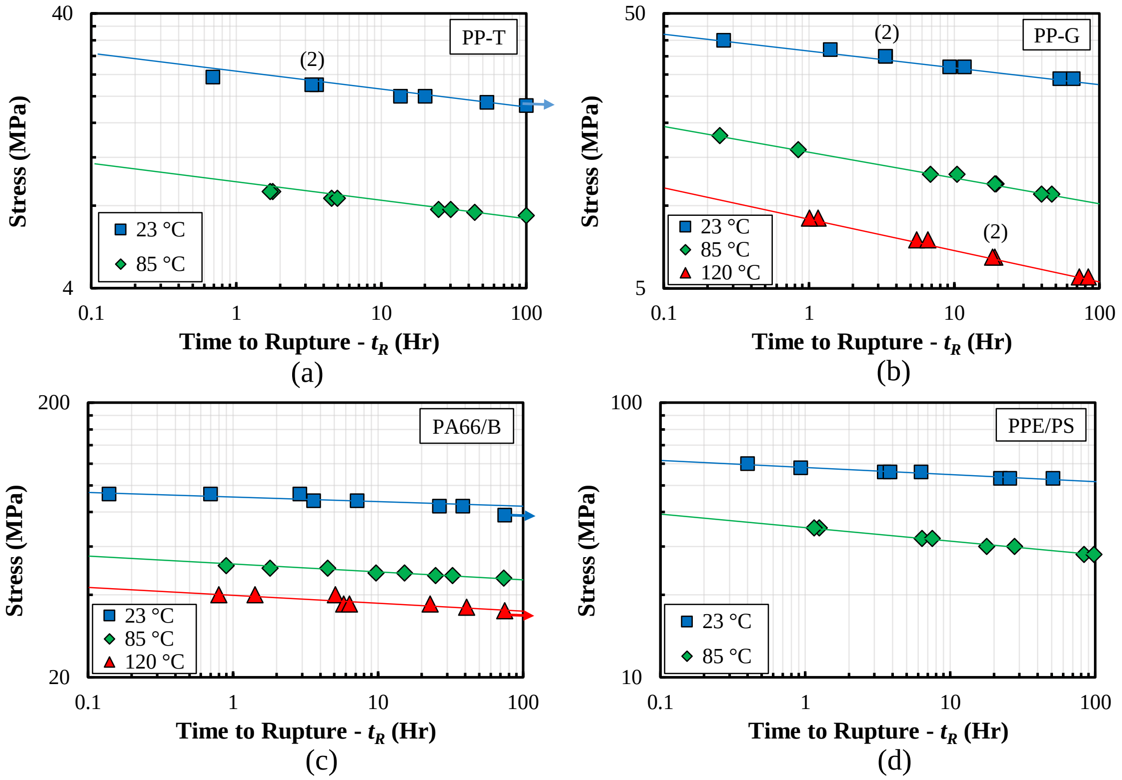

Figure 5-2: Effect of temperature on creep rupture of (a) PP-T, (b) PP-G, (c) PA66/B, and (d) PPE/PS in the transverse direction. Lines are fits to experimental data. Arrows show tests that did not fail and are not included in the fits.

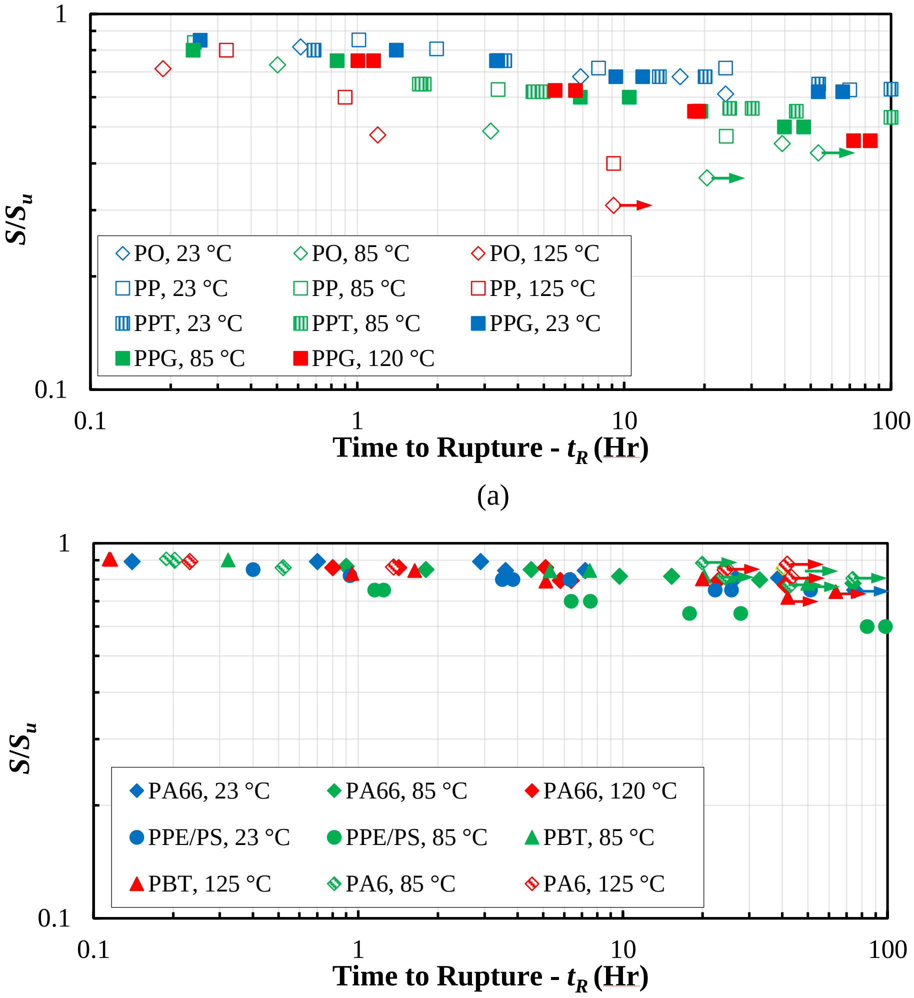

(a)

(b)

Figure 5-3: Normalized creep rupture data with tensile strength for (a) PO, PP, PP-T, and PP-G and, (b) PA66/B, PPE/PS, PBT, and PA6 at different temperatures.

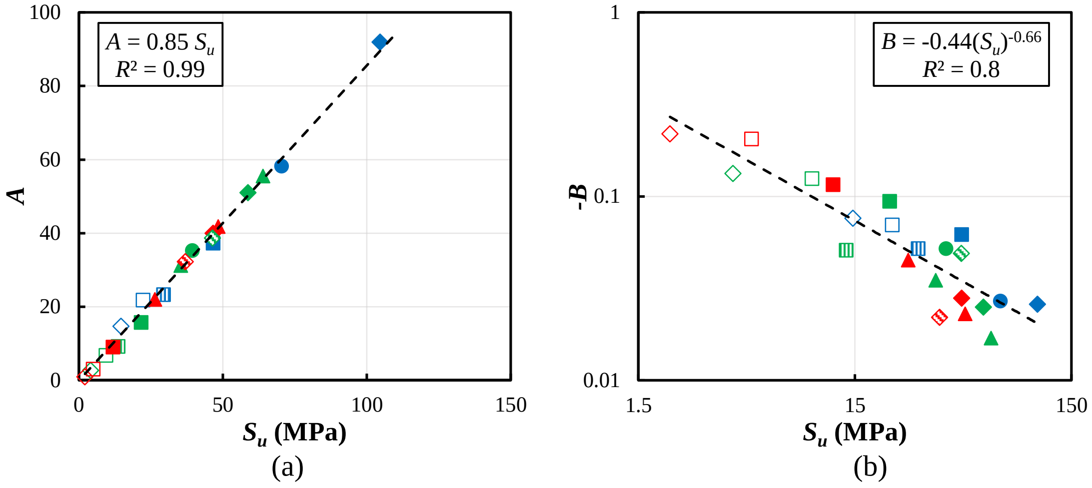

(a) (b)

Figure 5-4: Correlations of (a) A and, (b) B values with S_u for all the materials at different temperatures and fiber orientations. The conditions associated with the symbols are the same as those in Figure 5-3.

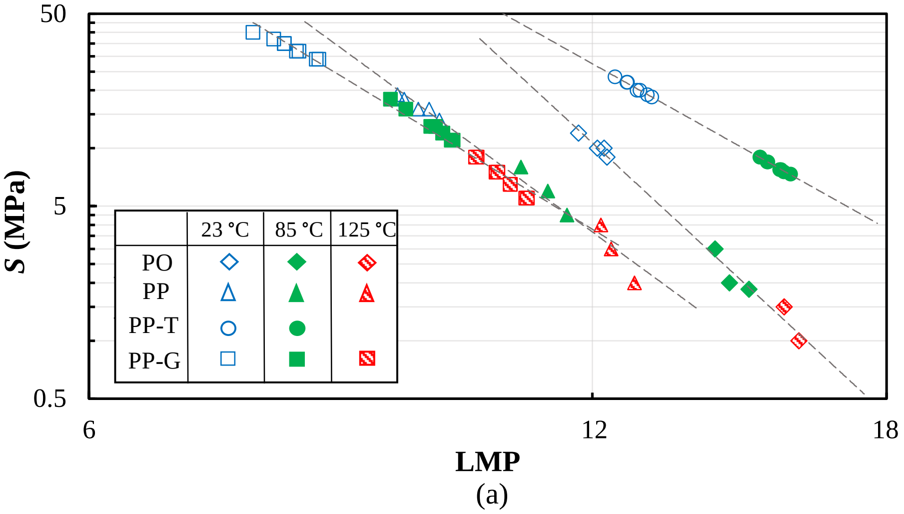

(a)

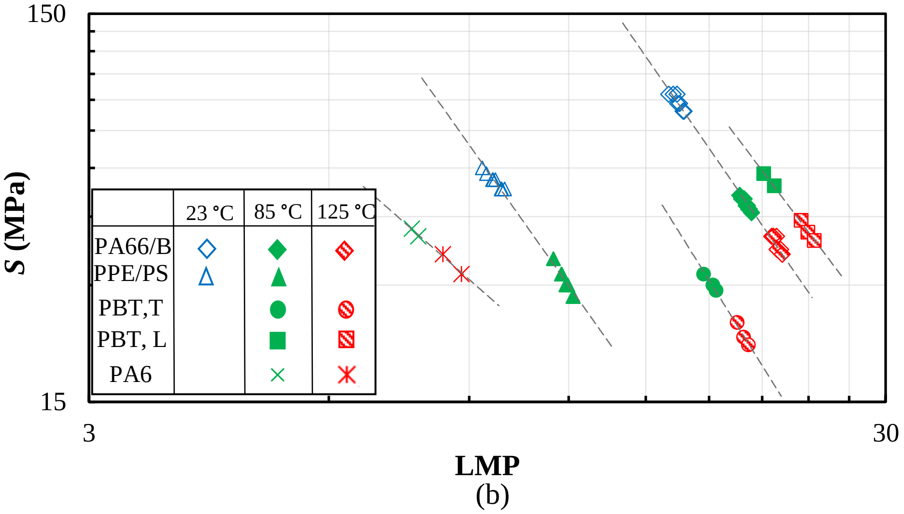

(b)

Figure 5-5: LMP master curves for (a) PO, PP, PP-T, and PP-G in the transverse direction and, (b) PA66/B, PPE/PS, PA6 in the transverse direction and for PBT in both transverse and longitudinal directions.

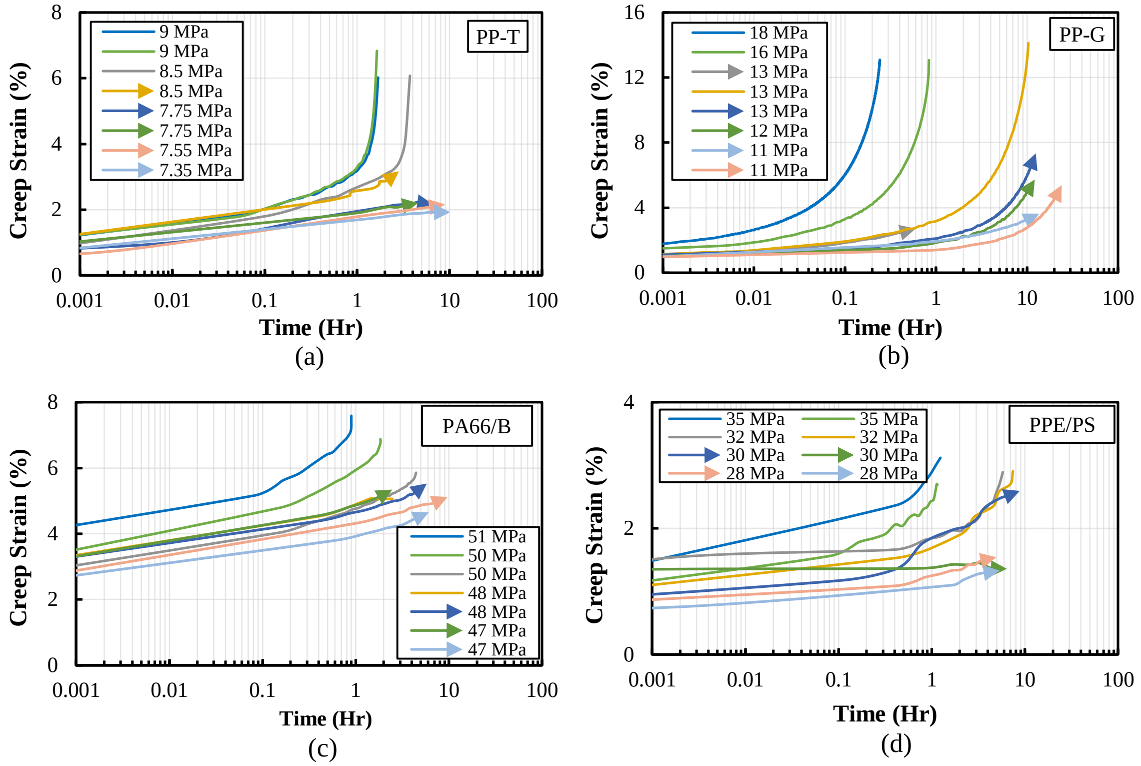

(a) (b) (c) (d)

Figure 5-6: Creep strain versus time curves for (a) PP-T, (b) PP-G, (c) PA66/B, (d) PPE/PS at 85 °C in the transverse direction.

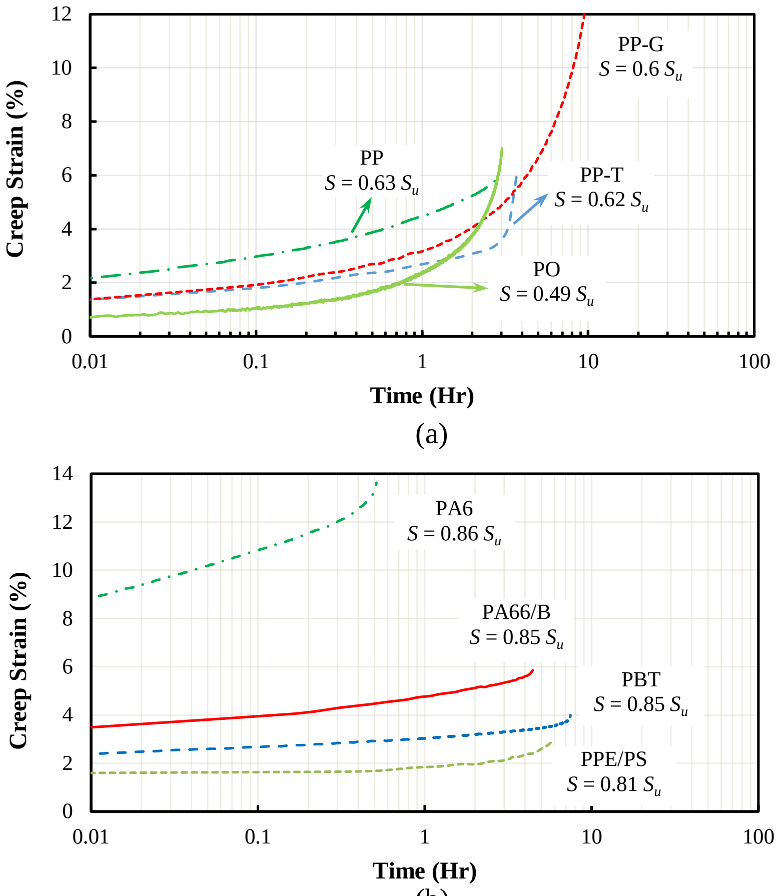

(a)

(b)

Figure 5-7: Creep strain versus time curves at 85 °C for (a) PO, PP, PP-T, and PP-G and for, (b) PA66/B, PPE/PS, PBT, and PA6.

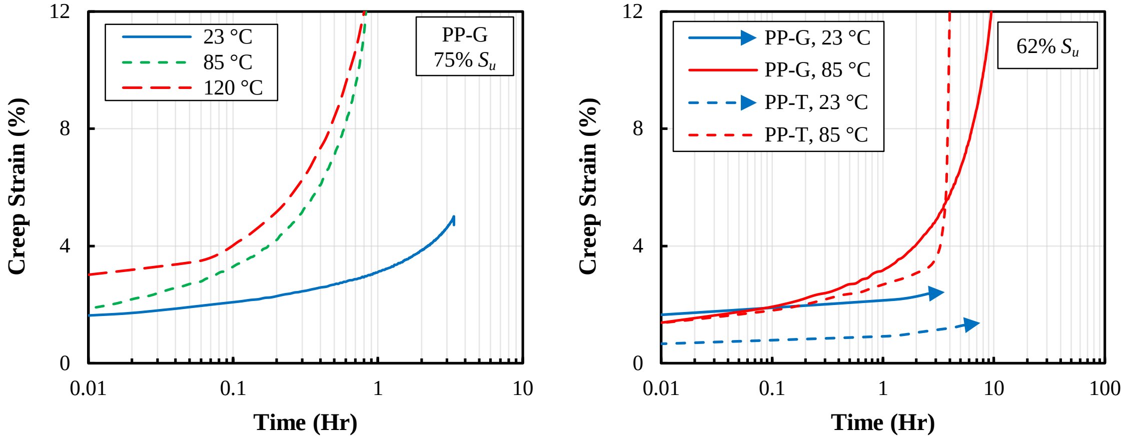

(a) (b)

Figure 5-8: (a) Effect of temperature on creep strain curves of PP-G under stress level of 75% of S_u. (b) Comparison of PP-T and PP-G creep strain curves at 23 °C and 85 °C under stress level of 62% of S_u.

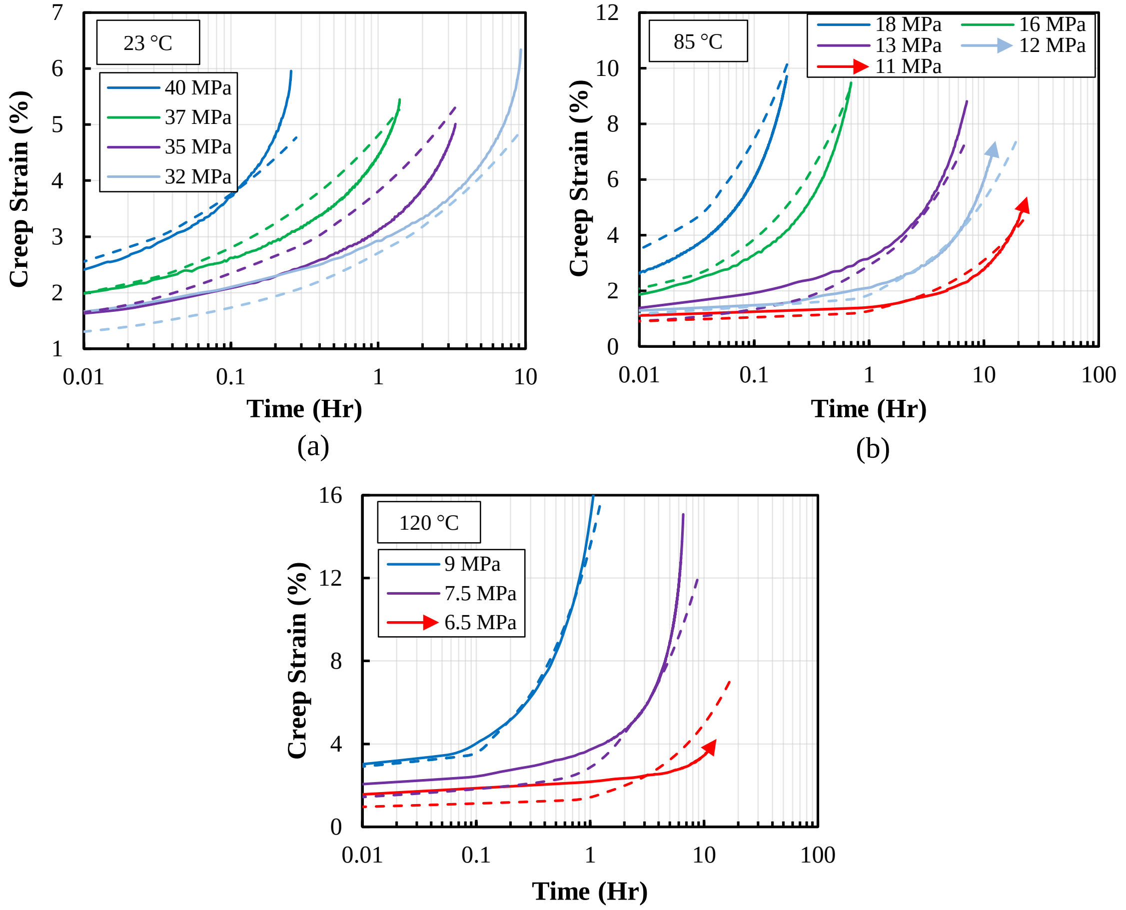

(a)

(b)

(c)

Figure 5-9: Comparison of predicted creep strain curves using Findley power law model (dash lines) with experimental creep strain curves of PP-G at different stress levels in the transverse direction at (a) 23 °C, (b) 85 °C, and (c) 120 °C.

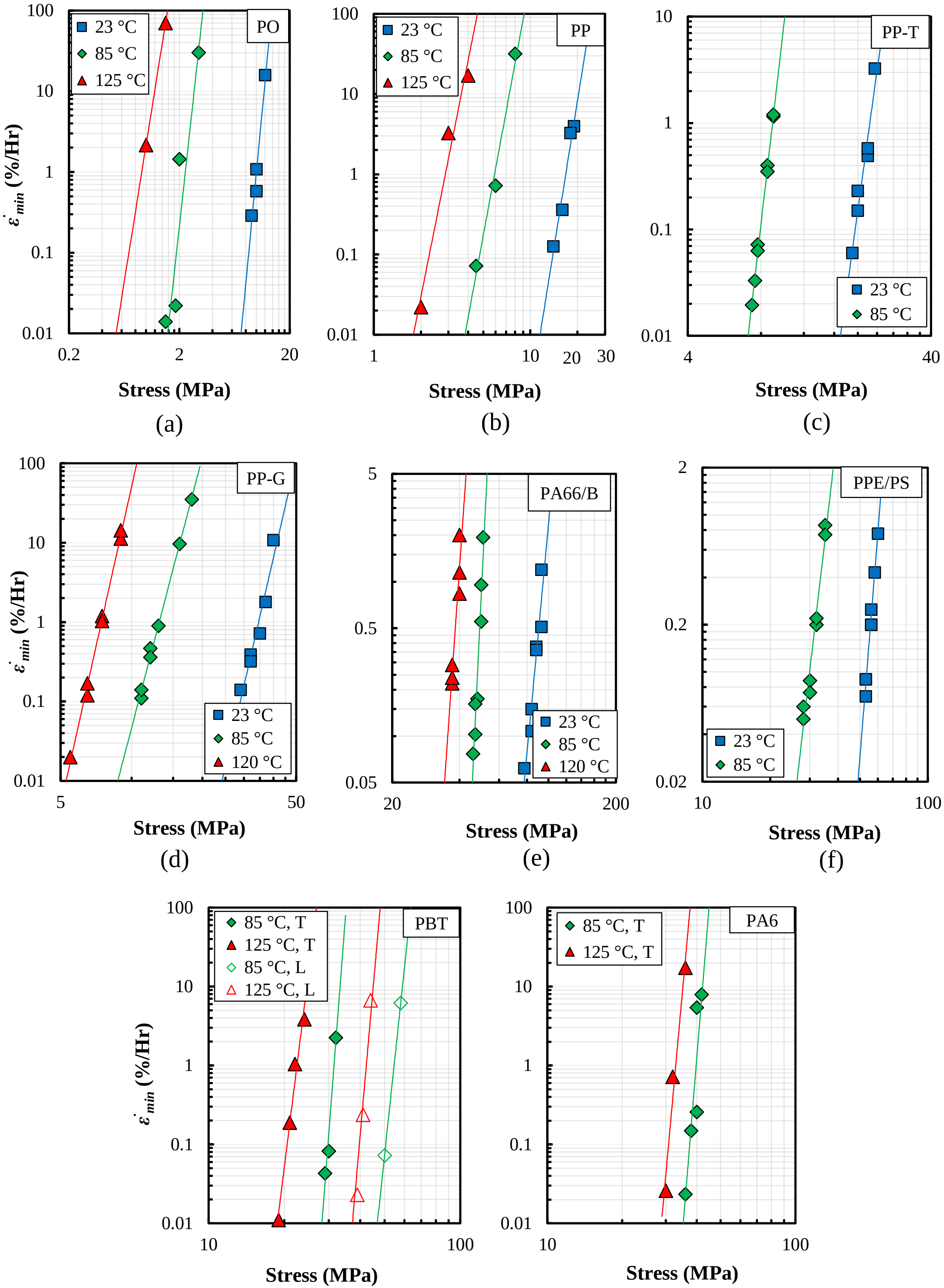

(a) (b) (c)

(d) (e) (f)

(g) (h)

Figure 5-10: Minimum creep rate versus stress data with corresponding power law fits for (a) PO, (b) PP, (c) PP-T, (d) PP-G, (e) PA66/B, (f) PPE/PS, (g) PBT, and (h) PA6.

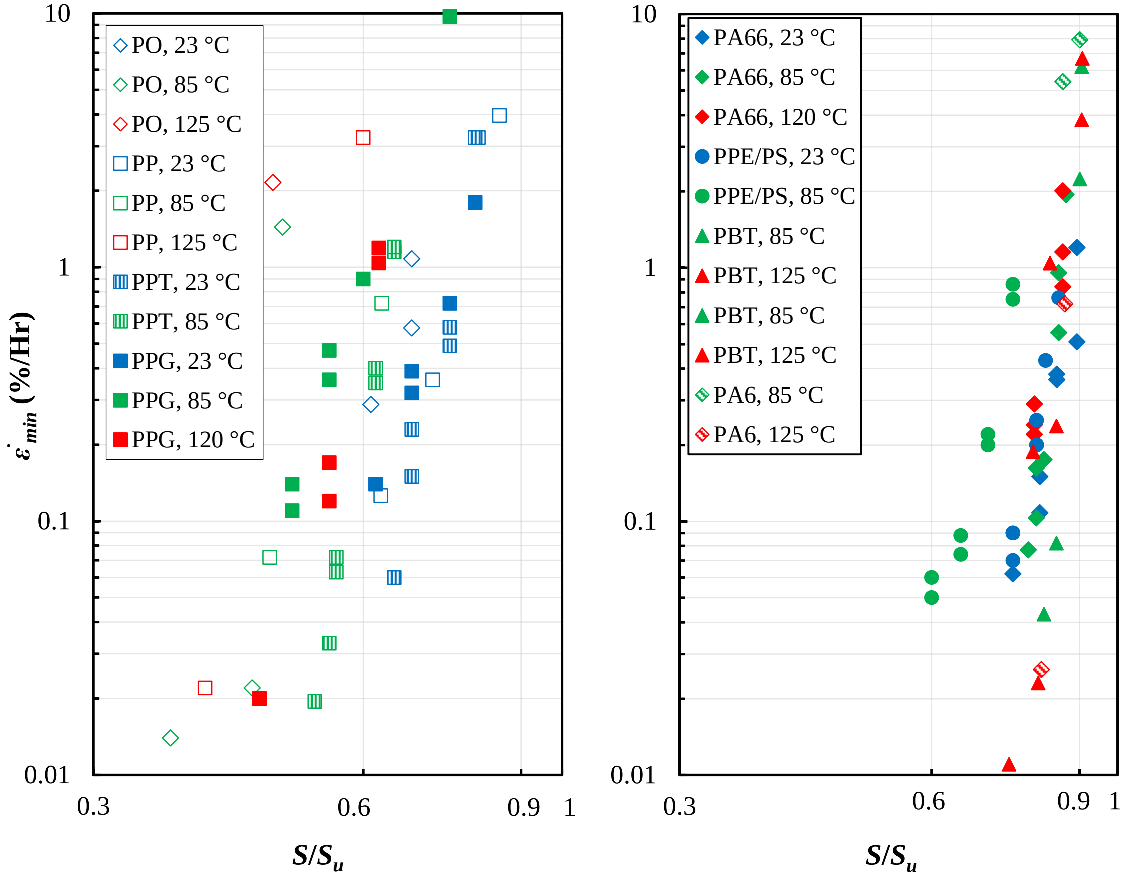

(a) (b)

Figure 5-11: Minimum creep rate versus normalized stress with tensile strength data for (a) PO, PP, PP-T, and PP-G and, (b) PA66/B, PPE/PS, PBT, and PA6 at different temperatures.

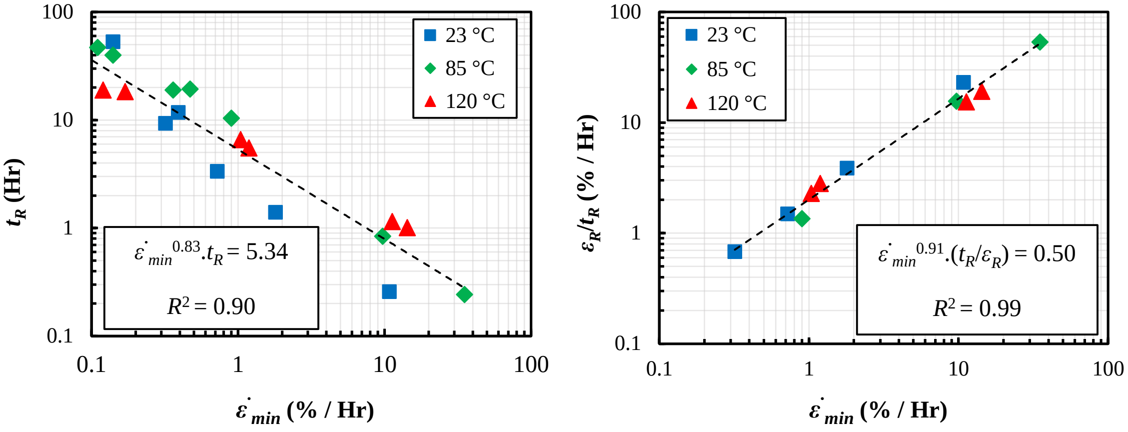

(a)

(b)

Figure 5-12: Correlation of (a) $\dot{\varepsilon}_{\min}$ and t_R using Monkman-Grant relation and (b) $\dot{\varepsilon}_{\min}$, t_R and ε_R using modified Monkman-Grant relation, for PP-G at 23, 85 and 120 °C.

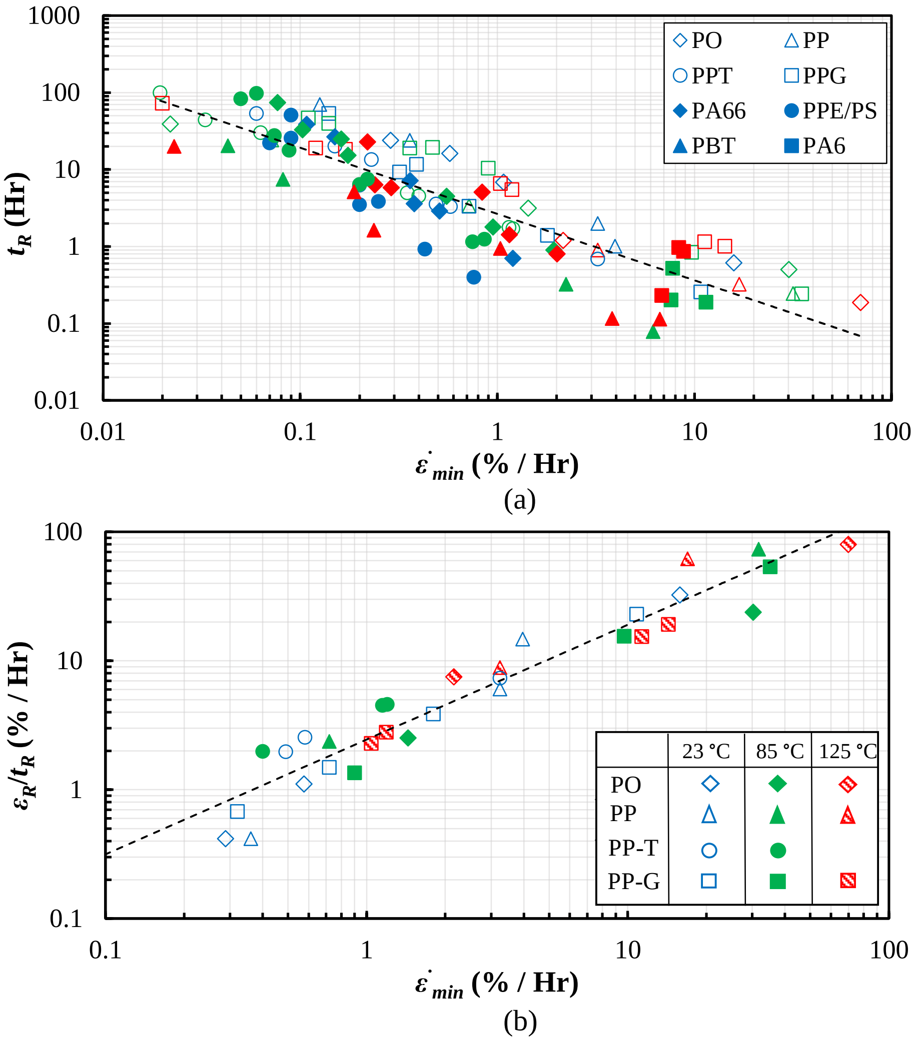

Figure 5-13: Correlation of $\dot{\varepsilon}_{\min}$ and t_R using Monkman-Grant relation for (a) all the studied materials. (b) Correlation of $\dot{\varepsilon}_{\min}$, t_R and ε_R using modified Monkman-Grant relation for PO, PP, PP-T, and PP-G.

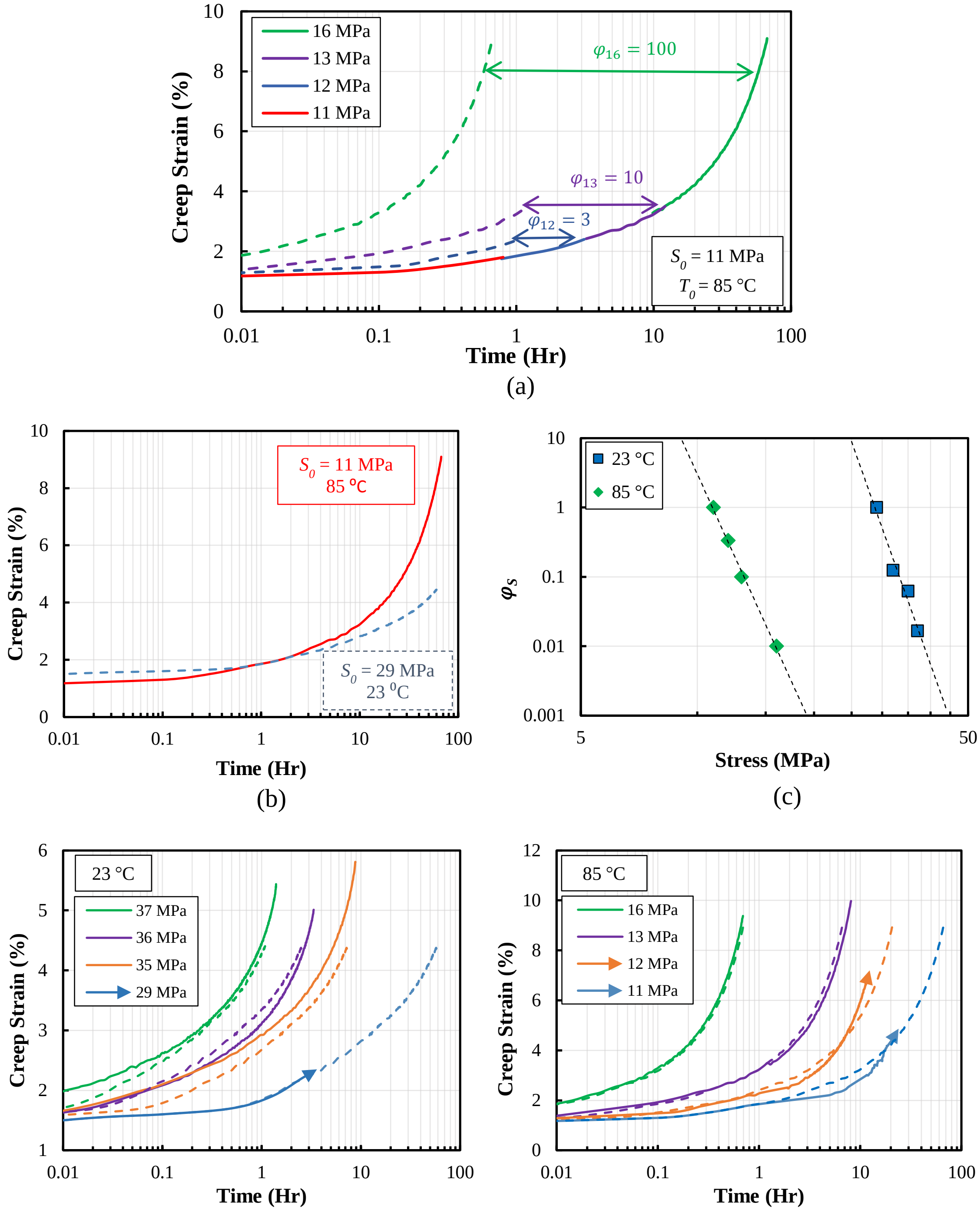

(a)

(b)

(c)

(d)

(e)

Figure 5-14: (a) TSS procedure for generating master curve and shift factors for PP-G at 85 °C. (b) Master curves and (c) corresponding shift factor versus stress plots for PP-G at 23 and 85 °C. Comparison of predictive creep strain (dash lines) using TSS and experimental creep strain curves for PP-G for different stress levels at (d) 23 °C and (e) 85 °C.

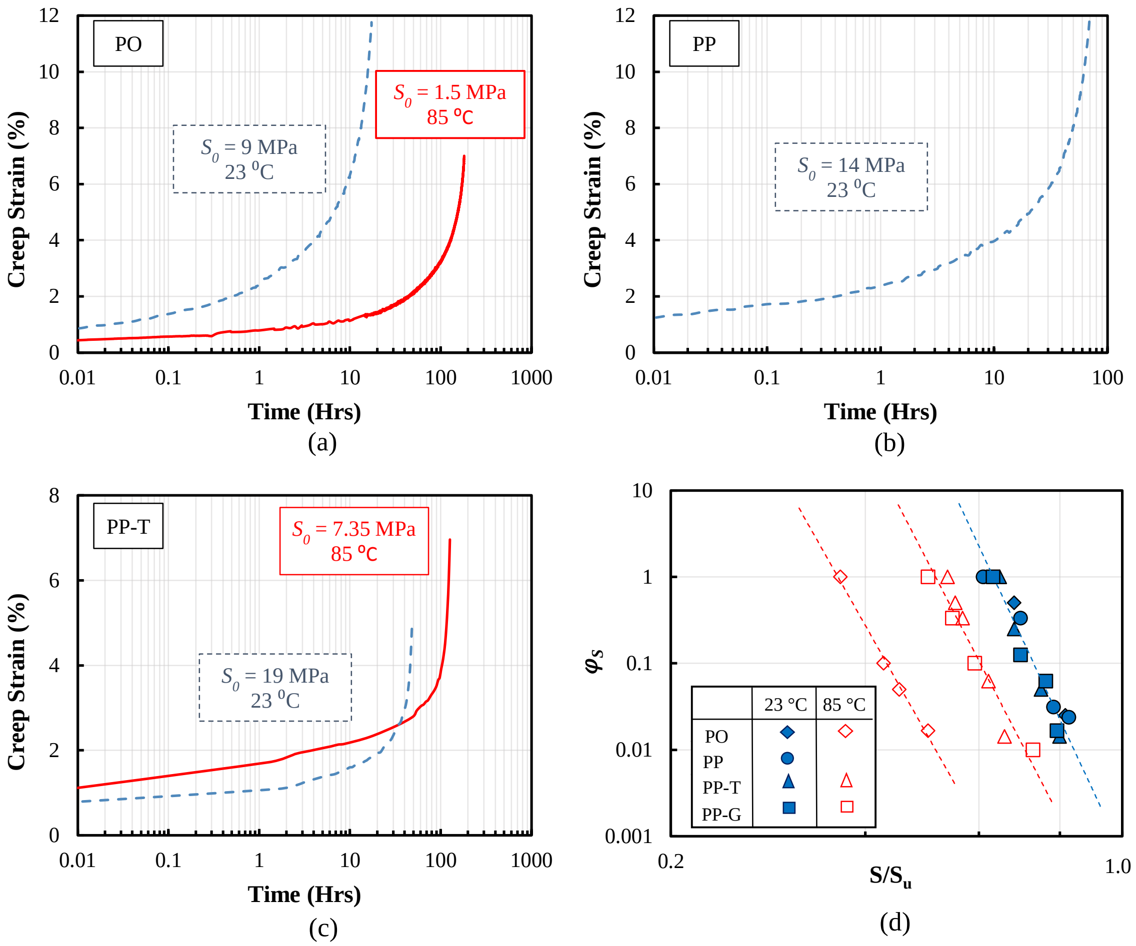

Figure 5-15: Creep strain master curves of (a) PO at 23 °C and 85 °C, (b) PP at 23 °C and, (c) PP-T at 23°C and 85 °C. Normalized plot of shift factor versus stress using S_u for PO, PP, PP-T, and PP-G at 23 °C and 85 °C.

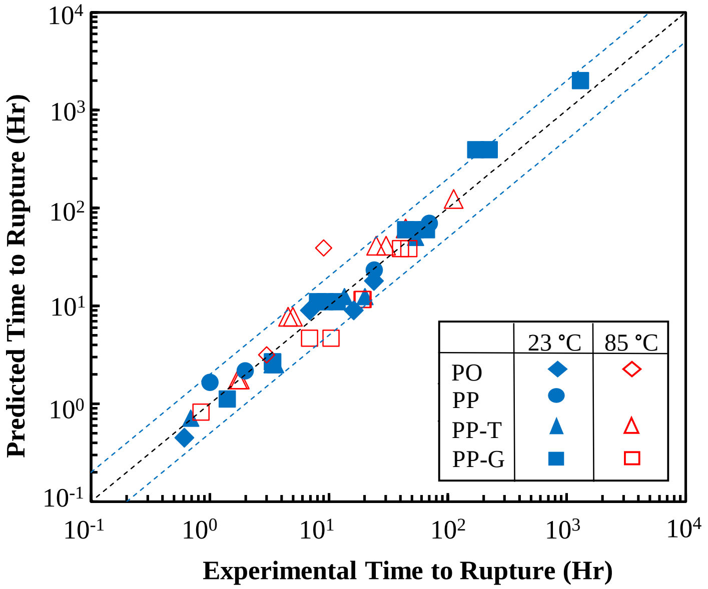

Figure 5-16: Predicted versus experimental time to rupture for PO, PP, PP-T, and PP-G at 23 °C and 85 °C using the TSS technique.

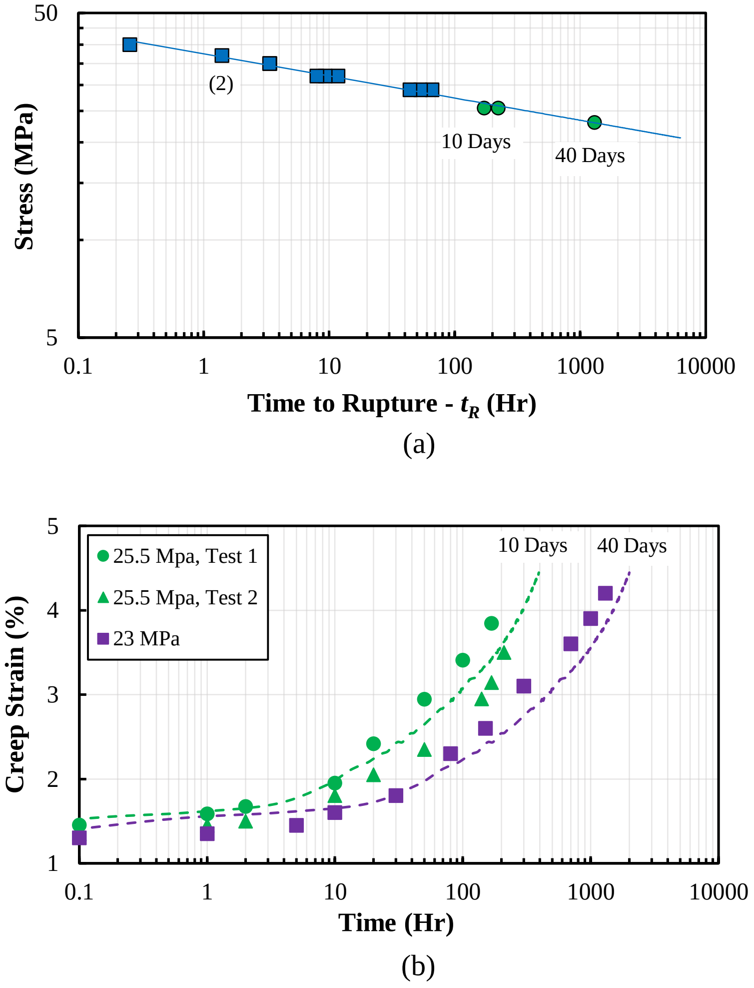

(a)

(b)

Figure 5-17: (a) Long-term (up to 40 days) creep rupture data superimposed on short-term (up to 3 days) creep rupture curve and, (b) comparison of experimental long-term creep strain (data points) and predicted creep strain curve using TSS for PP-G at 23 °C.

Chapter 6

Viscoelastic Deformation and Frequency Effect on Fatigue Behavior

In this chapter viscoelastic behavior as well as the beneficial or strengthening effect of increased frequency on fatigue behavior of PP, PP-T, PP-G, PA66/B, and PPE/PS are investigated. Viscoelastic behavior was characterized from the results of temperature and frequency sweep dynamic mechanical analysis tests. Fatigue tests were performed at 23 and 85 °C for PP and PPE/PS, at 85 °C for PP-T and PA66/B, and at 23, 85 and 120 °C for PP-G. Fatigue tests were conducted with stress ratio of 0.1 for PP, PP-T, PA66/B, and PPE/PS and with stress ratios of 0.1 and 0.3 for PP-G. A limited number of tests under stress ratio of -1 were also performed for PP-G. Scanning electron microscopy was performed on specimen fracture surfaces to study the frequency effect at the microstructural level. Larson-Miller parameter used to correlated experimental fatigue data at different frequencies. Experimental results and analysis presented in this chapter were published in [143].

6.1 Introduction

Structural components made of thermoplastics and their composites are subjected to cyclic loading during their service life, therefore, fatigue performance is an important consideration in their design. Generally, there is a stronger dependence of mechanical properties on time or frequency (in the frequency domain) in polymers and their composites, compared to metals, resulting from the viscoelastic nature of these materials. Their strain rate sensitivity and time-dependent failure under simple tension loading as well as their creep have been studied, for example in [26, 77, 78, 144]. However, the effect of frequency on fatigue behavior of polymers and their composites has been studied far less, in spite of its important consequence in many applications.

Depending on the mode of loading, stress level, material characteristics, and the in-service temperature, frequency affects the cyclic behavior of polymeric materials to various degrees. Self-heating is the major effect of cycling frequency on fatigue behavior of polymers, resulting from viscous energy dissipation and frictional heating. Friction mechanisms between the polymer chains cause dissipation of a part of the total mechanical strain energy. A part of this dissipated energy is converted into heat. Due to low thermal conductivity of polymers, the cumulated heat from continuously applied cycles causes thermal damage, in addition to fatigue damage, which can reduce fatigue life dramatically. Different studies in the literature have evaluated self-heating effects on fatigue behavior of thermoplastics and their composites, including microstructural overview, modeling temperature rise and estimating cyclic life [55, 56, 145-154]. A critical frequency at which frequency results in unstable temperature rise has been obtained from experimental results and relationships have been suggested to estimate the critical frequency for a given stress level. Energy-based models based on hysteresis energy loss and steady state heat conduction have been utilized to calculate temperature rise and correlate experimental fatigue life data.

Another effect of frequency on fatigue behavior of some polymers other than the self-heating effect is known as the beneficial or strengthening effect of frequency. A few studies have considered the beneficial effect of frequency on fatigue behavior of polymers and their composites in terms of crack initiation aspects by using un-notched specimens.

It has been observed that under certain conditions (including the loading type and level, polymer or polymer composite type, and the temperature), fatigue life increases and crack growth rate decreases with increasing frequency. Zhou and Mallick [155, 156] observed the beneficial effect of frequency on fatigue life for 40 wt% talc-filled polypropylene and 33 wt% short glass fiber reinforced polyamide-6.6 under stress ratio or of 0.1. For the talc-filled polypropylene composite, the fatigue life increased with increasing frequency up to 2 Hz at maximum stress levels of 80% and 85% of tensile strength at room temperature. Above 2 Hz fatigue life decreased with increasing frequency because of self-heating but remained constant above 5 Hz to 20 Hz. At high frequencies, the temperature rise was high enough to melt the specimens. The same behavior was also observed for the polyamide-6.6 composite at maximum stress levels of 55% and 70% of tensile strength at room temperature. Fatigue life increased proportionally with frequency up to 2 Hz. Increasing frequency from 0.5 to 2 Hz caused about four times increase in fatigue life at both stress levels. Above 2 Hz, fatigue life decreased continuously up to 20 Hz, because of the self-heating effect and the rate of reduction decreased with increasing frequency.

Shrestha et al. [154] investigated fatigue behavior of polyther ether kerone (PEEK) using fully-reversed strain-controlled fatigue tests at strain amplitudes ranging from 0.02 mm/mm to 0.04 mm/mm at several frequencies. The beneficial effect of frequency on fatigue life was observed at higher stain amplitudes, whereas at a lower strain amplitude of 0.02 mm/mm a minimal frequency effect was observed. For example, at strain amplitude of 0.03 increasing frequency from 0.5 Hz to 1 Hz caused increase in reversals to failure by factor of seven, although temperature rise on the surface of specimen increased from 37 to 66 °C.

In several studies, the beneficial effect of increasing frequency have been observed on fatigue crack propagation (FCP) behavior of polymers. It should be noted that the self-heating for notched or cracked specimens used for FCP investigations becomes less dominant than un-notched specimens with a much bigger highly stressed material volume, therefore, the studied frequencies for FCP investigations can be much higher. Hertzberg et al. [71, 145, 157, 158] studied the beneficial effect of frequency on the FCP rate of different polymers in the frequency range of 0.1 to 100 Hz. It was observed that for poly(methyl methacrylate) (PMMA), polystyrene (PS) and poly(vinyl chloride) (PVC), the FCP rate decreased and fatigue resistance significantly improved with increasing test frequency. On the other hand polycarbonate (PC), polysulfone (PSF), Nylon-6.6, and poly(vinylidene fluoride) (PVF_2) exhibited a slight worsening of FCP behavior with increasing test frequency. It was concluded that the frequency sensitivity is greatest in those polymers that show a high propensity for crazing. Also, the beneficial effect of higher frequency was related to competition between strain rate and creep effects, crack tip blunting because of hysteresis heating, and the role of beta transition in which bending and stretching of primary polymer bonds lead to increased toughness. The frequency sensitivity was stated to be maximum for polymers where the beta transition at test temperature occurs in the range of the experimental test frequency [157]. A higher frequency and, therefore, a higher strain rate causes an increase in modulus and strength. Localized heating due to increased frequency at the crack tip can blunt the crack tip and lower the effective intensity factor and, thus, decreases FCP rate.

Radon and Culver [159, 160] evaluated effect of frequency on FCP behavior of PMMA and PC in the frequency range of 0.1 to 100 Hz and temperature range of -60 to 21 °C. FCP rate of PMMA decreased continuously with increasing frequency, and the reduction was more at higher temperatures. The frequency effect was negligible for PC, compared to PMMA. It was suggested that the beneficial effect of frequency was because of the reduction of loss modulus with increasing test frequency.

The beneficial effect of frequency on FCP behavior of PMMA and polyethylene was also reported by Dumpleton and Bucknall [161], McKenna and Penn [162], and Chou and Sun [163]. Crack growth behavior and failure were related to the duration of loading rather than to load cycling (i.e. a time-dependent rather than a cycle-dependent phenomenon). Some conflicting reports concerning the beneficial effect of frequency also exist in the literature. Wyzgoski et al. [164] observed the beneficial effect of frequency on FCP behavior of neat Nylon-6.6, while no beneficial effect of frequency on FCP behavior of this material was observed in the studies of Sauer and Richardson [165] and Hertzberg et al. [71]. Possible reasons for this discrepancy were explained by Wyzgoski et al. [164] to be the specific frequency range considered and also the thickness effect which could change the FCP behavior from plane stress to plane strain condition.

Pegoretti and Ricco [48, 68-70] investigated the effect of frequency on FCP in polypropylene and short glass fiber reinforced polypropylene composite. A dramatic decrease in the crack growth rate per cycle at any crack length was observed as a result of increasing frequency. By separating total crack growth rate to fatigue and creep crack growth rates, it was concluded that for low frequencies (0.1 and 1 Hz) the crack propagation was governed by viscoelastic creep. However, for high frequency (10 Hz) creep and fatigue crack growth rates became comparable, making about the same contribution to the overall crack growth rate.

The strengthening effect of frequency on fatigue life has also been reported for continuous fiber polymer composites. Mandell and Meier [166] reported a factor of 10 increase in fatigue life of glass epoxy laminates with changing frequency from 0.01 to 1 Hz. Also, Saff [167] observed a decrease in FCP rate and consequently increase in fatigue life of laminated polymer composites with increasing frequency, provided that the increase in temperature was small.

To model the beneficial effect of frequency on fatigue life, Tsai et al. [168] proposed a damage accumulation model to consider time-dependent behavior of graphite/epoxy laminate composites. The model assumes that for testing conditions where different stress levels and test frequencies produce the same strain, the life is constant. Huang et al. [169] evaluated the fatigue life of PMMA at different frequencies based on non-linear incremental damage summation from pure fatigue and pure creep. A fatigue life prediction model based on strength degradation under constant amplitude loading was proposed by Epaarachchi and Clausen [170]. They assumed that for frequency dependent polymers, fatigue damage is time dependent, instead of being cycle dependent. This model was successfully applied to several continuous fiber reinforced polymer composites.

6.2 Viscoelastic Behavior and Characterization

Polymeric materials generally exhibit both viscous and elastic characteristics when subjected to deformation. Unlike purely elastic materials, a viscoelastic material loses energy when a load is applied and then removed. Viscoelastic characteristics of a polymer can be studied by dynamic mechanical analysis (DMA) where a sinusoidal input (stress or strain) is applied, and the resulting output (strain or stress) is measured. The input and output signal will be perfectly in phase for a perfectly elastic solid, while for viscoelastic polymers some phase lag will occur during DMA tests. This phase lag (δ) which is due to the excess time necessary for molecular motions and relaxations to occur, together with the amplitudes of the strain and stress waves, is used to define a variety of basic material parameters. These include storage modulus, loss modulus, and loss tangent (tan δ).

The storage modulus, E', represents the stiffness of a viscoelastic material and is proportional to the energy stored during one cycle. The loss modulus, E'', is defined as being proportional to the non-recoverable energy dissipated during one cycle, such as, energy loss as heat. E' and E'' are expressed as:

$$E' = \frac{\sigma_{\max}}{\varepsilon_{\max}} \cos \delta \tag{6.1}$$

$$E'' = \frac{\sigma_{\max}}{\varepsilon_{\max}} \sin \delta \tag{6.2}$$

where σ_{max} and ε_{max} are the maximum value of cyclic stress and strain, respectively. The damping term, tan δ, is a measure of the ratio of energy dissipated as heat to the maximum amount of energy stored in the material during one cycle, expressed as:

$$\tan \delta = \frac{E''}{E'} \tag{6.3}$$

Variations of storage modulus, loss modulus, and loss tangent with temperature obtained from temperature sweep DMA tests at a constant frequency of 1 Hz with temperature rise of 5 °C/min are shown in Figure 6-1 for PA66/B and PPE/PS. Glass transition temperature, T_g, can be defined as either the intersection of the two tangent lines from the storage modulus as defined by the ASTM D7028 test standard, or the peak of loss tangent and loss modulus [86]. T_g was also obtained from differential scanning calorimetry (DSC) test. The output of DSC test is a plot of the difference of heat delivered to the specimen and to the reference as a function of temperature and transitions appear as a step in the baseline of the recorded DSC signal. T_g values measured for all the materials from either DMA or DSC tests are listed in Table 3-2. T_g of PP-G is 12 °C higher than that of PP-T, indicating fiber reinforcement changes T_g because of a change in crystallinity of the material [72]. T_g of PPE/PS as a fire retardant material is quite high compared to the other materials.

Variation of viscoelastic properties of semi-crystalline polymers with temperature seen for PA66/B and PPE/PS in Figure 6-1 is typical. There is a maximum for both E'' and tan δ and a sudden drop in E' near T_g. Moving from very low temperature where the molecules are tightly compressed to a higher temperature, different transitions are generally observed. The first changes are the solid-state transitions where local motions or bending and stretching of primary bonds are the primary mechanisms that contribute to macroscopic deformations, known as the gamma transition. As the temperature increases, the free volume increases and the localized bond and side chain movements coupled with the bending and stretching of primary bonds lead to larger deformations, where this transition is called the beta transition. As heating continues, the glass transition appears when the chains in the amorphous regions begin to coordinate large scale motions. By increasing the test frequency, the temperature at which each transition occurs increases [171]. For the temperature range considered at frequency of 1 Hz, only glass transition (not beta and gamma transitions) is observed for both PA66/B and PPE/PS, as shown in Figure 6-1.

Variations of viscoelastic properties with frequency at 85 °C obtained from frequency sweep DMA tests for PP, PP-T, PP-G, PA66/B, and PPE/PS are shown in Figure 6-2. A slight increase in storage modulus with increasing frequency was observed for all the materials. tan δ decreased with increasing frequency for PP, PP-T, PP-G, and PPE/PS and the reduction was quite high for polypropylene-based materials. The damping factor was almost constant for PA66/B with increasing frequency.

6.3 Frequency Effect

6.3.1 Experimental results

Frequency effect tests were conducted for the polymeric materials investigated at different temperatures and stress ratios. For each specific condition (material, temperature, and stress ratio) fatigue tests were performed for one stress amplitude at different test frequencies. A summary of frequency effect test results is listed in Table 6-1 for PP, PP-T, PP-G, PA66/B, and PPE/PS. Fatigue life increases proportionally with increasing frequency up to a certain limit, then decreases for most of the conditions, except for PA66/B at 85 °C and PPE/PS at 23 °C, as shown in Figure 6-3. At higher frequencies self-heating due to hysteresis heating overtakes the beneficial effect of frequency and decreases the fatigue life.

Temperature rise at the surface of specimen gage section was measured during fatigue tests conducted at 23 °C. For the PP fatigue tests under $R = 0.1$ and maximum stress level of 78% of ultimate strength, the maximum temperature rise during the test was 2 °C for the test frequency of 2 Hz and 10 °C for the test frequency of 4 Hz. A reduction of fatigue life was observed at frequency of 4 Hz compared to 2 Hz, as shown in Figure 6-3(a). Since the range of applied cyclic stress and accordingly energy loss per cycle is much higher at R = -1 stress ratio, as compared to R = 0.1 and 0.3 stress ratios, the effect of self-heating starts to become dominant at even lower frequencies (i.e. 0.75 Hz), as shown in Figures 6-3(c) and (d) for PP-G. In the study of Zhou and Mallick [155, 156] an equilibrium between beneficial and detrimental effects of frequency, and accordingly a decrease in the rate of reduction of life and reaching to a constant life, was observed for talc-filled polypropylene and short glass fiber reinforced polyamide-6.6 at high frequencies (up to 20 Hz). The same behavior is expected for the materials in this study at higher frequencies than those considered.

The fatigue behavior for the conditions where the fatigue life improved by increasing frequency seems to be more related to time rather than to cycles, provided that fatigue life is not considerably influenced by self-heating. As shown in Figure 6-4 for PP, PP-T, and PP-G, differences between times to failure of tests at different frequencies are much less, as compared to differences between cycles to failure. For instance for PP-G at 85 °C under R = 0.3 loading, time to failure for the fatigue tests with frequency between 0.25 to 12 Hz is about 3.8 hours, with a variation of less than a factor of 1.3, while the variation in cycles to failure is about a factor of 63. It appears fatigue damage is more time-dependent than cycle-dependent for these cases.

Reduction of displacement amplitude with increasing frequency was observed for all the materials, mainly for the conditions where the strengthening effect of increased frequency occurred. Variations of displacement amplitude of midlife cycle and 1250th cycle with frequency for PP-G at 85 °C under R = 0.3 loading are shown in Figure 6-5(a). The displacement amplitude continuously decreases up to 8 Hz and slightly increases after that with increasing frequency because thermal softening resulting from hysteresis heating becomes dominant. The reduction of displacement amplitude can be related to increase in stiffness with increasing frequency, i.e. loading rate. The increase in storage modulus with increasing frequency was also observed in frequency sweep DMA test at 85 °C, as seen from Figure 6-2.

To evaluate the effect of frequency on cyclic creep during fatigue tests, mean displacement values at midlife cycle and at 1250th cycle for tests at different frequencies are compared for PP-G at 85 °C under stress ratio of 0.3 in Figure 6-5(b). Considering mean displacement of the loading actuator as representative of cyclic creep is reasonable, as the gripping position was identical for all the test specimens. A notable effect of frequency is not seen on mean displacement at midlife cycle, but the trend is similar to the variation of displacement amplitude (Figure 6-5(a)) when compared at a given number of cycles (i.e. 1250th cycle). Therefore, cyclic creep also appears to be more related to time than to cycles, which was also reported for PMMA in [169].

Hysteresis loops (i.e. stress versus displacement loops) of midlife cycles and at a given cycle were compared for different test frequency tests at the same stress level. For the conditions where the fatigue life improved by increasing frequency, the hysteresis area decreased with increasing frequency, provided that the temperature rise was negligible. Hysteresis loops of midlife cycle and a given cycle for PP-G at test temperature of 85 °C under stress ratios of 0.3 and -1 at different test frequencies are shown in Figure 6-6. A distinct reduction in the area of loops can be seen with increasing frequency. This behavior can be related to a reduction in viscoelastic damping with increasing frequency, which was also observed in frequency sweep DMA test for PP, PP-T, PP-G, and PPE/PS at 85 °C (see Figure 6-2). The area of loops at different test frequencies was nearly the same for PA66/B at 85 °C. Also, variation of the damping factor (tan δ) with frequency in DMA test of this material was negligible at this temperature, as can be seen from Figure 6-2.

To evaluate the amount of viscoelasticity during fatigue tests, the phase lag between cyclic load and displacement waveforms was measured for midlife cycle. Variations of tan δ values at mid-life with frequency obtained from fatigue tests at 85 °C under $R = 0.1$ condition for all the materials and at 23 °C under $R = 0.1$ condition for PP-G and PPE/PS at constant stress amplitude for a given material and temperature are shown in Figure 6-7. For the cases where the beneficial effect of increased frequency was observed (PP, PP-T, PP-G, PPE/PS at 85 °C and PP-G at 23 °C), tan δ values decrease with increasing frequency. The variation is much less for PPE/PS at 85 °C compared to PP, PP-T and PP-G. The damping factor of PA66/B at 85 °C and PPE/PS at 23 °C are almost constant with increasing frequency. The loss tangent values measured from fatigue tests were in the same range as from the DMA test results.

6.3.2 Discussion of results

According to the experimental results, it can be concluded that the beneficial effect of increased frequency on fatigue behavior directly relates to the polymer matrix and not the fiber reinforcement or the filler of the composite materials. Viscoelasticity plays the main role for this beneficial effect as it was observed that when the damping reduces with increasing frequency, fatigue life increases. The damping can be related to the area of hysteresis loops and tan δ values. In addition, crack blunting due to hysteresis heat at crack tip, higher stiffness due to increased loading rate, and the effect of creep which were addressed in the literature to explain beneficial effect of increased frequency on fatigue crack growth behavior [159, 164, 165, 172] cannot be neglected.

Zhou and Mallick [156] observed the beneficial effect of increased frequency on short glass fiber reinforced polyamide-6.6 which is in contrast with our observations. Polyamide-6.6 specimens were not dried prior to testing in their study. Polyamide is highly sensitive to moisture, as discussed in chapter 4, and moisture can dramatically change the viscoelastic behavior, therefore, this contrast is justifiable. Manson et al. [157] reported an apparent correlation between the frequency dependence of FCP and the frequency of the beta transition at the test temperature in polymeric materials. In all of the frequency insensitive materials, the beta transition frequency was far above the test range, while with the more frequency sensitive materials the beta frequency tended to be close to or within the test range. For example, for Nylon-6.6 the beta frequency at RT was reported to be 10^5. They also mentioned that the strengthening effect of frequency indirectly reflects the tendency of a given polymer to undergo a crazing type of response, at least under the conditions used in the tests. Crazing can be seen with naked eye on the surface of PP-T, PP-G, and PPE/PS specimens, as shown in Figure 6-8. There is no evidence of crazing on the surface of PA66/B specimen.

Scanning electron microscopy was conducted on fracture surface of a few PP, PP-G, and PA66/B specimens at 85 °C tested at different frequencies. Fracture surface of all the materials showed two distinct regions. In one region the matrix was highly deformed and stretched where microductile deformation was visible. This region is the crack initiation and stable crack growth region. In the second region, microbrittle fracture of the matrix was visible and fiber pullout mechanism was dominant for the short fiber reinforced composites. This region is the fast crack growth and final fracture region. The two distinct regions are shown macroscopically for PP and PA66/B in Figure 6-9. A transition area between the two regions is also distinguishable, mainly for the unreinforced polymer (PP).

The white or light areas in Figure 6-9 show the first region (crack initiation and stable growth) and the darker areas shows the second region (fast crack growth and final fracture). These two distinct regions were also observed for polyamide-based composites in [173, 174]. Crack initiation or stable crack growth region size decreased with increasing test frequency for all the materials, as can be seen macroscopically for PA66/B and PP at frequencies of 0.25 and 4 Hz in Figure 6-9. This may be because of a reduction in ductility and consequently in fracture toughness of the materials with increasing frequency, which resulted in a shorter stable crack growth region. The increase in storage modulus with increasing frequency observed in DMA tests for all the materials (Figure 6-2) and the reduction in displacement amplitude with increasing frequency (in Figure 6-5(a) shown for PP-G) are consistent with the macroscopic and microscopic observations of fracture surfaces.

SEM of the fatigue fracture surfaces of PP and PP-G specimens are compared at low and high frequencies in the crack initiation region in Figure 6-10. For both materials, matrix damage due to microductile behavior is much less at higher frequency, as compared to at lower frequency. Many microbrittle areas in the crack initiation region can be seen on fracture surface of PP at 4 Hz, while these areas are much fewer at 0.25 Hz. Also, ductile damage is seen on fracture surface of 0.25 Hz PP-G specimen, while brittle damage and fiber pullout are the main damage mechanisms for the 12 Hz specimen. Less ductile damage at higher frequency can be related to less viscoelastic damping and higher stiffness, which was also observed in DMA and fatigue tests, and resulted in longer fatigue life.

6.4 Correlation of Fatigue Data with a Larson-Miller Type Model

As mentioned earlier, for the materials for which the beneficial effect of increased frequency on fatigue life was dominant, e.g. PP, PP-T and PP-G, fatigue damage instead of being cycle dependent is a time-dependent phenomenon. Therefore, plots of stress amplitude versus time are used to represent experimental fatigue data for these materials, as shown in Figure 6-11. On the basis of this consideration, the Larson-Miller parameter [124] can be used in order to relate stress amplitude, temperature, and time to failure together. The Larson-Miller creep parameter [124] has been used to relate stress, temperature and time to rupture in creep tests for many years and is the most well-known creep stress-time-temperature parameter (STTP), which is expressed as:

$$\mathrm{LMP} = T\,(\log t_R + C_{LMP}) \tag{6.4}$$

In the above equation, T is the test temperature in Kelvin, t_R is the time to rupture in creep test and C_{LMP} is a material constant. LMP, which is the Larson-Miller creep parameter, can be expressed as a function of stress.

In this study this parameter is defined for fatigue as:

$$\mathrm{LMP_f} = \frac{T\,(\log t_f + C_{LMP})}{1000} \tag{6.5}$$

where t_f is time to failure in fatigue test in hours. C_{LMP} values were determined by fitting linear lines to log t_f versus $1/T$ data for a given stress amplitude. Intersection of the lines for different stress amplitudes at $1/T = 0$ defines the value of the Larson-Miller constant, C_{LMP}.

A power law equation is used to relate this Larson-Miller fatigue parameter to the stress amplitude, S_a, at each stress ratio for a given material:

$$S_a = A(\mathrm{LMP_f})^B \tag{6.6}$$

where S_a is in MPa. The time to failure (t_f) can be converted to cycles to failure (N_f) using the frequency of the test (f) according to the following relationship:

$$t_f = \frac{N_f}{f \times 3600} \tag{6.7}$$

Finally, by combining Equations 6.5 to 6.7 the general form of the model can be expressed as:

$$S_a = A\left[\frac{T\,(\log \dfrac{N_f}{f \times 3600} + C_{LMP})}{1000}\right]^B \tag{6.8}$$

According to Equation 6.8, stress amplitude, temperature, cycles to failure, and frequency can be related together for each material. The Larson-Miller master curves are shown in Figure 6-12 for PP, PP-T, and PP-G. It can be seen that this model correlate the experimental fatigue data very well. Constants of the model at different test conditions for different materials are included in Table 6-2. The C_{LMP} values are 31, 41, and 26 for PP, PP-T, and PP-G, respectively, independent of the stress ratio, R . The B values are in the range of -4.06 to -4.60 for all the materials at different stress ratios. To apply the model more generally, the frequency should be low enough so the fatigue life is not considerably reduced by self-heating. The temperature range used in generating the model constants should also be considered.

Table 6-1: Summary of frequency effect test results of PP, PP-T, PP-G, PA66/B, and PPE/PS.

Specimen ID	**Temp. (°C)**	**Stress Ratio (*R*)**	**Stress Amp. (MPa)**	**Freq. (Hz)**	**Midlife Disp. Amp. (mm)**	**Midlife Disp. Mean (mm)**	**Temp. Rise (°C)**	**Cycles to Failure**	**Failure Location**
PP									
AGN-F-R-1	23	0.1	8.75	0.125	0.235	0.687	0	1,856	IGIT
AGN-T-R-F-37	23	0.1	8.75	1	0.230	0.686	0.1	7,576	IGIT
AGN-T-R-F-41	23	0.1	8.75	1	0.232	0.523	0.1	11,741	IGIT
AGN-F-R-2	23	0.1	8.75	2	0.221	0.644	0.4	22,961	IGIT
AGN-F-R-3	23	0.1	8.75	4	0.230	0.589	4	15,510	IGIT
AGN-F-H1-1	85	0.1	3.5	0.25	0.242	1.235	-	7,072	IGIT
AGN-T-H-F-5	85	0.1	3.5	1	0.236	1.547	-	20,020	IGIT
AGN-T-H-F-8	85	0.1	3.5	1	0.234	1.342	-	16,931	IGIT
AGN-F-H1-2	85	0.1	3.5	1	0.232	1.658	-	32,910	IGIT
AGN-F-H1-3	85	0.1	3.5	4	0.221	1.652	-	172,621	IGIT
PP-T									
PPT-F-H1-8	85	0.1	5	0.25	0.167	0.515	-	1,246	No Break
PPT-F-H1-3	85	0.1	5	1	0.144	0.571	-	27,079	IGIT
PPT-F-H1-4	85	0.1	5	1	0.140	0.511	-	18,017	OGIT
PPT-F-H1-9	85	0.1	5	4	0.136	0.488	-	39,422	IGIT
PP-G									
PPG-F4-R-5	23	-1	26	0.25	0.301	0.101	0.1	7,466	IGIT
PPG-F4-R-3	23	-1	26	0.5	0.295	0.276	2	15,841	IGIT
PPT-F4-R-6	23	-1	26	0.75	0.291	0.496	4	19,381	IGIT
PPG-F4-R-4	23	-1	26	1	0.287	0.050	8.3	16,571	OGIT
PPG-F4-R-2	23	-1	26	2	0.299	0.167	23.5	7,348	IGIT
PPG-F-R-8	23	0.1	16	0.125	0.238	0.646	0	3,141	IGIT
PPG-F-R-3	23	0.1	16	0.5	0.249	0.330	0.7	3,531	IGIT
PPG-F-R-4	23	0.1	16	0.5	0.250	0.324	0.5	3,482	IGIT
PPG-F-R-11	23	0.1	16	2	0.219	0.565	1.5	16,064	IGIT
PPG-F-R-9	23	0.1	16	4	0.225	0.372	4.2	12,219	IGIT
PPG-F-R-10	23	0.1	16	8	0.239	0.300	14.2	5,895	IGIT
PPG-F4-H1-3	85	-1	15	0.25	0.421	0.105	-	707	IGIT
PPG-F4-H1-5	85	-1	15	0.5	0.412	0.280	-	1,765	IGIT
PPG-F4-H1-2	85	-1	15	1	0.367	0.232	-	3,996	IGIT
PPG-F4-H1-4	85	-1	15	2	0.377	0.205	-	2,505	IGIT
PPG-F-H1-9	85	0.1	7.5	0.25	0.192	0.542	-	6,005	IGIT
PPG-F-H1-3	85	0.1	7.5	1	0.187	0.575	-	26,126	IGIT
PPG-F-H1-4	85	0.1	7.5	1	0.183	0.443	-	25,466	IGIT
PPG-F-H1-8	85	0.1	7.5	8	0.173	0.948	-	173,660	OGIT
PPG-F-H1-10	85	0.1	7.5	12	0.180	0.527	-	135,111	IGIT
PPG-F3-H1-11	85	0.3	5.85	0.25	0.142	0.966	-	2,866	IGIT
PPG-F3-H1-12	85	0.3	5.85	0.25	0.142	0.770	-	2,714	IGIT
PPG-F3-H1-7	85	0.3	5.85	1	0.131	0.445	-	14,543	IGIT
PPG-F3-H1-10	85	0.3	5.85	1	0.134	0.599	-	14,799	IGIT
PPG-F3-H1-16	85	0.3	5.85	1	0.137	0.602	-	11,807	IGIT
PPG-F3-H1-14	85	0.3	5.85	2	0.130	0.707	-	27,569	OGIT
PPG-F3-H1-15	85	0.3	5.85	4	0.125	1.118	-	68,489	IGIT
PPG-F3-H1-17	85	0.3	5.85	8	0.123	0.996	-	127,857	IGIT
PPG-F3-H1-18	85	0.3	5.85	12	0.123	0.690	-	166,598	IGIT
PPG-F3-H1-19	85	0.3	5.85	16	0.125	0.684	-	145,264	IGIT
PPG-F3-H1-20	85	0.3	5.85	20	0.127	0.702	-	136,797	IGIT

Table 6-1 (cont'd): Summary of frequency effect test results of PP, PP-T, PP-G, PA66/B, and PPE/PS.

Specimen. ID	Temp. (°C)	Stress Ratio (*R*)	Stress Amp. (MPa)	Freq. (Hz)	Midlife Disp. Amp. (mm)	Midlife Disp. Mean (mm)	Temp. Rise (°C)	Cycles to Failure	Failure Location
PA66/B									
PAB-F-H1-9	85	0.1	17.5	0.25	0.457	1.151	-	4,238	IGIT
PAB-F-H1-12	85	0.1	17.5	1	0.466	1.062	-	5,598	IGIT
PAB-F-H1-11	85	0.1	17.5	2	0.497	1.006	-	4,945	IGIT
PAB-F-H1-10	85	0.1	17.5	4	0.457	1.053	-	8,836	IGIT
PPE/PS									
FRM-F-R-1	23	0.1	18	0.5	0.200	0.116	0	9,483	IGIT
FRM-F-R-9	23	0.1	18	1	0.203	0.033	0	7,389	IGIT
FRM-F-R-10	23	0.1	18	1	0.201	0.243	0	6,210	IGIT
FRM-F-R-2	23	0.1	18	2	0.204	0.065	0.1	4,058	OGIT
FRM-F-R-13	23	0.1	18	2	0.195	0.261	0.1	7,062	IGIT
FRM-F-H1-11	85	0.1	9	0.25	0.108	0.300	-	10,449	IGIT
FRM-F-H1-8	85	0.1	9	1	0.103	0.321	-	20,480	IGIT
FRM-F-H1-10	85	0.1	9	4	0.098	0.315	-	32,633	IGIT
FRM-F-H1-12	85	0.1	9	8	0.094	0.325	-	68,224	IGIT
FRM-F-H1-13	85	0.1	9	12	0.104	0.365	-	41,718	IGIT

Table 6-2: Larson-Miller model constants for PP, PP-T, and PP-G.

	Stress Ratio (*R*)	**Temp. (°C)**	**S_u (MPa)**	**C_{LMP}**	**$A \times 10^{-5}$**	**B**
PP	0.1	23 85	24.7 11.5	31	2.50	-4.60
PP-T	0.1	23 85	29.4 13.8	42	3.20	-4.06
	0.3	23 85	29.4 13.8	42	8.70	-4.54
PP-G	0.1	23 85 120	46.8 21.8 11.9	26	0.69	-4.05
	0.3	23 85 120	46.8 21.8 11.9	26	1.52	-4.53

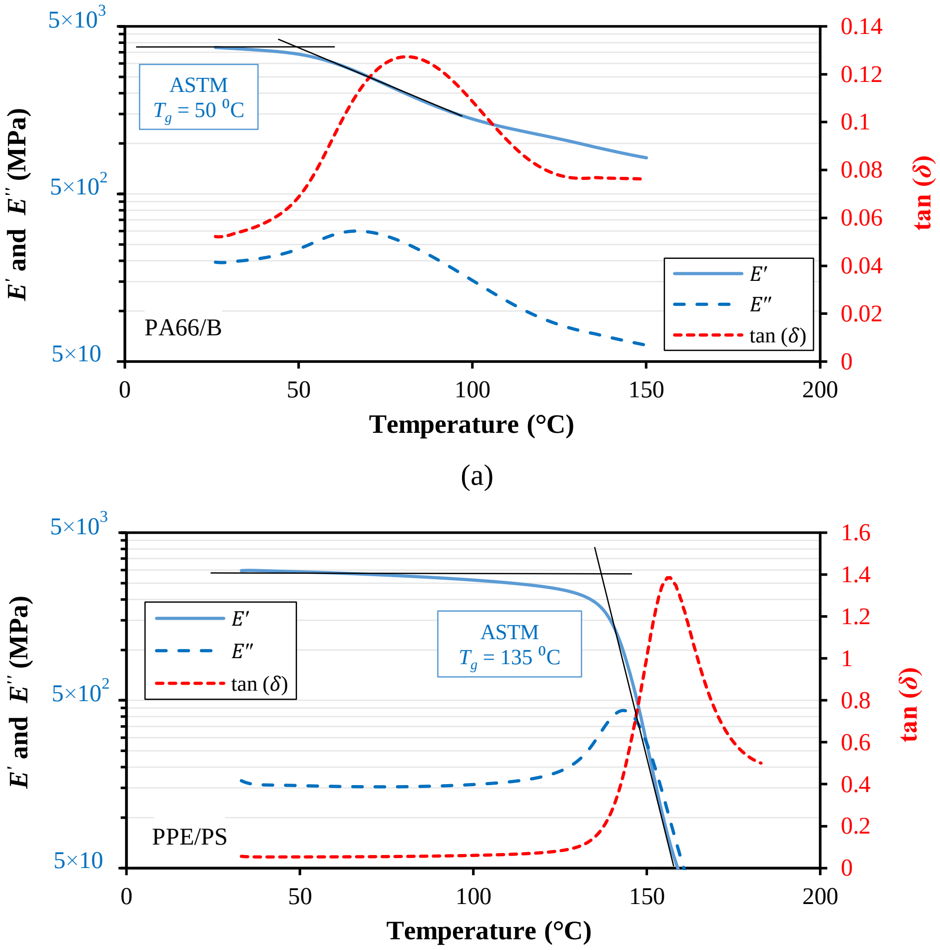

(a)

(b)

Figure 6-1: Temperature sweep DMA test results including variation of storage modulus, loss modulus, and loss tangent with temperature at frequency of 1 Hz with temperate rate of 5 °C/min for (a) PA66/B and, (b) PPE/PS.

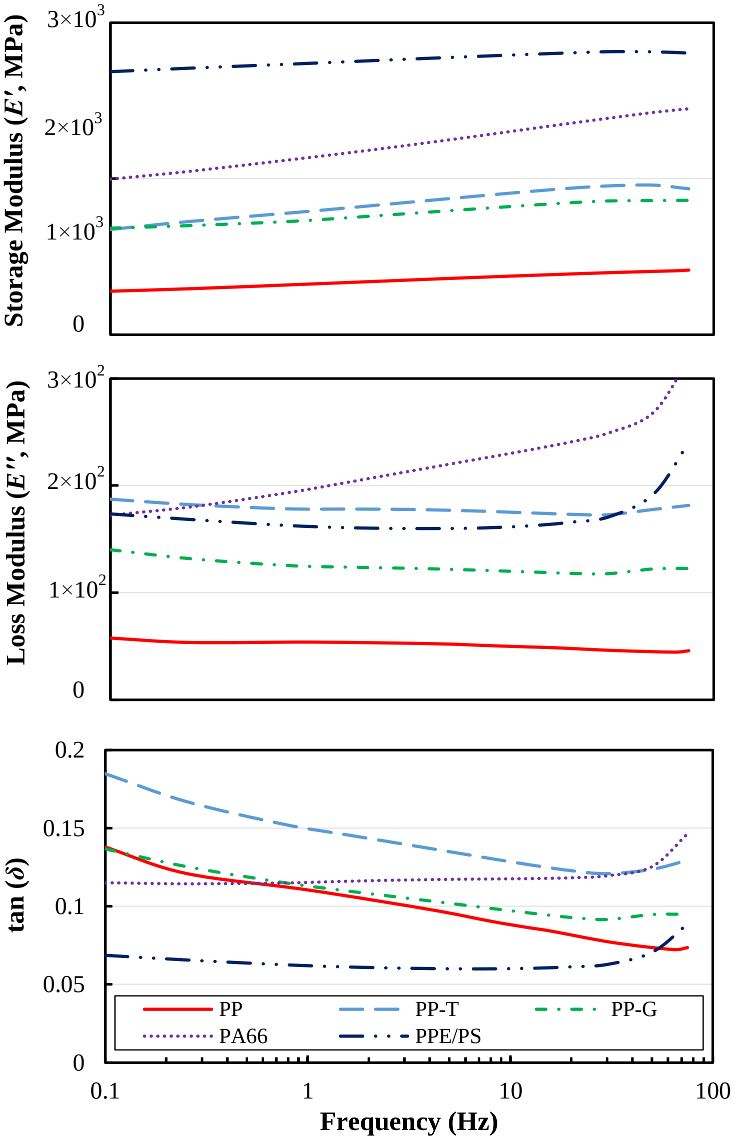

Figure 6-2: Frequency sweep DMA test results including variation of storage modulus, loss modulus, and loss tangent with frequency for PP, PP-T, PP-G, PA66/B, and PPE/PS at 85 °C.

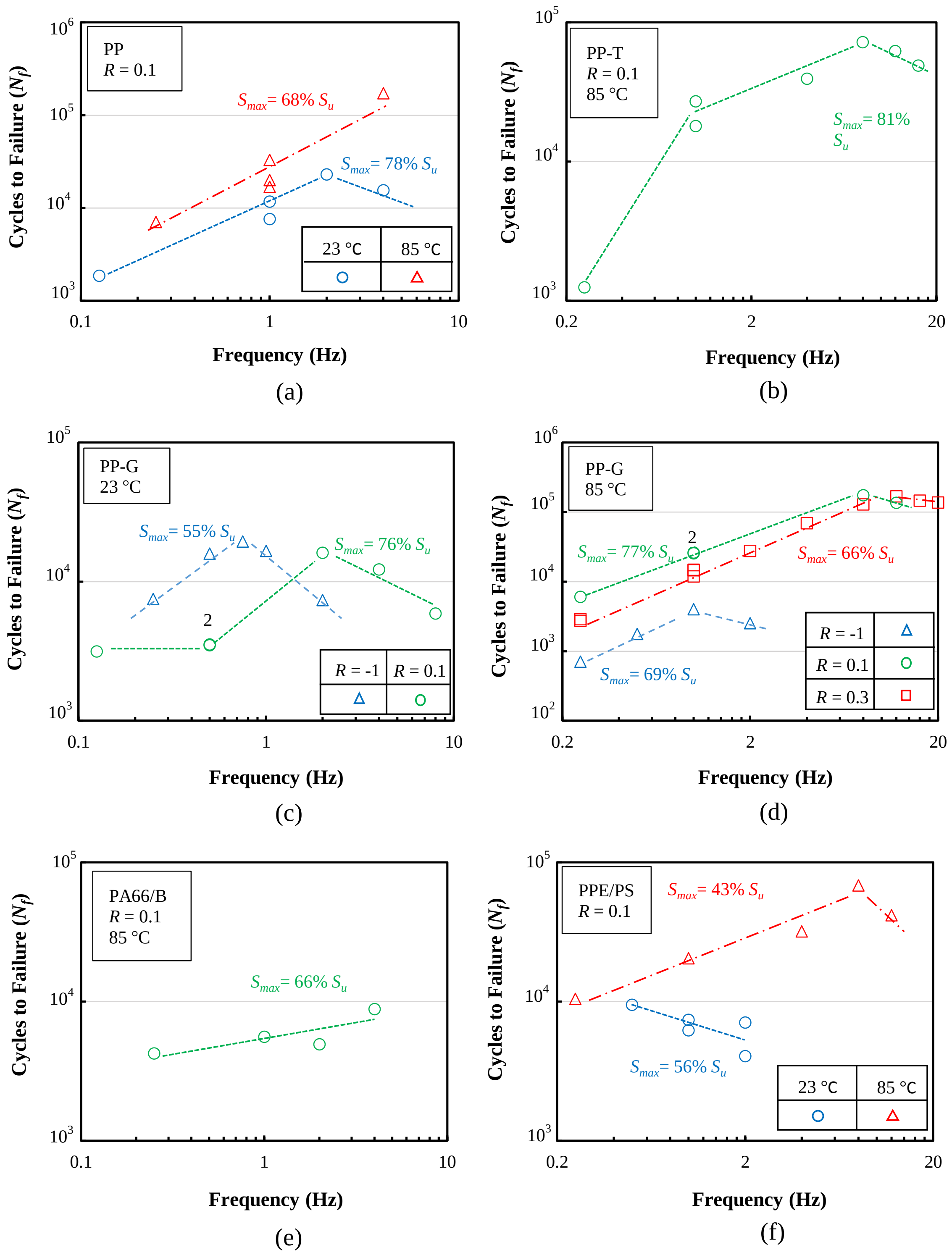

Figure 6-3: Effect of cyclic frequency on the fatigue life at different *R* ratios for (a) PP at 23 °C and 85 °C, (b) PP-T at 85 °C, (c) PP-G at 23 °C, (d) PP-G at 85 °C, (e) PA66/B at 85 °C and, (f) PPE/PS at 23 °C and 85 °C.

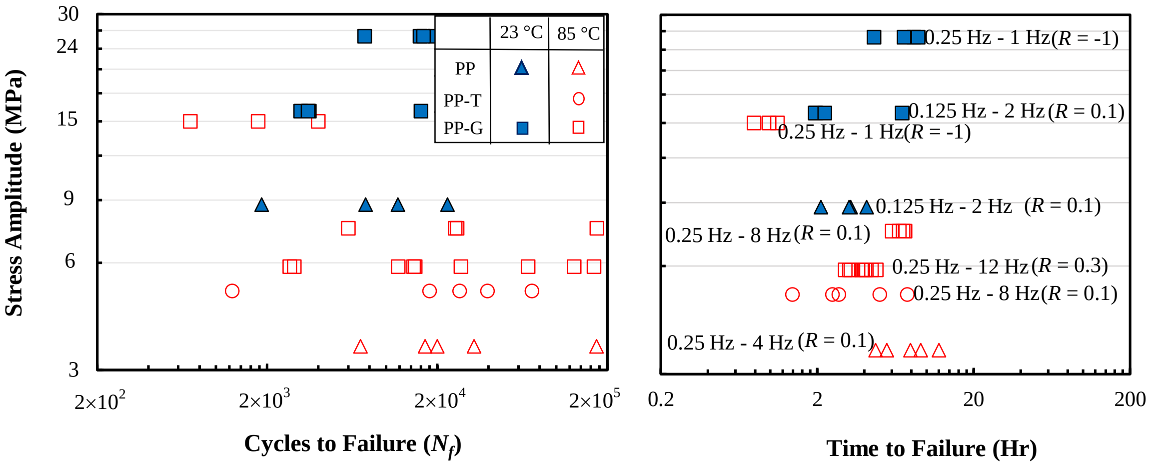

(a) (b)

Figure 6-4: (a) Cycles to failure and, (b) time to failure at a given stress amplitude for different test frequencies where the self-heating is not dominant for PP, PP-T, and PP-G at different R ratios. The range of test frequency is shown for each condition.

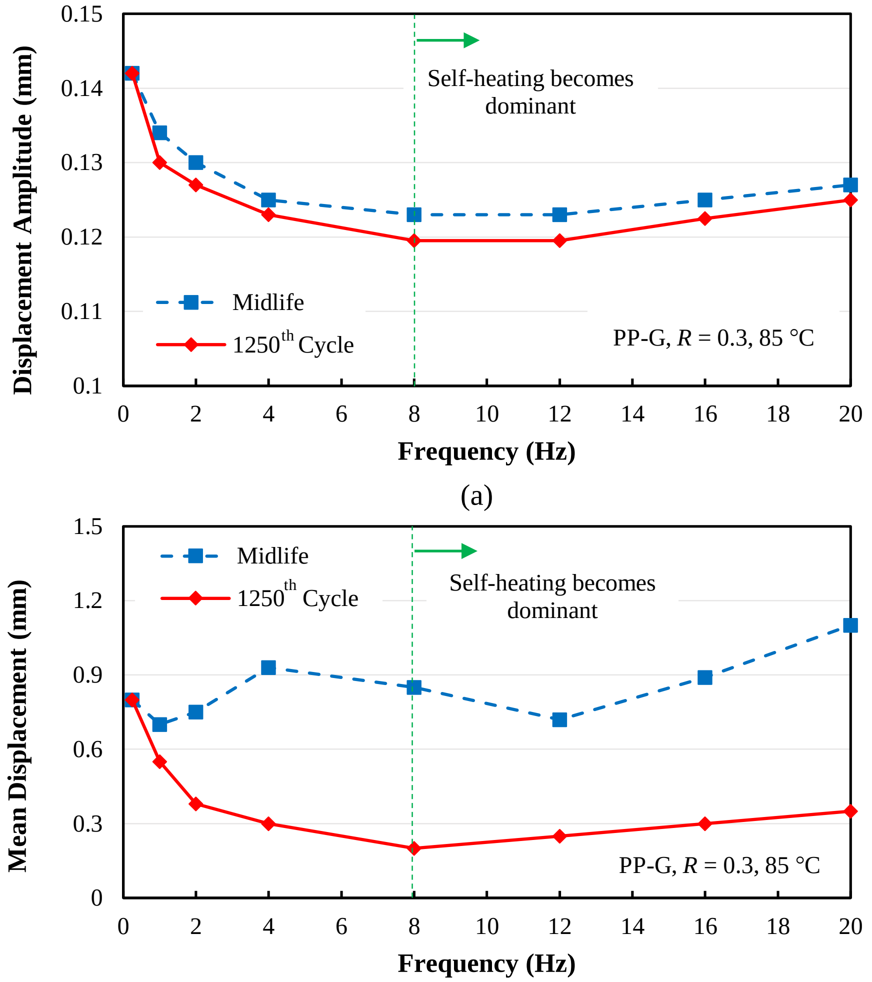

(a)

(b)

Figure 6-5: (a) Displacement amplitude and, (b) mean displacement values of midlife cycle and 1250th cycle for different test frequencies for PP-G at 85 °C under $R = 0.3$ loading.

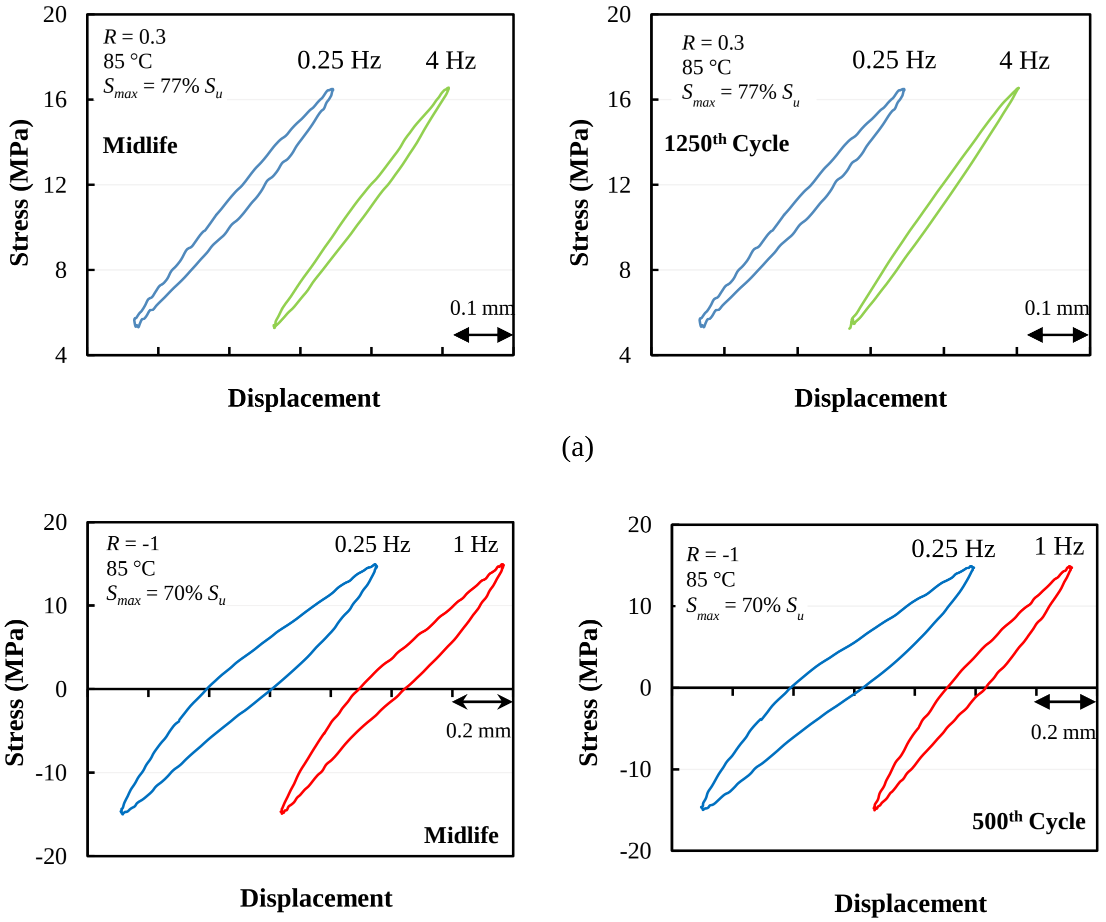

(a)

(b)

Figure 6-6: PP-G load-displacement hysteresis loops at midlife and at a given cycle at 85 °C for different test frequencies under (a) $R = 0.3$ and, (b) $R = -1$.

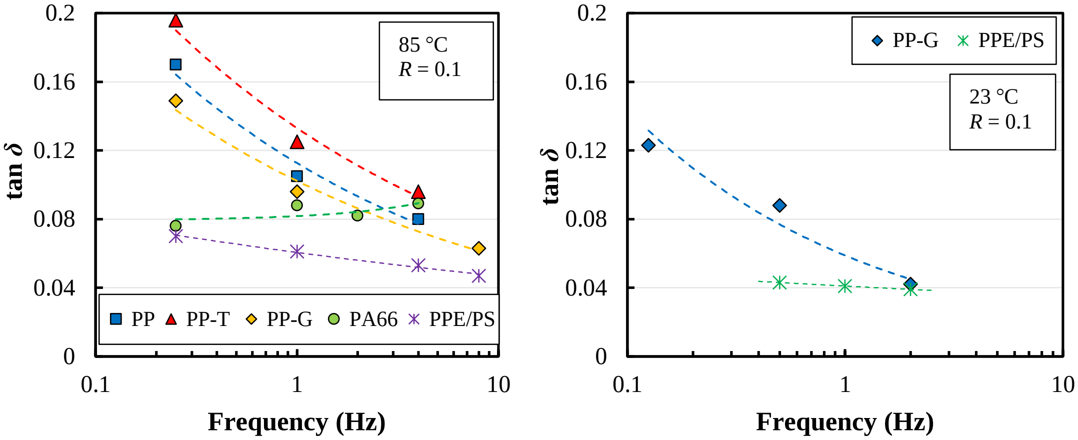

(a) (b)

Figure 6-7: Variation of loss tangent with frequency under R = 0.1 for (a) PP, PP-T, PP-G, PA66/B, and PPE/PS at 85 °C, and (b) PP-G and PPE/PS at 23 °C, measured in fatigue tests.

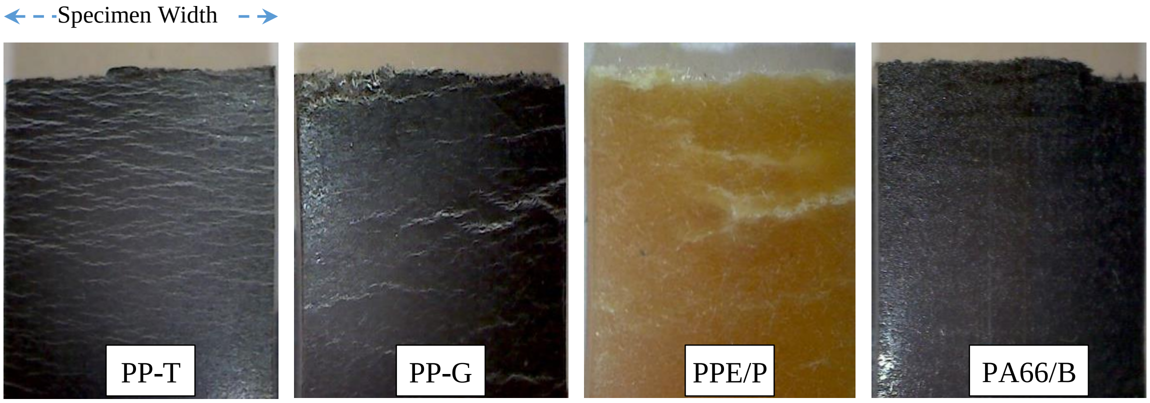

Figure 6-8: Failed specimen gage section pictures of PP-T, PP-G, PPE/PS, and PA66/B under fatigue test at 85 °C for R = 0.1 loading. Crazing occurred for PP-T, PP-G, and PPE/PS.

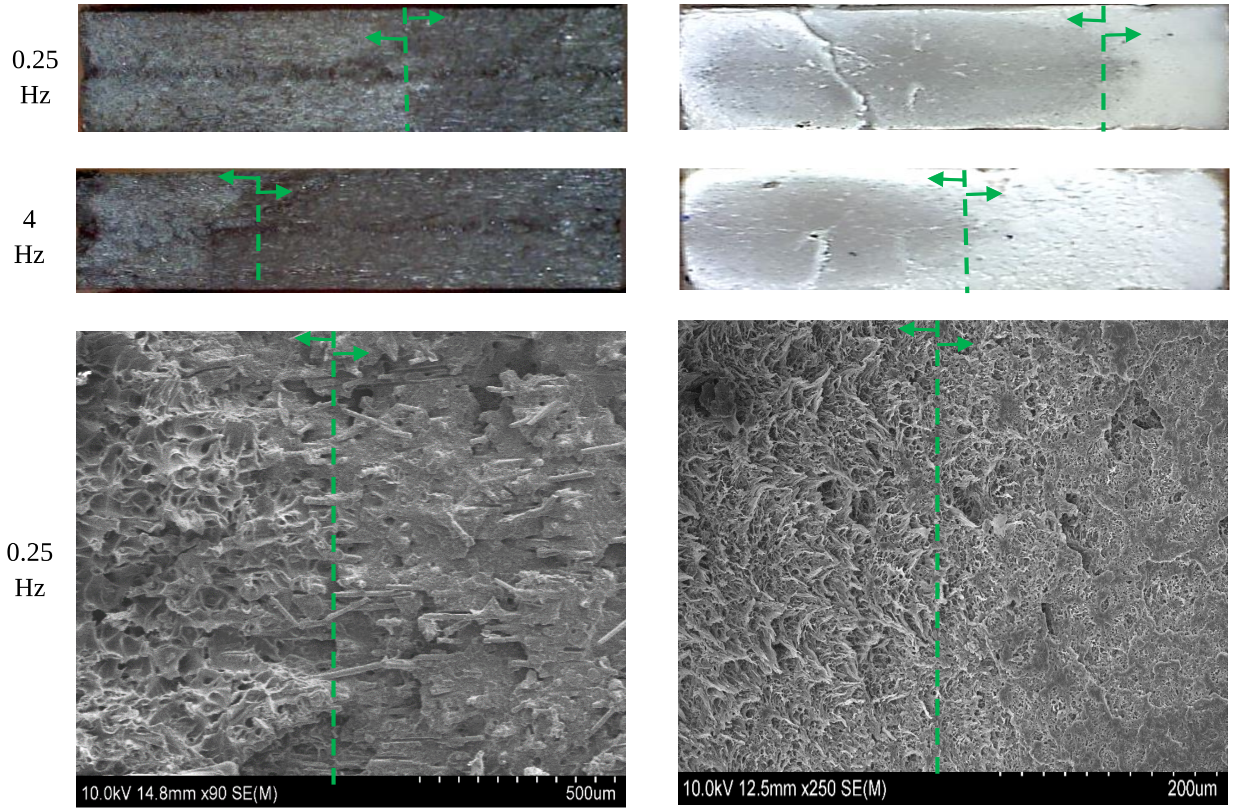

(a) (b)

Figure 6-9: Macroscopic fracture surface at frequencies of 0.25 and 4 Hz and microscopic fracture surface at frequency of 0.25 HZ at 85 °C under *R* = 0.1 condition for (a) PA66/B and, (b) PP. In each photo the left side shows crack initiation and stable crack growth region and the right side shows fast crack growth and final fracture region.

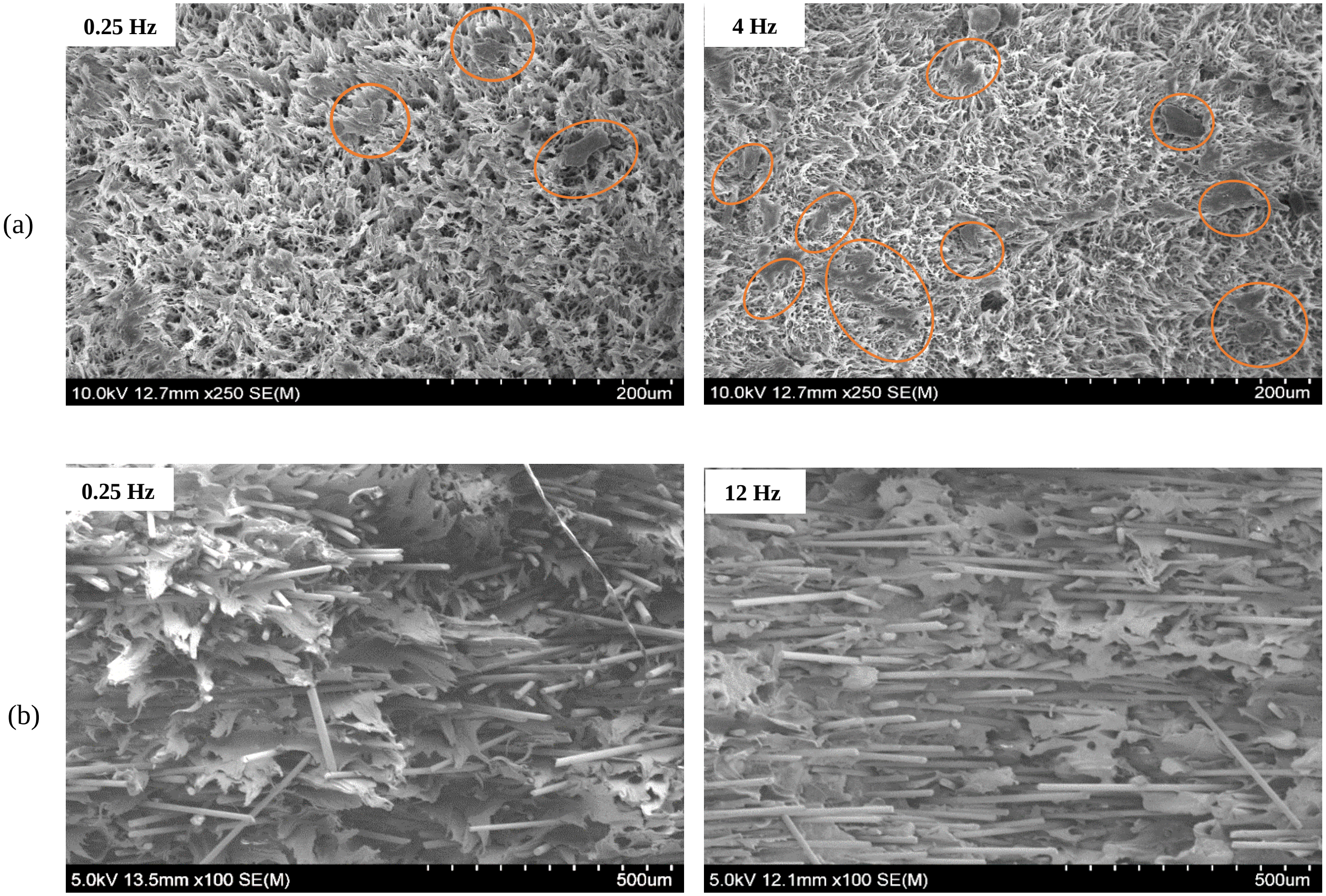

Figure 6-10: SEM of the fatigue fracture surface at 85 °C for (a) PP under $R = 0.1$ loading for frequencies of 0.25 and 4 Hz and, (b) PP-G under $R = 0.3$ loading for frequencies of 0.25 and 12 Hz. More damage in matrix is seen at lower frequencies for both PP and PP-G.

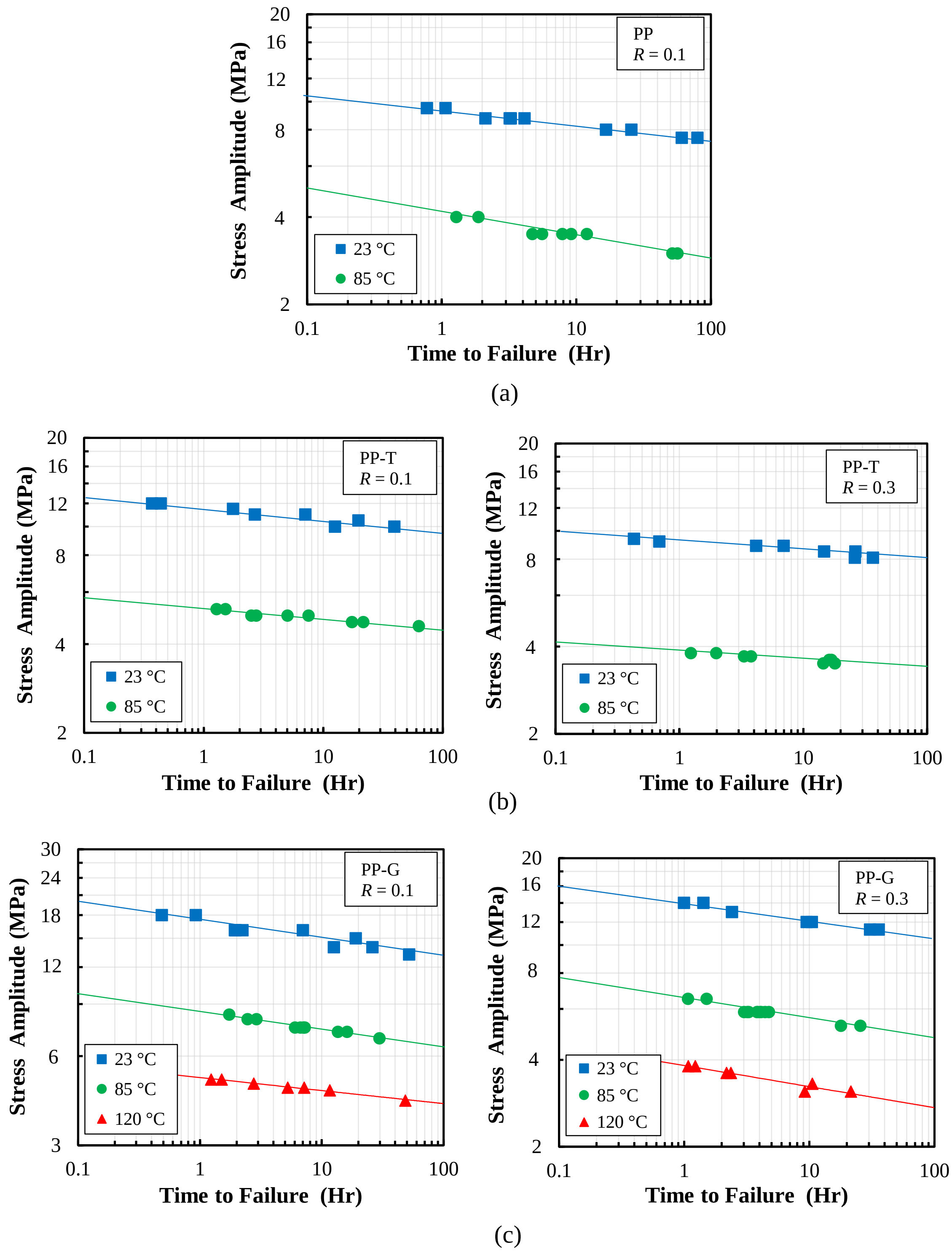

(a)

(b)

(c)

Figure 6-11: Stress amplitude versus time to rupture fatigue test data at different frequencies for (a) PP at 23 and 85 °C under $R = 0.1$ loading, (b) PP-T at 23 and 85 °C under $R = 0.1$ and 0.3 loadings and, (c) PP-G at 23, 85, and 120 °C under $R = 0.1$ and 0.3 loadings.

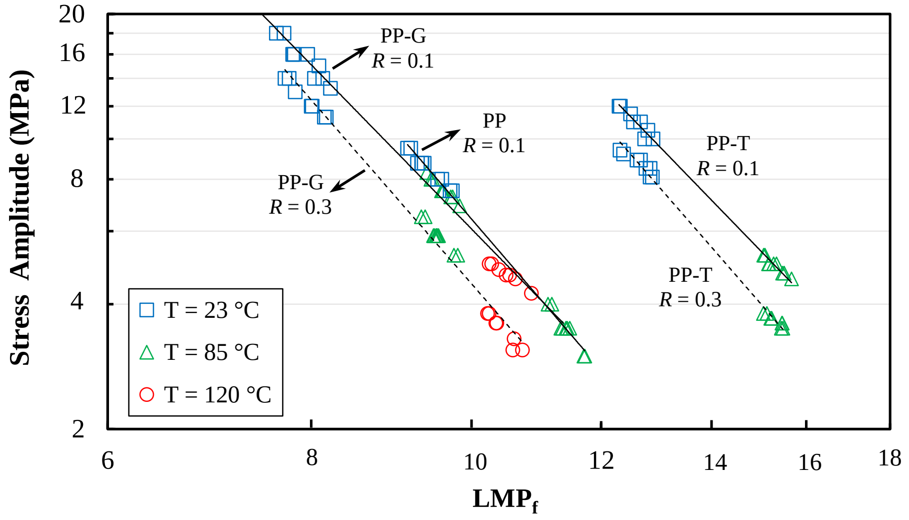

Figure 6-12: Larson-Miller master curves for PP at R = 0.1 and for PP-T and PP-G at R = 0.1 and 0.3.

Chapter 7

Isothermal Fatigue Test Results and Analysis

In this chapter isothermal fatigue behavior of PP-T, PP-G, PA66/B, PA66/D, and PPE/PS, including the effects of temperature and mean stress is investigated. Load-controlled fatigue tests were conducted at several temperatures and stress ratios. The effect of temperature was investigated at 23 °C and 85 °C for PP-T, PA66/D, and PPE/PS and at these temperatures in addition to at 120 °C for PP-G and PA66/B in the transverse to the mold flow direction. *R* ratios for most of the tests were 0.1 and 0.3 to investigate the effect of mean stress. Some tests with *R* ratio of -1 were also conducted for PP-G and PA66/B to verify the accuracy of mean stress models. For PP-T, fatigue tests were also conducted in the longitudinal direction at 23 °C under $R = 0.1$ condition to investigate the effect of mold flow direction. Models based on the superposition principle were used to correlate the temperature effect data. The ability of different mean stress correction parameters to correlate the data was evaluated. A fatigue life prediction model was also applied to experimental data to account for the effects of temperature, mean stress, anisotropy, and frequency. Experimental results and analysis presented in this chapter were published in [175].

7.1 Introduction

Most of the load bearing applications of thermoplastics and their composites are in components exposed to cyclic loadings. As a result, fatigue failure is one of the most common types of failure and must be taken into consideration in the design of components made of injection molded thermoplastic composites. Anisotropy due to fiber orientation, fiber length and its surface treatment, thickness, cycling frequency, temperature, and moisture have been observed to considerably affect the fatigue behavior of short fiber reinforced thermoplastic composites [54].

In injected modeled short fiber composites a shell-core morphology is typically observed where fiber orientation is mainly along the mold flow direction in the shell and transverse to the mold flow direction in the core [57, 61]. A significant reduction of fatigue strength has been observed with increasing fiber angle with respect to the loading direction [61, 176, 177]. Tsai-Hill criterion [176] and the master *S-N* curve approach [177] have been used to predict the dependence of fatigue strength upon the orientation angle of fibers. In the study of Zhou and Mallick [155], the effect of anisotropy was also observed on the fatigue behavior of talc-filled polypropylene, however it was much less, as compared to short fiber reinforced thermoplastics. Fatigue strength at 10^6 cycles of talc-filled polypropylene in the flow direction in that study was found to be 10% more than that in the transverse to the flow direction. This effect was observed to be more accentuated in the low cycle fatigue (LCF) regime.

As discussed in the previous chapter, depending on the mode of loading, stress level, material characteristics, and the in-service temperature, frequency affects the cyclic behavior of thermoplastic composites to various degrees. Self-heating is the major detrimental effect of cycling frequency on fatigue behavior of polymers, resulting from viscous energy dissipation and frictional heating. A beneficial effect of frequency on fatigue behavior of some polymers has also been observed. For the materials for which the beneficial effect of increased frequency on fatigue life was dominant (i.e. polypropylene-based composites), the fatigue behavior was observed to be more related to time, rather than cycles, provided that fatigue life was not considerably influenced by self-heating.

Effect of mean stress on fatigue life of thermoplastic composites has been found to be significant at different temperatures and in different mold flow directions [56, 62]. Fatigue strength significantly reduces in the presence of positive mean stress. The effect is more pronounced in LCF, resulting from increased dependence of fatigue life on the maximum stress [62]. For these materials, depending on the matrix type, cyclic ratcheting may add to the effect of mean stress on fatigue life. Several mean stress models have been utilized to model the effect of mean stress in short fiber thermoplastic composites. Among them, Walker equation and Smith-Watson-Topper (SWT) parameter have been found to correlate the mean stress data well [62].

Increasing temperature from below to above glass transition temperature, T_g, has been found to significantly reduce fatigue strength of thermoplastic composites [57, 61]. At temperatures above T_g, similar slopes and intercepts for S-N curves have been observed at different temperatures, while below T_g, the slope and the intercept increased with increasing reciprocal of temperature [55]. The fatigue mechanisms have also been observed to be different at temperatures below and above T_g. Below T_g, microcracks propagated around fiber ends, and then cracks propagated between fiber ends in a brittle manner. Above T_g, microcracks propagated accompanied by debonding along the fiber sides and forming crack walls, after which the crack walls connected by bridging in a ductile manner [58].

7.2 Temperature Effect

7.2.1 Experimental results and failure mechanisms

A summary of fatigue tests results for PP-T, PP-G, PA66/B, PA66/D, and PPE/PS is listed in Table 7-1. Superimposed *S-N* curves at different temperatures under *R* ratios of 0.1 and 0.3 for all the materials are shown in Figure 7-1. A significant effect of temperature is observed for all the materials for both *R* ratios, as expected. Comparison of the ratio of fatigue strength at elevated temperatures (85 °C and 120 °C) to fatigue strength at 23 °C at 10^6 cycles for studied materials shows that the effect of temperature was more pronounced for PP-T and PP-G, as compared to PA66/B, PA66/D, and PPE/PS. Also, for PP-T and PP-G this effect was more accentuated for $R = 0.3$ loading, as compared to $R = 0.1$ loading condition due to the effect of cyclic creep. Comparison of *S-N* lines of PA66/B and PA66/D at 23 °C and 85 °C for $R = 0.1$ loading condition are shown in Figure 7-2. The fatigue strength at 10^6 of PA66/B is about 90% and 85% of that of PA66/D at 23 °C and 85 °C, respectively.

The Basquin's equation was used to fit the stress amplitude (S_a) versus number of cycles to failure (N_f) data in log-log scale, expressed as:

$$S_a = A(N_f)^B \tag{7.1}$$

where *A* is the intercept of the *S-N* line at $N_f = 1$ and *B* is the slope of the *S-N* line. The fits were obtained by considering the S_a as independent variable and N_f as dependent variable. A summary of fatigue test conditions, the slope and the intercept of *S-N* lines, ultimate tensile strength, and elastic modulus of studied materials are included in Table 7-2.

Variations of *A*, normalized *A* with S_u, and *B* with temperature for $R = 0.1$ and 0.3 loading conditions are shown in Figure 7-3. *A* values decrease linearly by increasing temperature for all the materials, as shown in Figure 7-3(a). This is similar to variation of S_u with temperature. A/S_u values, however, are nearly independent of temperature for all the conditions, as shown in Figure 7-3(b). The B values are nearly constant for PA66/B and PPE/PS and increase with increasing temperature for PP-T and PP-G for both $R = 0.1$ and 0.3 loading conditions, as shown in Figure 7-3(c). There is a difference between values of B for $R = 0.1$ and $R = 0.3$ loading conditions at elevated temperatures for PP-G and PA66/B. This is related to different failure mechanisms for different R ratios, which is discussed in the mean stress section. Values of B for PPE/PS are much lower (steeper S-N lines), as compared to the other materials due to its brittle behavior. Overall, the variation of slope B with temperature and stress ratio for a given material is relatively small in most cases. The variations and fits represented in Figure 7-3 can be used to predict and extrapolate the S-N lines of the studied materials at other temperatures than studied temperatures.

Comparison of the micro-mechanisms of failure of PPE/PS fracture surfaces tested at 23 °C and 85 °C under $R = 0.1$ condition which failed at about 50,000 cycles is shown in Figure 7-4. Pictures are from the transition of core and shell layers. Flaky matrix, fiber pullouts regions, and breakage of fibers which are evidence of a brittle failure, can be observed. Both temperatures of 23 °C and 85 °C are below T_g of PPE/PS at 135 °C. In contrast, a ductile behavior, mainly in the damage initiation zone at 85 °C, was observed for both PP-G and PA66 for which this temperature is above T_g which was explained in the previouse chapter.

7.2.2 Modeling the temperature effect

As discussed in the previous chapter, for PP-T and PP-G the fatigue behavior was observed to be more related to time rather than cycles. A Larson-Miller type parameter was successfully used for these materials to correlate stress amplitude, cycling frequency, test temperature, and cycles to failure for each materials at a given R ratio.

For PA66/B and PPE/PS, fatigue behavior is more cycle dependent, than time dependent. Fatigue data can be correlated by shifting the fatigue life at various temperatures similar to in [61] for polyamide-6 (PA6) and Polybutylene terephthalate (PBT) short glass fiber reinforced composites. This method is used to generate master curves and shift factors to be able to predict fatigue life at any temperature in the range of interest. According to this procedure, a shift factor of Arrhenius type is defined to generate master curves for a given R ratio, expressed as:

$$a_{T0}(T) = \frac{N_f}{N'_f} \tag{7.2}$$

where N'_f is the reduced cycles to failure due to the effect of temperature. 23 °C was selected as the reference temperature and fatigue data at 85 °C and 120 °C were shifted to the extrapolated S-N line at 23 °C. Master curves for R = 0.1 and 0.3 conditions are shown in Figures 7-5(a) and (b) for PA66/B and PPE/PS, respectively. As mentioned earlier, the equation of master curve is the equation of S-N line at 23 °C for a given R ratio. a_{T0} values were obtained to be independent of R ratio for both materials, similar to what was observed for PBT and PA6 in [61]. Superimposed values of a_{T0} for PA66/B and PPE/PS and the obtained fit for PA6 and PBT for R = -1 and 0.1 conditions are shown in Figure 7-5(c). As can be seen, a_{T0} values for PA66/B are very close to what obtained for PA6 and PBT. However, a_{T0} values for PPE/PS are different from the other materials since its T_g is much higher.

7.3 The Effect of Talc and Short Glass Fiber Additions on Fatigue Behavior of Polypropylene

The fatigue strength of PP-G is much higher than PP-T at both 23 °C and 85 °C due to the strengthening effect of the glass fibers, as shown in Figure 7-6(a) for $R = 0.1$ loading condition, with similar behavior at $R = 0.3$. The main reason for incorporating talc in polymers is to increase the stiffness. However, incorporation of talc reduces fatigue strength because of creation of voids in polymer matrix, which are suitable regions for initiation and growth of fatigue cracks [72]. Comparison of fatigue data of PP-T and PP-G which were normalized using ultimate tensile strength is shown in Figure 7-6(b). It can be seen that normalizing data by tensile strength brings data close together, but cannot still correlate them well, particularly in high cycle fatigue regime. Similar behavior was observed for $R = 0.3$ loading condition.

The effect of mold flow direction on tensile and fatigue behaviors of PP-T was evaluated by comparison of experimental results for specimens cut in 0° and 90° directions relative to the injection mold flow direction. The 0° (longitudinal) specimens have about 8% higher tensile and fatigue strengths, as compared to 90° (transverse) specimens, as shown in Figure 7-7 for PP-T at 23 °C. However, anisotropy due to the mold flow direction for PP-T is much less than short glass fiber reinforced thermoplastics where 40% difference between fatigue strength in the longitudinal and transverse directions was observed [61].

Talc particles have flaky shape and can become aligned in the molding direction and carry more load, as compared to the transverse direction. Figure 7-8 shows SEM micrographs of PP-T fracture surfaces in the molding and normal to the molding directions. Distinct regions for the damage initiation zone with microductile behavior and final fracture zone with microbrittle failure are evident. As shown in Figure 7-8, it is clear that talc layers are aligned along molding direction and dispersed uniformly in polypropylene matrix. There are no obvious aggregates, but some thicker talc particles are seen.

7.4 Mean Stress Effect and Modeling

The effect of tensile mean stress on fatigue behavior of the materials was investigated for $R = 0.1$ with $S_m = 1.22\ S_a$ and $R = 0.3$ with $S_m = 1.86\ S_a$ loading conditions. As shown in Figure 7-9, a significant decrease of fatigue strength is observed for $R = 0.3$ loading, as compared to $R = 0.1$ loading, for PP-T and PP-G at all temperatures. This effect is less for PA66/B compared to PP-T and PP-G and is negligible for PPE/PS. The effect of tensile mean stress is more pronounced in the high cycle fatigue (HCF) regime for PP-G at elevated temperatures. For PA66/B an opposite trend is observed at elevated temperatures.

The linear damage rule can be applied to roughly quantify the contribution of creep and fatigue damage, expressed as:

$$D = D_{fatigue} + D_{creep} = \sum \frac{N}{N_f} + \frac{t}{t_R} = 1 \tag{7.3}$$

where t is the time of the fatigue test, t_R is time to rupture in creep test at a stress level equal to the mean stress in the fatigue test, N is applied cycles, and N_f is the hypothetical pure fatigue life. According to this model failure takes place when the summation of creep and fatigue damage becomes one. Creep rupture curves of the studied materials reported in chapter 5, were used to calculate t_R. For PA66/B, PPE/PS, and PP-T creep damage was found to be negligble at all studied temperatures. For PP-G at 120 °C, about 30% of total damage was found to be caused by creep in HCF regime. Therefore, for PP-G at 120 °C the effect of cyclic creep can add to the detrimental effect of mean stress and results in more reduction in fatigue strength, mainly in HCF regime. It should be mentioned, however, that creep and fatigue interaction often results in more damage, as compared to addition of each damage individually, which is not considered in Equation 7.3.

For PA66/B, similar to what was observed for PBT and PA6 in [62], the mean stress effect is more pronounced in LCF regime. For PPE/PS the mean stress effect is negligible at both 23 and 85 °C. Two types of failure are commonly observed for polymer composites under cyclic loading, matrix yielding dominated failure or plasticity-controlled failure, and crack growth dominated failure or crack growth-controlled failure which starts from fiber/matrix bond [178, 179]. For plasticity-controlled failure, fatigue life is more related to the maximum stress, however, for crack growth-controlled failure fatigue life is more related to the amplitude of stress. For PPE/PS, the maximum stress in fatigue tests at both 23 and 85 °C under $R = 0.1$ and 0.3 conditions was less than the yield stress of material (0.2% offset), except for one data point at 85 °C for $R = 0.3$ condition which had fatigue life of about 100 cycles. Therefore, fatigue failure for PPE/PS was more related to the stress amplitude than the maximum stress. For PA66/B in LCF regime, fatigue failure was more related to the maximum stress than the amplitude of stress since maximum stress was higher than the yield stress of material. However, an opposite trend was observed in HCF regime.

Several mean stress models which were reviewed in [77, 78] have been used in different studies to model the effect of mean stress on fatigue behavior of talc-filled and short glass fiber reinforced thermoplastics. Modified Goodman is the most common mean stress correction model, expressed as:

$$\frac{S_a}{S_{Nf}} + \frac{S_m}{S_u} = 1 \tag{7.4}$$

where S_m is the mean stress, S_u is the ultimate tensile strength, and S_{Nf} is the equivalent fatigue strength at cycle N_f for fully-reversed condition. S_u values were obtained from the average of duplicate tension tests at a displacement rate of 1 mm min^{-1} and are reported in Table 7-2 for the materials studied. The correlated experimental data for PP-T, PP-G, PA66/B, and PPE/PS are shown in Figure 7-10. For PP-T and PP-G, this model correlated data very well at 23 °C, but not at 85 and 120 °C due to the effect of cyclic creep which is not accounted for in this model. For PA66 and PPE/PS, correlation of data is acceptable at all studied temperatures (23, 85, and 120 °C) and a factor of about 2 difference was observed between correlated data for $R = 0.1$ and 0.3 conditions.

Some modified versions of the modified Goodman model have been proposed to take into account the effect of cyclic creep. These include Goodman-Boller relation and Crawford model. These models incorporate creep rupture strength (S_c) rather than tensile strength (S_u). However, neither of these model improved the correlation of the mean stress data at elevated temperatures for PP-T and PP-G, over the modified Goodman correlations, similar to what was also observed for neat polypropylene and talc-filled polyolefin in [77].

The Walker equation has been shown by Mortazavian and Fatemi [62] and Mellott and Fatemi [180] to better consider the effect of mean stress for thermoplastic composites. This model is expressed as:

$$S_{Nf} = (S_a + S_m)^{1-\gamma}(S_a)^{\gamma} \tag{7.5}$$

where γ is a mean stress sensitivity material parameter. A value of $\gamma = 1$ indicates no mean stress sensitivity and low γ values indicate high mean stress sensitivity. γ values are determined by the best correlations of data for R = 0.1 and 0.3 conditions. The fits of experimental data for PP-T, PP-G, PA66, and PPE/PS based on the Walker equation are shown in Figure 7-11. This model provides reasonable correlation of data for all the studied materials at all temperatures.

The value of γ was found to be one for PPE/PS at 23 and 85 °C (i.e. no mean stress sensitivity for these conditions evaluated). Comparison of γ values as a function of ultimate tensile strength for PP-T, PP-G, and PA66/B with those obtained for PA6 and PBT in the study of Mortazavian and Fatemi [62] and neat polypropylene (PP) and talc-filled polyolefin (PO) in the study of Mellott and Fatemi [180] are shown in Figure 7-12. For PA66/B at 23 and 85 °C, the γ value is 0.35, which is lower, as compared to what was obtained to be 0.47 for PBT and PA6 at 23 °C. However, for PA66 at 120 °C the γ value is 0.13 and is consistent with the fit obtained for PA6 and PBT at 125 °C, expressed as:

$$\gamma = 0.0043 S_u + 0.36 \tag{7.6}$$

For PP-T at 23 °C, the γ value is 0.12 and is consistent with the fit obtained for PP and PO at -40 and 23 °C, expressed as:

$$\gamma = -0.0022 S_u + 0.19 \tag{7.7}$$

For PP-T at 85 °C and PP-G at 120 °C, the γ value is -0.1 which is the same as that obtained for PP at 85 °C and indicates considerable mean stress sensitivity due to the cyclic creep effects for these conditions. For PP-G, γ values are 0.28 and 0.15 at 23 and 85 °C, respectively. These values are less than those obtained for PA66/B, indicating more mean stress sensitivity for PP-G, as compared to PA66/B.

7.5 Correlation of Fatigue Data with a General Model

A fatigue life prediction model based on strength degradation of a polymeric material under constant amplitude loading developed by Epaarachchi and Clausen [170] was applied to the experimental fatigue data in this study. A variation of this model which does not consider the effect of frequency was also applied to PA6 and PBT fatigue data (materials for which the strengthening effect of frequency is negligible) by Mortazavian and Fatemi [61, 62] to consider the effect of temperature, anisotropy, and mean stress. This model is expressed as:

$$S_u - S_{\max} = \alpha\ S_u^{1-\xi} S_{\max}^{\xi} (1-R)^{\xi}\ \frac{1}{f^{\beta}} (N_f{}^{\beta} - 1) \tag{7.8}$$

where S_{max} is the maximum stress, f is the cycling frequency, α and β are material constants, and ξ is a function of stress ratio and mold flow direction, expressed as:

$$\begin{aligned} &\xi = 1.6 - R\sin\theta && \text{for reinforced and filled polymers} \\ &\xi = 1.6 - R && \text{for neat polymers} \end{aligned} \tag{7.9}$$

where θ is the angle between the mold flow direction and the loading direction. For non-frequency sensitive materials, f is assumed to be 1 in the model.

The rearranged form of Equation 7.8 in the following form was used to find constants α and β:

$$\frac{f^{\beta}(S_u - S_{\max})}{S_u^{1-\xi} S_{\max}^{\xi} (1-R)^{\xi}} = \alpha\ (N_f{}^{\beta} - 1) \tag{7.10}$$

To determine appropriate values of α and β, the left side of Equation 7.10 was plotted against ($N_f{}^{\beta}-1$) for an arbitrary value of β for each material and testing condition. This procedure is repeated for different β values until a high degree of correlation for the fit of data which passes through origin was obtained.

This model was applied to the fatigue data of PP-T, PP-G, PA66/B, PA66/D and PPE/PS at different test temperatures and stress ratios. Data for the two mold flow directions for PP-T at 23 °C were also included. To evaluate robustness of the model, PO and PP data at different test temperatures and stress ratios [180] were also analyzed using this model. $\beta = 0.2$ was obtained for all the materials, except for PPE/PS for which β was found to be 0.35. The value of α at low temperatures (23 °C and -40 °C) was independent of R ratio for all the materials. However, for PP-T and PP-G at elevated temperatures (85 °C and 120 °C), there was a difference between the values for $R = 0.1$ and 0.3. This may because of the effect of creep at elevated temperatures. For PP-T at 23 °C, the value of α was found to be independent of mold flow direction at $\alpha = 0.048$. The α values at different test conditions are included in Table 7-2.

In the study of Mortazavian and Fatemi [61], for PBT and PA6 in the transverse direction, α values were suggested to be 0.074 for 23 °C tests and to be 0.105 for 125 °C tests. For PP-G, PA66/B, PA66/D, and PPE/PS for 23 °C tests in this study, $\alpha = 0.074$ is also a reasonable approximation. For PA66/B and PPE/PS at elevated temperatures (85 and 120 °C), α is also approximated as 0.105. The value of α was reported to be dependent to the fiber orientation for reinforced materials in [61] and $\alpha = -0.0005\,\theta + 0.118$ was suggeted at 23 °C. Applicability of this relation at other temperatures was not investigated. For PP, PO, and PP-T (un-reinforced materials) at 23 °C, α can be approximated as $\alpha = 0.0041\,S_u + 0.166$. For PP-T and PP-G at elevated temperatures (85 and 120 °C), α can be approximated as $\alpha = 0.0028\,S_u$. For PP and PO, no correlation was found for -40 and 85 °C tests. Above suggested α values and correlations along with those reported in the study of Mortazavian and Fatemi [61] can be used for prediction of fatigue life for different thermoplastic composites in absence of any fatigue data. A summary of the suggested values for α is provided in Table 7-3.

Based on Equation 7.10, an equivalent stress can be derived as:

$$S_{eq} = A\left(\frac{(S_u - \frac{\Delta S}{1-R})\,f^{\beta}}{\alpha\, S_u^{\,1-\xi}(\Delta S)^{\xi}} + 1\right)^{B/\beta} \tag{7.11}$$

where *A* and *B* are the intercept and slope of *S*-*N* line for a reference condition. Again, for non-frequency sensitive materials, *f* is assumed to be 1 in the model.

Plots of estimated fatigue lives versus experimental fatigue lives and correlation of equivalent stress values versus experimental fatigue life using the suggested α and β values are shown in Figures 7-13(a) and (b), respectively. PP, PO, PP-T, PP-G, and PPE/PS are materials for which the strengthening effect of increased frequency was observed. However, for PA66, PA6, and PBT the strengthening effect of increased frequency was not observed. These graphs include predictions or corelations for 9 different neat, talc-filled, and short glass fiber reinforced thermoplastics. Several effects, including temperature (-40, 23, 85, 120, and 125 °C), mean stress (*R* = -1, 0.1, and 0.3), thickness, and mold flow direction (longitudinal, 18°, 45°, and transverse with respect to the loading axis), and frequency (the strengthening effect) are considered. As can be seen in Figure 7-13(a), which include 540 data points, 86% of the predicted fatigue lives are within a factor of 3, 93% are within a factor of 5, and 99% are within a factor of 10 of the experimental lives.

Table 7-1: Summary of fatigue test results of PP-T, PP-G, PA66/B, PA66/D, and PPE/PS.

Mold Flow Dir.	Specimen ID	Temp. (°C)	Stress Ratio (*R*)	Stress Amp. (MPa)	Freq. (Hz)	Midlife Disp. Amp. (mm)	Midlife Disp. Mean (mm)	Cycles to Failure	Failure Location
PP-T									
T	PPT-F-R-1	23	0.1	12	0.25	0.179	0.245	333	IGIT
T	PPT-F-R-2	23	0.1	12	0.25	0.181	0.275	392	IGIT
T	PPT-F-R-2.5	23	0.1	11.5	0.5	0.153	0.268	3,154	IGIT
T	PPT-F-R-3	23	0.1	11	0.25-0.5	0.149	0.646	6,343	IGIT
T	PPT-F-R-4	23	0.1	11	0.5	0.146	0.251	4,814	IGIT
T	PPT-F-R-4.5	23	0.1	10.5	1	0.122	0.320	70,648	IGIT
T	PPT-F-R-5	23	0.1	10	2	0.115	0.467	282,059	IGIT
T	PPT-F-R-6	23	0.1	10	3	0.119	0.583	134,811	IGIT
T	PPT-F-R-7	23	0.1	9.5	5	-	-	>1,000,000	Run out
L	PPT-F-R-L-5	23	0.1	12.75	0.25	0.180	0.250	610	IGIT
L	PPT-F-R-L-6	23	0.1	12.75	0.25	0.178	0.244	587	IGIT
L	PPT-F-R-L-2	23	0.1	12	0.75	0.161	0.301	4,856	IGIT
L	PPT-F-R-L-1	23	0.1	12	0.25-0.75	0.159	0.233	9,376	IGIT
L	PPT-F-R-L-4	23	0.1	11	2	0.130	0.219	198,063	IGIT
L	PPT-F-R-L-3	23	0.1	11	2	0.129	0.258	178,992	IGIT
T	PPT-F3-R-1	23	0.3	9.4	0.25	0.131	0.228	386	IGIT
T	PPT-F3-R-2	23	0.3	9.2	0.25	0.128	0.298	621	IGIT
T	PPT-F3-R-3	23	0.3	8.9	1	0.110	0.576	7,504	IGIT
T	PPT-F3-R-4	23	0.3	8.9	1	0.115	0.434	6,248	IGIT
T	PPT-F3-R-5	23	0.3	8.5	2	0.100	0.513	47,451	IGIT
T	PPT-F3-R-6	23	0.3	8.5	2	0.095	0.385	53,131	IGIT
T	PPT-F3-R-7	23	0.3	8.1	4	0.0855	0.639	262,485	IGIT
T	PPT-F3-R-8	23	0.3	8.1	4	0.0835	0.696	282,503	IGIT
T	PPT-F3-R-9	23	0.3	8.1	4	0.0815	0.606	360,008	IGIT
T	PPT-F-H1-1	85	0.1	5.25	0.25	0.171	0.379	1,364	IGIT
T	PPT-F-H1-2	85	0.1	5.25	0.25	0.186	0.497	1,150	IGIT
T	PPT-F-H1-3	85	0.1	5	1	0.144	0.571	27,079	IGIT
T	PPT-F-H1-4	85	0.1	5	1	0.140	0.511	18,017	OGIT
T	PPT-F-H1-5	85	0.1	4.75	2	0.117	0.457	155,770	IGIT
T	PPT-F-H1-6	85	0.1	4.75	2	0.118	0.482	124,809	IGIT
T	PPT-F-H1-7	85	0.1	4.6	2-4	0.110	0.729	678,918	IGIT
T	PPT-F3-H1-1	85	0.3	3.8	0.5	0.1105	0.6305	2,231	No Break
T	PPT-F3-H1-2	85	0.3	3.8	0.5	0.1065	0.591	3,567	No Break
T	PPT-F3-H1-5	85	0.3	3.7	1	-	-	11,957	IGIT
T	PPT-F3-H1-6	85	0.3	3.7	1	0.093	0.567	13,628	IGIT
T	PPT-F3-H1-3	85	0.3	3.6	2	0.0795	0.6515	121,545	IGIT
T	PPT-F3-H1-4	85	0.3	3.6	2	0.0785	0.482	116,798	IGIT
T	PPT-F3-H1-7	85	0.3	3.5	3	0.073	0.506	194,328	IGIT
PP-G									
T	PPG-F-R-1	23	0.1	18	0.25	0.318	0.308	437	OGIT
T	PPG-F-R-2	23	0.1	18	0.25	0.286	0.295	833	OGIT
T	PPG-F-R-3	23	0.1	16	0.25-0.5	0.249	0.330	3,531	IGIT
T	PPG-F-R-4	23	0.1	16	0.5	0.250	0.324	3,482	IGIT
T	PPG-F-R-4.5	23	0.1	15	1-2	0.206	0.384	68,166	IGIT
T	PPG-F-R-5	23	0.1	14	2	0.200	0.719	90,340	IGIT
T	PPG-F-R-6	23	0.1	14	3	0.187	0.562	281,516	OGIT
T	PPG-F-R-7	23	0.1	13.25	5	0.163	0.704	935,406	IGIT

Table 7-1 (Cont'd): Summary of fatigue test results of PP-T, PP-G, PA66/B, PA66/D, and PPE/PS.

Mold Flow Dir.	**Specimen ID**	**Temp. (°C)**	**Stress Ratio (*R*)**	**Stress Amp. (MPa)**	**Freq. (Hz)**	**Midlife Disp. Amp. (mm)**	**Midlife Disp. Mean (mm)**	**Cycles to Failure**	**Failure Location**
PP-G									
T	PPG-F3-R-1	23	0.3	14	0.25	0.208	0.478	898	IGIT
T	PPG-F3-R-2	23	0.3	14	0.25	0.201	0.434	1,281	IGIT
T	PPG-F3-R-4	23	0.3	13	1	0.1775	0.523	8,691	IGIT
T	PPG-F3-R-3	23	0.3	12	1	0.156	0.609	37,733	OGIT
T	PPG-F3-R-3.5	23	0.3	12	1	0.156	0.408	34,299	IGIT
T	PPG-F3-R-5	23	0.3	11.3	2	0.139	0.400	257,962	IGIT
T	PPG-F3-R-6	23	0.3	11.3	3	0.137	0.540	330,337	IGIT
T	PPG-F3-R-7	23	0.3	10.8	5	-	-	>1,000,000	Run out
T	PPG-F-H1-0.5	85	0.1	8.3	0.25	0.235	0.813	1,561	IGIT
T	PPG-F-H1-1	85	0.1	8	0.25	0.223	0.573	2,214	IGIT
T	PPG-F-H1-2	85	0.1	8	0.25	0.219	0.512	2,612	IGIT
T	PPG-F-H1-3	85	0.1	7.5	1	0.187	0.575	26,126	IGIT
T	PPG-F-H1-4	85	0.1	7.5	1	0.183	0.443	25,466	IGIT
T	PPG-F-H1-5	85	0.1	7.25	2	0.173	0.527	116,328	IGIT
T	PPG-F-H1-6	85	0.1	7.25	3	0.173	0.609	146,194	IGIT
T	PPG-F-H1-7	85	0.1	6.9	5	0.152	0.546	534,842	IGIT
T	PPG-F3-H1-3	85	0.3	6.5	0.25	0.173	0.582	967	IGIT
T	PPG-F3-H1-6	85	0.3	6.5	0.25	0.164	0.832	1,360	IGIT
T	PPG-F3-H1-7	85	0.3	5.85	1	0.131	0.445	14,543	IGIT
T	PPG-F3-H1-10	85	0.3	5.85	1	0.134	0.599	14,799	IGIT
T	PPG-F3-H1-4	85	0.3	5.25	1	0.113	0.608	92,210	IGIT
T	PPG-F3-H1-5	85	0.3	5.25	2	0.109	0.48	129,023	IGIT
T	PPG-F3-H1-8	85	0.3	4.85	5	-	-	>1,000,000	Run out
T	PPG-F-H2-1	120	0.1	5	0.25	0.203	1.129	1,354	IGIT
T	PPG-F-H2-2	120	0.1	5	0.25	-	-	1,112	IGIT
T	PPG-F-H2-2.5	120	0.1	4.85	0.5	0.192	0.717	4,977	IGIT
T	PPG-F-H2-3	120	0.1	4.7	1	0.1765	0.744	18,911	IGIT
T	PPG-F-H2-5	120	0.1	4.7	1	0.174	0.741	25,788	IGIT
T	PPG-F-H2-4.5	120	0.1	4.6	2	0.155	0.675	83,717	IGIT
T	PPG-F-H2-4	120	0.1	4.25	1-4	0.132	0.592	349,497	IGIT
T	PPG-F-H2-6	120	0.1	4.25	4	-	-	>1,000,000	Run out
T	PPG-F3-H2-1	120	0.3	3.8	0.25	0.157	1.470	1,103	IGIT
T	PPG-F3-H2-22	120	0.3	3.8	0.25	0.158	1.488	972	IGIT
T	PPG-F3-H2-3	120	0.3	3.6	1	0.124	0.885	7,867	IGIT
T	PPG-F3-H2-6	120	0.3	3.6	0.5	0.132	1.436	4,259	IGIT
T	PPG-F3-H2-5	120	0.3	3.3	2	0.099	0.673	76,106	IGIT
T	PPG-F3-H2-7	120	0.3	3.1	4	0.090	0.745	132,774	IGIT
T	PPG-F3-H2-8	120	0.3	3.1	3	0.090	0.635	232,443	OGIT
PA66/B									
T	PAB-F-R-1	23	0.1	39	0.25	0.411	0.516	2,106	OGIT
T	PAB-F-R-2	23	0.1	39	0.25	0.402	0.207	1,958	OGIT
T	PAB-F-R-3	23	0.1	36	1	0.363	0.190	6,241	OGIT
T	PAB-F-R-4	23	0.1	33	1	0.321	0.241	26,001	IGIT
T	PAB-F-R-5	23	0.1	30	2	0.285	0.511	78,924	OGIT
T	PAB-F-R-6	23	0.1	30	3	0.285	0.225	81,008	OGIT
T	PAB-F-R-7	23	0.1	26	5	0.240	0.538	463,135	OGIT
T	PAB-F-R-8	23	0.1	26	5	0.237	0.531	915,004	OGIT

Table 7-1 (Cont'd): Summary of fatigue test results of PP-T, PP-G, PA66/B, PA66/D, and PPE/PS.

Mold Flow Dir.	**Specimen ID**	**Temp. (°C)**	**Stress Ratio (*R*)**	**Stress Amp. (MPa)**	**Freq. (Hz)**	**Midlife Disp. Amp. (mm)**	**Midlife Disp. Mean (mm)**	**Cycles to Failure**	**Failure Location**
PA66/B									
T	PAB-F3-R-2	23	0.3	31	0.25	0.337	0.761	971	IGIT
T	PAB-F3-R-3	23	0.3	31	0.25	0.337	0.524	824	IGIT
T	PAB-F3-R-9	23	0.3	28	0.5	0.282	0.780	9,442	OGIT
T	PAB-F3-R-4	23	0.3	27	1	0.270	0.844	20,677	OGIT
T	PAB-F3-R-5	23	0.3	27	1	0.270	0.791	18,667	OGIT
T	PAB-F3-R-6	23	0.3	22	2	0.211	0.525	259,448	OGIT
T	PAB-F3-R-7	23	0.3	22	3	0.210	0.549	348,328	OGIT
T	PAB-F-H1-1	85	0.1	21	0.25	0.519	0.504	745	OGIT
T	PAB-F-H1-2	85	0.1	21	0.25	0.500	0.536	1,290	IGIT
T	PAB-F-H1-3	85	0.1	17.5	1	0.373	0.487	17,889	IGIT
T	PAB-F-H1-4	85	0.1	17.5	1	0.354	0.629	19,977	OGIT
T	PAB-F-H1-5	85	0.1	15.5	2	0.295	0.455	95,141	IGIT
T	PAB-F-H1-6	85	0.1	15.5	2	0.289	0.386	53,694	OGIT
T	PAB-F-H1-7	85	0.1	13.7	5	0.239	0.464	264,698	IGIT
T	PAB-F3-H1-1	85	0.3	16	0.25	0.391	1.159	1,278	IGIT
T	PAB-F3-H1-2	85	0.3	16	0.25	0.411	0.917	1,136	IGIT
T	PAB-F3-H1-5	85	0.3	14.5	1	0.353	1.434	10,514	IGIT
T	PAB-F3-H1-3	85	0.3	13	1	0.297	1.255	40,904	OGIT
T	PAB-F3-H1-4	85	0.3	13	2	0.28	1.133	41,731	OGIT
T	PAB-F3-H1-7	85	0.3	12	3	0.251	1.143	232,235	OGIT
T	PAB-F3-H1-8	85	0.3	12	3	0.220	1.049	345,349	IGIT
T	PAB-F3-H1-6	85	0.3	11	3	0.197	0.590	869,528	IGIT
T	PAB-F-H2-1	120	0.1	17	0.25	0.550	0.498	444	IGIT
T	PAB-F-H2-2	120	0.1	16	0.25	0.544	0.735	1,219	IGIT
T	PAB-F-H2-3	120	0.1	14	0.5	0.454	0.615	4,919	IGIT
T	PAB-F-H2-4	120	0.1	14	0.5	0.423	1.048	13,301	IGIT
T	PAB-F-H2-5	120	0.1	12	2	0.296	0.690	98,209	OGIT
T	PAB-F-H2-6	120	0.1	12	2	0.310	0.424	94,256	IGIT
T	PAB-F-H2-7	120	0.1	10.5	3	0.235	0.817	287,761	OGIT
T	PAB-F-H2-8	120	0.1	10.5	3	0.241	0.333	281,467	OGIT
T	PAB-F3-H2-1	120	0.3	13	0.5	0.423	0.982	1,779	IGIT
T	PAB-F3-H2-2	120	0.3	13	0.25	0.390	1.057	2,626	IGIT
T	PAB-F3-H2-6	120	0.3	12	1	0.366	0.958	9,576	OGIT
T	PAB-F3-H2-5	120	0.3	12	1	0.344	1.269	8,974	IGIT
T	PAB-F3-H2-3	120	0.3	11	0.5-1	0.297	1.124	46,485	IGIT
T	PAB-F3-H2-4	120	0.3	11	2	0.277	1.201	103,001	IGIT
T	PAB-F3-H2-7	120	0.3	10	4	0.246	0.637	210,862	IGIT
T	PAB-F3-H2-8	120	0.3	10	4	0.221	0.985	419,326	IGIT
PA66/D									
T	PAD-F-R-1	23	0.1	41	0.25	0.420	0.571	2,400	OGIT
T	PAD-F-R-2	23	0.1	41	0.25	0.424	0.563	2,138	IGIT
T	PAD-F-R-3	23	0.1	37	1	0.355	0.251	21,884	IGIT
T	PAD-F-R-4	23	0.1	37	1	0.370	0.300	11,210	IGIT
T	PAD-F-R-5	23	0.1	34	2	0.319	0.428	64,068	OGIT
T	PAD-F-R-6	23	0.1	34	2	0.312	0.543	56,232	OGIT
T	PAD-F-R-7	23	0.1	31	4	0.290	0.534	172,743	OGIT
T	PAD-F-R-8	23	0.1	31	4	0.283	0.556	224,340	OGIT

Table 7-1 (Cont'd): Summary of fatigue test results of PP-T, PP-G, PA66/B, PA66/D, and PPE/PS.

Mold Flow Dir.	**Specimen ID**	**Temp. (°C)**	**Stress Ratio (*R*)**	**Stress Amp. (MPa)**	**Freq. (Hz)**	**Midlife Disp. Amp. (mm)**	**Midlife Disp. Mean (mm)**	**Cycles to Failure**	**Failure Location**
PA66/D									
T	PAD-F-R-9	23	0.1	29	5	0.265	0.313	511,721	OGIT
T	PAD-F-H1-1	85	0.1	22	0.25	0.553	0.568	1,093	OGIT
T	PAD-F-H1-2	85	0.1	22	0.25	0.525	0.507	1,670	IGIT
T	PAD-F-H1-3	85	0.1	19	1	0.447	0.512	13,099	IGIT
T	PAD-F-H1-4	85	0.1	19	1	0.379	0.801	28,070	IGIT
T	PAD-F-H1-5	85	0.1	17.25	2	0.314	0.798	119,472	IGIT
T	PAD-F-H1-6	85	0.1	17.25	2	0.337	0.686	77,934	IGIT
T	PAD-F-H1-7	85	0.1	15.7	5	0.259	0.771	408,221	OGIT
PPE/PS									
T	FRM-F-R-3	23	0.1	22	0.5	0.265	0.156	1,359	OGIT
T	FRM-F-R-4	23	0.1	22	0.5	0.255	0.090	1,733	IGIT
T	FRM-F-R-9	23	0.1	18	1	0.203	0.033	7,389	OGIT
T	FRM-F-R-10	23	0.1	18	1	0.201	0.243	6,210	OGIT
T	FRM-F-R-7	23	0.1	14	2	0.151	0.043	40,189	OGIT
T	FRM-F-R-6	23	0.1	14	2	0.151	0.041	51,296	IGIT
T	FRM-F-R-8	23	0.1	11	3	0.117	0.049	175,424	OGIT
T	FRM-F-R-11	23	0.1	11	3	0.116	0.2885	199,672	OGIT
T	FRM-F-R-12	23	0.1	9	5	0.097	0.049	536,934	IGIT
T	FRM-F3-R-1	23	0.3	18	1	0.203	0.056	2,790	IGIT
T	FRM-F3-R-5	23	0.3	18	1	0.200	0.072	3,897	IGIT
T	FRM-F3-R-2	23	0.3	14	2	0.148	0.063	21,174	IGIT
T	FRM-F3-R-3	23	0.3	11	3	0.112	0.052	88,893	IGIT
T	FRM-F3-R-4	23	0.3	11	3	0.118	0.122	138,808	IGIT
T	FRM-F-H1-3	85	0.1	14	0.25	0.187	0.181	835	OGIT
T	FRM-F-H1-4	85	0.1	14	0.25	0.181	0.147	1,061	IGIT
T	FRM-F-H1-1	85	0.1	11	0.5	0.130	0.376	4,960	IGIT
T	FRM-F-H1-2	85	0.1	11	1	0.137	0.036	3,556	IGIT
T	FRM-F-H1-8	85	0.1	9	1	0.103	0.321	20480	IGIT
T	FRM-F-H1-5	85	0.1	7	2	0.089	0.314	89,936	OGIT
T	FRM-F-H1-6	85	0.1	7	2	0.086	0.032	58,434	OGIT
T	FRM-F-H1-7	85	0.1	5	4	0.051	0.044	732,836	IGIT
T	FRM-F3-H1-4	85	0.3	14	0.25	0.215	0.125	124	IGIT
T	FRM-F3-H1-2	85	0.3	11	1	0.132	0.056	3,270	IGIT
T	FRM-F3-H1-3	85	0.3	9	1	0.100	0.035	14,169	IGIT
T	FRM-F3-H1-1	85	0.3	7	1-2	0.085	0.045	68,478	IGIT

Table 7-2: Summary of fatigue test conditions and results for PP-T, PP-G, PA66/B, PA66/D, and PPE/PS, as well as analysis results for PP and PO.

Temp. (°C)	**Stress Ratio (*R*)**	**Fatigue Strength Intercept (*A*) (MPa)**	**Fatigue Strength Exponent (*B*)**	**Tensile Strength (MPa)**	**Elastic Modulus (MPa)**	**α**
PP-T						
23(L)	0.1	15.0	-0.026	31.5	4540	0.048
23(T)	0.1	14.3	-0.029	29.4	4100	0.047
23	0.3	10.7	-0.022	//	//	0.047
85	0.1	6.2	-0.022	13.8	1100	0.046
85	0.3	4.4	-0.019	//	//	0.079
PP-G						
23	0.1	23.2	-0.042	46.8	3300	0.085
23	0.3	18.4	-0.040	//	//	0.095
85	0.1	10.1	-0.029	21.7	1500	0.060
85	0.3	9.1	-0.047	//	//	0.102
120	0.1	5.8	-0.020	11.9	900	0.029
120	0.3	5.0	-0.039	//	//	0.076
PA66/D						
23	0.1	68.0	-0.064	106.6	5700	0.080
85	0.1	33.6	-0.058	60.4	1600	0.110
PA66/B						
23	0.1	66.8	-0.071	103.9	4800	0.090
23	0.3	46.9	-0.063	103.9	4800	0.101
85	0.1	36.3	-0.077	58.8	2200	0.128
85	0.3	23.9	-0.056	58.8	2200	0.123
120	0.1	27.1	-0.074	46.7	1600	0.134
120	0.3	19.7	-0.054	46.7	1600	0.106
PPE/PS						
23	0.1	66.8	-0.149	70.8	4500	0.055
23	0.3	55.1	-0.141	//	//	0.058
85	0.1	40.7	-0.156	46.7	3800	0.106
85	0.3	37.0	-0.151	//	//	0.112
PP						
-40	0.1	24.2	-0.035	52.6	3404	0.120
-40	0.3	18.0	-0.029	//	//	0.129
23	0.1	12.8	-0.041	24.7	1630	0.065
85	0.1	5.9	-0.051	11.5	566	0.105
PO						
-40	0.1	20.4	-0.042	37.5	5010	0.073
-40	0.3	13.8	-0.026	//	//	0.072
23	0.1	10.5	-0.073	15.6	2123	0.103
23	0.3	7.0	-0.053	//	//	0.090
85	0.1	2.8	-0.060	5.0	670	0.097

T: Transverse (loading axis perpendicular to mold flow direction)

L: Longitudinal (loading axis along mold flow direction)

Table 7-3: Summary of suggested values for α in the general fatigue model.

α	**Material**	**Direction**	**Temperature**
0.135	Reinforced Materials (PBT, PA6)	L	-40 °C, 23 °C, 125 °C
0.074	Reinforced Materials (PP-G, PA66, PPE/PS, PBT, PA6)	T	-40 °C and 23 °C
$\alpha = -0.0005\,\theta + 0.118$	Reinforced Materials (PBT, PA6)	0°, 18°, 45°, 90°	23 °C
0.105	Reinforced Materials (PA66, PPE/PS, PBT, PA6)	T	85 °C, 120 °C, 125 °C
$\alpha = 0.0041\,S_u + 0.166$	Unreinforced Materials (PP-T, PO, PP)	T or L	23 °C
$\alpha = 0.0028\,S_u$	PP-T and PP-G	T	85 °C, 120 °C

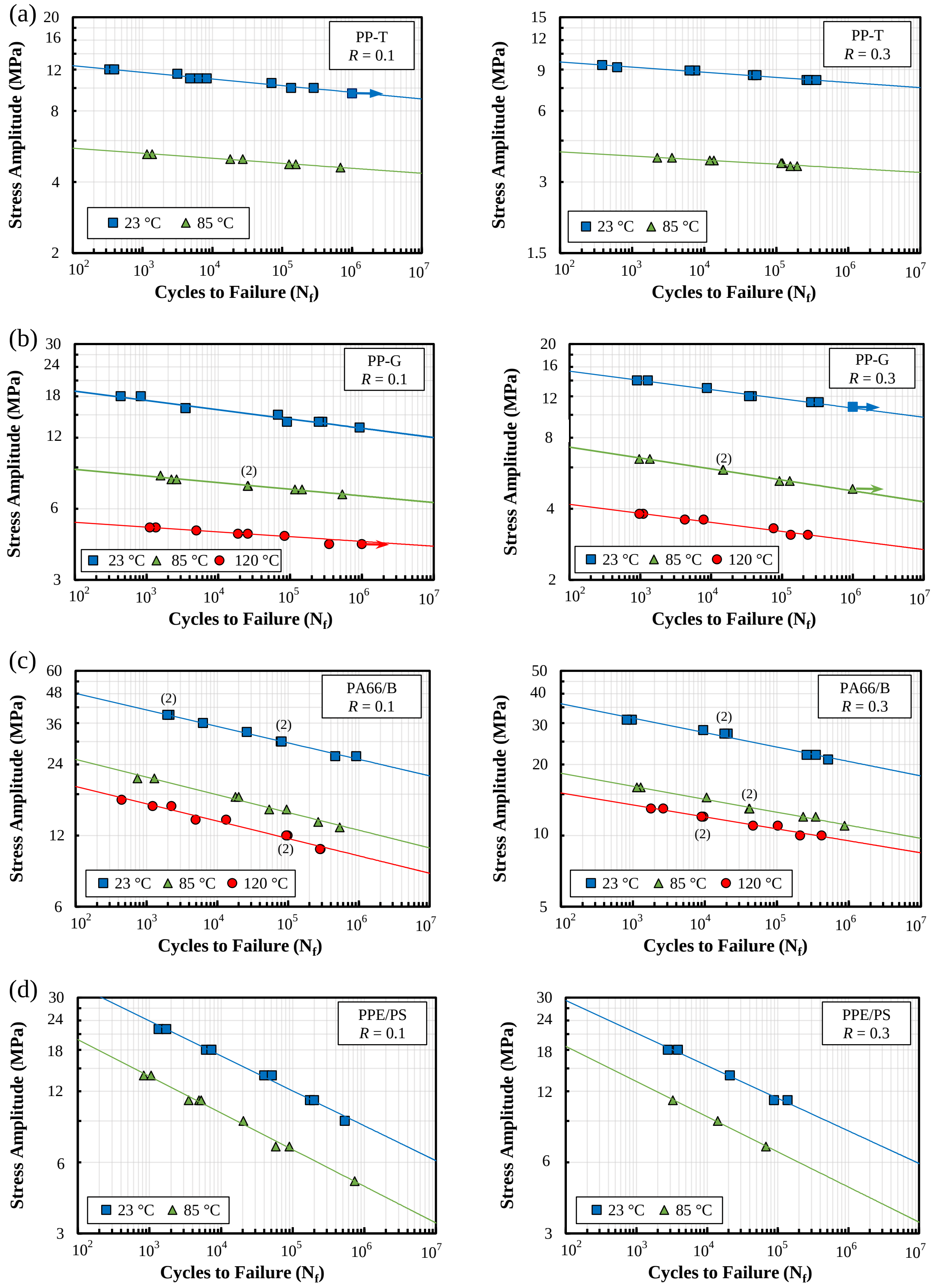

Figure 7-1: Effect of temperature on fatigue behavior under R = 0.1 and 0.3 loading conditions of (a) PP-T, (b) PP-G, (c) PA66/B, and, (d) PPE/PS.

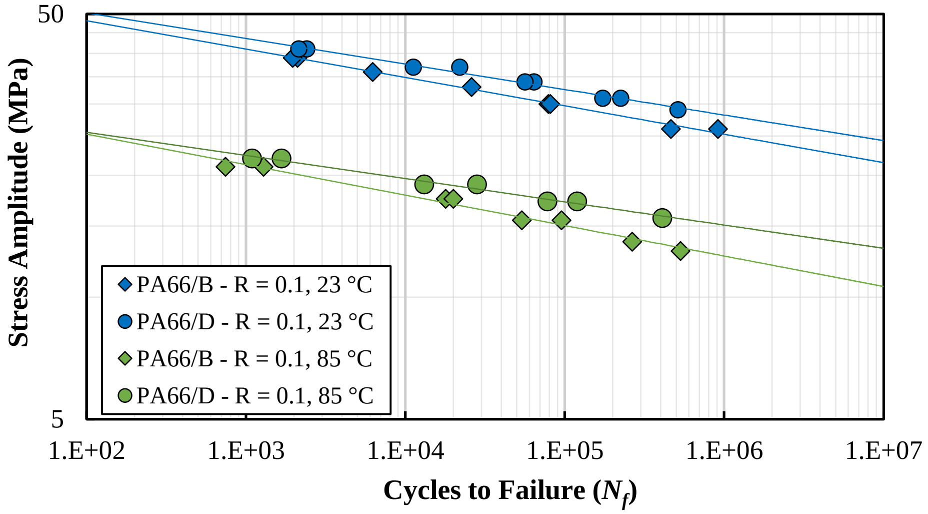

Figure 7-2: Comparison of fatigue *S*-*N* lines of PA66/B and PA66/D at 23 °C and 85 °C for $R = 0.1$ loading condition.

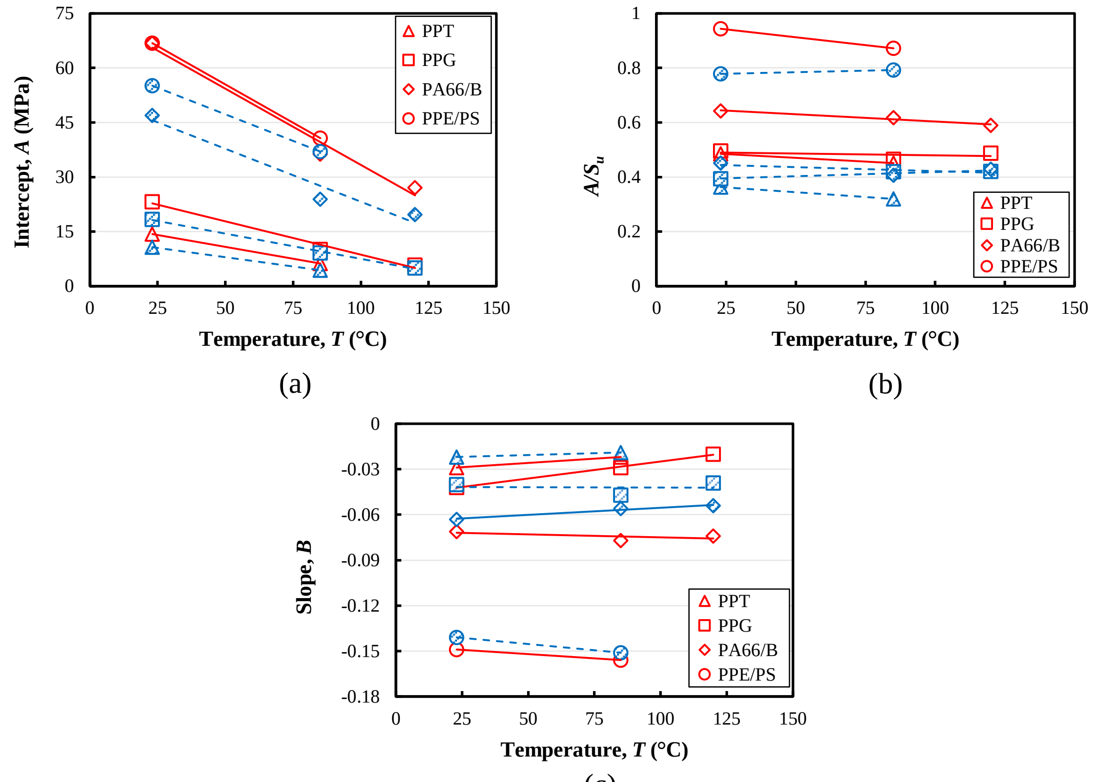

(a)

(b)

(c)

Figure 7-3: Variation of intercept *A* (a), normalized *A* values with S_u (b), and slope *B* (c) of *S*-*N* lines with temperature under *R* = 0.1 and 0.3 loading conditions. Hollow symbols and hashed symbols show *R* = 0.1 and *R* = 0.3 data, respectively. Solid lines and dashed lines are fit to *R* = 0.1 and *R* = 0.3 data, respectively.

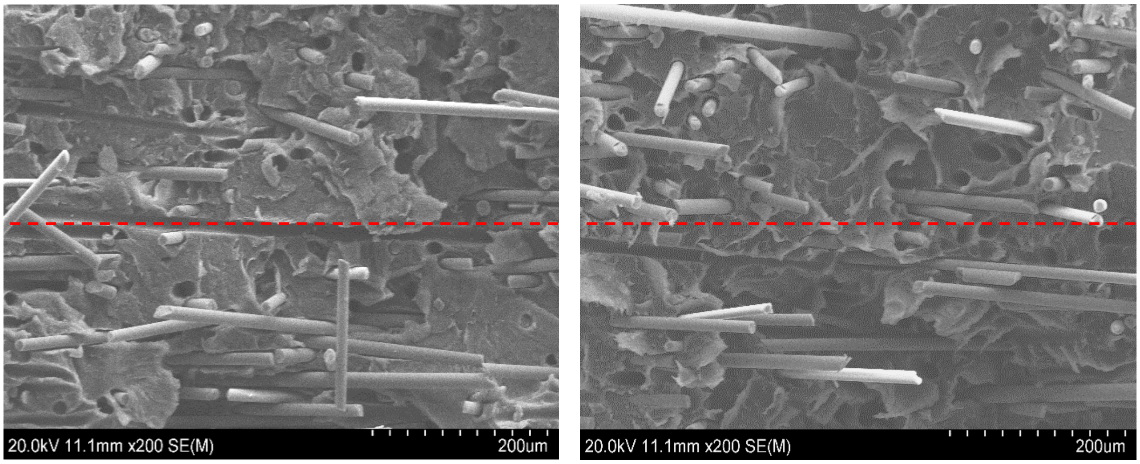

(a) (b)

Figure 7-4: SEM of fracture surface of PPE/PS under *R* = 0.1 loading condition with fatigue life of about 50,000 cycles at (a) 23 °C and, (b) 85 °C in the transverse to the mold flow direction. Upper part of the line is the core layer and lower part of the line is the shell layer.

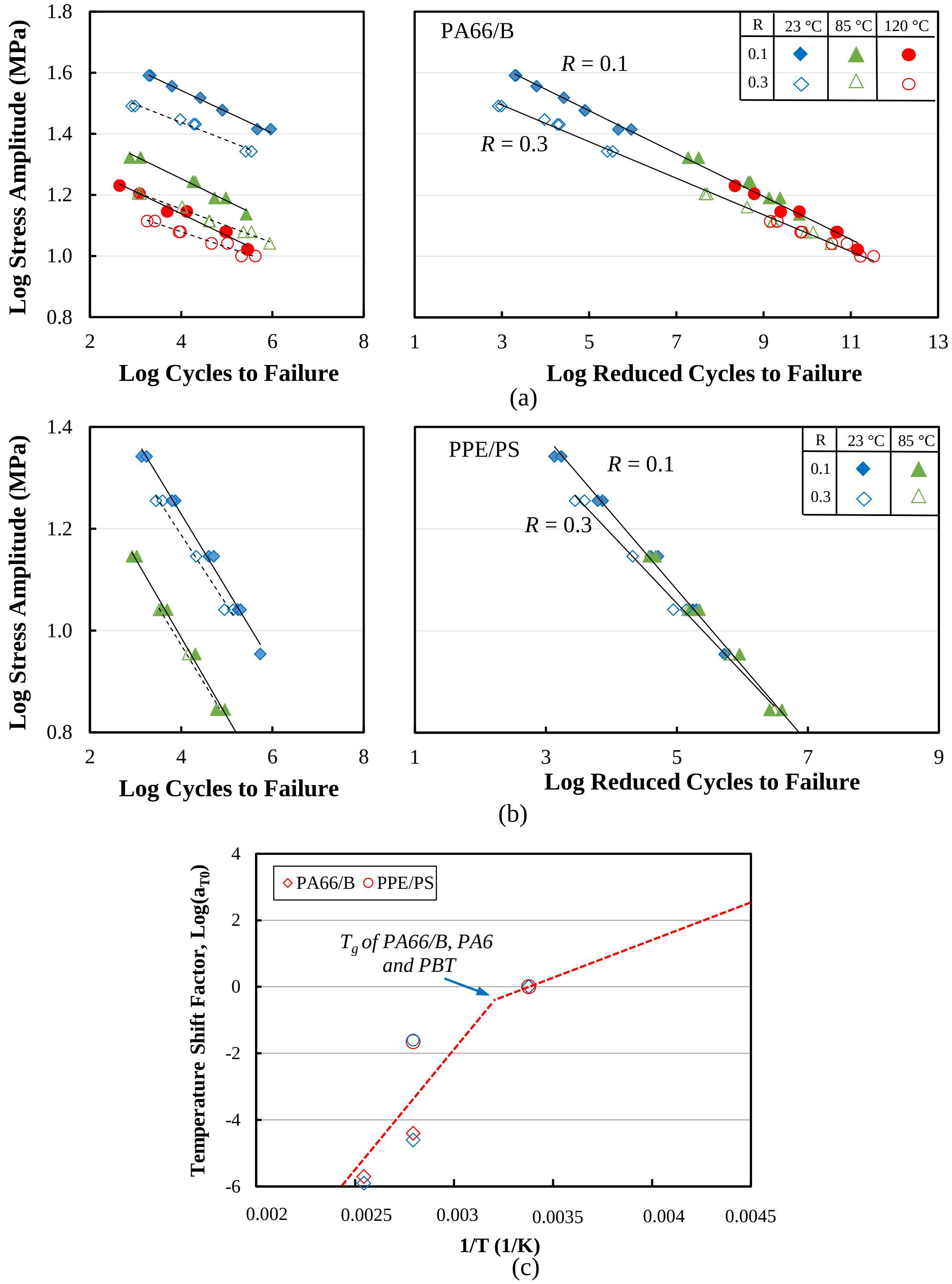

Figure 7-5: *S-N* master curves for R = 0.1 and 0.3 loading conditions for (a) PA66/B and (b) PPE/PS. (c) Variation of log shift factor with reciprocal of temperature for PA66/B and PPE/PS under R = 0.1 and 0.3 conditions. Solid lines are fits for PA6 and PBT data under R = -1 and 0.1 conditions [61].

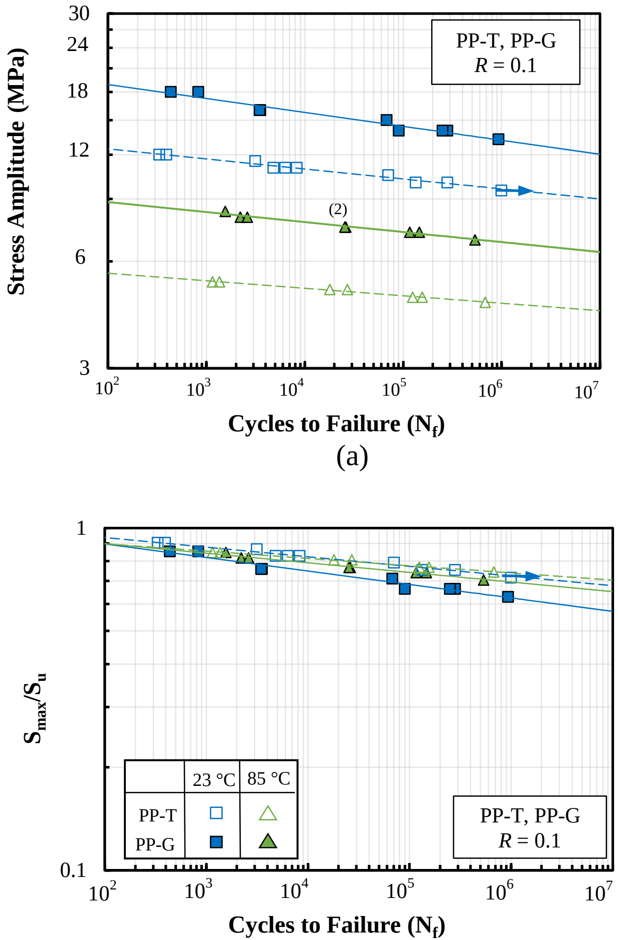

(a)

(b)

Figure 7-6: Comparison of fatigue data of PP-T and PP-G at 23 °C and 85 °C under R = 0.1 loading condition. (a) Stress amplitude versus cycles to failure data. (b) Normalized maximum stress with ultimate tensile strength versus cycles to failure data.

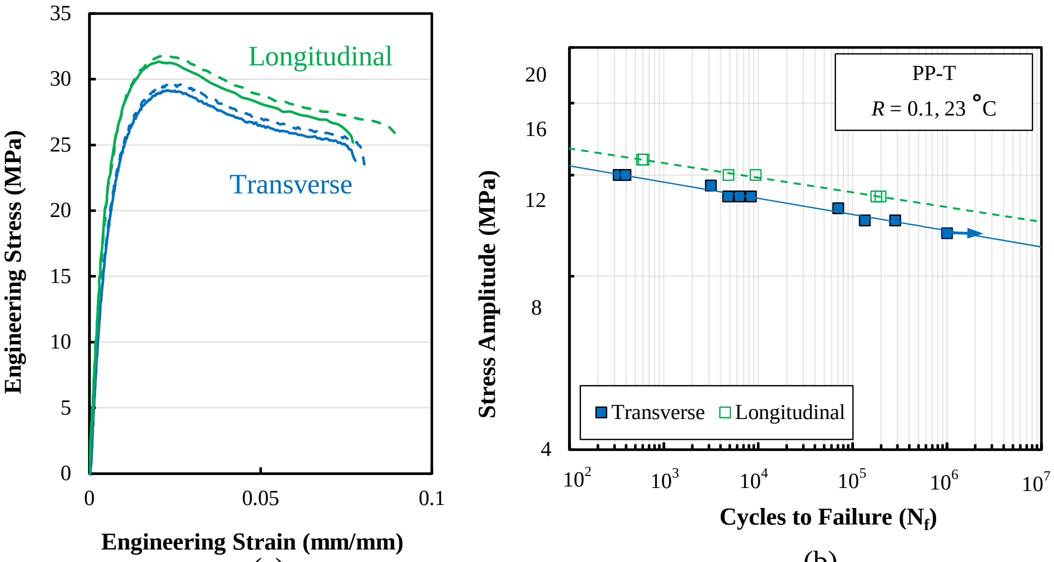

(a) (b)

Figure 7-7: Mold flow direction effect at 23 °C for PP-T (a) under tension test and (b) under fatigue test for R = 0.1 loading condition.

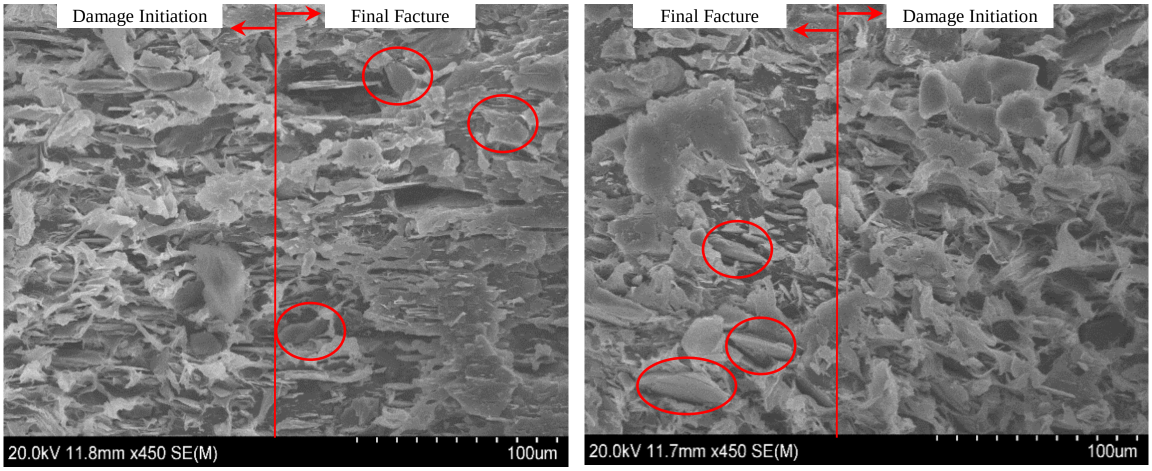

(a) (b)

Figure 7-8: SEM micrographs of PP-T fracture surfaces tested at 23 °C under R = 0.1 loading condition in (a) transverse and, (b) longitudinal directions. A few talc particles are distinguished in the final fracture zone in each picture.

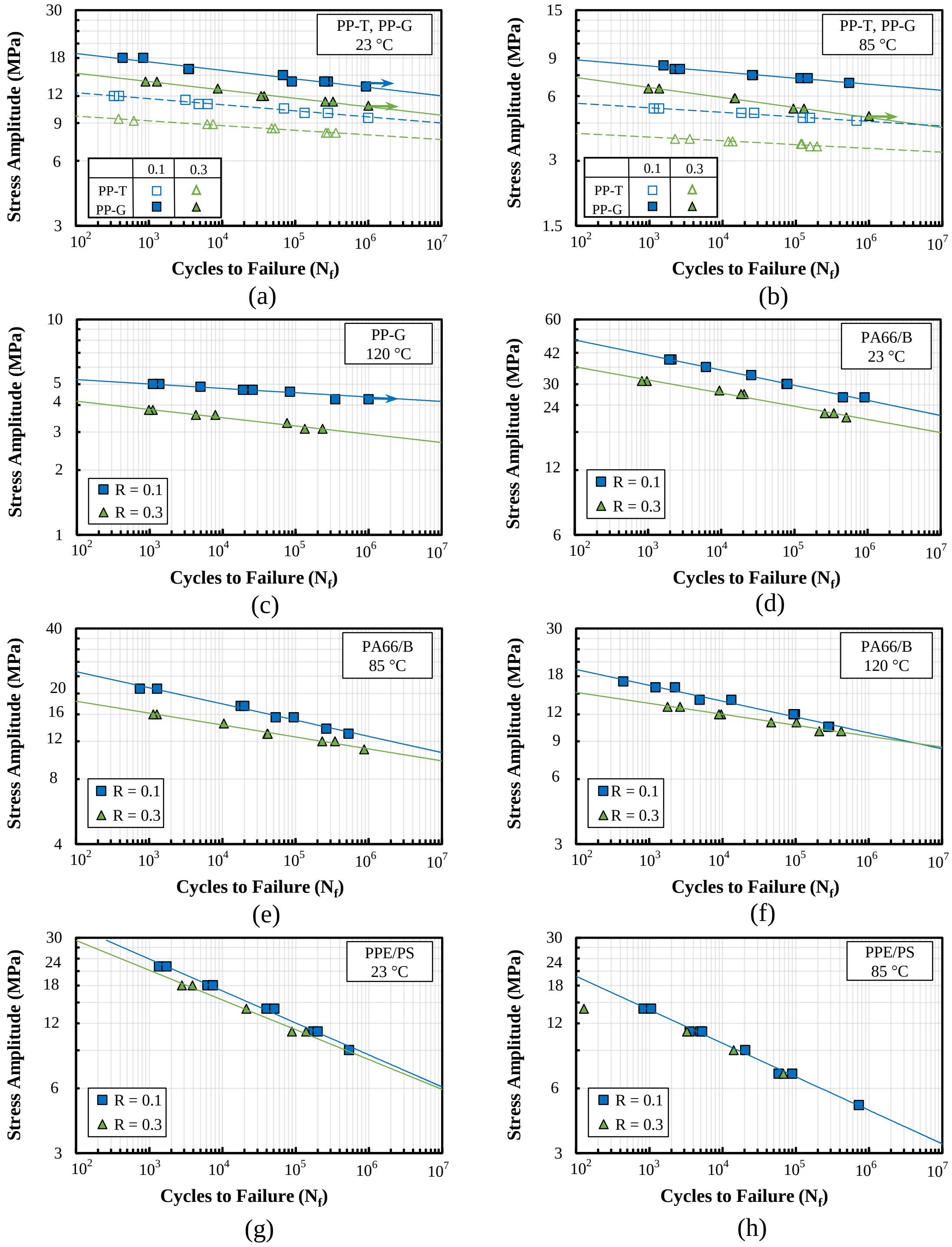

Figure 7-9: Effect of mean stress on fatigue behavior of (a) PP-T and PP-G at 23 °C, (b) PP-T and PP-G at 85 °C, (c) PP-G at 120 °C, (d) PA66/B at 23 °C, (e) PA66/B at 85 °C, (f) PA66/B at 120 °C, (g) PPE/PS at 23 °C and, (h) PPE/PS at 85 °C.

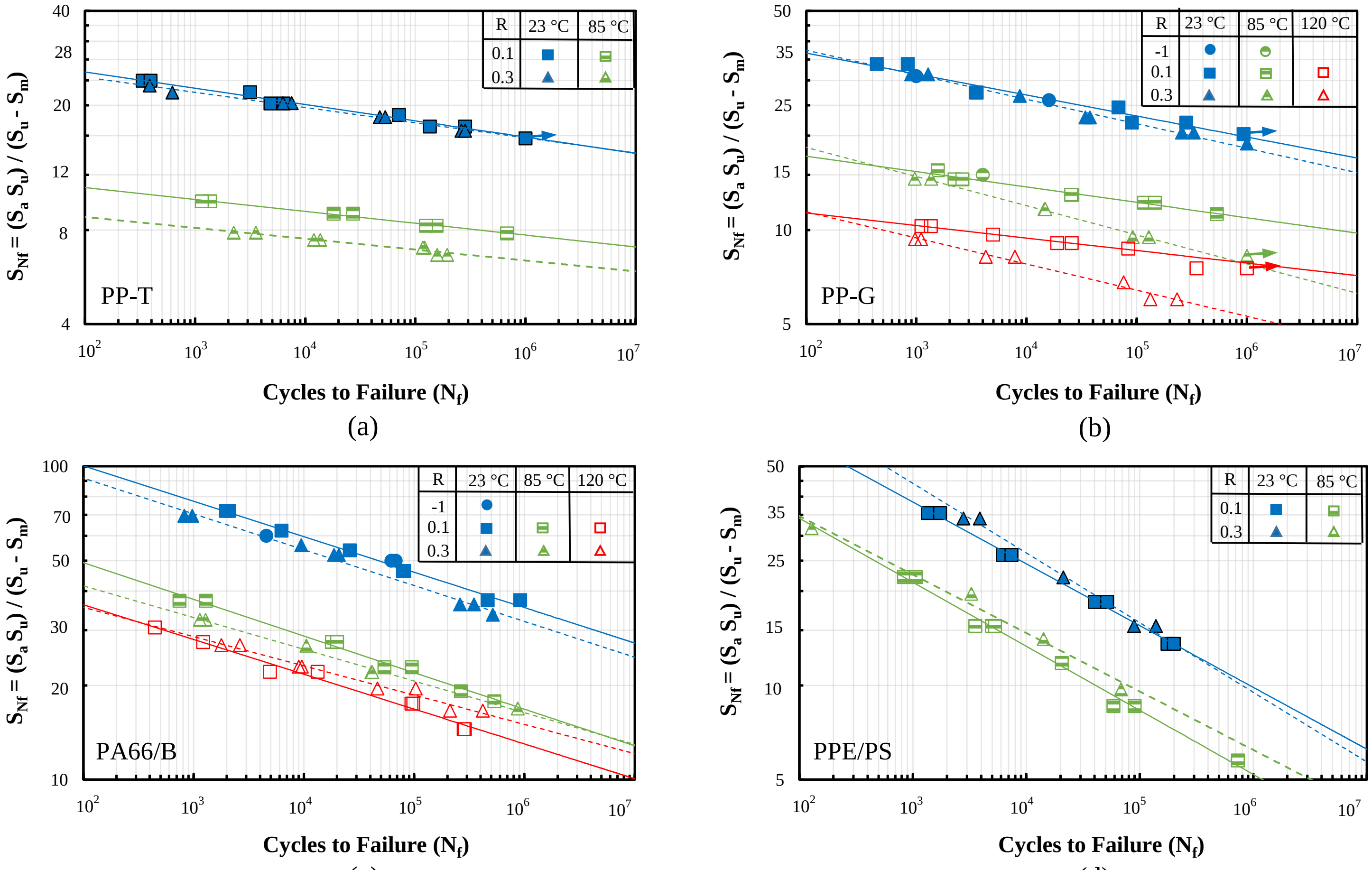

(a) (b)

(c) (d)

Figure 7-10: Correlations of fatigue data for different stress ratios and temperatures using modified Goodman mean stress parameter for (a) PP-T, (b) PP-G, (c) PA66/B, and (d) PPE/PS.

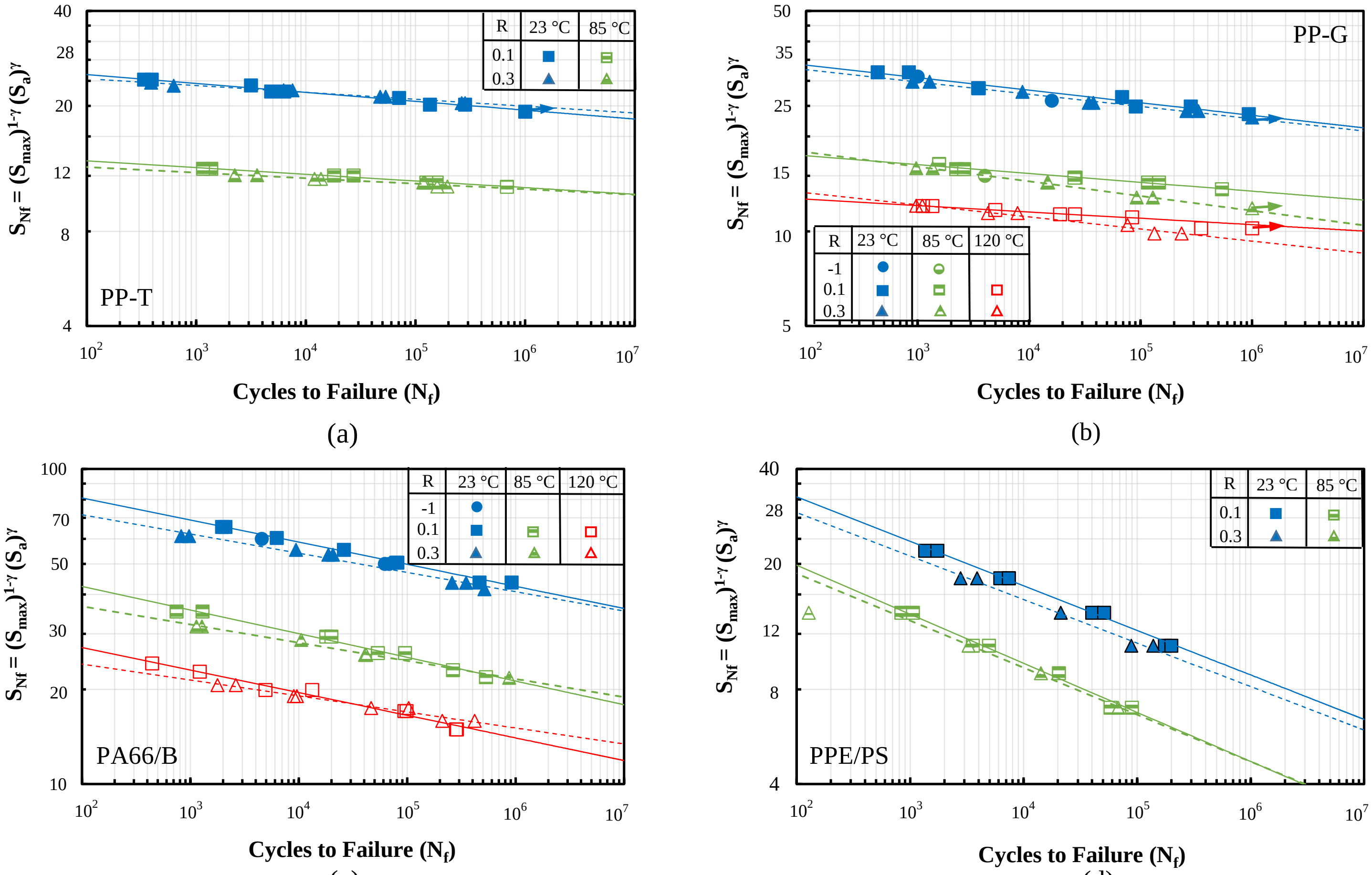

(a) (b) (c) (d)

Figure 7-11: Correlations of fatigue data for different stress ratios and temperatures using Walker mean stress parameter for (a) PP-T, (b) PP-G, (c) PA66/B, and (d) PPE/PS.

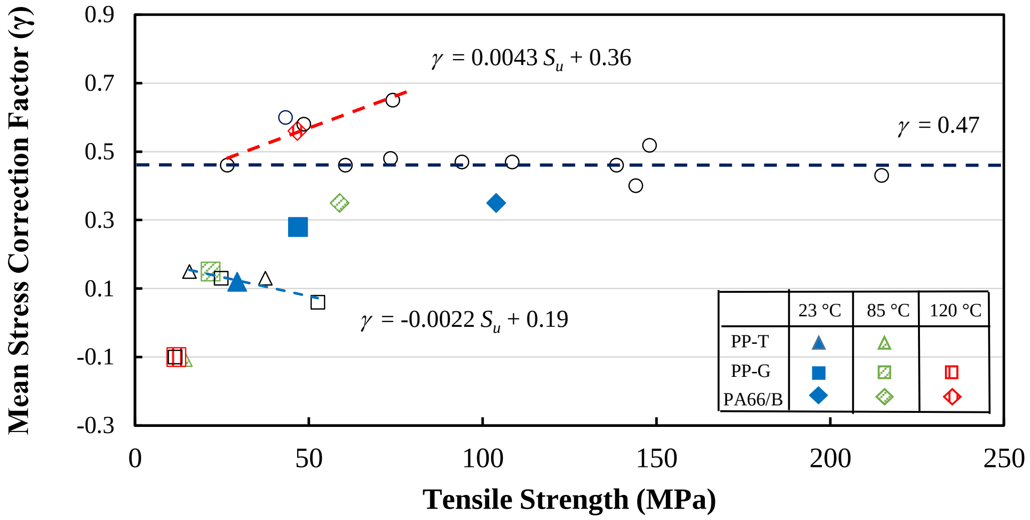

Figure 7-12: Comparison of γ values in the Walker equation as a function of tensile strength for PP-T, PP-G, and PA66/B at 23, 85, and 125 °C with those reported for PBT and PA6 (○) in [62] and PP (□) and PO (△) in [180].

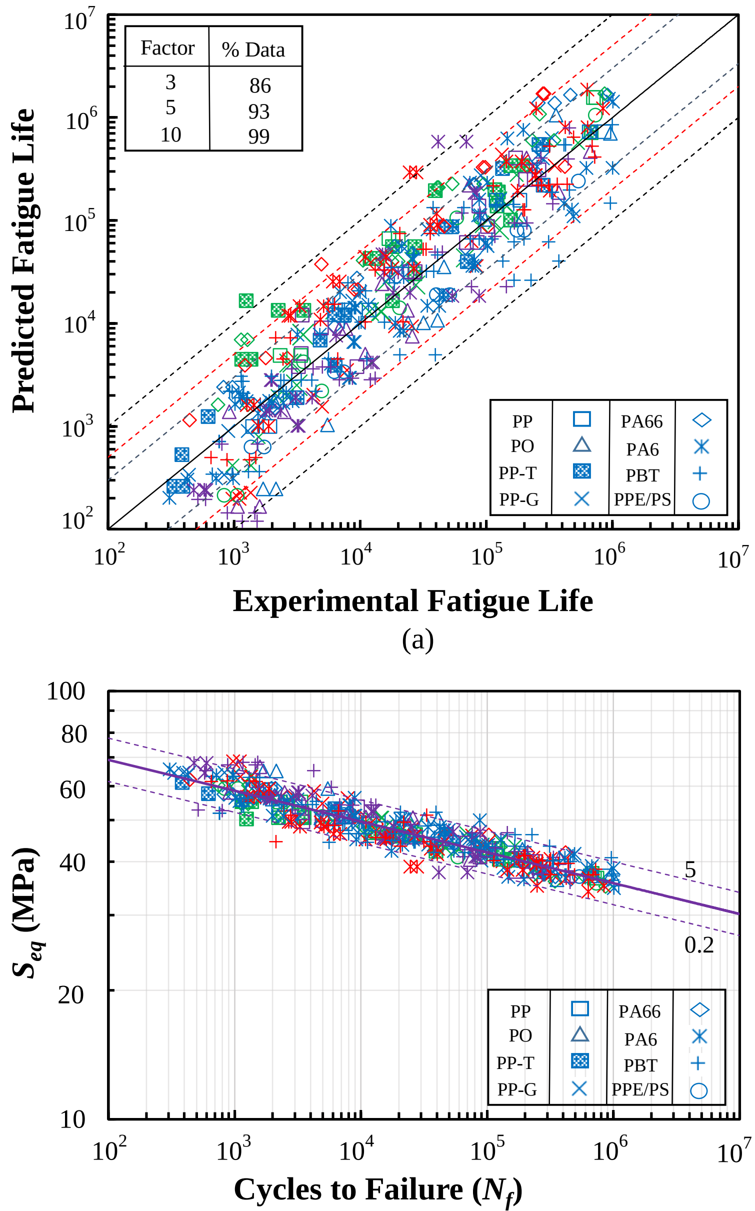

(a)

(b)

Figure 7-13: (a) Predicted fatigue life versus experimental fatigue life and, (b) equivalent stress amplitude versus fatigue life using general fatigue model for PP, PO, PP-T, PP-G, PA66/B, PA66/D, PPE/PS, PA6, and PBT. Purple, blue, green, and red color denote -40, 23, 85, 120 or 125 °C, respectively. A total of 540 fatigue data are included in each figure.

Chapter 8

Creep-Fatigue Interaction and Thermo-Mechanical Fatigue Test Results and Analysis

In this chapter creep-fatigue interaction and TMF behaviors of PP-T, PP-G, PA66/B, and PPE/PS are investigated. A comprehensive experimental study was conducted to consider the effects of frequency, load level, stress ratio, hold-time duration, and hold-time position on creep-fatigue interaction behavior. Creep-fatigue tests were conducted at 85 °C and 120 °C for PP-G and PA66/B and at 85 °C for PP-T and PPE/PS. Hold-time was at the maximum cyclic load for PA66/B and PPE/PS and was at mean cyclic load for PP-T. For PP-G, load signals with different hold-time positions were used. In addition, the effects of frequency (0.125 to 1 Hz), R ratio (0.1 and 0.3), stress level, and waveform (triangular or sinusoidal) on creep-fatigue interaction behavior were investigated for this material. The range of stress level, R ratio, and frequency were chosen such that the tests would produce fatigue damage dominated, creep damage dominated, or similar creep-fatigue damage. It should be noted that fully-reversed (R = -1) loading was not used due to buckling at elevated temperatures for this loading condition. TMF tests were conducted only for PA66/B and T_{min} and T_{max} were considered to be 85 °C and 120°C, respectively. Failure criterion was specimen fracture for all the tests. However, for the loading conditions used the majority of the fatigue life was spent on crack initiation and crack growth life was small [62].

Creep-fatigue and TMF tests were conducted in load-controlled mode using trapezoidal load signals according to ASTM E2714 [85], as shown in Figure 8-1. Each block of load consists of ramps with hold-time, therefore, both fatigue damage and creep damage are generated simultaneously within a given block. For creep-fatigue tests, temperature was constant during the tests, while for TMF tests temperature varied in-phase according to the load signal (maximum values of load and temperature occur at the same time), as shown in Figure 8-1(b). In-phase loading condition is common in real applications and is more damaging than out-of-phase condition.

Chaboche creep-fatigue interaction model was used to predict creep-fatigue data considering the aforementioned effects, as well as the TMF data. To the author's best knowledge, Chaboche creep-fatigue interaction model is applied to the polymeric materials for the first time in this study. Experimental results and analysis presented in this chapter were published in [181].

8.1 Introduction

Components made of thermoplastics and their composites are often subjected to cyclic stresses as well as loading and environmental conditions causing creep deformation. Therefore, for such components combined creep and fatigue damages can occur, for example, when there are hold-time periods with mean stress during cyclic loading at constant or variable elevated temperatures. These conditions can give rise to TMF or creep-fatigue failures. TMF is caused by a combination of cyclic mechanical and cyclic thermal loadings where both the stress and temperature vary with time. This combination can be in-phase (IP) or out-of-phase (OP). Components and structures in high-temperature applications, for instance in their start up or shut down cycles, are often subjected to such TMF loading.

Damage developed by interaction of thermal and fatigue or creep and fatigue loadings can be completely different from the damage from each type of loading, separately. In most cases, the synergistic effect of combined damage is more detrimental, compared to addition of damage caused by each loading condition, separately [4].

While creep in metallic materials occurs only at elevated temperatures, creep of thermoplastics can be significant at any temperature [4]. In addition, fatigue behavior of thermoplastic composites has been observed to be very sensitive to temperature [61]. Therefore, creep-fatigue interaction and TMF behaviors of thermoplastics and their composites are major considerations in their structural applications at any temperature.

Modeling creep-fatigue interaction behavior is of great interest, since conducting experiment under this loading condition is expensive and time consuming. Different models have been developed over the years for metallic materials to be able to model damage initiation and growth and predict their life under the aforementioned conditions. In a study by Rees [182], several stress-based, strain-based, and combined strain-based and stress-based life prediction techniques for combined creep and fatigue loadings at elevated temperatures for metallic materials were reviewed. The majority of the models were reported to be empirical.

Strain range partitioning (SRP) method [183] which is a strain-based model, was reported [182] to be the simplest model in terms of application. In SRP method, the total inelastic strain is considered to consist of time-independent plastic and time-dependent creep strain with four possible combination cycles. The basic assumption is that a complex cycle can always be decomposed into four parts corresponding to the four damage relations. Strain-life curves are obtained for each condition separately. A hysteresis loop is divided to the introduced cycles and the total damage is calculated using linear damage rule by adding damage calculated from each obtained strain-life curve. This method is relatively temperature independent, however, partitioning strain for TMF cycles is one of the main challenges [183]. In addition, applying this model for stress-controlled conditions would be difficult. This method can be used in situations where there is significant amount of inelastic strain. For polymeric materials which often have ductile behavior and have significant creep deformation, this method may work well.

Chaboche creep-fatigue interaction model [184], which is a stress-based model and is relying on the continuum damage mechanics, has been reported to predict the non-linear creep-fatigue damage accumulation behavior for some of the metallic materials very well [182]. In this model, a non-linear damage accumulation is considered for the sum of pure fatigue damage and pure creep damage. The damage evolution equations are determined independently for pure creep and pure fatigue loading conditions. An effective stress concept is proposed to find an equivalent isothermal condition for TMF condition. There is no specific assumption in this model to confine it to any particular material or class of materials and can, therefore, be applied to polymeric materials.

Another strain-based TMF life prediction model is a model developed by Neu and Sehitoglu [185, 186] for crack nucleation and early crack growth. The model considers fatigue, environment (oxidation), and creep damages separately. The model can also consider different strain-temperature phasings (i.e. isothermal fatigue and in-phase and out-of-phase TMF). By understanding the damage mechanism of fatigue, creep, and oxidation, a relation for determining the life under each damage term is developed and a linear damage accumulation is assumed for the total damage sum. The fatigue term is represented by the traditional strain-life equation. For the creep damage, a stress-based model which accounts for the phasing effect is introduced and creep in tension and compression modes are assumed to be different. In addition, a constitutive viscoplastic model was developed by Slavik and Sehitoglu [187] to consider the rate dependency of the stress-strain behavior.

8.2 Application of Chaboche Creep-Fatigue Interaction Model to the Studied Materials

Chaboche non-linear creep-fatigue model [184] is used in this study to perform damage analysis and predict life for creep-fatigue and TMF loading conditions. This model is chosen since it can account for the non-linear creep-fatigue interaction behavior, it is stress-based and does not need a constitutive equation for stress-controlled loading condition, it can account for the case of variable temperature (TMF), and it has the capability to consider anisotropic behavior and multiaxial loading condition.

It is assumed in this model that creep and fatigue damages can be added together to give the total creep-fatigue damage. The model consists of four parts, 1) creep damage modeling, 2) fatigue damage modeling, 3) creep-fatigue interaction modeling, and 4) TMF modeling. Although this stress-based model is more complex and has several constants compared to strain-based models, it contains information corresponding to extreme situations (pure creep and pure fatigue). Moreover, for fatigue damage, mean stress effect is taken into account and the model is based on non-linear damage evolution. The fatigue damage model can also be used to predict the non-linear behavior under step cyclic loading conditions observed for neat and short glass fiber reinforced thermoplastics [188]. The anisotropy effect for metallic materials with different crystallographic orientations was also taken into account in the extension of the model [189]. A similar methodology can also be used to consider the anisotropy due to the fiber orientation for composite materials. Satisfactory predictions have been made by this model for various metallic materials under different loading conditions, including isothermal fatigue, TMF, and two step fatigue and creep loadings [190, 191].

8.2.1 Creep damage model

Based on the extension of the Rabotnov [192] and Kachanov [193] works, Chaboche and Lemaitre [184] proposed a non-linear creep damage evolution equation, expressed as:

$$dD_C = (\frac{S}{A})^r (1 - D_C)^{-K} dt \tag{8.1}$$

where D_c is the damage variable, S is the stress, and A, r, and K are temperature dependent material constants. D_c values change between zero for the virgin or un-damaged condition and one for the failed condition. By integrating Equation 8.1 for $D_c = 0$ to 1 and $t = 0$ to t_R which is time to rupture of specimen in hours, t_R can be expressed as:

$$t_R = \frac{1}{K+1} (\frac{A}{S})^r \tag{8.2}$$

where r and $\frac{A^r}{K+1}$ are obtained by fitting a line in log-log coordinate to creep-rupture (stress versus time to rupture) data at a given temperature. K is used to describe the non-linear damage evolution as observed from damage measurements and a value of $K = 0$ implies linear damage accumulation. K value can be obtained from either damage accumulation curves or using creep-fatigue interaction data and it has been assumed to be independent of stress level [190].

The damage evaluation for creep condition can also be obtained by integrating Equation 8.1 for $D_c = 0$ to D_c and $t = 0$ to t and expressed as:

$$D_C = 1-(1-\frac{t}{t_R})^{\frac{1}{K+1}} \tag{8.3}$$

This equation can also be used for two step or multiple step creep loading conditions, however, constant K should be determined for the given loading condition.

8.2.2 Fatigue damage model

Chaboche et al. [184, 189, 190, 194] proposed several non-linear continuous fatigue damage models based on constant amplitude and variable amplitude stress-controlled or strain-controlled fatigue tests. These models were used to describe the progressive deterioration for the crack initiation process. The evolution of fatigue damage during the tests at both room and elevated temperatures was used to suggest the fatigue damage model. A typical model for pure fatigue damage for stress-controlled condition was suggested to be:

$$dD_f = [1-(1-D_f)^{\beta+1}]^{\alpha}(\frac{S_{\max}-S_m}{M(1-D_f)})^{\beta} dN \tag{8.4}$$

where D_f is the fatigue damage variable, S_{max} is the maximum stress, S_m is the mean stress, β is a temperature dependent constant, and α and M are temperature and stress dependent functions expressed as:

$$\alpha = 1-a\left\langle \frac{S_{\max}-S_{l0}-(1-bS_{l0})S_m}{S_u-S_{\max}} \right\rangle \tag{8.5}$$

$$M = M_0(1 - bS_m) \tag{8.6}$$

where S_{l0} is the fatigue endurance limit, S_u is the ultimate tensile strength, and a, b, and M_0 are temperature dependent constants. The symbol $\langle\quad\rangle$ in Equation 8.5 is the Macaulay bracket, where $\langle x\rangle = 0$ if $x < 0$ and $\langle x\rangle = m$ if $x \geq 0$. Number of cycles to failure, N_f is obtained by integrating Equation 8.4 for D_f = 0 to 1 and N = 0 to N_f, and is expressed as:.

$$N_f = \frac{1}{(\beta+1)(1-\alpha)}\left(\frac{S_{\max} - S_m}{M}\right)^{-\beta} \tag{8.7}$$

Damage evaluation for fatigue loading condition can then be obtained by integrating Equation 8.4 for D_f = 0 to D_f and N = 0 to N and expressed as:

$$D_f = 1 - \left(1 - \left(\frac{N}{N_f}\right)^{\frac{1}{1-\alpha}}\right)^{\frac{1}{\beta+1}} \tag{8.8}$$

Similar to creep loading condition, the damage evolution expression can be used for modeling fatigue behavior under multiple step loading conditions.

By combining Equations 8.7, 8.5, and 8.6 the final form for the fatigue life prediction model is given by:

$$N_f = \frac{1}{aM_0^{-\beta}(\beta+1)\left\langle\frac{S_{\max} - S_{l0} - (1 - bS_{l0})S_m}{S_u - S_{\max}}\right\rangle}\left[\frac{S_{\max} - S_m}{(1 - bS_m)}\right]^{-\beta} \tag{8.9}$$

The Chaboche fatigue model is a very good representation of standard established *S*-*N* fatigue theory. It can capture low cycle fatigue, high cycle fatigue, and intermediate fatigue regions. It also includes the mean stress correction parameter. The model coefficients β and $aM_0^{-\beta}$ can be determined for a given temperature from *S*-*N* fatigue data (for R = -1) by fitting a line to $\log\left[N_f \frac{(S_a - S_{l0})}{(S_u - S_a)}\right]$ versus $\log(S_a)$ data. In such a graph, β is the slope of the line and $\log[aM_0^{-\beta}(\beta+1)]^{-1}$ is the intercept. The coefficient b reflects the influence of the mean stress on the fatigue behavior. Its identification requires an S-N curve with non-zero mean stress and its value is obtained using and optimization process. The a value, similar to the K value, can be obtained from either damage accumulation curves or by using creep-fatigue interaction data.

As explained in chapter 6, fatigue life of some polymers is significantly increased with increasing frequency, before self-heating became dominant for these materials. Therefore, the effect of frequency should be considered for the fatigue life prediction model for such polymers. The effect of frequency can be incorporated in the fatigue life model by considering the fatigue damage to be time dependent rather than cycle dependent in Equation 8.4 and by changing the time to failure to cycles to failure. According to this assumption, the frequency is added in numerator of Equation 8.9 for frequency sensitive materials (i.e. for materials and frequency range where increased frequency results in increased fatigue life and prior to self-heating becoming dominant and shortening fatigue life), expressed as:

$$N_f = \frac{f}{aM_0^{-\beta}(\beta+1)\left\langle \frac{S_{\max} - S_{l0} - (1 - bS_{l0})S_m}{S_u - S_{\max}} \right\rangle} \left[\frac{S_{\max} - S_m}{(1 - bS_m)} \right]^{-\beta} \tag{8.10}$$

where f is the cycling frequency.

8.2.3 Interaction effects of creep and fatigue damages

When the creep damage (linked to the loading duration) and fatigue damage (due to cyclic loading) are present simultaneously, the interaction effect can be represented macroscopically by introducing a coupling as [184]:

$$dD_C = f_c(S, T, D_C, D_f \ldots)dt \tag{8.11}$$

$$dD_f = f_f(S_{\max}, S_m, T, D_C, D_f \ldots)dN \tag{8.12}$$

In order to simplify and make predictions from pure creep and pure fatigue, it was assumed [190] that the damage D_c and D_f have additive macroscopic effects. Therefore, only one damage variable is introduced by adding the creep damage and fatigue damage as, $D = D_c + D_f$. The total damage then can be expressed as:

$$dD = dD_C + dD_f = f_c(S, T, D, \ldots)dt + f_f(S_{\max}, S_m, T, D, \ldots)dN \tag{8.13}$$

The non-linear accumulation and interaction can be derived by substituting creep damage and fatigue damage formulations from Equations 8.1 and 8.4, respectively, in Equation 8.13, which leads to the following equation:

$$dD = (\frac{S}{A})^r (1-D\ )^{-K} dt + [1-(1-D)^{\beta+1}]^{\alpha} (\frac{S_{\max} - S_m}{M(1-D_f)})^{\beta} dN \tag{8.14}$$

By integrating Equation 8.14 for D = 0 to 1 and doing some rearrangements, the number of blocks to failure, N_R, can be estimated as:

$$\frac{N_R}{N_F} = \int_0^1 \left[\frac{N_F}{N_C} \frac{(1-D)^{-K}}{K+1} + \frac{(1-(1-D)^{\beta+1})^{\alpha}}{(\beta+1)(1-\alpha)(1-D)^{\beta}} \right] dD \tag{8.15}$$

where $N_C = \frac{t_R}{t_H}$ and t_H is the hold-time in each block. The value of α is obtained from Equation 8.5. One creep-fatigue interaction test data can be used to optimize the constants

a (in Equation 8.5) and K. N_R was observed to be more sensitive to the a value. For a given value of K, which can be $K = 1$, several iterations should be done to find an optimized value of a for the given experimental data. Then, the K value can be changed to increase the prediction accuracy. Although using the rule of linear accumulation is satisfactory for some cases, this method proves ineffective for many materials, especially for polymers. Therefore, using the non-linear damage accumulation formulation is necessary.

8.2.4 TMF modeling

For the condition of variable temperature during loading, Chaboche and Lemaitre [190] suggested an alternative approach based on a temperature-compensated effective stress. In this case, an effective stress is calculated for an isothermal condition. In this approach it is assumed that an equivalent master curve can be obtained by normalizing fatigue data using the tensile strength of the material. An example of this procedure is shown in Figure 8-2 for which the isothermal condition is considered to be at T_{min}. For the equivalent condition, the minimum stress is the same as the original stress value. However, the maximum stress is increased by a factor based on the effective stress concept. For this block of loading, the effective stress is calculated using the following relation:

$$S' = S\,\frac{S_u(T_{\min})}{S_u(T_{\max})} \tag{8.16}$$

where S' is the effective stress.

8.3 Results of Experimental Work and Predictive Models

8.3.1 Creep and fatigue behaviors

Creep behavior of PP-T, PP-G, PA66/B, and PPE/PS was investigated in detail in chapter 5, including creep rupture and deformation behaviors for short-term and long-term conditions. Creep-rupture data represented in Figure 5-2, were used to fit the Chaboche creep damage model (Equation 8.2) and find its constants. The fits were obtained by considering stress S as independent variable and time to rupture t_R as dependent variable. The values of creep model constants are reported in Table 8-1.

Fatigue behavior of the studied composite thermoplastics was studied in chapters 6 and 7 including temperature, mean stress, and frequency effects. Fatigue data for $R = -1$ loading condition obtained from mean stress correction models were used to obtain β and $[aM_0^{-\beta}(\beta+1)]^{-1}$ for a given condition based on the previously explained procedure. An example of the fit to $\log\left[N_f \frac{(S_a - S_{l0})}{(S_u - S_a)}\right]$ versus $\log(S_a)$ data is shown in Figure 8-3 for PPE/PS at 85 °C. Experimental fatigue data for $R = 0.1$ condition for a given temperature were used to obtain the constant b by finding the best fit of the data.

After defining all the fatigue constants, experimental fatigue life for $R = 0.3$ condition were predicted. Experimental fatigue life and superimposed Chaboche fatigue life model for PA66/B and PPE/PS are shown in Figure 8-4. Acceptable predictions for $R = 0.3$ loading condition are observed, except for high cycle fatigue regime for PA66/B, which is related to the effect of creep damage because of mean stress during cyclic loading.

The beneficial effect of increased frequency on fatigue life was observed for PP-T and PP-G. Therefore, a frequency term, as explained previously, was considered in the fatigue model (Equation 8.10). In addition to fatigue data for $R = 0.3$ loading condition shown in Figure 8-5(a), experimental frequency effect data represented in chapter 6 were also predicted by the model (see Figure 8-5(b)). For the effect of stress ratio, 74% of predicted fatigue life are within a factor of 3 of experimental fatigue life (see Figure 8-5(a)). Predictions are not good for high cycle fatigue regime. This is due to the damaging effect of creep during cyclic loading, as explained earlier. The fatigue model which was modified by adding the frequency term by considering time dependency of damage could also very well predict the strengthening effect of increasing cycling frequency before self-heating becomes dominant. As can be seen in Figure 8-5(b), 85% of predicted fatigue lives are within a factor of 3 of experimental fatigue lives. The values of fatigue model constants are reported in Table 8-1.

8.3.2 Creep-fatigue interaction behavior

Isothermal fatigue tests results used for analysis were obtained using a sinusoidal waveform. To ensure that waveform does not affect the fatigue and creep-fatigue interaction results, some of the fatigue and creep-fatigue tests were repeated using triangular or sinusoidal signal for PP-G at 85 °C. As shown in Figure 8-6, for both fatigue and creep-fatigue loading conditions, nearly identical life for the tests with sinusoidal and triangular loading waveforms at a given stress amplitude were obtained. Therefore, it can be concluded that the effect of waveform on fatigue and creep-fatigue life was negligible.

A summary of experimental results under creep-fatigue loading condition is presented in Table 8-2. Cyclic life ratio, $\frac{N_R}{N_f}$, and hold-time life ratio, $\frac{N_R}{N_C}$, and sum of the life ratios are reported in Table 8-2. Sum of the life ratios (sum of the cyclic and hold-time damages based on LDR) is less than unity for all the conditions which confirms a non-linear behavior in terms of damage accumulation. The non-linear behavior can also be observed from the cross plots of fatigue life ratio versus hold-time life ratio, shown in Figure 8-7 for the studied materials at 85 °C, as well as for PP-G and PA66/B at 120 °C. Duplicate tests were conducted for most of the conditions and very good repeatability of results were obtained. Tests were conducted for three stages of damage based on LDR, including tests with equal cyclic and hold-time damage, tests with more hold-time damage and tests with more cyclic damage.

Non-linear behavior is different for each material, where PP-T has the most and PA66/B has the least non-linear behavior. However, it should be mentioned that the non-linearity also depends on the stress level and stress ratio, as will be discussed later. As can be seen in Figure 8-7, linear damage rule (LDR) results in non-conservative predictions for all the conditions. For example, for PP-T at 85 °C for the condition with equal cyclic and hold-time damage (based on LDR), the difference between prediction of LDR and experiments is about a factor of 5.

Figure 8-8 shows experimental creep-fatigue interaction and superimposed predictions of Chaboche model for different conditions. For a given temperature and material, one creep-fatigue interaction data was used to obtain constants *a* and *K* with an optimization process explained earlier. *a* and *K* values have been reported in Table 8-1 for different conditions. *K* values are observed to be independent of temperature for PP-G and PA66/B, similar to what was observed for metallic materials [190, 191]. As can be seen in Figure 8-8, the model can very well predict the non-linear creep-fatigue interaction behavior for all the conditions.

The non-linearity of interaction decreases with increasing stress level for PP-G and PA66/B at 85 °C, as shown in Figures 8-8(b) and (d). In addition, non-linearity depends on the stress ratio as shown in Figure 8-8(b) for PP-G at 85 °C. This behavior is predicted very well by the model, particularly when comparing to the prediction by the LDR. Similar behavior was reported for many metallic materials in [190]. Although the cycling frequency and position of hold-time stress did affect the pure fatigue and pure creep life, respectively, and consequently creep-fatigue life, they did not affect the interaction behavior or non-linear creep-fatigue curve, which is in agreement with prediction of Chaboche model, as illustrated in Figure 8-9 for PP-G at 85 °C for the test data with S_a = 5.85 MPa.

Plot of predicted number of blocks to failure versus experimental number of blocks to failure for creep-fatigue test data (shown in Table 8-2) using Chaboche model is shown in Figure 8-10. In this graph, effects of material, temperature, stress level, frequency (the strengthening effect for PP-T and PP-G), stress ratio, and hold-stress position are incorporated. As can be seen in this figure, predictions are very good for all the materials and 90% of the predicted lives are within a factor of 2 of experimental lives.

8.3.3 TMF behavior

In-phase TMF tests were conducted for PA66/B for two different conditions to verify the capability of the Chaboche model for TMF life predictions. Summary of test conditions and predicted results are included in Table 8-3. For both conditions, temperature was changed between 85 °C to 120 °C. For the first condition (TMF1 and TMF2 specimens), 90% of total damage based on LDR was caused by creep. For the second condition (TMF3 and TMF4 specimens), fatigue and creep damage had equal contributions to the total damage based on LDR. For the second condition, stress ratio of the test was -0.5. Two repeat fatigue tests at isothermal condition of 85 °C were also conducted to verify the capability of Chaboche fatigue model for life prediction for R = -0.5, in addition to R = 0.1 and 0.3 loading conditions. Experimental cycles to failure for these tests were obtained to be 1049 and 755 cycles with an average of 902 cycles, while predicted cycles to failure using Chaboche fatigue model was 650. This confirms that the Chaboche fatigue model could satisfactorily predict fatigue life for $R = -0.5$ condition.

The prediction for TMF tests was done using the effective stress concept by considering an isothermal condition at 85 °C and using an equivalent or effective stress signal. The maximum stress for each condition was increased by a factor of 1.26, which is the ratio of S_u at 85 °C (58.8 MPa) over S_u at 120 °C (46.7 MPa). Minimum stress and frequency of the cyclic part of the stress signal were considered to be constant. The predicted number of blocks to failure versus experimental number of blocks to failure for PA66/B are included in Figure 8-10. It can be seen that Chaboche creep-fatigue interaction model based on the concept of effective stress could very well predict the life for TMF condition.

8.4 Discussion of Results and Extension of the Chaboche Model for General Cases

Chaboche creep damage model could very well represent the creep rupture data. Constant K was assumed to be stress independent and was obtained to be also temperature independent. Therefore, for creep condition the damage evolution is non-linear (Equation 8.3), however the damage accumulation is linear since K is independent of stress level. For metallic materials K values were obtained to be higher than r values [190], while for thermoplastics an opposite trend is observed in this study.

Non-linear damage evolution and accumulation are considered in Chaboche fatigue damage model where the non-linearity increases with decreasing the stress level. The model could very well consider the mean stress and frequency effects for most of the conditions. However, the predictions were non-conservative for HCF regime, mainly for the higher stress ratio (R = 0.3) and at higher temperature (T = 120 °C). In presence of mean stress, damage due to cyclic creep mainly in HCF regime, adds to the fatigue damage and causes reduction in fatigue life. This discrepancy did not affect the predictions of creep-fatigue loading since all the conditions were in LCF regime. In most real application also, most of the TMF loading situations typically occur in LCF regime.

Non-linearity of creep-fatigue interaction was very well predicted by the Chaboche model. Position of hold-time stress was observed to not affect the interaction curve. However, for some metallic materials due to the hardening effect and also the effect of oxidation, position of hold-stress was observed to significantly affect the creep-fatigue behavior [195]. The predictions of Chaboche model for TMF loading conditions were also very good since the predictions of fatigue and creep models were very good and non-linearity of the interaction was also considered. Although the oxidation which significantly affects the TMF behavior of metallic materials does not affect the TMF behavior of polymers, the hygrothermal aging effect under TMF loading condition may also have to be considered, particularly for polyamide-based materials.

The Chaboche model can also be used for other loading conditions, including strain-controlled loading, notched conditions, and multiaxial and variable amplitude loadings. For strain-controlled condition, a constitutive model is needed to consider the viscoelastic or viscoplastic behavior of thermoplastics, particularly at elevated temperatures. A similar procedure to that used by Pierantoni et al. [63] can be utilized for calculating the stress signal. For notched behavior, Helfpenny et al. [191] suggested using local stresses or strains obtained from FEA for which the viscoelastic materials behavior was accounted for in the creep and the fatigue damage models for metallic materials.

Extension of the model for multiaxial loading condition was explained in details by Chaboche et al. [189, 190] for metallic materials. The basis of the creep, fatigue, and creep-fatigue interaction damage models are similar to that of uniaxial condition, but the stress terms could be substituted by their multiaxial equivalent quantities. For creep condition, an equivalent stress can be defined by introducing a sensitivity coefficient material parameter to the stress triaxiality. For fatigue condition, an octahedral shear amplitude tensor, hydrostatic pressure stress using Sine criterion, or an equivalent von Mises stress can be used to express the multiaxial stress term. For variable amplitude loading condition, damage terms in Equation 8.14 should be integrated incrementally for each fatigue cycle and each period of time. The complex numerical integration would be very time consuming for these cases, however.

To consider the anisotropy effect on pure creep, pure fatigue, and creep-fatigue life for crystalline metallic materials, material structural anisotropy tensors were used by Chaboche and Gallerneau [189]. A similar procedure can be used to consider the anisotropic behavior of short fiber reinforced or continuous fiber reinforced polymers due to the fiber orientation. The methodology used in this study for modeling creep-fatigue and TMF behaviors of talc-filled and short fiber reinforced thermoplastic composites for a given mold flow direction, can also be extended to thermoset polymers or continuous fiber reinforced polymer composites.

Table 8-1: Chaboche creep-fatigue interaction model constants.

		Fatigue damage model constants					**Creep damage model constants**		
Temp. (°C)	**S_u (MPa)**	**S_{l0} (MPa)**	**α**	**β**	**M_0**	**b**	**K**	**r**	**A**
PP-T									
85	13.8	10.9	0.10	5.48	61.04	0.106	0.5	19.6	9.42
PP-G									
85	21.7	12.5	0.65	5.06	110.4	0.056	7.5	10.6	19.7
120	12.1	9.60	0.10	5.31	66.48	0.110	7.5	8.62	11.5
PA66									
85	58.8	17.0	0.35	7.04	83.80	0.014	5.0	41.7	53.2
120	46.7	14.5	0.60	7.30	71.20	0.015	5.0	35.7	41.7
PPE/PS									
85	46.5	4.80	0.28	3.19	91.50	0	2.0	19.2	37.4

Table 8-2: Summary of creep-fatigue interaction test conditions and results.

Specimen ID	S_a (MPa)	R	f (Hz)	N_f (Cycles)	S_H (MPa)	t_R (Hr)	t_H (Sec)	Blocks to Failure (N_R)	$\frac{N_R}{N_f}$	$\frac{N_R}{N_C}$	$\frac{N_R}{N_f}+\frac{N_R}{N_C}$
PP-T, 85 °C											
H1-1	3.8	0.3	0.5	2,900	7.1	193	64	956	0.33	0.09	0.42
H1-2	3.8	0.3	0.5	2,900	7.1	193	64	896	0.31	0.08	0.39
H1-3	3.8	0.3	0.5	2,900	7.1	193	240	330	0.11	0.11	0.23
H1-4	3.8	0.3	0.5	2,900	7.1	193	240	358	0.12	0.12	0.25
H1-5	3.8	0.3	0.5	2,900	7.1	193	719	236	0.08	0.24	0.33
H1-6	3.8	0.3	0.5	2,900	7.1	193	719	225	0.08	0.23	0.31
PP-G, 85 °C											
H1-8	5.85	0.3	1	14,671	10.9	52	13	3,822	0.26	0.27	0.53
H1-16	5.85	0.3	1	14,671	10.9	52	13	3,251	0.22	0.23	0.45
H1-9	5.85	0.3	1	14,671	10.9	52	39	2,180	0.15	0.45	0.60
H1-15	5.85	0.3	1	14,671	10.9	52	39	2,051	0.14	0.43	0.57
H1-10	5.85	0.3	1	14,671	10.9	52	4.25	6,563	0.45	0.15	0.60
H1-17	5.85	0.3	1	14,671	10.9	52	4.25	6,762	0.46	0.15	0.61
H1-14	5.85	0.3	1	14,671	10.9	52	73	1,508	0.10	0.59	0.69
H1-5	5.85	0.3	0.25	2,800	10.9	52	39	907	0.32	0.19	0.51
H1-18	5.85	0.3	0.25	2,800	10.9	52	13	1,851	0.66	0.13	0.79
H1-20	5.85	0.3	0.25	2,800	10.9	52	13	1,862	0.67	0.13	0.79
H1-1	6.5	0.3	0.125	385	12	19.2	60	213	0.55	0.18	0.74
H1-2	6.5	0.3	0.125	385	12	19.2	180	145	0.38	0.38	0.75
H1-3	6.5	0.3	0.125	385	12	19.2	20	435	1.13	0.13	1.26
H1-11	5.25	0.3	1	92,201	9.75	169	6.7	19,822	0.21	0.22	0.43
H1-7	5.85*	0.3	1	14,671	10.9	52	13	3,510	0.24	0.24	0.48
H1-6	6.5*	0.3	0.125	385	12	19.2	60	200	0.52	0.17	0.69
H1-13	5.85	0.3	0.25	2,800	5.05	100,000	30	2,650	0.96	0.00	0.96
H1-19	8	0.1	0.25	2,413	9.8	163	243	519	0.22	0.21	0.43

* Conducted with sinusoidal waveform

Table 8-2 (cont’d): Summary of creep-fatigue interaction test conditions and results.

Specimen ID	S_a **(MPa)**	R	f **(Hz)**	N_f **(Cycles)**	S_H **(MPa)**	t_R **(Hr)**	t_H **(Sec)**	**Blocks to Failure** (N_R)	$\frac{N_R}{N_f}$	$\frac{N_R}{N_C}$	$\frac{N_R}{N_f}+\frac{N_R}{N_C}$
PP-G, 120 °C											
H2-2	3.6	0.3	0.5	4,259	6.7	15	12.5	1,093	0.26	0.25	0.51
H2-4	3.6	0.3	0.5	4,259	6.7	15	12.5	1,024	0.24	0.24	0.48
H2-3	3.6	0.3	0.5	4,259	6.7	15	4.2	2,296	0.54	0.18	0.72
H2-5	3.6	0.3	0.5	4,259	6.7	15	4.2	2,211	0.52	0.17	0.69
H2-1	3.6	0.3	0.5	4,259	6.7	15	37.5	656	0.15	0.46	0.61
H2-6	3.6	0.3	0.5	4,259	6.7	15	37.5	713	0.17	0.50	0.66
PA66/B, 85 °C											
H1-2	21	0.1	0.25	1,020	46.7	40.7	144	359	0.35	0.35	0.70
H1-3	21	0.1	0.25	1,020	46.7	40.7	144	335	0.33	0.33	0.66
H1-4	21	0.1	0.25	1,020	46.7	40.7	48	602	0.59	0.20	0.79
H1-5	21	0.1	0.25	1,020	46.7	40.7	48	558	0.55	0.18	0.73
H1-6	21	0.1	0.25	1,020	46.7	40.7	432	214	0.21	0.63	0.84
H1-7	21	0.1	0.25	1,020	46.7	40.7	432	232	0.23	0.68	0.91
H1-8	20	0.1	0.25	2,268	44.4	321	168	980	0.43	0.14	0.57
H1-9	20	0.1	0.25	2,268	44.4	321	510	550	0.24	0.24	0.49
PA66/B, 120 °C											
H2-1	16	0.1	0.25	1,672	35.6	67.5	200	540	0.32	0.44	0.77
H2-2	16	0.1	0.25	1,672	35.6	67.5	145	548	0.33	0.33	0.65
H2-3	16	0.1	0.25	1,672	35.6	67.5	145	530	0.32	0.32	0.63
H2-4	16	0.1	0.25	1,672	35.6	67.5	435	395	0.24	0.71	0.94
H2-5	16	0.1	0.25	1,672	35.6	67.5	435	333	0.20	0.60	0.80
H2-6	16	0.1	0.25	1,672	35.6	67.5	48	1,002	0.60	0.20	0.80
H2-7	16	0.1	0.25	1,672	35.6	67.5	48	936	0.56	0.18	0.74
PPE/PS, 85 °C											
H1-2	12	0.1	0.25	2,512	26.7	221	316	499	0.20	0.20	0.40
H1-3	12	0.1	0.25	2,512	26.7	221	316	431	0.17	0.17	0.34
H1-4	12	0.1	0.25	2,512	26.7	221	105	870	0.35	0.11	0.46
H1-5	12	0.1	0.25	2,512	26.7	221	105	954	0.38	0.13	0.51
H1-6	12	0.1	0.25	2,512	26.7	221	750	329	0.13	0.31	0.44
H1-7	12	0.1	0.25	2,512	26.7	221	750	375	0.15	0.35	0.50

Table 8-3: Summary of TMF test conditions and experimental and predicted results using Chaboche model for PA66/B.

Specimen ID	**S_{max} (MPa)**	**S_{min} (MPa)**	**T_{max} (°C)**	**T_{min} (°C)**	**Heating Time (min)**	**Cooling Time (min)**	**t_H (min)**	**Experimental Blocks to Failure**	**Predicted Blocks to Failure**
TMF-1	37	3.7	120	85	10	10	30	38	51
TMF-2	37	3.7	120	85	10	10	30	42	51
TMF-3	37	-18.8	120	85	10	10	20	18.5	20
TMF-4	37	-18.8	120	85	10	10	20	21	20

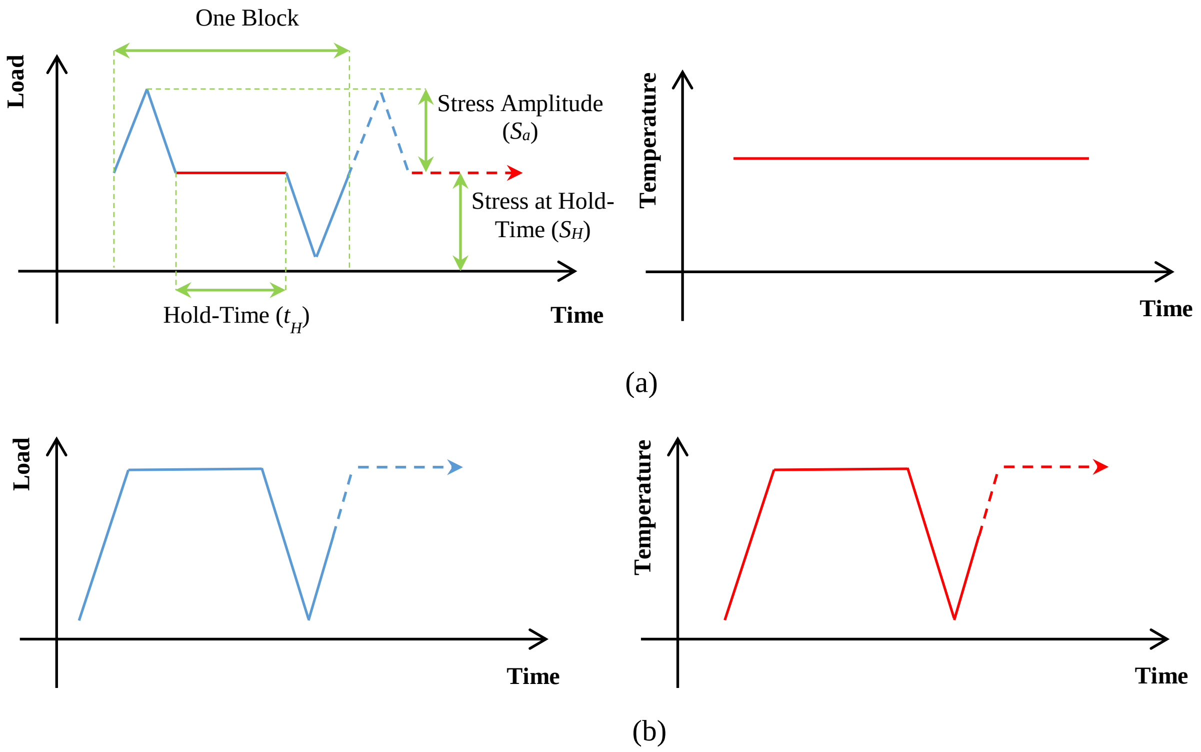

(a)

(b)

Figure 8-1: (a) Load and temperature signals used for creep-fatigue tests, and (b) load and temperature signals used for TMF tests.

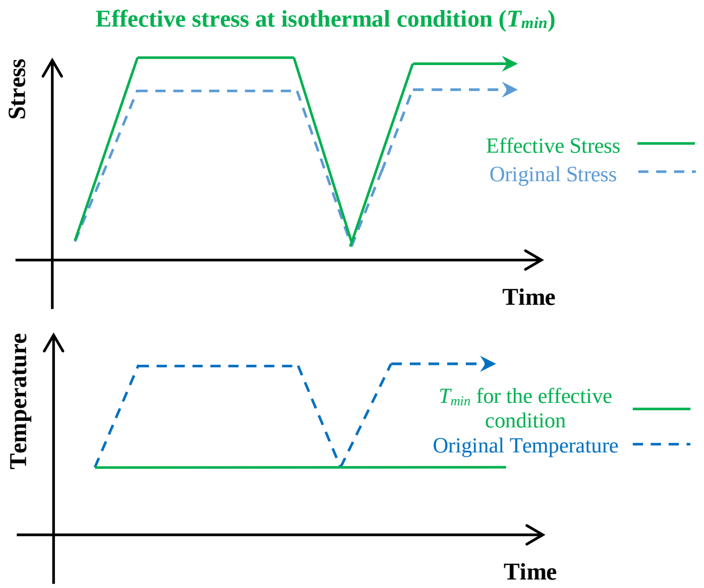

Figure 8-2: Original and effective stress and temperature signals for TMF modeling.

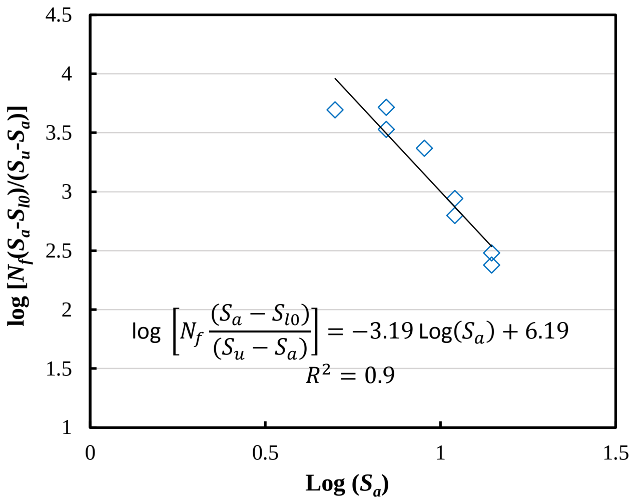

Figure 8-3: Fit of $\log\left[N_f\frac{(S_a-S_{l0})}{(S_u-S_a)}\right]$ versus $\log(S_a)$ data of PPE/PS for R = -1 loading condition at 85 °C.

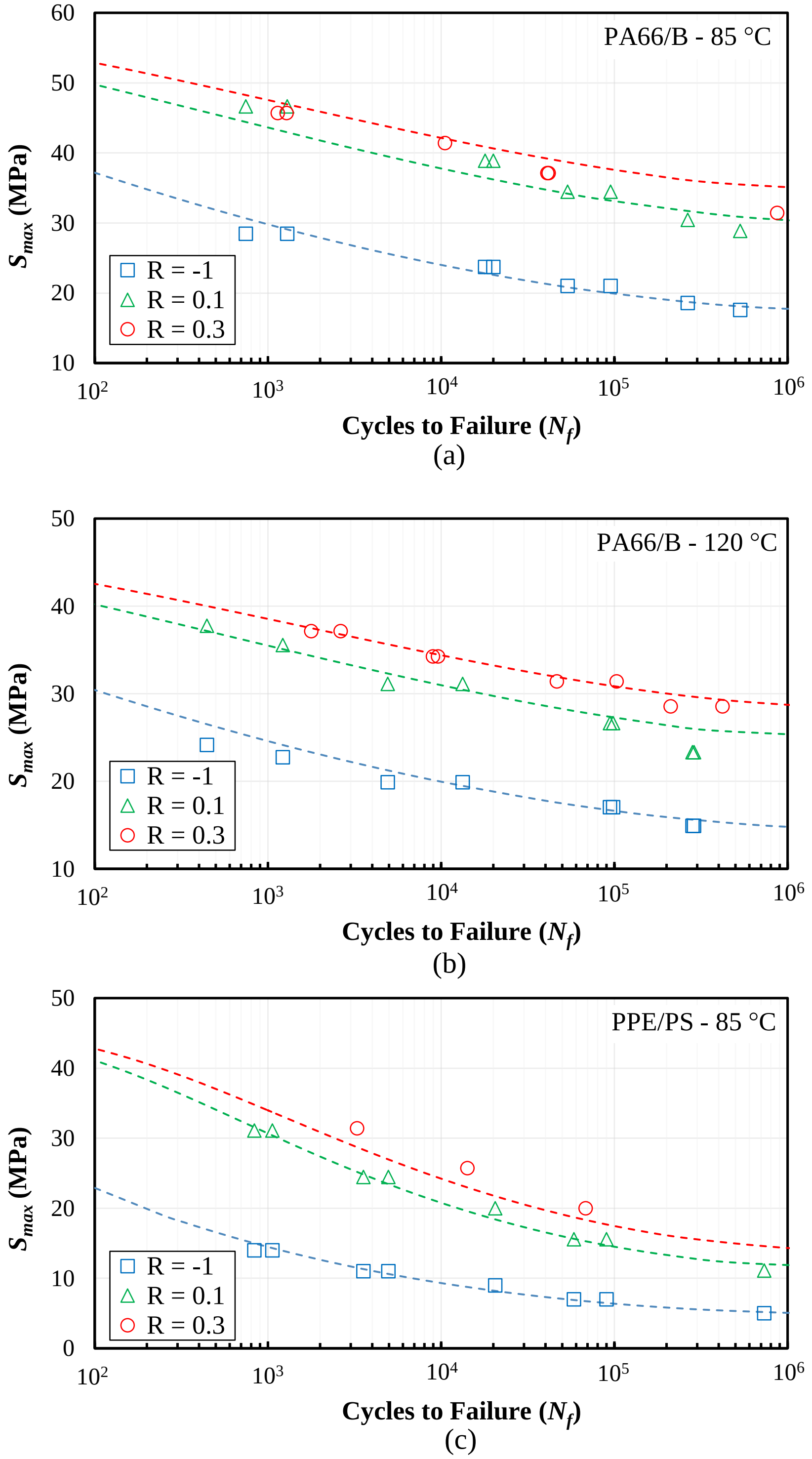

Figure 8-4: Experimental fatigue data and superimposed Chaboche fatigue model for (a) PA66/B at 85 °C , (b) PA66/B at 120 °C, and (c) PPE/PS at 85 °C. Curves are Chaboche fatigue life prediction model.

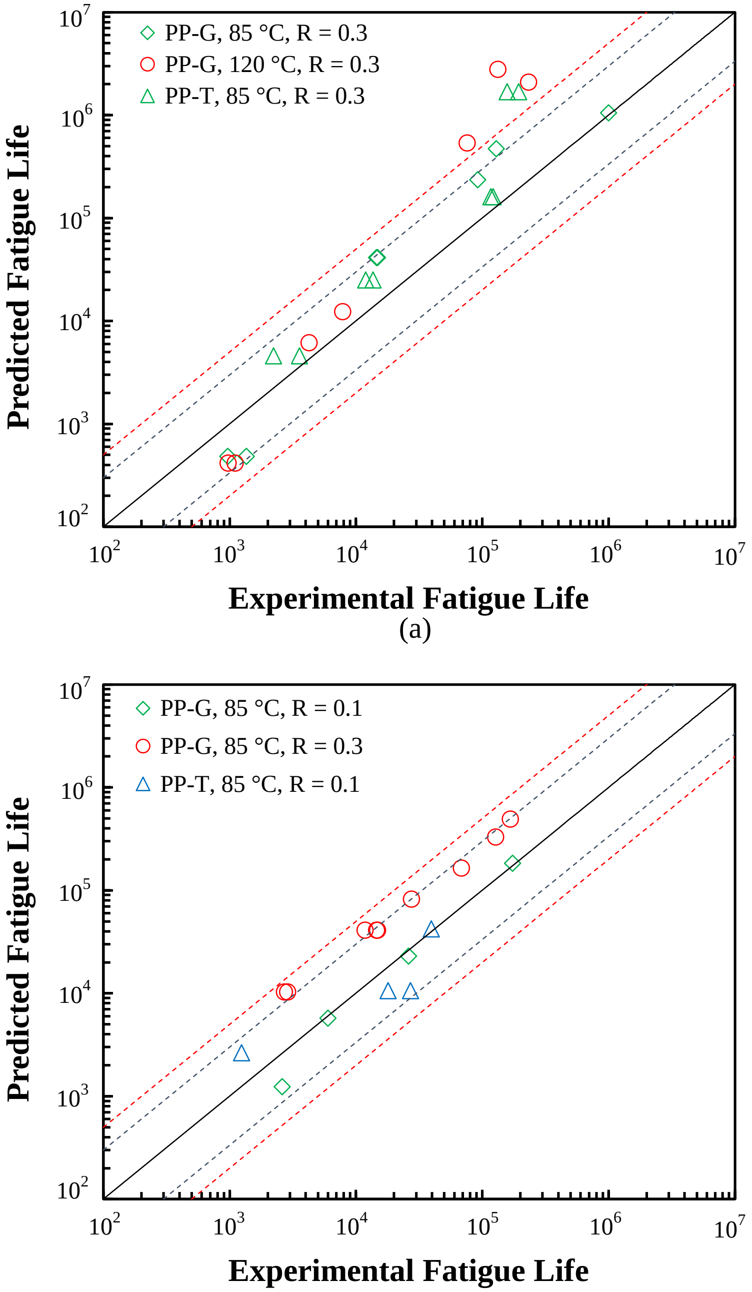

(a)

(b)

Figure 8-5: Predicted fatigue life using Chaboche fatigue model versus experimental fatigue life for PP-T and PP-G for (a) *R* = 0.3 loading condition and, (b) for frequency effect data at a given stress level.

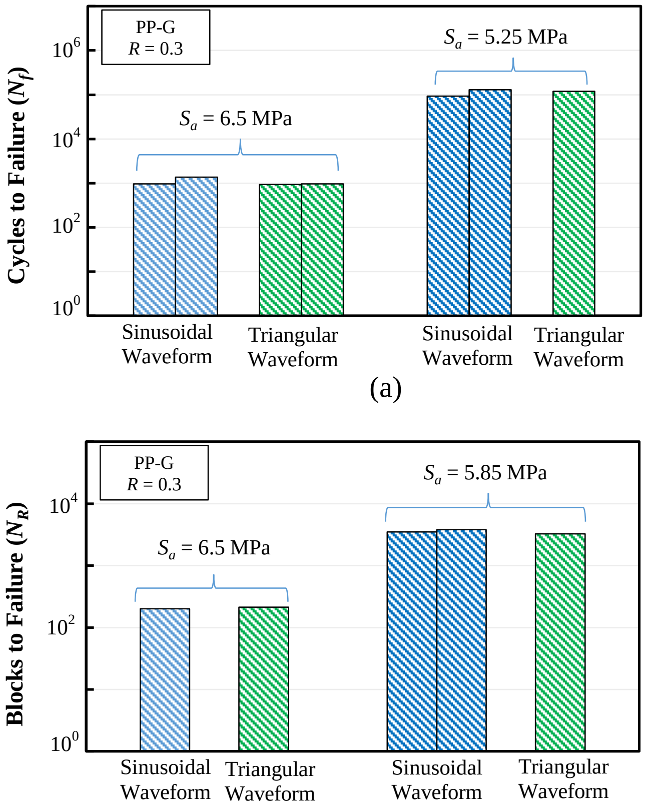

(a)

(b)

Figure 8-6: Effect of loading waveform (sinusoidal or triangular) on life of PP-G at different stress levels for (a) fatigue loading condition and, (b) creep-fatigue loading condition.

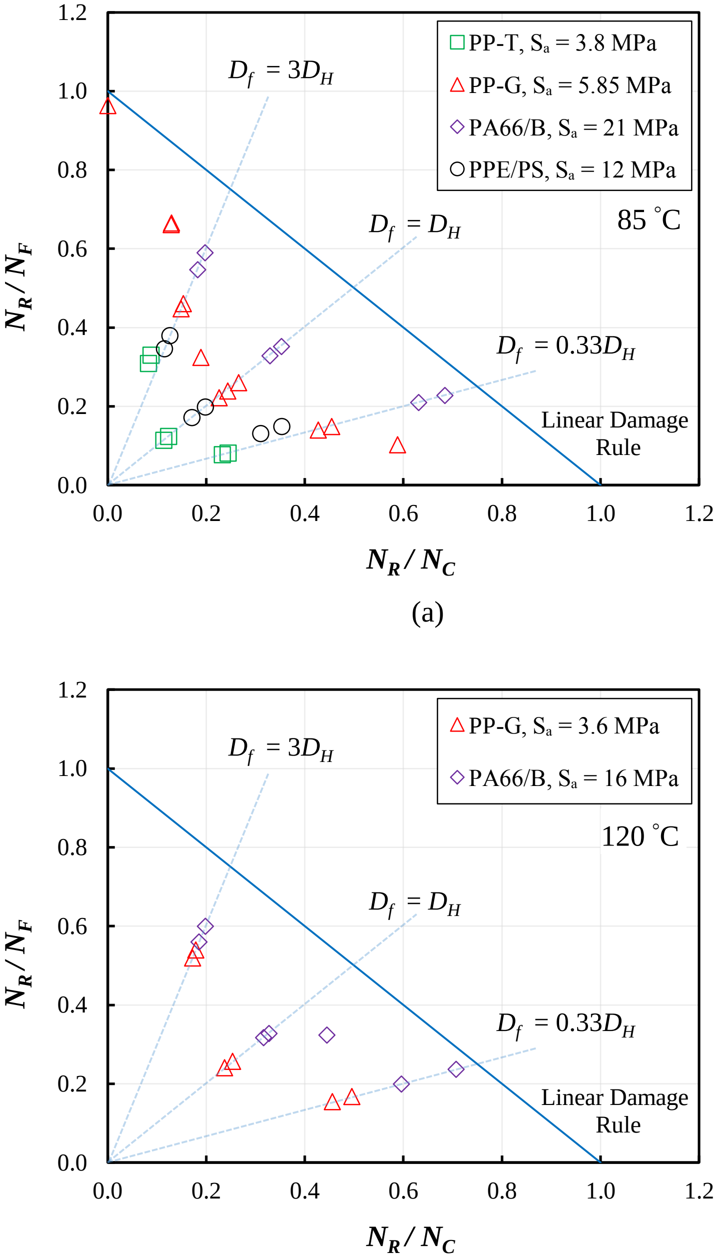

(a)

(b)

Figure 8-7: Cross plot of fractional cyclic life ratio versus hold-time life ratio (a) at 85 °C for all the studied materials and, (b) at 120 °C for PP-G and PA66/B.

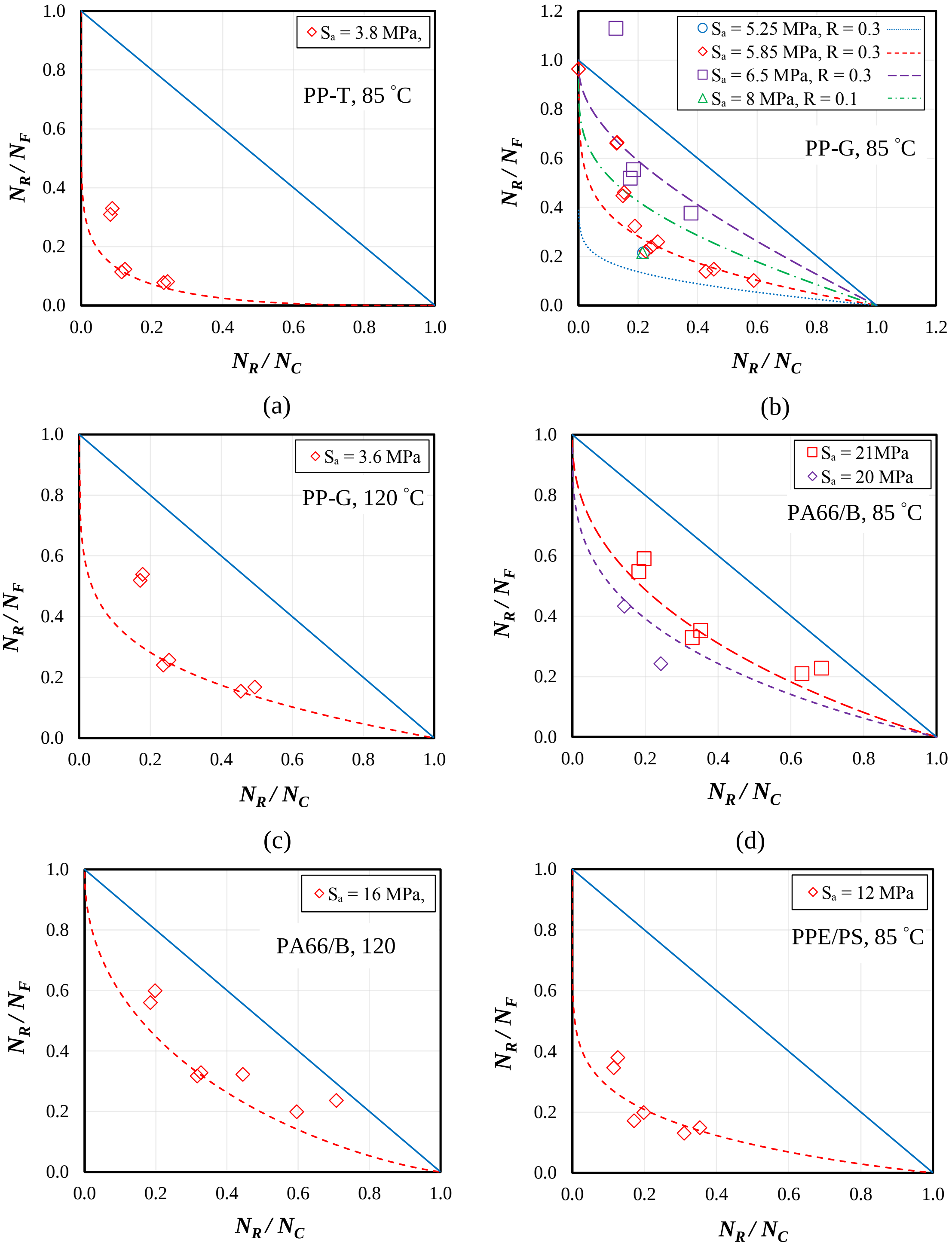

(a) (b)

(c) (d)

(e) (f)

Figure 8-8: Prediction of the non-linear interaction for cyclic and hold-time damages for (a) PP-T at 85 °C, (b) PP-G at 85 °C, (c) PP-G at 120 °C, (d) PA66/B at 85 °C, (e) PA66/B at 120 °C, and (f) PPE/PS at 85 °C. Data points are experimental results. Curves are predictions of Chaboche model and solid line is prediction of linear damage rule.

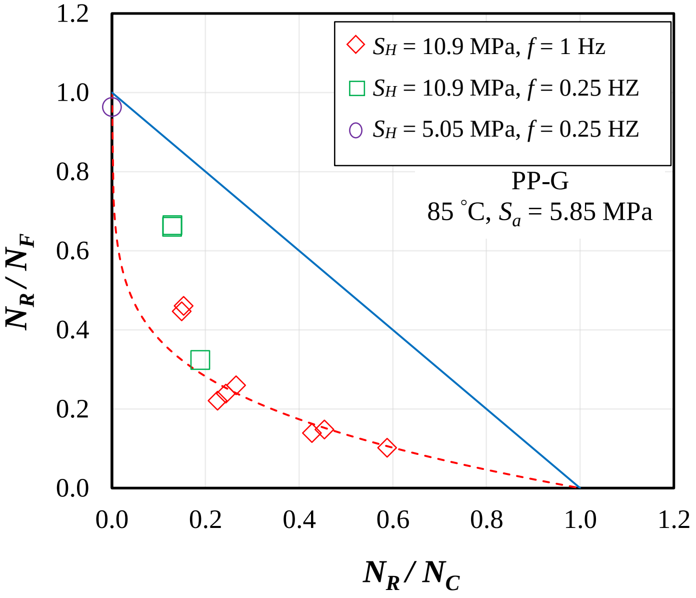

Figure 8-9: Effects of frequency and hold-stress position on creep-fatigue behavior of PP-G at 85 °C.

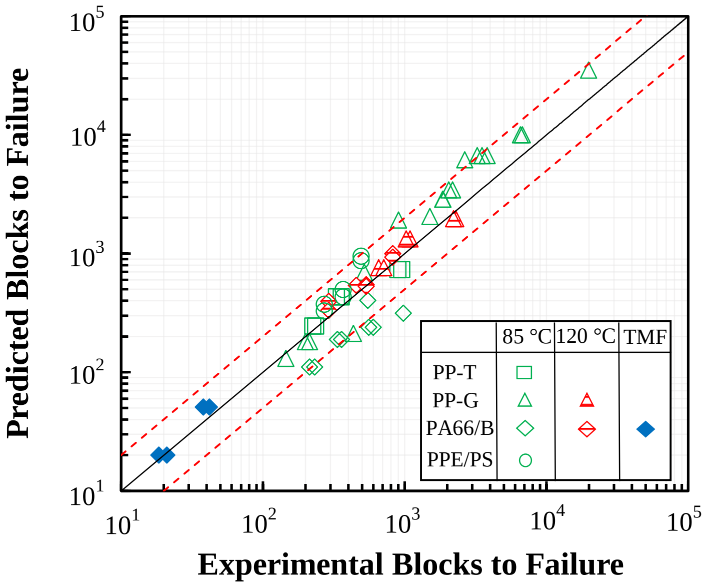

Figure 8-10: Predicted blocks to failure using Chaboch model versus experimental blocks to failure for creep-fatigue interaction and TMF test conditions.

Chapter 9

Summary and Conclusions

This study investigated tensile, creep, fatigue, creep-fatigue interaction, and thermo-mechanical fatigue behaviors and modeling of short glass fiber reinforced and talc-filled thermoplastic composites at elevated temperatures. An extensive literature survey was performed on mechanical behaviors of these materials at elevated temperatures. The mechanical behaviors included in this review, as well as the current study consist of tensile, creep, isothermal fatigue, thermo-mechanical fatigue, and creep-fatigue interaction. The main conclusions regarding each aspect studied, as well as some possible directions for the future research are summarized below.

9.1 Conclusions of Tensile Behavior Characterization

1) Stress-strain curve was considerably influenced by temperature for all materials. A linear reduction in tensile strength and elastic modulus with temperature was observed for PP-T, PP-G, and PPE/PS, materials for which T_g is not in the range of studied temperatures. However, for PA66/B and PA66/D, two different slopes were identified for variation of strength and stiffness at temperatures near and above T_g.
2) Polypropylene with short glass fibers was observed to have higher tensile strength and lower elastic modulus, as compared to talc-filled polypropylene. Talc has relatively high stiffness and increases the crystallinity index of the material.

However, it has a weak interfacial bond with polypropylene and creates voids resulting in reduced strength.

3) A Ramberg-Osgood type relation often used for metallic materials, represented the stress-strain relationship at all test conditions for all the studied materials well.

4) Polyamide-based composite was found to be highly moisture sensitive. However, full recovery of tensile properties was obtained by drying aged specimens in the laboratory environment at 80 °C for 24 hours in a vacuum chamber.

5) A Fickian behavior was observed for water absorption of PA66/B specimens immersed in 23 °C and 85 °C water. Maximum water absorption was independent of temperature, while the rate of water absorption increased dramatically with increasing temperature. Strength, elastic modulus, and strain at failure were considerably influenced by the amount of absorbed water. A parameter which incorporate both %wt of absorbed water and aging time in the form of $M_t\, t^{0.5}$ was used to correlate normalized elastic modulus and stiffness at different temperatures.

6) Water aging and also drying at elevated temperature increased crystallinity, and in turn that increased both stiffness and strength of PA66/B. For the aged specimens (both in 23 °C and 85 °C water), matrix yielding and plastic deformation were observed and hygrothermal aging at 85 °C were observed to considerably affect the fiber/matrix interface.

9.2 Conclusions of Creep Behavior Characterization

7) Creep resistant of studied thermoplastics significantly decreased with increasing temperature.

8) For polypropylene composites, the type of reinforcement (talc or short glass fiber) had the same effect on creep deformation. Reinforcement or filler did not change the creep mechanism noticeably and only resulted in improved creep strength (i.e. reduction of both creep strain and rate), as compared to the neat polymer.

9) The Larson-Miller parameter widely used for creep rupture correlations of metallic materials was used to correlate creep rupture data of all the materials. This parameter could also be used to predict long-term creep rupture data, based on short-term data.

10) The Findley power law model and time-stress superposition (TSS) method represented creep strain curves well. The TSS method could be used to predict long-term creep curves based on short-term creep data. This method could also satisfactory predict creep rupture data.

11) Minimum creep rate data were very well correlated by the Monkman-Grant relation and its modified version. Using the modified version, creep rupture strain, time to creep rupture, and creep rate are related together.

9.3 Conclusions of Isothermal Fatigue Behavior Characterization

12) Polypropylene with or without talc additive or short glass fiber reinforcement showed extended fatigue life with increasing frequency at a constant stress level, provided the effect of self-heating was not dominant. Loss tangent and area of hysteresis loop decreased with increasing frequency.

13) A higher matrix ductility was observed at lower frequencies, compared to at higher frequencies, based on SEM analysis. This was related to higher viscoelastic

damping and lower stiffness at lower frequencies which are believed to explain the shorter fatigue life at the lower frequencies.

14) For the materials for which the beneficial effect of increased frequency on fatigue life was dominant, the fatigue behavior observed to be more related to the time rather than cycles, provided that fatigue life was not considerably influenced by self-heating. Therefore, for these materials fatigue damage in addition to being cycle dependent is also a time-dependent phenomenon.

15) A Larson-Miller type parameter was successfully used to correlate stress amplitude, cycling frequency, test temperature, and cycles to failure for each materials at a given stress ratio.

16) Fatigue strength significantly reduced by increasing temperature for all the studied materials, as expected. For the materials for which T_g was less than the temperature range studied, the effect of temperature was observed to be larger. Also, the effect of temperature was more pronounced at higher stress ratio ($R = 0.3$ as compared to $R = 0.1$). The slope of S-N was observed to be nearly independent of temperature for a given material. Models based on time (or cycle) and temperature superposition principle were used to correlate the data.

17) Fatigue strength of PA66/D was higher than PA66/B, similar to tensile strength. The fatigue strength at 10^6 of PA66/B was about 90% and 85% of PA66/D at 23 °C and 85 °C, respectively.

18) For the conditions for which the testing temperature was less than T_g, brittle failure with flaky matrix, fiber pullouts regions, and breakage of fibers were observed.

When the test temperature was higher than T_g, ductile failure with a highly deformed matrix was evident.

19) The effect of mold flow direction on fatigue behavior was observed for talc-filled composite where fatigue strength was higher in the longitudinal direction, as compared to the transverse to the mold flow direction. However, this effect was much less as compared to what has been observed for short fiber reinforced thermoplastic composites. The slope of *S-N* line was observed to be independent of mold flow direction for this material.

20) The effect of mean stress on fatigue life was observed to depend on the stress level. For the conditions for which the maximum stress was higher than 0.2% yield stress of the material (matrix dominated failure), fatigue life was more related to the maximum stress with higher mean stress sensitivity. When the maximum stress was less than the yield stress of the material (crack growth dominated failure), fatigue life was more related to the amplitude of stress and mean stress sensitivity was lower. In addition, in low creep resistant materials, the detrimental effect of cyclic creep (mainly in HCF regime) added to the fatigue damage and caused a reduction in fatigue life. Depending on the mode of failure and the effect of cyclic creep on fatigue behavior, the slope of *S-N* line decreased, increased, or remained nearly constant with increasing stress ratio for a given material.

21) A general fatigue life prediction model was applied to correlate the fatigue data of different materials at different temperatures, frequencies, mean stress levels, and mold flow directions. The model resulted in good correlation of a total of 540 fatigue data (86% within a factor of 3 and 93% within a factor of 5).

9.4 Conclusions of Creep-Fatigue Interaction and TMF Behavior Characterizations

22) A non-linear creep-fatigue interaction behavior was observed for all the studied materials. The non-linearity of the interaction decreased with increasing stress level, while frequency and position of hold-time stress did not affect the creep-fatigue interaction curve.

23) The Chaboche pure fatigue model provides a good representation of *S*-*N* fatigue behavior and includes the mean stress correction parameter. A frequency term was added to the fatigue model in this study to be able to consider the beneficial effect of increased frequency for some thermoplastics.

24) Predictions of LDR were non-conservative for all the conditions evaluated. Chaboche creep-fatigue interaction model was used to predict the creep-fatigue life. This model which is based on continuum damage mechanics, considers the non-linear damage accumulation for creep-fatigue condition.

25) For TMF condition, an effective stress signal was obtained for an equivalent isothermal condition. Chaboche creep-fatigue interaction model within the concept of effective stress could very well predict the creep-fatigue interaction and TMF behavior with 91% of predicted lives within a factor of 2 of experimental lives.

9.5 Possible Directions for Future Investigation

1) This study emphasized on fatigue crack initiation. Crack growth life and application of fracture mechanics need to be evaluated.

2) Tests and modeling were conducted under uniaxial loading. Multiaxial stresses undoubtedly present in many components made of these materials. The multiaxial

behavior under proportional and non-proportional loadings can be explored and the results can be compared to the uniaxial loading.

3) All of the experiments were performed under constant amplitude loading for the smooth specimens. The cumulative damage from variable amplitude load histories and also for notched condition need to be evaluated.

4) For creep-fatigue interaction and TMF loading conditions, effect of hygrothermal aging similar to the effect of oxidation for metallic materials should be investigated and incorporated in the models.

5) All the models were generated and evaluated based on the experimental results for the test specimen. Applicability of the models for design of components should also be investigated.

References

[1] Biron M. Basic Criteria for the Selection of Thermoplastics. 2 ed: Elsevier, Oxford; 2013.

[2] Bhagwan DA, Lawrence JB, Chandrashekhara K. Analysis and Performance of Fiber Composites. 3 ed: Wiley, New Jersey; 2006.

[3] McCrum NG, Buckley CP, Bucknall CB. Principles of Polymer Engineering. 2 ed: Oxford University Press, Oxford; 1997.

[4] Eftekhari M, Fatemi A. Tensile, creep and fatigue behaviours of short fibre reinforced polymer composites at elevated temperatures: a literature survey. Fatigue & Fracture of Engineering Materials & Structures. 2015;38(12):1395-418.

[5] Schultz JM, Friedrich K. Effect of temperature and strain rate on the strength of a PET/glass fibre composite. Journal of Materials Science. 1984;19(7):2246-58.

[6] Valentin D, Paray F, Guetta B. The hygrothermal behaviour of glass fibre reinforced Pa66 composites: A study of the effect of water absorption on their mechanical properties. Journal of Materials Science. 1987;22(1):46-56.

[7] Liello VD, Martuscelli E, Ragosta G, Zihlif A. Mechanical properties of nylon 66/nickel-coated-carbon fibers composite. International Journal of Polymeric Materials and Polymeric Biomaterials. 1992;17(1-2):93-102.

[8] Zihlif AM, Liello VD, Martuscelli E, Ragosta G. Tensile properties and fracture behaviour of polycarbonate/PAN-based carbon fiber composite. International Journal of Polymeric Materials and Polymeric Biomaterials. 1995;29(3-4):211-20.

[9] Liello VD, Martuscelli E, Ragosta G, Zihlif A. Tensile properties and fracture behaviour of polypropylene-nickel-coated carbon-fibre composite. Journal of Materials Science. 1990;25(1):706-12.

[10] Liello VD, Martuscelli E, Ragosta G, Zihlif A. Effect of fibre surface treatment on yielding and fracture behaviour of glass fibre-polypropylene composite. Journal of Materials Science. 1991;26(8):2100-6.

[11] Eyring H. The activated complex in chemical reactions. The Journal of Chemical Physics. 1935;3(2):107-15.

[12] Miwa M, Endo I. Critical fibre length and tensile strength for carbon fibre-epoxy composites. Journal of Materials Science. 1994;29(5):1174-8.

[13] Miwa M, Horiba N. Strain rate and temperature dependence of tensile strength for carbon/glass fibre hybrid composites. Journal of Materials Science. 1993;28(24):6741-7.

[14] Miwa M, Horiba N. Effects of fibre length on tensile strength of carbon/glass fibre hybrid composites. Journal of Materials Science. 1994;29(4):973-7.

[15] Miwa M, Takeno A, Yamaguchi K, Watanabe A. Relation between shear strength at the fibre-matrix interphase and shear properties of resin matrix. Journal of Materials Science. 1995;30(8):2097-100.

[16] Gong X, Hine PJ, Duckett RA, Ward IM. The elastic properties of random-in-plane short fiber reinforced polymer composites. Polymer Composites. 1994;15(1):74-82.

[17] McGee S, McCullough RL. Combining rules for predicting the thermoelastic properties of particulate filled polymers, polymers, polyblends, and foams. Polymer Composites. 1981;2:149-53.

[18] Wang Z, Zhou Y, Mallick PK. Effects of temperature and strain rate on the tensile behavior of short fiber reinforced polyamide-6. Polymer Composites. 2002;23(5):858-71.

[19] Mouhmid B, Imad A, Benseddiq N, Benmedakhène S, Maazouz A. A study of the mechanical behaviour of a glass fibre reinforced polyamide 6,6: Experimental investigation. Polymer Testing. 2006;25(4):544-52.

[20] Hashemi S. Temperature, strain rate and weldine effects on strength and micromechanical parameters of short glass fibre reinforced polybutylene terephthalate (PBT). Polymer Testing. 2011;30(8):801-10.

[21] De Monte M, Moosbrugger E, Quaresimin M. Influence of temperature and thickness on the off-axis behaviour of short glass fibre reinforced polyamide 6.6 – Quasi-static loading. Composites Part A: Applied Science and Manufacturing. 2010;41(7):859-71.

[22] De Monte M, Moosbrugger E, Quaresimin M. Influence of temperature and fiber orientation on static and fatigue behavior of a short glass fiber reinforced polyamide 6.6. In Proceedings of XXXV AIAS National Conference, Ancona, Italy, 2006.

[23] Takahashi R, Shohji I, Seki Y, Maruyama S. Effect of fiber direction and temperature on mechanical properties of short fiber-reinforced PPS. In Proceedings of International Conference of Electronics Packaging (ICEP), Toyama, Japan, 2014.

[24] Lockwood KT, Zhang Y, Bates PJ, DuQuesnay DL. Effect of temperature on fatigue strength of vibration welded and unwelded glass reinforced nylon 6. International Journal of Fatigue. 2014;66:111-7.

[25] Zhang Y, Lockwood KT, Bates PJ, DuQuesnay DL. Fatigue properties of vibration-welded postindustrial waste nylon with glass fibers at room and elevated temperatures. Polymer Engineering & Science. 2014;55(4):799-806.

[26] Mortazavian S, Fatemi A. Tensile behavior and modeling of short fiber-reinforced polymer composites including temperature and strain rate effects. Journal of Thermoplastic Composite Materials. In Press, doi: 10.1177/0892705716632863, 2016.

[27] Mortazavian S, Fatemi A. Tensile and fatigue behaviors of polymers for automotive applications. Materialwissenschaft und Werkstofftechnik. 2015;46(2):204-13.

[28] Mortazavian S, Fatemi A. Effects of fiber orientation and anisotropy on tensile strength and elastic modulus of short fiber reinforced polymer composites. Composites Part B: Engineering. 2015;72:116-29.

[29] Lyons JS. Time and temperature effects on the mechanical properties of glass-filled amide-based thermoplastics. Polymer Testing. 1998;17(4):237-45.

[30] Jia N, Kagan VA. Effects of time and temperature on the tension-tension fatigue behavior of short fiber reinforced polyamides. Polymer Composites. 1998;19(4):408-14.

[31] Sinmazcelik T, Yilmaz T. Thermal aging effects on mechanical and tribological performance of PEEK and short fiber reinforced PEEK composites. Materials & Design. 2007;28(2):641-8.

[32] Fick A. Ueber diffusion. Annalen der Physik. 1855;170(1):59-86.

[33] Bastioli C, Guanella I, Romano G. Effects of water sorption on the physical properties of PET, PBT, and their long fibers composites. Polymer Composites. 1990;11(1):1-9.

[34] Ishak ZAM, Lim NC. Effect of moisture absorption on the tensile properties of short glass fiber reinforced poly(butylene terephthalate). Polymer Engineering & Science. 1994;34(22):1645-55.

[35] Ishak ZAM, Berry JP. Hygrothermal aging studies of short carbon fiber reinforced nylon 6.6. Journal of Applied Polymer Science. 1994;51(13):2145-55.

[36] Ishak ZAM, Berry JP. Effect of moisture absorption on the dynamic mechanical properties of short carbon fiber reinforced nylon 6, 6. Polymer Composites. 1994;15(3):223-30.

[37] Czigány T, Ishak ZAM, Karger-Kocsis J. On the failure mode in dry and hygrothermally aged short fiber-reinforced injection-molded polyarylamide composites by acoustic emission. Applied Composite Materials. 1995;2(5):313-26.

[38] Bergeret A, Pires I, Foulc MP, Abadie B, Ferry L, Crespy A. The hygrothermal behaviour of glass-fibre-reinforced thermoplastic composites: a prediction of the composite lifetime. Polymer Testing. 2001;20(7):753-63.

[39] Carrascal I, Casado JA, Polanco JA, Gutiérrez-Solana F. Absorption and diffusion of humidity in fiberglass-reinforced polyamide. Polymer Composites. 2005;26(5):580-6.

[40] Hassan A, Rahman N, Yahya R. Moisture absorption effect on thermal, dynamic mechanical and mechanical properties of injection-molded short glass-fiber/polyamide 6,6 composites. Fibers and Polymers. 2012;13(7):899-906.

[41] Ghasemzadeh-Barvarz M, Duchesne C, Rodrigue D. Mechanical, water absorption, and aging properties of polypropylene/flax/glass fiber hybrid composites. Journal of Composite Materials. In Press, doi: 10.1177/0021998314568576, 2015.

[42] Cessna LC. Stress-time superposition of creep data for polypropylene and coupled glass-reinforced polypropylene. Polymer Engineering & Science. 1971;11(3):211-9.

[43] Gupta VB, Lahiri J. Non linear viscoelastic behavior of polypropylene and glass reinforced polypropylene in creep. Journal of Composite Materials. 1980;14(4):286-96.

[44] Findley WN. Mechanism and mechanics of creep of plastics. SPEJ. 1960;16:57-65.

[45] Pipes BR, McCullough RL, Taggart DG. Behavior of discontinuous fiber composites: fiber orientation. Polymer Composites. 1982;3(1):34-9.

[46] Silverman EM. Effect of glass fiber length on the creep and impact resistance of reinforced thermoplastics. Polymer Composites. 1987;8(1):8-15.

[47] Hugo J, Sova M, Čižinský J. Creep and creep damage of glass fibre reinforced polypropylene. Composite Structures. 1993;24(3):233-44.

[48] Pegoretti A, Ricco T. Creep crack growth in a short glass fibres reinforced polypropylene composite. Journal of Materials Science. 2001;36(19):4637-41.

[49] Hadid M, Rechak S, Zouani A. Empirical nonlinear viscoelastic model for injection molded thermoplastic composite. Polymer Composites. 2002;23(5):771-8.

[50] Chevali VS, Dean DR, Janowski GM. Flexural creep behavior of discontinuous thermoplastic composites: non-linear viscoelastic modeling and time–temperature–

stress superposition. Composites Part A: Applied Science and Manufacturing. 2009;40(6–7):870-7.

[51] Houshyar S, Shanks RA, Hodzic A. Tensile creep behaviour of polypropylene fibre reinforced polypropylene composites. Polymer Testing. 2005;24(2):257-64.

[52] Plaseied A, Fatemi A. Tensile creep and deformation modeling of vinyl ester polymer and its nanocomposite. Journal of Reinforced Plastics and Composites. 2009;28(14):1775-88.

[53] Kouadri-Boudjelthia A, Imad A, Bouabdallah A, Elmeguenni M. Analysis of the effect of temperature on the creep parameters of composite material. Materials & Design. 2009;30(5):1569-74.

[54] Mortazavian S, Fatemi A. Fatigue behavior and modeling of short fiber reinforced polymer composites: a literature review. International Journal of Fatigue. 2015;70(0):297-321.

[55] Handa K, Kato A, Narisawa I. Fatigue characteristics of a glass-fiber-reinforced polyamide. Journal of Applied Polymer Science. 1999;72(13):1783-93.

[56] Sonsino CM, Moosbrugger E. Fatigue design of highly loaded short-glass-fibre reinforced polyamide parts in engine compartments. International Journal of Fatigue. 2008;30(7):1279-88.

[57] De Monte M, Moosbrugger E, Quaresimin M. Influence of temperature and thickness on the off-axis behaviour of short glass fibre reinforced polyamide 6.6 – cyclic loading. Composites Part A: Applied Science and Manufacturing. 2010;41(10):1368-79.

[58] Noda K, Takahara A, Kajiyama T. Fatigue failure mechanisms of short glass-fiber reinforced nylon 66 based on nonlinear dynamic viscoelastic measurement. Polymer. 2001;42(13):5803-11.

[59] Guster C, Pinter G, Mösenbacher A, Eichlseder W. Effects of temperature and moisture on the tensile/tensile fatigue behavior of an injection molded sgf-reinforced partial aromatic polyamide. 12th International Conference on Fracture. Ottawa, Canada, 2009.

[60] Guster C, Pinter G, Mösenbacher A, Eichlseder W. Evaluation of a simulation process for fatigue life calculation of short fibre reinforced plastic components. Procedia Engineering. 2011;10(0):2104-9.

[61] Mortazavian S, Fatemi A. Fatigue behavior and modeling of short fiber reinforced polymer composites including anisotropy and temperature effects. International Journal of Fatigue. 2015;77:12-27.

[62] Mortazavian S, Fatemi A. Effects of mean stress and stress concentration on fatigue behavior of short fiber reinforced polymer composites. Fatigue & Fracture of Engineering Materials & Structures. 2016;39(2):149-66.

[63] Pierantoni M, De Monte M, Papathanassiou D, De Rossi N, Quaresimin M. Viscoelastic material behaviour of PBT-GF30 under thermo-mechanical cyclic loading. Procedia Engineering. 2011;10(0):2141-6.

[64] Schaaf A, De Monte M, Hoffmann C, Vormwald M, Quaresimin M. Damage mechanisms in PBT-GF30 under thermo-mechanical cyclic loading. AIP Conference Proceedings. 2014;1593(1):600-5.

[65] Schaaf A, De Monte M, Moosbrugger E, Vormwald M, Quaresimin M. . Life estimation methodology for short fiber reinforced polymers under thermo-mechanical loading in automotive applications. 4th symposium on structural durability. Darmstadt, Germany, 2014.

[66] Bowman J, Barker MB. A methodology for describing creep-fatigue interactions in thermoplastic components. Polymer Engineering & Science. 1986;26(22):1582-90.

[67] Crowther MF, Wyatt RC, Phillips MG. Creep-fatigue interactions in glass fibre/polyester composites. Composites Science and Technology. 1989;36(3):191-210.

[68] Pegoretti A, Ricco T. Fatigue fracture of neat and short glass fiber reinforced polypropylene: effect of frequency and material orientation. Journal of Composite Materials. 2000;34(12):1009-27.

[69] Pegoretti A, Ricco T. Crack growth in discontinuous glass fibre reinforced polypropylene under dynamic and static loading conditions. Composites Part A: Applied Science and Manufacturing. 2002;33(11):1539-47.

[70] Pegoretti A, Ricco T. Fatigue crack propagation in polypropylene reinforced with short glass fibres. Composites Science and Technology. 1999;59(7):1055-62.

[71] Hertzberg RW, Manson JA, Skibo M. Frequency sensitivity of fatigue processes in polymeric solids. Polymer Engineering & Science. 1975;15(4):252-60.

[72] Harutun GK. Handbook of Polypropylene and Polypropylene Composites. 2 ed: Marcel Dekker, New York; 2003.

[73] Wilkes CE, Summers JW, Daniels CA. PVC Handbook. Hanser-Gardner, Cincinnati; 2005.

[74] www.asahi-kasei.co.jp.

[75] Harper C. Modern Plastics Handbook. McGraw-Hill, New York; 2000.

[76] Brydson JA. Plastics Materials. Butterworth-Heinemann, Oxford; 1999.

[77] Mellott SR. Tensile, creep, and fatigue behaviors of thermoplastics including thickness, mold flow direction, mean stress, temperature, and loading rate effects. Master Thesis, The University of Toledo, Toledo, Ohio, 2012.

[78] Mortazavian S. Fatigue behavior and modeling of short fiber reinforced polymer composites. PhD Dissertation, The University of Toledo, Toledo, Ohio, 2015.

[79] ASTM E1012-05. Standard practice for verification of testing frame and specimen alignment under tensile and compressive axial force application. ASTM International, West Conshohocken, PA; 2005.

[80] ISO 527-1. Plastics - determination of tensile properties. International Organization for Standardization, Geneva, Switzerland; 1993.

[81] ASTM D638-10. Standard test method for tensile propertie of plastics. ASTM International, West Conshohocken, PA; 2009.

[82] ASTM D2990-09. Standard test methods for tensile, compressive, and flexural creep and creep-rupture of plastics, ASTM International, West Conshohocken, PA; 2009.

[83] ISO 899-1. Plastics - determination of creep behavior. International Organization for Standardization, Geneva, Switzerland; 2003.

[84] ASTM D7791-12. Standard test method for uniaxial fatigue properties of plastics, ASTM International, West Conshohocken, PA, 2012.

[85] ASTM E2714-13. Standard test method for creep-fatigue testing, ASTM International, West Conshohocken, PA, 2013.

[86] ASTM D7028-07. Standard test method for glass transition temperature (DMA Tg) of polymer matrix composites by dynamic mechanical analysis (DMA). ASTM International, West Conshohocken, PA, 2007.

[87] ASTM D5418-07. Standard test method for plastics: dynamic mechanical properties: in flexure (dual cantilever beam). ASTM International, West Conshohocken, PA, 2007.

[88] ASTM D4065-12. Standard practice for plastics: dynamic mechanical properties: determination and report of procedures. ASTM International,West Conshohocken, PA, 2012.

[89] ASTM D3418-03. Standard test method for transition temperatures and enthalpies of fusion and crystallization of polymers by differential scanning calorimetry. ASTM International, West Conshohocken, PA, 2003.

[90] www2.dupont.com

[91] www.basf.com.

[92] www.sabic-ip.com.

[93] www.matweb.com.

[94] www.chemistryrules.me.uk.

[95] Eftekhari M, Fatemi A. Tensile behavior of thermoplastic composites including temperature, moisture, and hygrothermal effects. Polymer Testing. 2016;51:151-64.

[96] Thomason JL. The influence of fibre length and concentration on the properties of glass fibre reinforced polypropylene: 5. Injection moulded long and short fibre PP. Composites Part A: Applied Science and Manufacturing. 2002;33(12):1641-52.

[97] Mortazavian S, Fatemi A, Khosrovaneh A. Effect of water absorption on tensile and fatigue behavior of short glass fiber polyamide-6 and short glass fiber polybutylene terephthalate. SAE International Journal of Material and Manufacturing. 2015;8(2):435-43.

[98] Illing T, Schoßig M, Bierögel C, Grellmann W. Influence of hygrothermal aging on dimensional stability of thin injection-molded short glass fiber reinforced PA6 materials. Journal of Applied Polymer Science. 2015;132(28):1-12.

[99] Ishak ZAM, Ishiaku US, Karger-Kocsis J. Hygrothermal aging and fracture behavior of short-glass-fiber-reinforced rubber-toughened poly(butylene terephthalate) composites. Composites Science and Technology. 2000;60(6):803-15.

[100] Foulc MP, Bergeret A, Ferry L, Ienny P, Crespy A. Study of hygrothermal ageing of glass fibre reinforced PET composites. Polymer Degradation and Stability. 2005;89(3):461-70.

[101] Ishak ZAM, Ariffin A, Senawi R. Effects of hygrothermal aging and a silane coupling agent on the tensile properties of injection molded short glass fiber reinforced poly(butylene terephthalate) composites. European Polymer Journal. 2001;37(8):1635-47.

[102] Bian XS, Ambrosio L, Kenny JM, Nicolais L, Dibenedetto AT. Effect of water absorption on the behavior of E-glass fiber/nylon-6 composites. Polymer Composites. 1991;12(5):333-7.

[103] ASTM E646-16. Standard test method for tensile strain-hardening exponents (n -Values) of metallic sheet materials, ASTM International, West Conshohocken, PA, 2016.

[104] Zhou Y, Mallick PK. Effects of temperature and strain rate on the tensile behavior of unfilled and talc-filled polypropylene. Part I: Experiments. Polymer Engineering & Science. 2002;42(12):2449-60.

[105] Zihlif AM, Ragosta G. Mechanical properties of talc-polypropylene composites. Materials Letters. 1991;11(10–12):368-72.

[106] Meijer HEH, Govaert LE. Mechanical performance of polymer systems: the relation between structure and properties. Progress in Polymer Science. 2005;30(8–9):915-38.

[107] Ishida H, Koenig JL. The reinforcement mechanism of fiber-glass reinforced plastics under wet conditions: a review. Polymer Engineering & Science. 1978;18(2):128-45.

[108] Cran J. The Mathematics of Diffusion. 2 ed: Clarendon Press, Oxford; 1975.

[109] Broudin M, Le Gac PY, Le Saux V, Champy C, Robert G, Charrier P, et al. Water diffusivity in PA66: experimental characterization and modeling based on free volume theory. European Polymer Journal. 2015;67(0):326-34.

[110] Thomason JL, Porteus G. Swelling of glass-fiber reinforced polyamide 66 during conditioning in water, ethylene glycol, and antifreeze mixture. Polymer Composites. 2011;32(4):639-47.

[111] Thomason JL, Ali JZ. The dimensional stability of glass–fibre reinforced polyamide 66 during hydrolysis conditioning. Composites Part A: Applied Science and Manufacturing. 2009;40(5):625-34.

[112] Belmonte E, De Monte M, Quaresimin M, Hoffmann C. Damage mechanisms of short glass fiber reinforced polyamide 6.6 under fatigue loading. 16th European Conference on Composite Materials. Seville, Spain, 2014.

[113] Eftekhari M, Fatemi A. Creep behavior of thermoplastic and their composites. Journal of Composite Part B: Engineering. 2016;97:68-83.

[114] Drozdov AD. Creep rupture and viscoelastoplasticity of polypropylene. Engineering Fracture Mechanics. 2010;77(12):2277-93.

[115] Hamouda HBH, Simoes-betbeder M, Grillon F, Blouet P, Billon N, Piques R. Creep damage mechanisms in polyethylene gas pipes. Polymer. 2001;42(12):5425-37.

[116] Dean GD, Broughton W. A model for non-linear creep in polypropylene. Polymer Testing. 2007;26(8):1068-81.

[117] Luo W-b, Wang C-h, Vu-Khanh T, Jazouli S. Time-stress equivalence: application to nonlinear creep of polypropylene. Journal of Central South University of Technology. 2007;14(1):310-3.

[118] Zhao R-g, Chen C-z, Li Q-f, Luo W-b. Effects of stress and physical ageing on nonlinear creep behavior of poly(methyl methacrylate). Journal of Central South University Technology. 2008;15(1):582-8.

[119] Qaiser A, Price J. Estimation of long-term creep behavior of polycarbonate by stress-time superposition and effects of physical aging. Mechanics of Time-Dependent Materials. 2011;15(1):41-50.

[120] Spathis G, Kontou E. Creep failure time prediction of polymers and polymer composites. Composites Science and Technology. 2012;72(9):959-64.

[121] Teoh SH, Cherry BW, Kausch HH. Creep rupture modelling of polymers. International Journal of Damage Mechanics. 1992;1(2):245-56.

[122] Seltzer R, Mai Y-W, Frontini PM. Creep behaviour of injection moulded polyamide 6/organoclay nanocomposites by nanoindentation and cantilever-bending. Composites Part B: Engineering. 2012;43(1):83-9.

[123] Arrhenius SA. Über die Dissociationswärme und den Einflusß der Temperatur auf den Dissociationsgrad der Elektrolyte. Z Physik Chem. 1889;4:96-116.

[124] Larson FR, Miller. Time-temperature relationship for rupture and creep stresses. Trans ASME. 1952;74:765-75.

[125] Manson SS, Haferd AM. A linear time-temperature relation for extrapolation of creep and stress-rupture data. Technical Note 2890, NACA. 1953.

[126] Sherby OD, Dorn JE. Creep correlations in alpha solid solutions of aluminum. Transactions of AIME. 1952;194.

[127] Manson SS, Succop G. Stress-rupture properties of inconel 700 alloy and their correlation with some time-temperature curve parameters. in: Heat-Resisting Metallic Materials [Russian translation], IL, Moscow. 1958.

[128] Manson SS, Muralidharan U. Analysis of creep rupture data for five multi-heat alloys by the minimum commitment method using double het term centering technique. EPRI CS 317, Electric Power Research Institute, Palo Alto, CA. 1983.

[129] Wilson DJ, Marrone RE, Freeman JW. Larson-Miller and Manson-Haferd parameter extrapolation of rupture data for type 304 (18Cr-8Ni), Grade 22 (2-1/4Cr-1Mo) and grade 11 (1-1/4Cr-1/2Mo-3/4Si) steels. The University of Michigan, Office of Research Administration, Ann Arbor, Michigan. 1968.

[130] Raghavan J, Meshii M. Creep of polymer composites. Composites Science and Technology. 1998;57(12):1673-88.

[131] Hadid M, Rechak S, Tati A. Long-term bending creep behavior prediction of injection molded composite using stress–time correspondence principle. Materials Science and Engineering: A. 2004;385(1–2):54-8.

[132] Lai JSY, Findley WN. Elevated temperature creep of polyurethane under nonlinear torsional stress with step changes in torque. Transactions of The Society of Rheology. 1973;17(1):129-50.

[133] David W. Scott JSL. Creep behavior of fiber-reinforced polymeric composites: a review of the technical literature. Journal of Reinforced Plastics and Composites. 1995;14(6):588-617.

[134] Norton FH. The Creep of Steel at High Temperature. McGraw Hill, New York; 1929.

[135] Pang F, Wang CH. Activation theory for creep of woven composites. Composites Part B: Engineering. 1999;30(6):613-20.

[136] Monkman FC, Grant NJ. An empirical relationship between rupture life and minimum creep rate in creep-rupture tests. ASTM Proceeding. 1956;56:593-620.

[137] Dobes F, Milicka K. The relation between minimum creep rate and time to fracture. Metal Science. 1976;10.

[138] Povolo F. Comments on the Monkman-Grant and the modified Monkman-Grant relationships. Journal of Materials Science. 1985;20(6):2005-10.

[139] Lai J, Bakker A. Analysis of the non-linear creep of high-density polyethylene. Polymer. 1995;36(1):93-9.

[140] Jazouli S, Luo W, Bremand F, Vu-Khanh T. Application of time–stress equivalence to nonlinear creep of polycarbonate. Polymer Testing. 2005;24(4):463-7.

[141] Malcolm LW, Landel RF, Ferreira JD. The temperature dependence of relaxation mechanisms in amorphous polymers and other glass-forming liquids. Journal of the American Chemical Society. 1955;77:3701-7.

[142] Findley WN. 26-Year creep and recovery of poly(vinyl chloride) and polyethylene. Polymer Engineering & Science. 1987;27(8):582-5.

[143] Eftekhari M, Fatemi A. On the strengthening effect of increasing cycling frequency on fatigue behavior of some polymers and their composites: Experiments and modeling. International Journal of Fatigue. 2016;87:153-66.

[144] Fatemi A, Mellot SR, Khosrovaneh A, Buehler C. Tensile and fatigue behaviors of two thermoplastics including strain rate, temperature, and mean stress effects. SAE Technical Paper. 2014, 2014-01-0901.

[145] Hahn MT, Hertzberg RW, Manson JA, Lang RW, Bretz PE. Effect of test frequency and water content on localized crack-tip heating in nylon-6,6. Polymer. 1982;23(11):1675-9.

[146] Lang RW, Manson JA. Crack tip heating in short-fibre composites under fatigue loading conditions. Journal of Materials Science. 1987;22(10):3576-80.

[147] Takahara A, Magome T, Kajiyama T. Effect of glass fiber-matrix polymer interaction on fatigue characteristics of short glass fiber-reinforced poly(butylene terephthalate) based on dynamic viscoelastic measurement during the fatigue process. Journal of Polymer Science Part B: Polymer Physics. 1994;32(5):839-49.

[148] Bellenger V, Tcharkhtchi A, Castaing P. Thermal and mechanical fatigue of a PA66/glass fibers composite material. International Journal of Fatigue. 2006;28(10):1348-52.

[149] Bernasconi A, Kulin RM. Effect of frequency upon fatigue strength of a short glass fiber reinforced polyamide 6: a superposition method based on cyclic creep parameters. Polymer Composites. 2009;30(2):154-61.

[150] Berrehili A, Nadot Y, Castagnet S, Grandidier JC, Dumas C. Multiaxial fatigue criterion for polypropylene – Automotive applications. International Journal of Fatigue. 2010;32(8):1389-92.

[151] Esmaeillou B, Ferreira P, Bellenger V, Tcharkhtchi A. Fatigue behavior of polyamide 66/glass fiber under various kinds of applied load. Polymer Composites. 2012;33(4):540-7.

[152] Jegou L, Marco Y, Le Saux V, Calloch S. Fast prediction of the Wöhler curve from heat build-up measurements on Short Fiber Reinforced Plastic. International Journal of Fatigue. 2013;47(0):259-67.

[153] Mortazavian S, Fatemi A, Mellott SR, Khosrovaneh A. Effect of cycling frequency and self-heating on fatigue behavior of reinforced and unreinforced thermoplastic polymers. Polymer Engineering & Science. 2015;55(10):2355-67.

[154] Shrestha R, Simsiriwong J, Shamsaei N, Moser RD. Cyclic deformation and fatigue behavior of polyether ether ketone (PEEK). International Journal of Fatigue. 2016;82(3):411-27.

[155] Zhou Y, Mallick PK. Fatigue performance of an injection molded talc-filled polypropylene. Polymer Engineering & Science. 2005;45(4):510-6.

[156] Zhou Y, Mallick PK. Fatigue performance of an injection-molded short E-glass fiber-reinforced polyamide 6,6. I. Effects of orientation, holes, and weld line. Polymer Composites. 2006;27(2):230-7.

[157] Manson JA, Hertzberg RW, Kim SL, Skibo M. The β transition and frequency sensitivity in fatigue crack propagation of polymers. Polymer. 1975;16(11):850-1.

[158] Cheng WM, Miller GA, Manson JA, Hertzburg RW, Sperling LH. Mechanical behaviour of poly(methyl methacrylate). Journal of Materials Science. 1990;25:1917-23.

[159] Radon JC, Culver LE. Effect of temperature and frequency in fatigue of polymers. Polymer. 1975;16(7):539-44.

[160] Radon JC, Culver LE. Fatigue crack growth in polymers. I. Effect of frequency and temperature. Polymer Engineering & Science. 1975;15(7):500-6.

[161] Dumpleton P, Bucknall CB. Comparison of static and dynamic fatigue crack growth rates in high-density polyethylene. International Journal of Fatigue. 1987;9(3):151-5.

[162] McKenna GB, Penn RW. Time-dependent failure in poly(methyl methacrylate) and polyethylene. Polymer. 1980;21(2):213-20.

[163] Chou YF, Sun CT. Modeling of the frequency effect on fatigue crack propagation in PMMA. Engineering Fracture Mechanics. 1983;17(1):17-26.

[164] Wyzgoski MG, Novak GE, Simon DL. Fatigue fracture of nylon polymers. Journal of Materials Science. 1990;25(10):4501-10.

[165] Sauer JA, Richardson GC. Fatigue of polymers. International Journal of Fracture. 1980;16(6):499-532.

[166] Mandell JF, Meier U. Effect of stress ratio, frequency and loading time on the tensile fatigue of glass-reinforced epoxy. ASTM STP 813. 1982:55-77.

[167] Saff CR. Effect of load frequency and lay-up on fatigue life of composites. ASTM STP 813. 1983:78-91.

[168] Tsai GC, Doyle JF, Sun CT. Frequency effects on the fatigue life and damage of graphite/epoxy composites. Journal of Composite Materials. 1987;21(1):2-13.

[169] Huang A, Yao W, Chen F. Analysis of fatigue life of PMMA at different frequencies based on a new damage mechanics model. Mathematical Problems in Engineering. 2014;8.

[170] Epaarachchi JA, Clausen PD. An empirical model for fatigue behavior prediction of glass fibre-reinforced plastic composites for various stress ratios and test frequencies. Composites Part A: Applied Science and Manufacturing. 2003;34(4):313-26.

[171] Seidel A. Characterization and Analysis of Polymers. Wiley, New Jersey; 2008.

[172] Parsons M, Stepanov EV, Hiltner A, Baer E. Effect of strain rate on stepwise fatigue and creep slow crack growth in high density polyethylene. Journal of Materials Science. 2000;35(8):1857-66.

[173] Horst JJ, Spoormaker JL. Mechanisms of fatigue in short glass fiber reinforced polyamide 6. Polymer Engineering and Science. 1996;36(22):2718-26.

[174] Horst JJ, Spoormaker JL. Fatigue fracture mechanisms and fractography of short-glassfibre-reinforced polyamide 6. Journal of Materials Science. 1997;32(14):3641-51.

[175] Eftekhari M, Fatemi A. Fatigue behavior and modeling of talc-filled and short glass fiber reinforced thermoplastics, including temperature and mean stress effects. Fatigue & Fracture of Engineering Materials & Structures. 2016. Accepted for Publication.

[176] Bernasconi A, Davoli P, Basile A, Filippi A. Effect of fibre orientation on the fatigue behaviour of a short glass fibre reinforced polyamide-6. International Journal of Fatigue. 2007;29(2):199-208.

[177] Jain A, Veas JM, Straesser S, Van Paepegem W, Verpoest I, Lomov SV. The master SN curve approach – A hybrid multi-scale fatigue simulation of short fiber reinforced composites. Composites Part A: Applied Science and Manufacturing. doi:10.1016/j.compositesa.2015.11.038, 2015.

[178] Kanters MJW, Kurokawa T, Govaert LE. Competition between plasticity-controlled and crack-growth controlled failure in static and cyclic fatigue of polymer systems. Polymer Testing. 2016;50:101-10.

[179] Zhou J, D'Amore A, Yang Y, He T, Li B, Nicolais L. Flexural fatigue of short glass fiber reinforced a blend of polyphenylene ether ketone and polyphenylene sulfide. Applied Composite Materials. 2010;1(3):183-95.

[180] Mellott SR, Fatemi A. Fatigue behavior and modeling of thermoplastics including temperature and mean stress effects. Polymer Engineering & Science. 2014;54(3):725-38.

[181] Eftekhari M, Fatemi A. Creep-fatigue interaction and thermo-mechanical fatigue behavior of thermoplastics and their composites. International Journal of Fatigue. 2016;91(1):136-48.

[182] Rees DWA. Life prediction techniques for combined creep and fatigue. Progress in Nuclear Energy. 1987;19(3):211-39.

[183] Halford GR, Hirschberg MH, Manson SS. Temperature effects on the strain-range partitioning approach for creep-fatigue analysis. American Society for Testing and Materials, Symposium on Fatigue at Elevated Temperatures, Storrs, CT. 1972.

[184] Lemaitre J, Chaboche JL. A non-linear model of creep-fatigue damage accumulation and interaction. In Proceedings of Symposium on Mechanics of Viscoelastic Media and Bodies. Guthenburd, Sweden, 1974.

[185] Neu RW, Sehitoglu H. Thermomechanical fatigue, oxidation, and creep: Part I. Damage mechanisms. Metallurgical Transactions A. 1989;20(9):1755-67.

[186] Neu RW, Sehitoglu H. Thermomechanical fatigue, oxidation, and Creep: Part II. Life prediction. Metallurgical Transactions A. 1989;20(9):1769-83.

[187] Slavik D, Sehitoglu H. Constitutive models suitable for thermal loading. Journal of Engineering Materials and Technology. 1986;108(4):303-12.

[188] Eftekhari M, Fatemi A, Khosrovaneh A. Fatigue behavior of neat and short glass fiber reinforced polymers under two-step loadings and periodic overloads. SAE International Journal of Materials and Manufacturing. 2016;9(3). doi:10.4271/2016-01-0373.

[189] Chaboche JL, Gallerneau F. An overview of the damage approach of durability modelling at elevated temperature. Fatigue & Fracture of Engineering Materials & Structures. 2001;24(6):405-18.

[190] Lemaitre J, Chaboche JL. Mechanics of Solid Materials. Cambridge University Press, Cambridge; 1990.

[191] Halfpenny A, Anderson R, Lin X. Isothermal and thermo-mechanical fatigue of automotive components. SAE Technical Paper. 2015, 2015-01-0548.

[192] Rabotnov YN. Creep Problems in Structural Members. North-Holland Publishing, Amsterdam; 1969.

[193] Kachanov LM. Time of the rupture process under creep conditions: Izv. Akad. Nauk. SSSR. Otd. Tekh. Nauk, 1958(8):26-31.

[194] Chaboche JL, Lesne PM. A non-linear continuous fatigue damage model. Fatigue & Fracture of Engineering Materials & Structures. 1988;11(1):1-17.

[195] Telesman J, Gabb TP, Ghosn LJ, Gayda J. Effect of notches on creep–fatigue behavior of a P/M nickel-based superalloy. International Journal of Fatigue. 2016;87:311-25.